A Study of Brass Instrument Acoustics using an Artificial Lip Reed Mechanism, Laser Doppler Anemometry and Other Techniques

John Stuart Cullen

A thesis submitted in fulfilment of the requirements

for the degree of Doctor of Philosophy

to the

University of Edinburgh

2000

Abstract

The self-sustained oscillation of a brass wind musical instrument involves a complex aerodynamic coupling between a multimode mechanical vibratory system (the lips of the player) and a multimode acoustical vibratory system (the air column of the instrument). In this thesis the behaviour of the coupled system near the threshold of oscillation is investigated using a simplified model in which a single mechanical lip mode is coupled to a single mode of the acoustical resonator by air flow through the lips. The theoretical threshold behaviour is compared with the measured threshold behaviour of a trombone sounded by an artificial lip reed mechanism. Comparability between theory and experiment is ensured by using model parameter values derived from mechanical response measurements on the artificial lips and input impedance measurements on the trombone.

The mechanical response measurements can be used to classify mechanical modes of the artificial lips unambiguously as either "inward striking" or "outward striking". Each of the embouchures considered is found to have at least one mechanical mode of each category. The experimentally observed threshold frequencies of the coupled system suggest a behaviour which passes smoothly from "inward striking" to "outward striking" character as the trombone slide is extended or the embouchure parameters changed. It seems unlikely that this type of behaviour can be explained using a lip model with only a single degree of freedom.

After a discussion of the theory of laser Doppler anemometry (LDA), the technique is applied to the problem of measuring the instantaneous acoustic particle velocity within a standing wave pipe driven by a loudspeaker. The resulting Doppler signals display quasi-periodic amplitude modulation with a fundamental frequency equal to the frequency of the acoustic field. The phenomenon of amplitude modulation is investigated in some detail.

Two different methods of analysing Doppler signals are compared: the digital Hilbert transform and the Disa analogue frequency tracker; the analogue tracker is found to offer the greater signal-to-noise ratio and dynamic range. Experiments are carried out to establish how phase errors introduced by the analogue tracker can be minimised.

Velocity measurements extracted from Doppler signals using the analogue tracker are compared with the velocity deduced by applying basic theory to probe microphone pressure measurements. It is found that the acoustic particle velocity amplitude can be measured accurately over the entire frequency range considered, and the phase of the acoustic particle velocity also agrees well with theory, but not at low frequencies. LDA is successfully applied to the measurement of multi-harmonic sound fields. The technique of ensemble averaging velocity signals is shown to be particularly useful.

LDA is used to measure the velocity in the backbore of a specially designed transparent mouthpiece, driven by the artificial lip reed. Although significant levels of turbulence are encountered, it is shown that acoustic components can still be clearly distinguished in frequency domain representations of the measured velocity. However LDA measurements in the mouthpiece are restricted to conditions where the acoustic particle velocity amplitude and the turbulent intensity are sufficiently low to ensure that the bandwidth of the Doppler signal is less than the bandwidth of the apparatus used to capture or process the Doppler signal.

LDA measurements in brass instrument mouthpieces should provide a better understanding of the air flow into the mouthpiece and may lead to an improved model for self-sustained oscillation of the coupled system which more accurately describes the air flow.

Declaration

I declare that this thesis was composed by myself and that the work contained therein is my own, except where explicitly stated otherwise in the text.

(*John S. Cullen*)
May 2000

Acknowledgements

I would like to thank Murray Campbell and Clive Greated, my supervisors, for their continual support and guidance during the course of this research programme. I am also very grateful to my collaborator Joël Gilbert for passing on some of his great enthusiasm and for sharing his interesting research ideas.

I would also like to thank members of the University of Edinburgh Acoustics and Fluid Dynamics group for their help and support, particularly Tim Dewhirst, John Pullen, Alistair Young and Alistair Shawcross for setting up and looking after the group's computer network; Vince Devine for constructing the artificial mouth; Frank Morris for frequently providing rapid technical assistance; Howard Wright for helping me with the Matlab application; Maarten van Walstijn for making useful suggestions; and Narumon Emarat for being a pleasant and considerate office–mate.

Financial support was provided by EPSRC.

I am grateful to Peter Jones of Dantec for providing invaluable advice on the use of Dantec LDA apparatus and for repairing apparatus free of charge. Special thanks are due to David Sharp who painstakingly read through this work and made many useful comments.

Finally, I would like to express gratitude to my parents for their constant moral support.

Table of Contents

Chapter 1

Introduction

1.1 General Introduction to Brass Instrument Acoustics

Sound production in the brass wind musical instrument family is a result of self-sustained lip oscillation. The mechanical oscillator (the lips of the player), acts as a valve which modulates the air flow into the instrument. The destabilization of the mechanical element is the result of a complex aeroelastic coupling between (1) the lips, (2) the air flow entering the instrument due to the static overpressure in the mouth of the musician, and (3) the resonant acoustic field in the instrument itself. The phenomenon thus belongs to the class of flow-induced vibrations which has been extensively studied both theoretically and experimentally (see for example Blevins [8]).

Any global model of brass instrument behaviour must consider each of the three elements listed above, *i.e* the lips, the air flow entering the instrument and the instrument itself (the acoustic resonator). The acoustical behaviour of the mouthpiece and air column of a brass instrument has been extensively studied, with convincing theoretical and experimental results [6] [17] [35] [75]; in comparison, understanding of the behaviour of the buzzing lips and the air flow into the instrument is less advanced.

The first global study modeling the behaviour of a 'simplified' player coupled to a brass instrument was proposed by Elliot and Bowsher [34]. They modelled the lips by one mode of flexural vibration; the description 'one mass motion' or 'one mass model' recalls the single mechanical degree of freedom of this model. Applying the small oscillation hypothesis, they compared experimental measurements obtained using a trombone player with behaviour predicted by their theory. Their pioneering work, which has already been extensively discussed by Campbell and Greated [16], provides the foundation for much of this thesis.

Some published observations of lip oscillations [4] [7] [20] [65] show that the one mass model is not sufficient to describe the lip vibration and a more complex model, analogous to the two mass-model developed for the human vocal folds, must be adopted. However, convincing time-domain simulations based on simple one mass models have been developed [1] [27] [77] [83]. A large portion of the dynamic behaviour of real instruments is already described by these simplified models, which give very realistic sound synthesis. To further improve the synthesis, large amplitude effects such as lip collisions must be taken into account. In addition, for rasping sounds, nonlinear acoustic propagation in the instrument must be considered [44] [54] [69].

Following the pioneering work of Helmholtz [51] and Bouasse [10], several theoretical and experimental studies have been carried out on the oscillation threshold behaviour of a basic one-mass model coupled with acoustical resonators. Wind instruments are separated into two categories: the 'inward striking reeds' (the valve closes as the supply pressure increases) and the 'outward striking reeds' (the valve opens as the supply pressure increases). These two categories have very distinct vibrational and acoustical behaviour [37] [38] [79]. From frequency measurements the reed can be classified as 'inward striking' if the threshold playing frequency is

lower than both the mechanical and acoustical resonance frequencies or 'outward striking' if the threshold playing frequency is greater than both the mechanical and acoustical resonance frequencies. It has been clearly established that single reed wind instruments exhibit 'inward striking' behaviour [5] [23] [72] [97] [98]. However experimental studies to categorize the lip reed in brass instrument excitation have not produced any definitive conclusions [19] [44] [79] [99].

As pointed out by Elliot and Bowsher [34], one major obstacle in achieving a comprehensive study of the the sound produced by brass instruments is the number of lip and instrument parameters which can influence the sound and the considerable range of values which some of these parameters can take. In order to avoid the major difficulty of experimental study on human vibrating lips Gilbert and Petiot [43] developed an artificial mouth with artificial buzzing lips in which the 'embouchure' is controlled by only a small number of parameters. Gilbert, Ponthus and Petiot [44] used this apparatus to obtain preliminary measurements of the mechanical response of the artificial lips, allowing the estimation of several lip parameters. Vergez and Rodet used an artificial mouth to investigate how the area between the lips evolves over an acoustic cycle [92] [93].

In modeling the air flow into the instrument several assumptions are usually made: for example, that the air flow is quasi-stationary, incompressible and frictionless. It is usual to assume that volume flow is conserved as the air passes from the lip channel into the instrument mouthpiece. However, there has been no experimental verification that these assumptions are valid. In fact, with the exception of Elliot and Bowsher's [34] preliminary hot-wire anemometry[i] measurements in the throat of trombone and trumpet mouthpieces, it appears that no attempt has been made to measure the air flow velocity in brass instruments

[i] see section 4.2.1

under playing conditions. Presumably there is an absence of published material in such a crucial area of research only because of the great technical difficulty involved in performing the measurements. One aim of this thesis is to investigate the feasibility of measuring the air flow velocity in brass instruments, under playing conditions, using laser Doppler anemometry (LDA).

1.2 General Introduction to Laser Doppler Anemometry

Laser Doppler anemometry is an established point measuring technique in the area of fluid mechanics where it has been used in the measurement of laminar and turbulent flows in liquids and gases [30] [31]. Several researchers have applied LDA to the measurement of acoustic particle velocity amplitude and acoustic frequency [81] [84]. Recently studies have been published of LDA measurement of instantaneous acoustic particle velocity in water [50] and in air [53] [62].

In this study all measurements will be carried out using real fringe LDA. In such a system interference fringes are formed at the intersection of two laser beams. Micro-particles suspended in the flow scatter light into a photodetector as they move across the ellipsoidal fringe volume defined by the interference region. Rather than relying on natural micro-particles suspended in the fluid, such as dust particles, artificial neutrally buoyant seeding particles are introduced to increase the intensity at the detector surface. As seeding particles cross the fringes the intensity of the scattered light oscillates with a frequency proportional to the seeding particle velocity. If the particles oscillate under the influence of an acoustic field, the photodetector signal takes the form of a frequency modulated wave with modulation frequency equal to the fundamental acoustic frequency. The high pass filtered photodetector signal, known as the Doppler signal, can be

processed using analogue or digital techniques to yield the particle velocity.

1.3 Aim and Contents of Thesis

The aims of the present study are to:

1. develop an improved artificial lip reed mechanism.

2. develop apparatus and software for automatically measuring the mechanical response of artificial lips over an appropriate frequency range and to use this arrangement to systematically measure the mechanical response with a variety of different embouchures and other conditions.

3. develop software which models the oscillation threshold behaviour of a trombone by applying linear stability analysis to a one mass model of the lips.

4. measure the oscillation threshold behaviour of a trombone driven by the artificial mouth, with several different embouchures and several different acoustical conditions, and to compare the measured behaviour with that predicted by the above computational model.

5. investigate different techniques for processing Doppler signals, writing new software as required.

6. investigate different methods of seeding the flow.

7. verify that a particular LDA system correctly measures instantaneous acoustic particle velocity by performing LDA measurements in mono-frequency and multi-frequency standing waves and comparing results with the velocity predicted by applying basic acoustic theory to pressure measurements.

8. assess the feasibility of applying LDA to the measurement of air flow velocity inside a trombone mouthpiece when the trombone is excited using an artificial lip reed mechanism.

The present study is in three distinct parts. Chapters 2 and 3, which form the first part, are concerned with the sound generation of brass instruments at the threshold of oscillation. Chapters 4, 5 and 6, which form the second part, investigate how LDA may be used to measure acoustic particle velocity. Chapter 7 is the third part of the study. This part unifies the earlier parts by investigating the feasibility of using LDA in the field of brass instrument acoustics.

In chapter 2 a simplified physical model of the lips and air flow is derived. The theory of linear stability analysis is reviewed and illustrated using classic examples before the theory is applied to the physical model of the lips. The model is used to investigate eigenvalue evolution as a function of static mouth pressure. The variation of threshold pressure and frequency as a function of various acoustical and mechanical parameters is also studied using the model. The theoretical discussion makes use of experimental results to be presented in full in chapter 3.

Chapter 3 begins with a description of the experimental arrangements and procedures used to measure input impedance, mechanical response of the artificial lips, and oscillation threshold behaviour. Mechanical response measurements are then presented for a range of static mouth pressures from zero (no aeroelastic coupling) to a value slightly below the oscillation threshold. Finally threshold measurements performed using a trombone coupled to artificial lips are compared to threshold behaviour predicted by the model.

Chapter 4 contains a detailed discussion of the basic theory behind LDA. Laminar and turbulent flows are considered in addition to sound fields.

Chapter 5 introduces the general method and procedures used in the LDA validation experiments. The experimental arrangement of the LDA system is first described and the signal-to-noise ratio of the LDA system is considered. Two particular methods of analysing the Doppler signal are then discussed: the digital Hilbert transform and the Dantec analogue frequency tracker; measurements of the phase lag of the analogue tracker are presented. Finally, the microphone calibration procedures are discussed.

The measurements presented in chapter 6 demonstrate that LDA can be used to successfully measure instantaneous acoustic particle velocity. The measurements also indicate the limitations of the technique. The chapter first considers the problem of periodic amplitude modulation of the Doppler signal. Periodic amplitude modulation was often found to occur when measurements were made in acoustic sound fields. Additional LDA velocity measurements in mono-frequency sound fields are used to assess the relative merits of the digital Hilbert transform and analogue frequency tracker methods, and also to estimate the dynamic range of the measuring technique. Measurements in multi-harmonic sound fields are then presented. Finally, simultaneous LDA and probe microphone measurements are used to measure the acoustical impedance of a cylindrical pipe as a function of frequency. These measurements are compared with the theoretical acoustic impedance.

Chapter 7 investigates the feasibility of applying LDA to brass instrument acoustics. The chapter introduces acoustic impedance measurements of the artificial mouth, measured using LDA, and uses the impedance measurements to discuss the possible influence of the mouth cavity. LDA is then used to measure high mean flow velocities within a pipe, in preparation for measurements in brass instruments. Finally, preliminary LDA measurements are presented of the

velocity inside a specially designed transparent trombone mouthpiece when the trombone is excited by the artificial lip reed mechanism. In this case there is a significant mean flow velocity in addition to the acoustic particle velocity.

The thesis concludes with chapter 8 which summarises the findings of this work and suggests areas which could be investigated in the future.

Chapter 2

Theory of Lip Reed Modeling

2.1 Introduction

As researchers have attempted to improve the sound synthesis of brass instruments their lip reed models have become increasingly complex [1] [27] [36] [92]. Whilst such models can provide very impressive sound synthesis it is still not yet clear if such models accurately represent the true motion of the lips and their interaction with the air column. The study of threshold pressure and frequency can provide an indication of how successfully the models emulate the physical behaviour of the lips. In chapters 2 and 3 the threshold behaviour of a trombone, driven by the artificial lip reed mechanism, will be compared to the threshold behaviour predicted by a lip reed model. In this initial study of threshold behaviour in brass instruments it seems appropriate to adopt a relatively simple model.

Section 2.2 introduces the basic one-mass model, a simplified physical model for a brass instrument coupled to lips by air flow. In this model lips and air column are each represented in the time domain by a second order harmonic oscillator and the oscillators are coupled by air flow. The theory of linear stability analysis is briefly reviewed in section 2.3; some classic results in the theory of elastic stability are presented, including the flutter effect. In section 2.4.1 the equations which define the one-mass model are linearized and then linear stability analysis

is applied to the linearized equations in section 2.4.2.

The theoretical results presented here are not based on new theoretical insight: one mass models of the lips have previously been proposed by several other researchers and, for woodwind instruments, theoretical investigations of threshold values have also been carried out. However the linear stability analysis representation provides an interesting comparison between 'flow induced vibrations' in two aerodynamically coupled mechanical oscillators, and acoustic oscillations in the case of one acoustical oscillator aerodynamically coupled to one mechanical oscillator.

2.2 Brass Instruments Coupled to Lips by Air Flow: The One-Mass Model

The lips are flexible, continuous structures submitted to aerodynamic forces depending on the pressure field around them (see figure 2.1a). In this study the lip motion is approximated by a 'one-mass model': each lip is allowed to oscillate with a 1-dimensional motion along an axis making an angle θ with the vertical axis (see figure 2.1b). This angle is determined by the aerodynamic forces acting on the lip. The pair of lips act as a valve, controlling the air flow into the mouthpiece. It is assumed that the flow control depends only on the vertical component of the motion of the lips, and that the longitudinal component of the lip motion does not generate a significant additional volume flow.

If it is assumed that the two lips are identical, and are placed symmetrically on the mouthpiece, then the dynamics of each lip can be represented by the simple second order oscillator equation

$$\frac{d^2X}{dt^2} + \frac{\omega_L}{Q_L}\frac{dX}{dt} + \omega_L^2 X = \frac{F}{m} \tag{2.1}$$

where $X(t)$ is the instantaneous distance of each lip from the axis of symmetry

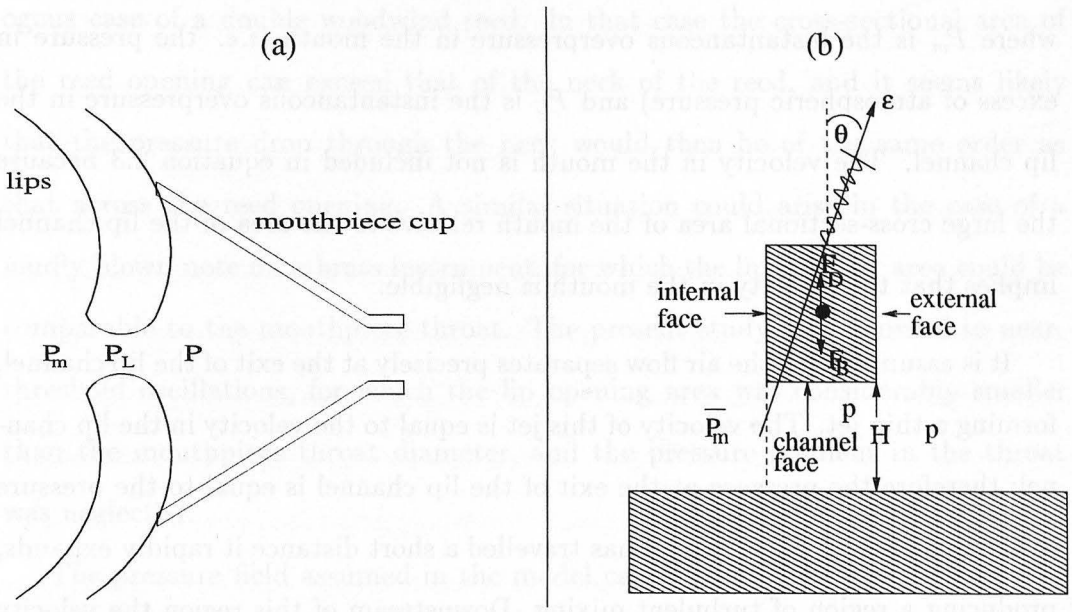

Figure 2.1: (a) Two continuous flexible lips. (b) One-mass model of lip vibration.

at time t. Each lip has natural (angular) frequency ω_L, quality factor Q_L, mass m and is acted on by a force with vertical component F. The dynamics of the entire system (lower lip plus upper lip) can be represented by a single second order oscillator (see figure 2.1b) described by the equation

$$\frac{d^2H}{dt^2} + \frac{\omega_L}{Q_L}\frac{dH}{dt} + \omega_L^2 H = \frac{F}{m_L} \tag{2.2}$$

where $H(t) = 2X(t)$ is the instantaneous distance between the lips at time t and the effective mass of the system is $m_L = m/2$.

The channel between the lips is assumed to have rectangular cross-section with width b. The flow through this channel is assumed to be quasi-stationary, frictionless and incompressible; therefore the velocity field in the lip channel is uniform and has magnitude U_L, determined by the Bernoulli relation

$$P_m = P_L + \frac{1}{2}\rho U_L^2 \tag{2.3}$$

where P_m is the instantaneous overpressure in the mouth (*i.e.* the pressure in excess of atmospheric pressure) and P_L is the instantaneous overpressure in the lip channel. The velocity in the mouth is not included in equation 2.3 because the large cross-sectional area of the mouth relative to the area of the lip channel implies that the velocity in the mouth is negligible.

It is assumed that the air flow separates precisely at the exit of the lip channel, forming a thin jet. The velocity of this jet is equal to the velocity in the lip channel; therefore the pressure at the exit of the lip channel is equal to the pressure in the lip channel. After the jet has travelled a short distance it rapidly expands, producing a region of turbulent mixing. Downstream of this region the velocity field can be considered uniform across the entire cross-section of the mouthpiece. Although the velocity decreases as the flow expands, the turbulent dissipation of kinetic energy implies that there will be no pressure recovery across the turbulent region. The pressure in the lip channel, P_L, can therefore be considered to be equal to the pressure at the input of the instrument mouthpiece, P.

The overpressure in the mouth, P_m, subsequently referred to as static overpressure, can be written as the sum of the mean (time averaged) value of P_m, $\overline{P_m}$, and the alternating component of P_m, p_m. In fact generally in chapters 2 and 3 upper case letters with an overbar denote time averaged values and lower case letters denote alternating components. The alternating pressure in the mouth, p_m, is assumed to be negligible relative to the alternating pressure in the mouthpiece, p, which is equivalent to assuming that the input impedance of the mouth cavity is zero. In this case $P_m \approx \overline{P_m}$.

In the current model it is assumed that the static overpressure in the mouthpiece, $\overline{P}$, is negligible relative to the static overpressure in the mouth, $\overline{P_m}$, and therefore $P_L \approx P \approx p$. This assumption has been questioned [96] for the anal-

ogous case of a double woodwind reed. In that case the cross-sectional area of the reed opening can exceed that of the neck of the reed, and it seems likely that the pressure drop through the neck would then be of the same order as that across the reed opening. A similar situation could arise in the case of a loudly blown note on a brass instrument, for which the lip opening area could be comparable to the mouthpiece throat. The present study was confined to near-threshold oscillations, for which the lip opening area was considerably smaller than the mouthpiece throat diameter, and the pressure gradient in the throat was neglected.

The pressure field assumed in the model can be summarised as follows: the internal faces of the lips are subjected to a purely static pressure, $\overline{P_m}$, whereas the channel and external faces are subjected to the purely alternating input mouthpiece pressure, p. By applying this simplified pressure field, equation 2.3 may be expressed in the form

$$\overline{P_m} = p + \frac{1}{2}\rho(\overline{U_L} + u_L)^2 \tag{2.4}$$

where $\overline{U_L}$ is the mean velocity in the lip channel and u_L is the alternating velocity in the lip channel.

Conservation of volume flow implies that, at each instant in time, the volume flow at the entrance to the mouthpiece, V, is equal to the volume flow through the lip channel:

$$\overline{V} + v = b(\overline{H} + h)(\overline{U_L} + u_L) \tag{2.5}$$

where $\overline{V}$ and $\overline{H}$ are the mean values of V and H, respectively and v and h denote small fluctuations in V and H, respectively, about their mean values.

The total aerodynamic force, F, acting on the lips is often separated into two forces, F_D and F_B, which have opposite effects on the aperture. One of the

forces is proportional to the pressure difference between mouth and mouthpiece *i.e.* $F_D/m_L = (\overline{P_m} - p)/\mu_D$, where μ_D is equal to m_L divided by the area of the internal face of the lip system (see figure 2.1b); the force implies an 'outward striking behaviour', because an increase in the overpressure in the mouth tends to make the lips move outwards, into the mouthpiece. Of course the lips can also strike outwards in response to a decrease in the mouthpiece pressure, p. The second force is proportional to the pressure in the lip channel, *i.e.* $F_B/m_L = p/\mu_B$ where μ_B is equal to m_L divided by the area of the channel face of the lip system (see figure 2.1b). This force implies an 'inward striking reed behaviour': in direct contrast to the F_D force, a decrease in the mouthpiece pressure p results in an identical decrease in the lip channel pressure which causes the lip to move inwards, narrowing the lip channel. In musical acoustic literature F_B is often named the 'Bernoulli force'. From the above discussion it is clear that the total alternating force per unit mass exerted on the lips is equal to $p(1/\mu_B - 1/\mu_D)$. Substituting this expression for the right hand side of equation 2.2, and replacing H with the alternating component of lip separation, h, yields the following expression describing the dynamics of the lip motion:

$$\frac{d^2h}{dt^2} + \frac{\omega_L}{Q_L}\frac{dh}{dt} + \omega_L^2 h = \left(\frac{1}{\mu_B} - \frac{1}{\mu_D}\right) p. \tag{2.6}$$

A suitably simplified mathematical model of the acoustic oscillation of the air column is also required. It is common practice in musical acoustics to quantify the response of an instrument air column to different frequencies of excitation by measuring the input impedance of the instrument. The acoustic input impedance of a brass instrument is defined as

$$Z(\omega) = p(\omega)/v(\omega) \tag{2.7}$$

where $p(\omega)$ and $v(\omega)$ are the complex pressure and velocity amplitudes, respec-

tively, at the input end of the mouthpiece. A typical input impedance curve for a trombone is shown in figure 3.1; each of the air column resonances is represented by a well defined peak. In the present study of near-threshold coupled oscillations of the lip-air column system, it is assumed that only a single air column mode participates significantly in a given oscillation regime of the coupled system. If this air column mode has resonance frequency ω_A, peak impedance Z_A, and quality factor Q_A, the input impedance in the frequency region close to ω_A can be represented approximately by the equation

$$Z(\omega) = \frac{Z_A}{1 + \frac{jQ_A(\omega^2 - \omega_A^2)}{\omega\omega_A}}. \tag{2.8}$$

(see Chang [18], equation 3). Equation 2.8 forms the basis of a curve fitting routine used in the present study to extract acoustical parameters from input impedance measurements; the equation will be discussed again in chapter 3.

To incorporate the acoustic resonance into the coupled oscillators formalism the equivalent time domain representation of equation 2.8 is required:

$$\frac{d^2\psi}{dt^2} + \frac{\omega_A}{Q_A}\frac{d\psi}{dt} + \omega_A^2\psi = \left(\frac{Z_A\omega_A}{Q_A}\right)v \tag{2.9}$$

where $d\psi/dt = p$.

Equations 2.4, 2.5, 2.6 and 2.9 form a simple one-mass model. Equation 2.6 describes the mechanical oscillator while equation 2.9 describes one mode of the acoustical oscillator. The oscillators are coupled by the air flow through the lips, which is described by equations 2.4 and 2.5.

Many supplementary non-stationary terms neglected here are suggested in the literature, representing, for example, a secondary volume source due to the motion of the lips, the inertial effect of air in the channel and a moving point of flow separation in the neck of the lip channel. The effect of each of these terms can easily be estimated theoretically but it is difficult to choose realistic values

for the parameters involved. In the crude model defined above, as there is no a priori evidence that either of the forces F_D or F_B is dominant, the assignment of the lip reed to one of the pressure controlled valve categories initially defined by Helmholtz is not obvious. This problem has been discussed at length in several papers [19] [37] [38] [44] [79] [99] and will be revisited in chapter 3.

2.3 General Introduction to Linear Stability Analysis

Solving problems of vibrations and stability almost inevitably involves solving eigenvalue problems [87]. Many systems with two coupled modes can be modelled by linearizing equations for the system about a 'fixed point' and then writing the linearized equations in the general form

$$\frac{d\mathbf{x}}{dt} = \mathbf{M}\mathbf{x} \tag{2.10}$$

where $\mathbf{x}$, the vector transpose of $(x_1, x_2, \dot{x_1}, \dot{x_2})$, describes the state of the system and

$$\mathbf{M} = \begin{bmatrix} \mathbf{0} & \mathbf{I} \\ -\mathbf{K} & -\mathbf{C} \end{bmatrix}, \tag{2.11}$$

where the 2×2 matrices $\mathbf{0}$, $\mathbf{I}$, $\mathbf{K}$ and $\mathbf{C}$ are the zero, identity, 'stiffness' and 'damping' matrices respectively [87].

There are in general four solutions to equation 2.10, each taking the form

$$\mathbf{x} = \mathbf{w}e^{\lambda t} \tag{2.12}$$

where $\mathbf{w}$ is a four dimensional vector and λ is a complex valued constant. The system is unstable when the real part of λ is greater than zero. Substitution of equation 2.12 into equation 2.10 yields the eigenvalue problem

$$(\mathbf{M} - \lambda\mathbf{I})\mathbf{w} = \mathbf{0} \tag{2.13}$$

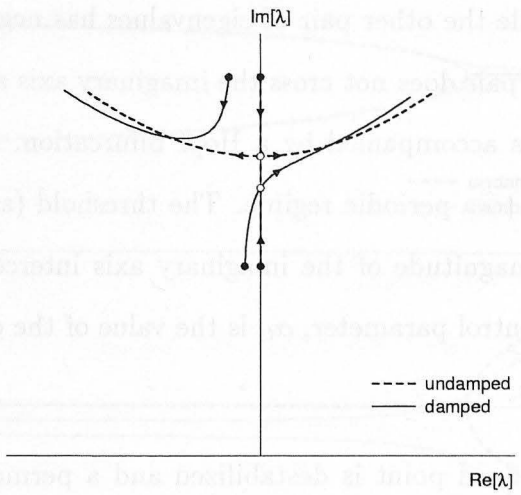

Figure 2.2: Complex plane representation of eigenvalue evolution as a function of control parameter α (adapted from Bolotin [9]). The dotted lines illustrate an example of the eigenvalues for a system of two coupled oscillators without damping, while the solid lines illustrate the same system with damping. Filled circles represent eigenvalues evaluated at $\alpha = 0$; unfilled circles represent Hopf bifurcations at $\alpha = \alpha_t$.

for the eigenvalues λ_n and eigenvectors $\mathbf{w}_n$, $n = 1$ to 4. The eigenvalues can be found by solving the equation

$$|\mathbf{M} - \lambda\mathbf{I}| = \mathbf{0}. \tag{2.14}$$

Figure 2.2 demonstrates how the eigenvalues can evolve as a function of a control parameter, α. For the case illustrated, the four eigenvalues are in the form of two complex conjugate pairs but only the eigenvalues with positive imaginary parts are displayed in the figure. Linear stability is preserved provided the real parts of all eigenvalues remain negative but the system becomes unstable when the real part of one of the complex eigenvalue pairs becomes positive. A bifurcation is said to occur when there is a marked qualitative change in the system behaviour [87]. A Hopf bifurcation, which creates periodic oscillations out of equilibria, occurs when one pair of eigenvalues has purely imaginary parts,

$\lambda = \pm j\omega_t$, while the other pair of eigenvalues has negative real parts. Provided the eigenvalue pair does not cross the imaginary axis at the origin, an imaginary axis crossing is accompanied by a Hopf bifurcation, indicating loss of stability and transition to a periodic regime. The threshold (angular) frequency of oscillation is the magnitude of the imaginary axis intercept, ω_t, and the threshold value of the control parameter, α_t, is the value of the control parameter α at the imaginary axis.

When the fixed point is destabilized and a permanent oscillatory regime is sustained the state variables oscillate with a finite amplitude. The equations describing the system cannot be applied in their linearized form to this situation; information about the permanent oscillatory regimes can only be extracted using the equations in their original nonlinear form. However it is reasonable to assume that the theoretical threshold frequency is approximately equal to the fundamental frequency of a very small amplitude quasi-sinusoidal oscillation.

Holmes [56] carried out extensive stability and dynamical studies applied to a fourth order dynamical system representing a coupled two mode model of a pipe conveying fluid. In Holmes' paper, two different generic kinds of instability are defined: flutter and divergence. In both cases the instability develops rapidly as a function of time initially, but soon settles down into a steady state. In the case of flutter the state variables oscillate, initially with continuously increasing amplitude, but after a short time the amplitude of the oscillation becomes constant. The name flutter recalls the motion of a flag fluttering in the wind. In the case of divergence there is initially a rapid and continuous change in the state variables, but after a short time they assume constant values, different form their pre-bifurcation values. Flutter is said to occur if the eigenvalues form complex conjugate pairs and at least one complex conjugate pair has positive real parts;

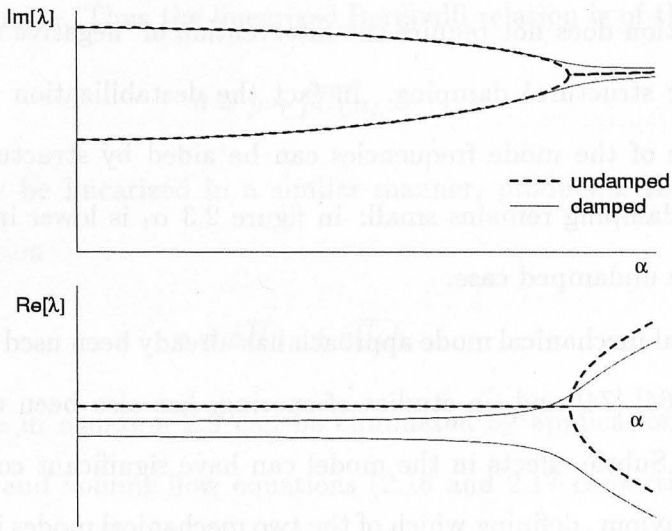

Figure 2.3: Imaginary and real parts of eigenvalues as a function of a control parameter, α, which is characteristic of the flow. This figure demonstrates coalescence of eigenfrequencies (imaginary parts of eigenvalues), in the undamped case, because of the flow coupling effect. The introduction of structural damping lowers the threshold value of α.

divergence occurs if at least one of the eigenvalues is purely real and positive.

One established example of the flutter effect in flow-induced vibrations is the destabilization of an aircraft wing. Some of the basic conclusions obtained from such aircraft wing studies are briefly reviewed here as they can be applied to the buzzing lips problem. Destabilization of the wings is a result of the flutter effect produced by aerodynamic coupling between two elastic modes; a bending mode and a torsional mode [76]. The flow coupling is modelled by a non-diagonal element in the 'stiffness matrix' which makes the matrix unsymmetric. The introduction of the coupling term causes the natural angular frequencies of the two modes (*i.e.* the magnitudes of the imaginary parts of the eigenvalues) to move towards each other as the air flow speed (the control parameter) increases. This coalescence effect is illustrated in figure 2.3 for the analogous case of two mechanical modes of the lips coupled by airflow. Rocard [76] pointed out that

destabilization does not require the intervention of 'negative resistance' to compensate for structural damping. In fact the destabilization resulting from the coalescence of the mode frequencies can be aided by structural damping, provided the damping remains small: in figure 2.3 α_t is lower in the damped case than in the undamped case.

The dual mechanical mode approach has already been used to model the vocal folds [57] [64] [74] and, in studies of snoring, has also been applied to the soft palate [3]. Subtle effects in the model can have significant consequences on the flutter behaviour, defining which of the two mechanical modes is destabilized. For example, in Auregan and Depollier's [3] snoring model the first mechanical mode is destabilized if flow induced damping is neglected, but the second mechanical mode is destabilized if the flow induced damping resulting from non-stationary flow around the soft palate is included.

2.4 The One-Mass Model Revisited

2.4.1 Linearization

In order to carry out linear stability analysis on the one-mass model defined by equations 2.4, 2.5, 2.6 and 2.9 equations 2.4 and 2.5 must first be linearized about the lips' equilibrium position; equations 2.6 and 2.9 are already linear. Equation 2.4 can be written in the form

$$\overline{P_m} = p + \frac{1}{2}\rho\overline{U_L}^2 + \rho\overline{U_L}u_L + \frac{1}{2}\rho u_L^2. \tag{2.15}$$

Linearization involves neglecting all terms which are not a linear function of an alternating variable (h, ψ, p, u_L or v). Therefore to linearize equation 2.15 the terms $\overline{P_m}$ and $\rho\overline{U_L}^2/2$ must be removed because they do not contain an alternating variable, and the term $\rho u_L^2/2$ must be removed since it is a quadratic function of

an alternating variable. Thus the linearized Bernoulli relation is of the form

$$0 = p + \rho\overline{U_L}u_L. \tag{2.16}$$

Equation 2.5 may be linearized in a similar manner, producing the linearized volume flow equation

$$v = b\overline{H}u_L + b\overline{U_L}h. \tag{2.17}$$

The v variable in equation 2.9 can be eliminated by application of the linearized Bernoulli and volume flow equations (2.16 and 2.17 respectively). This leads to the following expression for two coupled second order oscillators as a function of h and ψ

$$\frac{d^2}{dt^2}\begin{bmatrix} h \\ \psi \end{bmatrix} + \mathbf{C}\frac{d}{dt}\begin{bmatrix} h \\ \psi \end{bmatrix} + \mathbf{K}\begin{bmatrix} h \\ \psi \end{bmatrix} = 0 \tag{2.18}$$

where

$$\mathbf{K} = \begin{bmatrix} \omega_L^2 & 0 \\ -\left(\frac{Z_A\omega_A}{Q_A}\right)(b\overline{U_L}) & \omega_A^2 \end{bmatrix} \tag{2.19}$$

and

$$\mathbf{C} = \begin{bmatrix} \frac{\omega_L}{Q_L} & \frac{1}{\mu_D} - \frac{1}{\mu_B} \\ 0 & \frac{\omega_A}{Q_A} + \left(\frac{Z_A\omega_A}{Q_A}\right)\left(\frac{b\overline{H}}{\rho\overline{U_L}}\right) \end{bmatrix}. \tag{2.20}$$

Equation 2.18 can be arranged into a set of 4 simultaneous first order ordinary differential equations [56] with matrix representation

$$\frac{d}{dt}\begin{bmatrix} h \\ \psi \\ \frac{dh}{dt} \\ \frac{d\psi}{dt} \end{bmatrix} = \begin{bmatrix} \mathbf{0} & \mathbf{I} \\ -\mathbf{K} & -\mathbf{C} \end{bmatrix}\begin{bmatrix} h \\ \psi \\ \frac{dh}{dt} \\ \frac{d\psi}{dt} \end{bmatrix} \tag{2.21}$$

of the same form as equation 2.10.

The interaction of a reed and a resonant air column has been modelled by two coupled simple harmonic oscillators in several previous studies, but only Weinreich [95] and Chang [18] have used a 4×4 matrix representation.

2.4.2 Application of Linear Stability Analysis

In this section linear stability analysis is applied to the excitation of brass instruments using the simplified model derived in section 2.2 and linearized in section 2.4.1. In this particular case the control parameter of the flow-induced vibrations is $\overline{P_m}$ and the 'fixed point' is $H(\overline{P_m}) = \overline{H}(\overline{P_m})$, $U_L(\overline{P_m}) = \overline{U_L}(\overline{P_m})$ and $P(\overline{P_m}) = 0$.

It is interesting to note how the 'stiffness' and 'damping' matrices defined in equations 2.19 and 2.20 describe flow coupling. The inclusion of flow coupling in the model introduces non-zero terms for the bottom left element of the stiffness matrix, $\mathbf{K}$, and the top right element of the damping matrix, $\mathbf{C}$. The bottom right element of $\mathbf{C}$ is also modified by the addition of a second flow induced damping term.

Linear stability analysis was performed on the simplified model by numerically solving the equations of the model (equations 2.19, 2.20 and 2.21) for the eigenvalues. The computer program 'matrix.c' was written to carry out the linear stability analysis. It is described in appendix C.1 and listed in appendix D. Each of the simulations presented in this chapter makes use of realistic parameters obtained from input impedance measurements on a trombone and dynamic and static mechanical response measurements (described in section 3.2). To simplify notation the parameter $1/\mu_L = (1/\mu_D - 1/\mu_B)$ is used. For a lip reed with dominant outward behaviour $1/\mu_L > 0$ but for a lip reed with dominant inward behaviour $1/\mu_L < 0$. For each case considered in this section $\overline{H_0} = 0.44mm$, $b = 11mm$ and the control parameter $\overline{P_m}$ was varied between 0 and 100mbar; since $\overline{H}$ depends on $\overline{P_m}$, the subscript '0' has been added to $\overline{H}$ to denote the value of $\overline{H}$ when $\overline{P_m} = 0$.

The eigenvalue evolution as a function of $\overline{P_m}$ is displayed in figures 2.4 and 2.5

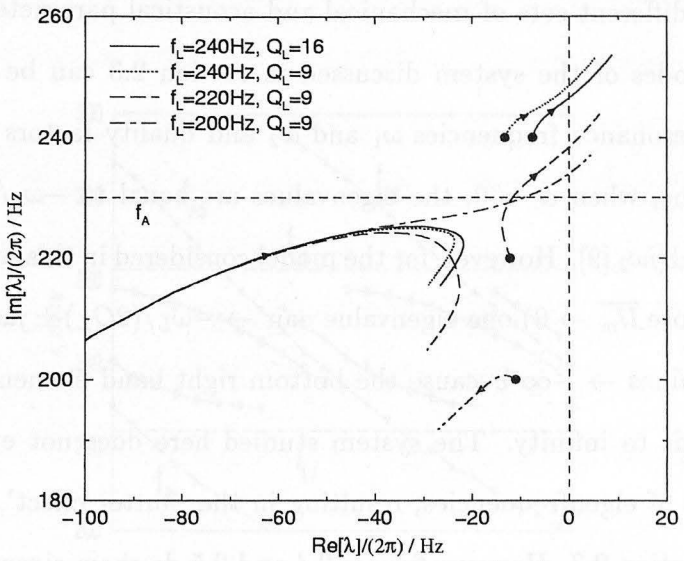

Figure 2.4: Complex plane representation of eigenvalue evolution as a function of $\overline{P_m}$ for four different sets of mechanical parameters. In each case $1/\mu_L = 0.09m^2Kg^{-1}$, $f_A = 230$Hz, $Q_A = 24$, and $Z_A = 20M\Omega$.

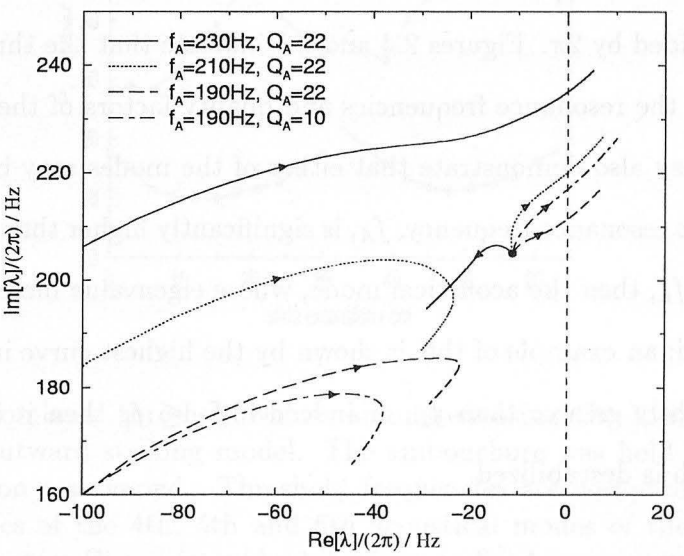

Figure 2.5: Complex plane representation of eigenvalue evolution as a function of $\overline{P_m}$ for four different sets of acoustical parameters. In each case $Z_A = 20M\Omega$, $f_L = 205$Hz, $Q_L = 9$, and $1/\mu_L = 0.09m^2Kg^{-1}$.

for several different sets of mechanical and acoustical parameters. The two mechanical modes of the system discussed in section 2.3 can be characterised by (angular) resonance frequencies ω_1 and ω_2 and quality factors Q_1 and Q_2. For such systems, when $\alpha = 0$, the eigenvalues are equal to $-\omega_1/(2Q_1) \pm j\omega_1$ and $-\omega_2/(2Q_2) \pm j\omega_2$ [9]. However, for the model considered in this section, as $\overline{P_m} \to 0$ (and therefore $\overline{U_m} \to 0$) one eigenvalue pair $\to -\omega_L/(2Q_L) \pm j\omega_L$ while the other two eigenvalues $\to -\infty$ because the bottom right hand element of the damping matrix tends to infinity. The system studied here does not exhibit the strong coalescence of eigenfrequencies, resulting in the 'flutter effect', which was illustrated in section 2.3. However figures 2.4 and 2.5 do show eigenvalue crossings of the imaginary axis. The eigenvalue crossing, the point at which the equilibrium position becomes linearly unstable, defines what is defined as the threshold of stability. The value of the mouth pressure at this point is known as the threshold pressure, P_t; the threshold frequency, f_t, is defined to be the imaginary axis intercept divided by 2π. Figures 2.4 and 2.5 indicate that the threshold values are affected by the resonance frequencies and quality factors of the lips and the resonator. They also demonstrate that either of the modes may be destabilized. If the acoustic resonance frequency, f_A, is significantly higher than the lip resonance frequency, f_L, then the acoustical mode, whose eigenvalue increases from $-\infty$, is destabilized; an example of this is shown by the highest curve in figure 2.5. If f_A is only slightly greater than f_L, or indeed if $f_A \leq f_L$ then it is the mechanical mode which is destabilized.

It was noted earlier that numerical evaluation of eigenvalues is not the only method which has been applied to the study of the threshold of stability. Chang [18] carried out a systematic study of reed stability using the Routh test; he produced stability maps in terms of threshold pressure and the ratio of resonance frequen-

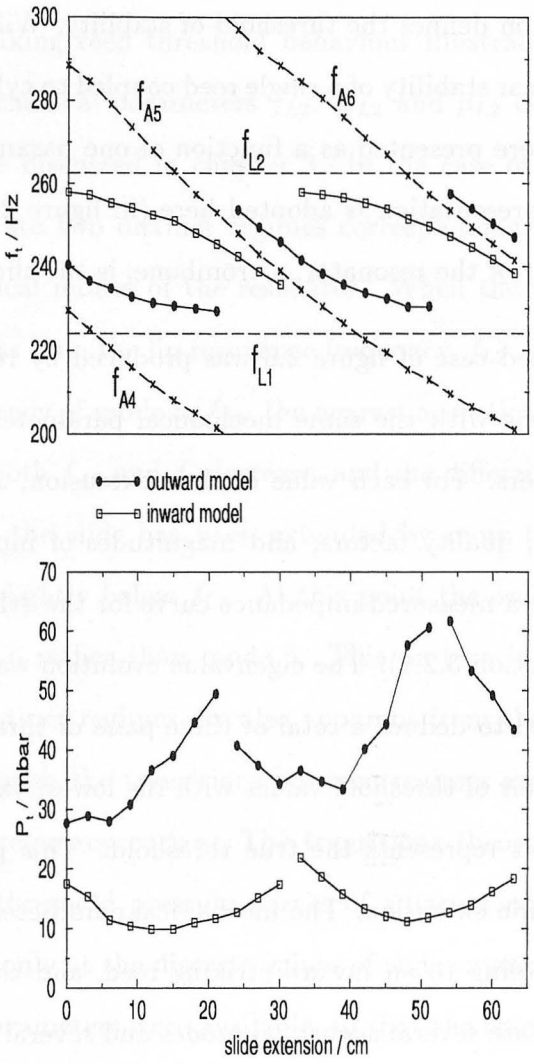

Figure 2.6: Trombone threshold values simulated using the inward striking model and the outward striking model. The embouchure was held constant as the slide extension was varied. Threshold frequencies are compared with resonance frequencies of the 4th, 5th and 6th acoustical modes of the trombone. Acoustical parameters (listed in table A.1 of appendix A) were extracted from input impedance measurements. Lip parameters used: $f_{L1} = 224Hz$, $Q_{L1} = 9.0$, $1/\mu_{L1} = 0.09m^2Kg^{-1}$; $f_{L2} = 261$Hz, $Q_{L2} = 14.5$, $1/\mu_{L2} = -0.11m^2Kg^{-1}$.

cies. Several systematic studies of linear stability have also been carried out using the closed loop transfer analogy [33] [37] [79]; in this method the open loop transfer function condition defines the threshold of stability. Wilson and Beavers [97] investigated the linear stability of a single reed coupled to cylindrical tubes. Their threshold results were presented as a function of one parameter of the tube: its length. A similar presentation is adopted here (in figure 2.6), where the representative parameter of the resonator, a trombone, is the slide extension.

The outward reed case of figure 2.6 was produced by repeatedly calculating eigenvalue evolutions with the same mechanical parameters but with different acoustical parameters. For each value of slide extension, x, the acoustical resonance frequencies, quality factors, and magnitudes of input impedance peaks were obtained from a measured impedance curve for the 4th, 5th and 6th acoustical modes (see section 3.2.1). The eigenvalue evolution was then calculated for each mode and used to deduce a total of three pairs of threshold values (P_t, f_t); however only the pair of threshold values with the lowest value of P_t was plotted in figure 2.6 as that represents the true threshold. This process was repeated for each value of slide extension. The mechanical parameters were then changed to values corresponding to an inward striking reed, and the entire process was repeated. As there are several acoustical modes and several mechanical modes of the lips (see chapter 3), acoustical parameters are distinguished when necessary by the subscript 'An' where n is the acoustic mode number to which the parameter belongs; similarly, lip parameters are given the subscript 'Lm', where m is the mechanical mode number to which the parameter belongs.

The $P_t(x)$ curve can be viewed as a prediction of the minimum mouth pressure required by a trombone player to sustain a note with a fixed embouchure characterized by the parameters used in the model, with the slide extended to

position x. The $f_t(x)$ curve represents the frequency of the note played with slide extension x and mouth pressure P_t.

The inwards striking reed threshold behaviour illustrated in figure 2.6 was produced using mechanical parameters f_{L2}, Q_{L2} and μ_{L2} deduced from experimental results to be discussed in chapter 3. In the case of the inward striking reed, f_t is divided into two distinct regimes corresponding, respectively, to the 5th and 6th acoustical modes of the resonator. When the slide extension is at 0cm, f_t is slightly less than the lip resonance frequency, f_{L2}, and much lower than the resonance frequency of mode 5, f_{A5}, the nearest acoustical mode. As the slide is slowly extended both f_{A5} and f_t decrease, and the difference between f_{A5} and f_t decreases. After the slide has been extended by more than 30cm f_t jumps up in frequency to slightly below f_{L2}. At this point the oscillation is supported by acoustical mode 6 rather than mode 5. This pattern is repeated for higher modes. The two distinct regimes are also apparent from the threshold pressure measurements, although the transitions between regimes are less clear cut than in the case of the frequency curves. The transitions theoretically occur at the intersection of the threshold pressure curves of adjacent regimes. However, P_t has been calculated only at the discrete values of slide extension for which experimentally derived parameters were available, so that the transition points can be deduced from figure 2.6 only by extrapolation of the pressure curves for adjacent regimes.

In the case of the outward striking reed, f_t is divided into three distinct regimes corresponding, respectively to the 4th, 5th and 6th acoustical modes of the resonator. The threshold behaviour of the outward striking reed is very different to that of the inward striking reed. For a particular regime in the outward striking reed case, as the slide is extended, f_t moves from being slightly

above an acoustical resonance frequency (*e.g.* f_{A5}) to being slightly above the lip resonance frequency, f_{L1}. Figure 2.6 confirms that with the outward striking reed model the playing frequency must always lie above both the lip resonance frequency and the acoustic resonance frequency; with the inward striking reed model the playing frequency must lie below both the lip resonance frequency and the acoustic resonance frequency. In the outward striking reed case the regimes are not so apparent in the threshold pressure curve because the curve does not vary smoothly. This reflects the fact that the curve was calculated using experimentally measured acoustical parameters: as the slide extension is varied the quality factor and shape of the acoustical resonances vary in addition to the acoustic frequency. In chapter 3 figure 2.6 will be compared with playing tests conducted using the artificial mouth.

It is also possible to fix the acoustical parameters and vary the lip parameters. In figure 2.7 the threshold results are displayed as a function of the lip resonance frequency and as a function of the lip quality factor. This is a somewhat artificial representation of the lip behaviour as the resonance frequency and quality factor do not vary independently of each other, or the other lip parameters (see chapter 3). However this figure does illustrate several important points. In figure 2.7 the lip resonance frequency and quality factor vary over a range of values which were observed experimentally using the artificial lips. The other mechanical parameters were held constant in both cases and are typical of the values measured using the artificial lips.

Figure 2.7a can be viewed as a prediction of the variation of threshold values as a trombone player tightens the embouchure. The note which is produced depends on both the mechanical parameters of the lips and the acoustical parameters of the instrument. With a lip frequency $f_L = 182$Hz the third acoustical

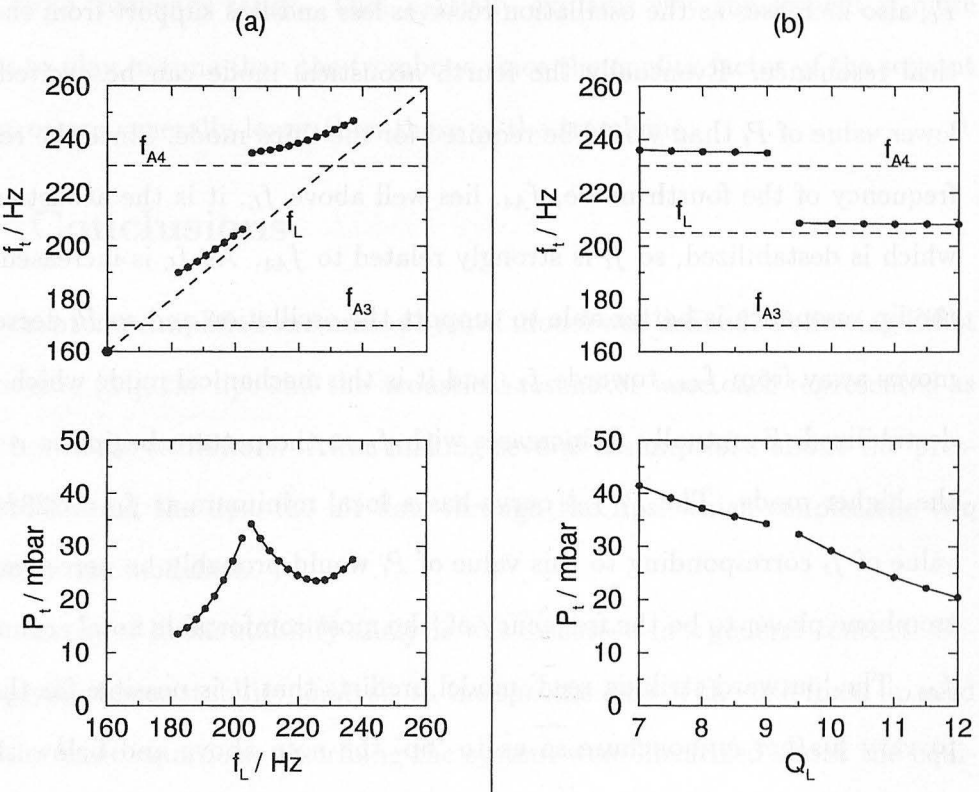

Figure 2.7: Trombone threshold values simulated using the outward striking model. The slide remained unextended while (a) the natural resonance frequency of the lip was increased and (b) lip quality factor was increased. Parameters used to obtain figures (a) and (b): $f_{A3} = 170Hz$, $Q_{A3} = 18$, $Z_{A3} = 20M\Omega$; $f_{A4} = 230Hz$, $Q_{A4} = 24$, $Z_{A4} = 20M\Omega$; $1/\mu_L = 0.09m^2Kg^{-1}$. In figure (a) $Q_L = 9$; in figure (b) $f_L = 205Hz$.

mode of the trombone is excited. In this case f_L lies well above the acoustical resonance frequency, f_{A3}, so it is the mechanical mode which is destabilized, resulting in a threshold frequency, f_t, which is strongly related to f_L. As f_L increases f_t continues to increase. The model predicts that the threshold pressure, P_t, also increases as the oscillation receives less and less support from the acoustical resonance. Eventually the fourth acoustical mode can be excited with a lower value of P_t than would be required for the third mode. Since the resonance frequency of the fourth mode, f_{A4}, lies well above f_L, it is the acoustical mode which is destabilized, so f_t is strongly related to f_{A4}. As f_L is increased further the lip resonance is better able to support the oscillation and so P_t decreases; f_t moves away from f_{A4}, towards f_L, and it is the mechanical mode which is again destabilized. Eventually P_t increases with f_L as the pattern begins to repeat for the higher mode. The $P_t(f_L)$ curve has a local minimum at $f_L = 228Hz$. The value of f_t corresponding to this value of P_t would probably be perceived by the trombone player to be the frequency of 'the most comfortable note' around mode f_{A4}. The 'outward striking reed' model predicts that it is possible for the player to vary his/her embouchure so as to 'lip' the note above and below the most comfortable note, but not below the acoustical resonance frequency. According to this model, when the player attempts to 'lip' the note below the acoustical resonance frequency a frequency gap is encountered before f_t jumps down to a value well above the lower resonance frequency.

The relative values of the acoustic and lip quality factors determine how strongly the instrument influences the frequency of the note produced. This is illustrated in figure 2.7b: as Q_L is increased from a low value, f_t continues to lie slightly above f_{A4} until a critical value of Q_L is reached when f_t jumps down to lie slightly above f_L. The critical value of Q_L required for this transition depends

on the acoustical parameters and on the other mechanical parameters. When the quality factor of the instrument, Q_A, is reduced the variation of P_t with f_L is reduced. In this case the 'most comfortable note' is not clearly defined, the instrument does not strongly influence f_t and the player is able to lip the notes over a large frequency range. That partially explains why the serpent is more difficult to play in tune than the trombone since the quality factor of the serpent resonances are generally lower than those of the trombone.

2.5 Conclusions

In this chapter a simplified one-mass physical model was defined. Following Elliot and Bowsher [34], the lips and the acoustical resonator were each represented as simple harmonic oscillators. After making several assumptions about the pressure field around the lips, the air flow through the lips, which couples the two oscillators, was modelled.

The theory of linear stability analysis was discussed in a general context. Before applying linear stability analysis to the specific case of the one-mass lip reed model the basic equations describing the system were linearized about the equilibrium position of the lips and then arranged into four simultaneous first order differential equations. The complex plane eigenvalue evolution resulting from the linear stability analysis was briefly studied but particular emphasis was placed on investigating the variation of threshold values with changes in acoustical and mechanical parameters. Simulations were run using lip parameters and acoustical parameters based entirely on systematic experimental measurements. These measurements are described in the next chapter.

Chapter 3

Mechanical Response of Artificial Lips and Oscillation Threshold

3.1 Introduction

Section 3.2 is devoted to the experimental procedures used to measure the acoustical input impedance of the instrument, the mechanical response of the artificial lips and the oscillation threshold values. The experimental measurements are compared with theoretical predictions in section 3.3. Mechanical response measurements are presented for a range of static mouth overpressures from zero (no aeroelastic coupling) to a value slightly below the oscillation threshold. These response measurements were carried out with the artificial lips coupled only to a mouthpiece rim (with the cup removed) and also to a complete mouthpiece. Threshold measurements carried out using a trombone coupled to artificial lips are compared with the threshold behaviour predicted by the theoretical model. The qualitative features recovered by the simplified one-mass model are extensively discussed and the limits of this approach are considered. The results lead to a discussion of the possibility of including a second mechanical mode in the lip model.

3.2 Experimental Methods

3.2.1 Input Impedance Measurements

The instrument studied was a King tenor trombone, made around 1960. In order to characterize the acoustical response of the instrument, the magnitude of its input impedance was measured as a function of frequency using a standard technique [15]. Input impedance measurements were made at 1 Hz intervals over the frequency range 50–1000 Hz for each of 22 slide positions located at 3 cm intervals (corresponding to pitch intervals of around 30 cents). The first acoustical mode was not within the range of measurement, but the parameters of this mode were not required because the first mode was not excited in the threshold measurements. The acoustical parameters are listed in table A.1 of appendix A.

From equation 2.8 the magnitude of the input impedance near the resonance frequency ω_A, can be written as

$$|Z(\omega)| = \frac{Z_A}{\sqrt{1 + \frac{Q_A^2(\omega^2-\omega_A^2)^2}{\omega^2\omega_A^2}}}. \tag{3.1}$$

However since

$$\omega^2 - \omega_A^2 = (\omega + \omega_A)(\omega - \omega_A) \approx 2\omega(\omega - \omega_A) \tag{3.2}$$

the magnitude of the input impedance can be approximated as

$$|Z(\omega)| \approx \frac{Z_A}{\sqrt{1 + 4Q_A^2\left(\frac{\omega-\omega_A}{\omega_A}\right)^2}}. \tag{3.3}$$

At each slide position the acoustical parameters, Z_A, Q_A and $f_A = \omega_A/2\pi$ were estimated for modes 2 to 6 by numerically fitting equation 3.3 around local maxima, using an 11 point least squares fit routine, 'lsf_reson.c'. This routine is described briefly in appendix C.2 and a complete listing is provided in appendix D. A typical input impedance magnitude curve is displayed in figure 3.1 along with

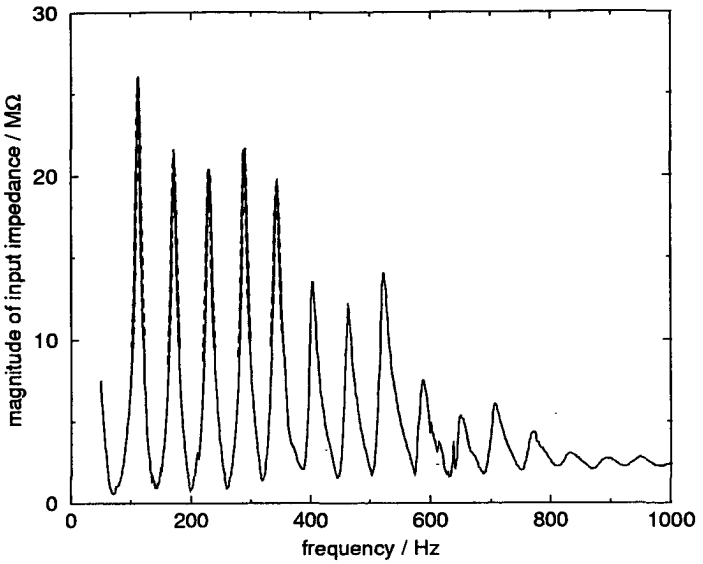

Figure 3.1: Measured input impedance magnitude of trombone with slide unextended (solid line) and least squares fit to modes 2 to 6 (dashed line).

the least squares fit to the peaks. The acoustical parameters used in the one mass model threshold simulations of section 2.4.2 were extracted from such input impedance curves.

3.2.2 Artificial Mouth

Both the mechanical response measurements and the threshold behaviour measurements were performed using an artificial mouth. The use of an artificial lip mechanism to replace the human player offers great advantages in long term stability, ease of instrumentation and the ability to make small and reproducible adjustments to the embouchure. The present study used an artificial mouth which is a development of the design introduced by Gilbert and Petiot [43].

Figure 3.2 is a photograph of the new artificial mouth, figure 3.3 is a plan view of the artificial mouth from above with the top plate removed and figure 3.4 is a vertical cross-section of the artificial mouth along the central line $\alpha - \alpha$. The

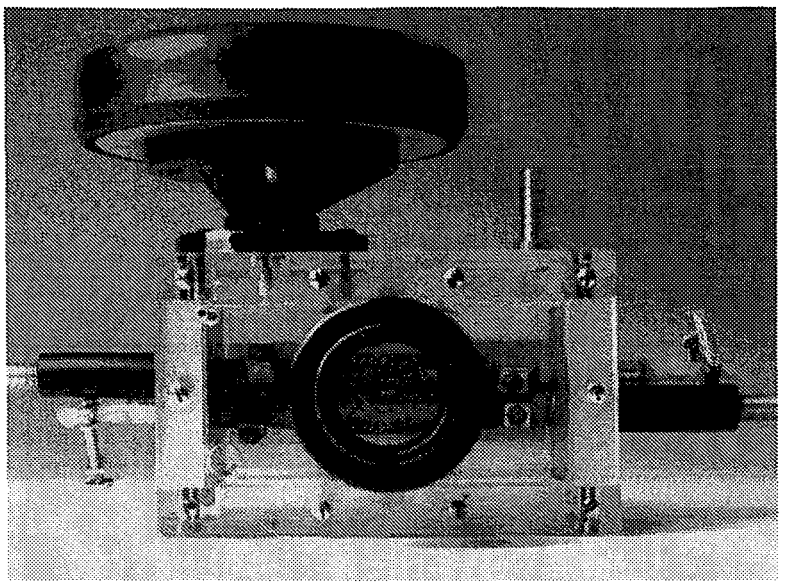

Figure 3.2: Photograph of artificial mouth, looking at the lips through the teeth.

alphabetic characters in the figure label various parts of the apparatus which will be referred to in the text below, whilst the numerical characters indicate dimensions in mm.

The new artificial mouth comprises a hermetically sealed box encapsulating a pair of water filled latex rubber lips (a,b) which are clamped between the instrument mouthpiece (c) and plastic "teeth" (d).

The hermetically sealed box comprises a top plate (e), bottom plate (f), front plate (g), rear plate (h), left side plate (i) and right side plate (j). The top plate (e) and bottom plate (f) are provided with thick front sections (k and l respectively) and thick rear sections (m and n respectively) to give an increased area of contact with the front plate (g) and with the rear plate (h), thus providing a good air tight seal between the various plates. Vacuum grease was applied liberally to all interfacing surfaces.

Each of the lips (a, b) is a cylindrical tube of latex rubber, with internal diameter 16mm and wall thickness 0.3mm. The left end of the upper lip (a) is

mounted on a movable lip support rod (o) which passes through, and is itself supported by, the left side plate (i). The right end of the lip (a) is mounted on a fixed lip support rod (p) which passes through, and is supported by, the right side plate (j). Each end of the lip (a) fits over a respective lip support rod (o, p) and is held in place with jubilee clips (q, r). The movable lip support rod (o) has an external screw thread (s) which interfaces with an internal screw thread of the lip tension control mechanism (t). One end of the lip tension control mechanism (t) abuts the outer face of the left side plate (i). Rotating the lip tension control mechanism (t) displaces the movable lip support rod in a longitudinal (left-right) direction, thus adjusting the longitudinal tension of the lips. Plastic tubes (u, v) fitted to the ends of the support rods (o, p) communicate with hollow axial passages provided in each support rod (o, p). Water can be introduced into the lips through either of the plastic tubes (u, v). The water can be contained by closing clamps (w, x) provided on each of the plastic tubes (u, v).

The lower lip (b) is provided with similar lip support means except the lower lip fixed support rod is mounted on the left side wall (i), beneath the upper lip movable support rod and the lower lip movable support rod is mounted on the right side wall (j), beneath the upper lip fixed support rod (p). The lower lip support means has been omitted from figure 3.3 for clarity.

The teeth (d) are formed from a rectangular shaped piece of perspex with a circular 2cm hole in the centre. They are supported on an annular rim (A) of teeth support tube (B). The annular rim (A) can rotate freely within the teeth annular channel (C) but the annular rim (A) and teeth (d) cannot be separated. The teeth (d) are further provided with pins (D, E) which slide in grooves (F, G) cut into extended thick front sections (H, I) of the top and bottom plates (e, f). An outer screw thread (J) at the rear end of the teeth support tube (B) interfaces

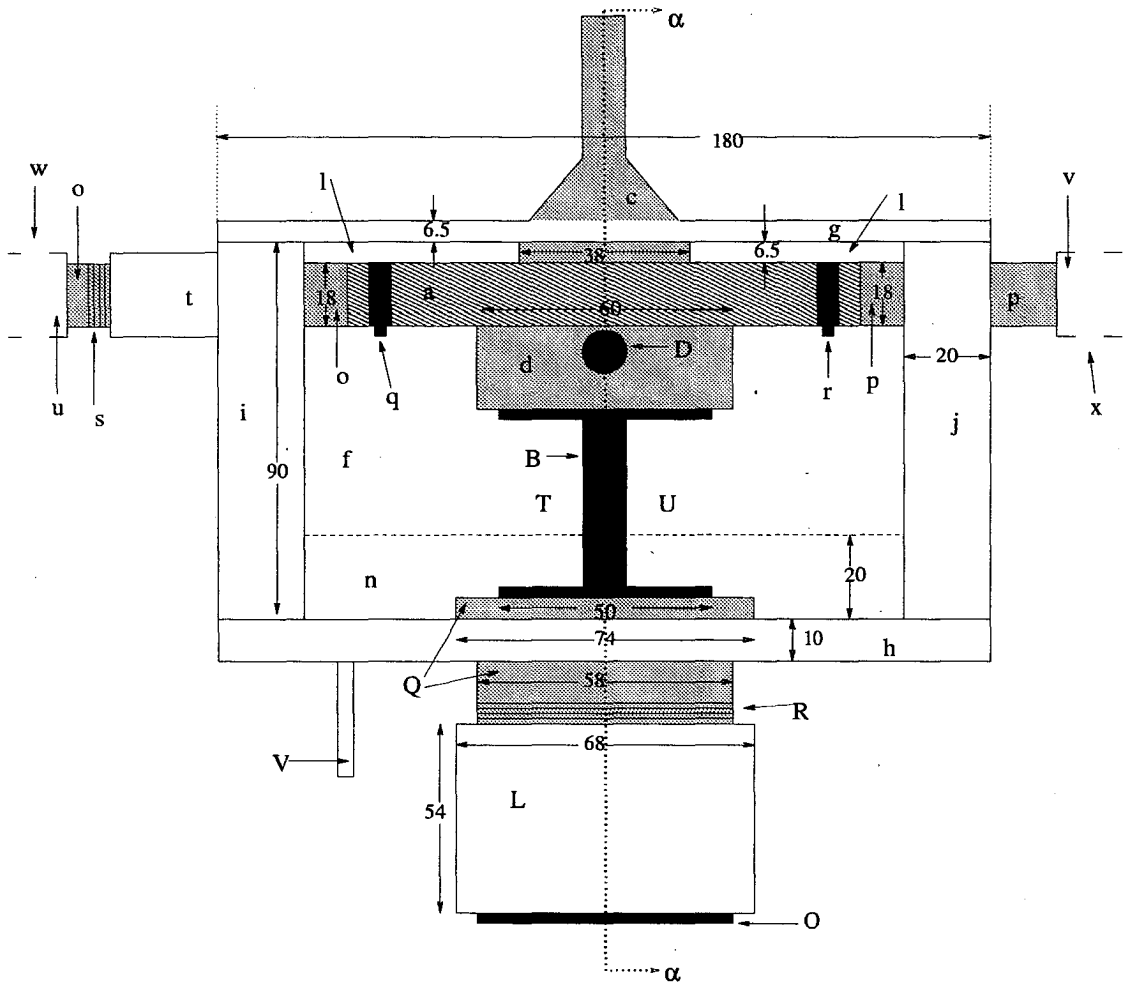

Figure 3.3: Plan view of artificial mouth with top plate (e) removed. The numbers in the figure indicate dimensions in mm, the alphabetic letters label various elements referenced in the text.

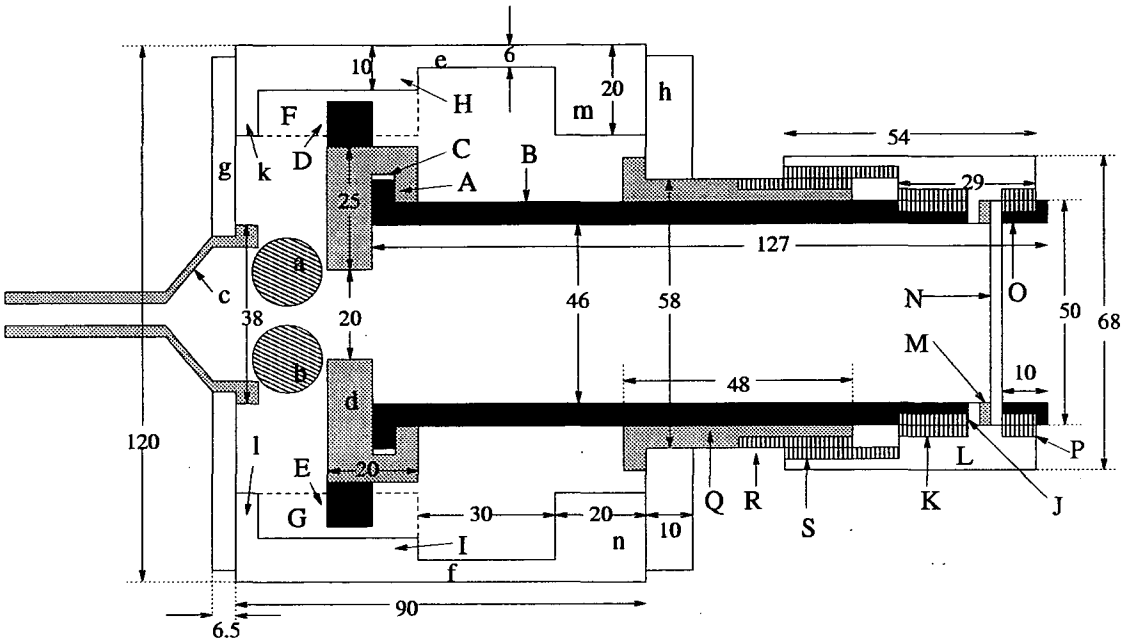

Figure 3.4: Vertical cross-section of the artificial mouth along the line $\alpha - \alpha$. The numbers in the figure indicate dimensions in mm, the alphabetic letters label various elements referenced in the text.

with a first inner screw thread (K) of a teeth control mechanism (L). A rubber annular ring (M) and circular glass window (N) are pressed against the rear end of the teeth support tube (B) by an annular ring (O). The annular ring (O) has an outer screw thread which interfaces with a second inner screw thread (P) of the teeth control mechanism (L). In use the teeth support tube (B), annular ring (O) and teeth control mechanism (L) are in fixed relation: neither the teeth support tube (B) or annular ring (O) rotate relative to the teeth control mechanism (L) or to each other. The teeth support tube (B) slides in and is itself supported by a rear flange (Q). The flange is provided with an outer screw thread (R) which interfaces with a third inner screw thread (S) of teeth control mechanism (L). Rotating the teeth control mechanism (L) displaces the teeth support tube (B) and hence the teeth (d) in a transverse (front-rear) direction, thus varying the mechanical pressure of the lips (a, b) against the mouthpiece (c). Figure 3.3 shows

that large sections (T, U) of the teeth support tube (B) have been removed to ensure a uniform pressure field exists across the rear face of the lips (a, b).

The artificial mouth described above differs from Gilbert and Petiot's prototype design in two respects. Firstly, in the prototype artificial mouth there were no hollow axial passageways in the lip support rods (o, p) and so the lips (a, b) had to be filled with water before they were positioned on the support rods (o, p) and therefore the artificial mouth had to be partially dismantled in order to vary the volume of water in the lips. Secondly, in the prototype artificial mouth the teeth were in fixed relation with the top and bottom plates (e, f) and nearly all of the mouthpiece was enclosed in a cylindrical housing. To adjust the mechanical pressure of the lips against the teeth the mouthpiece could be displaced in the transverse (front-back direction) by rotating part of the mouthpiece housing. In the artificial mouth of the present study only the mouthpiece rim is enclosed and access is provided to the mouthpiece cup and backbore.

The embouchure of the artificial mouth may be altered by adjusting the tension of the lips, changing the volume of water in the lips, or moving the teeth to increase or decrease the pressure of the lips against the mouthpiece. In this investigation, to limit the number of control parameters, alterations to the embouchure were restricted to changing the position of the teeth by rotating the teeth control mechanism (L).

An air pump, connected to an air inlet port (see figure 3.2) on the artificial mouth top plate (e), was employed to maintain the static mouth overpressure. The air pump was manufactured by Air Control Industries Limited and had serial number 9MSB 12452-81710-AA. The static mouth overpressure was measured by a Digitron P200UL piezoceramic manometer connected to a manometer port (V) on the artificial mouth rear plate (h). The alternating pressure in the mouth was

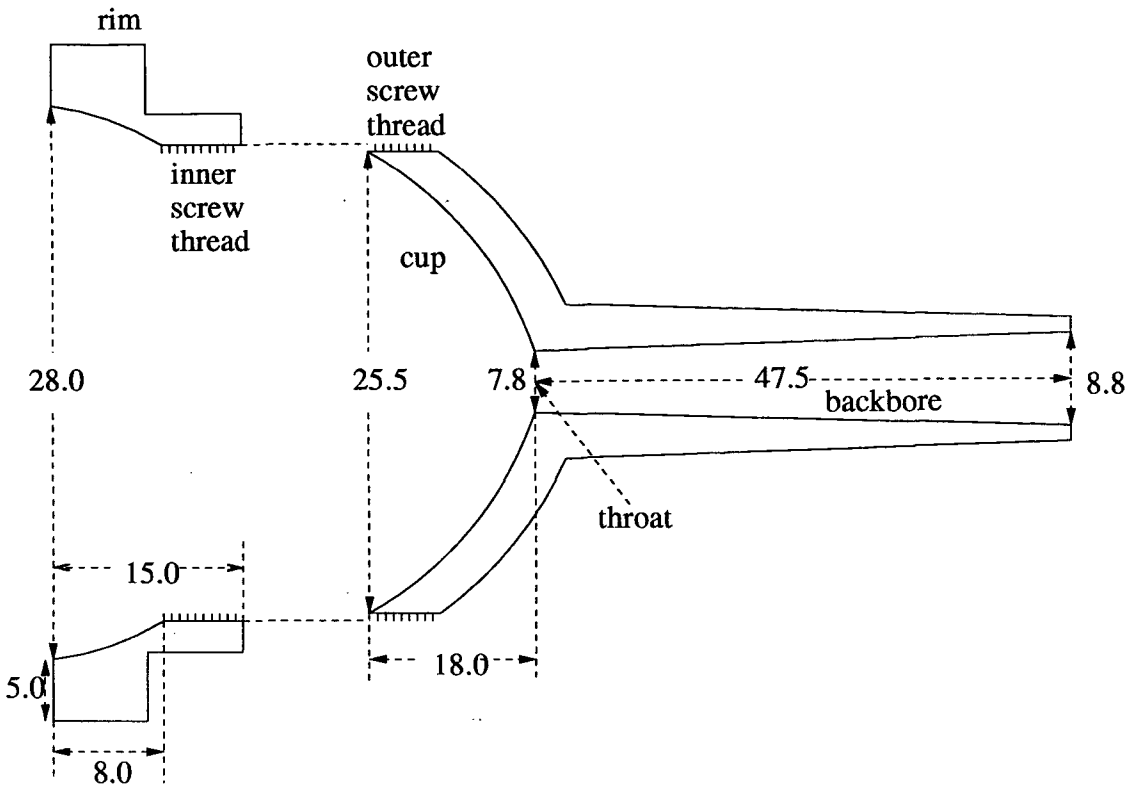

Figure 3.5: Cross-sectional view of two-piece mouthpiece showing the cup section removed from the rim. The numbers in the figure indicate dimensions in mm.

measured using a small BT-1759 Knowles microphone positioned immediately behind the teeth. For mechanical response measurements a FANE HF100 8Ω loudspeaker was used to generate an alternating pressure in the mouth. The loudspeaker was screwed into a flange on the artificial mouth top plate (e).

Throughout the present series of measurements the artificial mouth was used with a specially constructed mouthpiece with a removable cup section. The mouthpiece, when complete, has a total internal volume of 12.7ml, a Helmholtz resonance frequency of 518Hz and a quality factor of 7.1. The mouthpiece dimensions are indicated in figure 3.5.

3.2.3 Mechanical Response Measurements

During self-sustained oscillation of the lips and air column, the standing wave in the air column is characterised by the non-zero alternating pressure in the mouthpiece, p, but the alternating pressure in the mouth is assumed to be zero (see section 2.2). However during mechanical response measurements the pressure field surrounding the lips is very different. In this situation the loudspeaker, which is connected to the mouth cavity, acts as the sound source. The loudspeaker produces a very strong pressure field within the mouth cavity ($p_m \neq 0$), but a much weaker sound field on the instrument side of the lips ($p \approx 0$). In this investigation the mechanical response of the lips to forcing at (angular) frequency ω is defined as

$$C(\omega) = \frac{h(\omega)}{p_m(\omega)}. \tag{3.4}$$

Recall that $h(\omega)$ is the complex amplitude of the alternating component of the distance between the lips and $p_m(\omega)$ is the complex amplitude of the alternating component of pressure in the mouth. The lip parameters ω_L, Q_L and μ_L can all be deduced from mechanical response measurements [44].

The apparatus used for measuring the mechanical response is shown in figure 3.6. A laser beam was expanded, passed through the lip aperture and the artificial mouth, and brought to focus on a light sensitive diode. The light sensitive diode was an RS 308–067 Silicon Photodiode with integrated amplifier. The 633nm wavelength laser beam with an unfocused diameter of 0.68mm was produced by a Spectra-Physics 106-1 He-Ne 10mW laser. The beam was expanded using a converging lens positioned less than one focal length downstream from the end of the laser. Downstream of the artificial mouth a second converging lens was used to bring the beam to focus on the surface of a light sensitive diode. Obviously it would be impossible to use this experimental arrangement with a

human player. The position of the upstream lens was adjusted until the beam diameter was slightly larger than the mean distance between the lips, $\overline{H}$, but smaller than the width of the lip channel, b. With this arrangement the diode voltage was considered to be directly proportional to the distance between the lips, H. Neutral density filters were inserted in the path of the laser beam to reduce the beam intensity, avoiding saturation of the diode. To optimize the response measurements it was important to select carefully the attenuation of the neutral density filters. The diode was calibrated by replacing the lips of the artificial mouth with a variable width single slit and measuring the diode voltage as a function of slit width. A graph of diode voltage, S_d, versus slit width was plotted (see figure 3.7); the best fit straight line through the data points had gradient $m = 10.8 \pm 0.2\text{V/mm}$ and S_d axis intercept $S_{d0} = 0.46 \pm 0.06\text{V}$. The lip separation, H, can therefore be deduced from the diode voltage, S_d, using the relation

$$S_d = mH + S_{d0}. \tag{3.5}$$

However in the measurement of mechanical response it is the alternating component of lip displacement, h, which is of interest. Inspection of equation 3.5 reveals

$$h = \frac{s_d}{m} \tag{3.6}$$

where s_d is the alternating component of the diode signal.

The FANE HF100 8Ω loudspeaker was driven by a swept sine wave signal output form the PC's sound card, and then amplified using one channel of a Pioneer A–119 stereo amplifier. The PC sound card was controlled by a '.wav' file which was created especially using Matlab. This arrangement enabled mechanical response measurements to be made at 5Hz intervals over the frequency range 100–

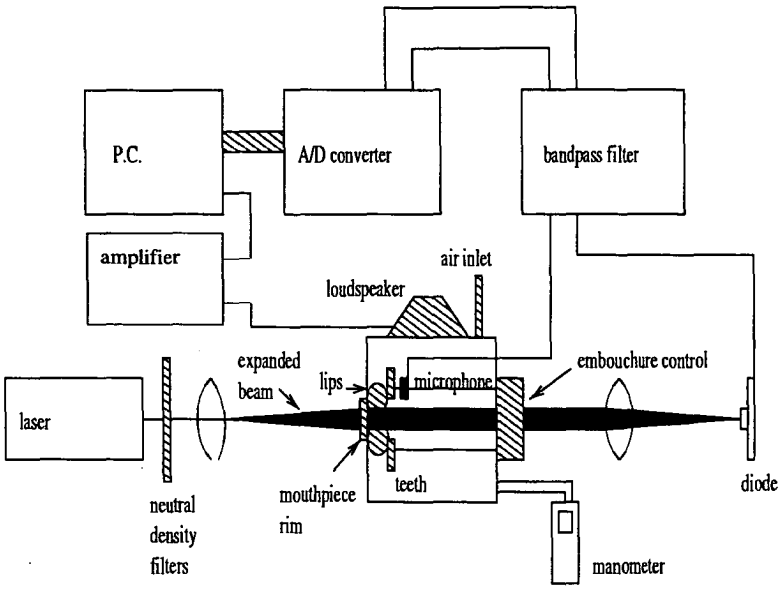

Figure 3.6: Apparatus for measuring mechanical response of artificial lip reed.

600 Hz. Each sinusoidal frequency burst was of 1s duration so a complete sweep was obtained in 101s. The signals from the diode and the BT-1759 Knowles microphone were passed through identical Kemo VBF/3 bandpass filters, each set to pass frequency components in the range 60–900 Hz. The filtered signals were then sampled with a 4096Hz sample frequency using a WaveBook 512 A/D converter connected to the PC. Identical bandpass filters were used to ensure the filtering process did not introduce an additional phase difference between the two signals.

Further filtering was applied in the digital signal processing: for each of the 101 1s frequency bursts, both signals were Hanning windowed and Fast Fourier Transformed and the amplitude and phase of the Fourier series components at the excitation frequency, ω, were extracted. The phase angle of the mechanical response, $\angle C(\omega)$, was calculated using the relation $\angle C(\omega) = \angle S_d(\omega) - \angle S_m(\omega)$, where $\angle S_d(\omega)$ and $\angle S_m(\omega)$ are the phase angles of the diode and microphone signals, respectively. The amplitude of the mechanical response, $|C(\omega)|$, was

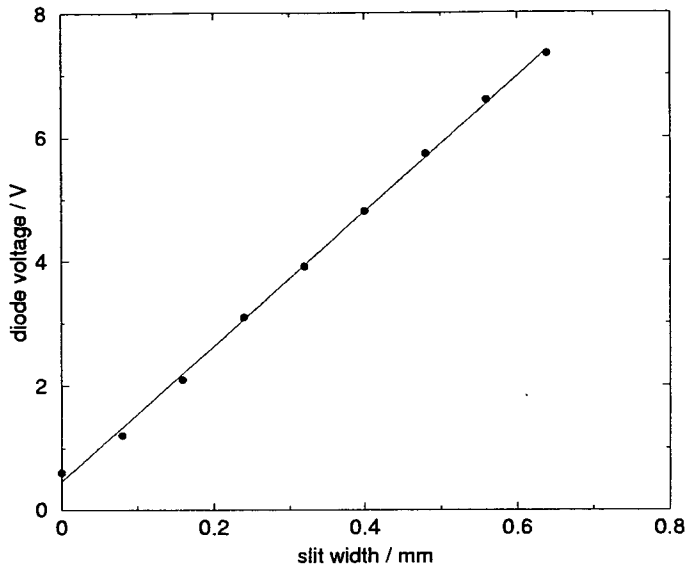

Figure 3.7: Calibration of diode using slit of variable width.

calculated using the relation $|C(\omega)| = |S_d(\omega)|/(km|S_m(\omega)|)$, where $|S_d(\omega)|$ and $|S_m(\omega)|$ are the amplitudes of the diode and microphone signals respectively, m is the gradient of the diode calibration curve and k is the Knowles microphone calibration factor (in Pa/V) over the frequency range considered. Microphone calibration is discussed in section 5.5. An example of a mechanical response curve of the lips is shown in figure 3.8. The program for producing the mechanical response, 'auto.c', is described in appendix C.3 and is listed in full in appendix D.

For the mechanical response measurements presented in this investigation the driving pressure pressure is provided by the loudspeaker, which is positioned on the upstream side of the lips (the mouth side). When the lips are forced from the upstream side in this manner, at a frequency near the resonance frequency ω_L, the dynamics of lip motion can be described by equation 3.7 (recall $1/\mu_L = (1/\mu_D - 1/\mu_B)$).

$$\frac{d^2h}{dt^2} + \frac{\omega_L}{Q_L}\frac{dh}{dt} + \omega_L^2 h = \frac{p_m}{\mu_L} \tag{3.7}$$

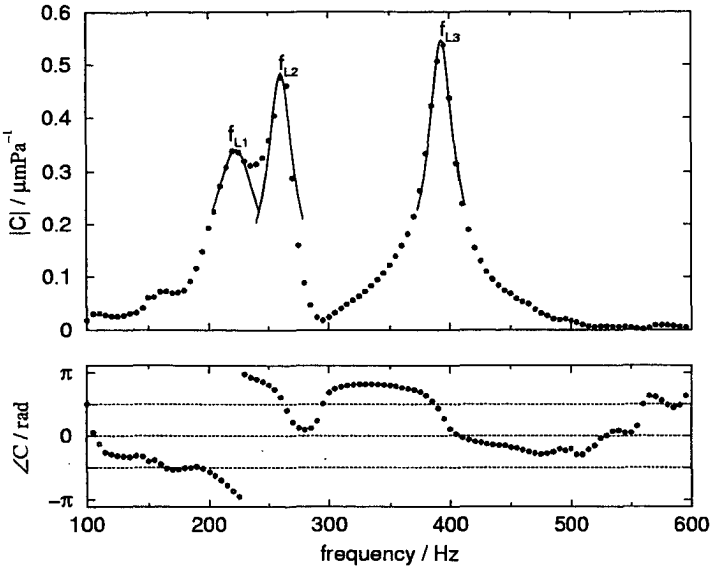

Figure 3.8: Measured mechanical response of artificial lip reed with tight embouchure (entire mouthpiece fitted). A static mouth pressure of 18.3mbar was applied.

It is instructive to compare equation 3.7 with equation 2.6, which describes the dynamics of the lip motion when the driving pressure is provided on the downstream side (the mouthpiece side). Equation 2.6 can be written in the form

$$\frac{d^2h}{dt^2} + \frac{\omega_L}{Q_L}\frac{dh}{dt} + \omega_L^2 h = \frac{-p}{\mu_L}. \tag{3.8}$$

Consider the situation where the F_D force is greater than the F_B force so that $\mu_L > 0$ and the 'outward striking' behaviour prevails. In this case if the driving pressure is provided on the downstream side of the lips, *e.g.* during self-sustained oscillation, then a decrease in mouthpiece pressure, p, increases the separation of the lips (see equation 3.8); however if the driving pressure is provided on the upstream side of the lips, *e.g.* during the mechanical response measurements of this investigation, then a decrease in mouth pressure, p_m, decreases the separation of the lips (see equation 3.7).

The equivalent frequency domain representation to equation 3.7 is

$$C(\omega) = \frac{h(\omega)}{p_m(\omega)} = \frac{-j\frac{Q_L}{\omega\omega_L}\frac{1}{\mu_L}}{1 + \frac{jQ_L(\omega^2-\omega_L^2)}{\omega\omega_L}}. \tag{3.9}$$

A mechanical mode can be categorized as 'inward striking' or 'outward striking' purely from $\angle C(\omega_L)$, the phase of the mechanical response evaluated at the resonance frequency. From equation 3.9 it is clear that $\angle C(\omega_L) = -\pi/2$ for dominant outward striking reed behaviour ($\mu_L > 0$) but $\angle C(\omega_L) = \pi/2$ for dominant inward striking reed behaviour ($\mu_L < 0$). In their theoretical models of mechanical response Adachi and Sato [1] and Elliot and Bowsher [34] considered the driving pressure to be applied from the downstream side of the lips. In this case the lip dynamics can be described by equation 3.8 and the mechanical response of the lips must be redefined, for example as

$$G(\omega) = \frac{h(\omega)}{p(\omega)}, \tag{3.10}$$

in which case

$$G(\omega) = \frac{j\frac{Q_L}{\omega\omega_L}\frac{1}{\mu_L}}{1 + \frac{jQ_L(\omega^2-\omega_L^2)}{\omega\omega_L}}. \tag{3.11}$$

This equation differs from equation 3.9 only in sign. Therefore with the definition of mechanical response adopted by Elliot and Bowsher and Adachi and Sato the phase angle of the mechanical response is $+\pi/2$ for an outward striking reed and $-\pi/2$ for an inward striking reed. In the present investigation the loudspeaker was positioned on the upstream side of the lips rather than the downstream side to simplify the experimental apparatus.

From equation 3.9 it is clear that near the resonance frequency, ω_L, the magnitude of the mechanical response can be approximated as

$$|C(\omega)| \approx \frac{\frac{Q_L}{\omega_L^2}\frac{1}{|\mu_L|}}{\sqrt{1 + 4Q_L^2\left(\frac{\omega-\omega_L}{\omega_L}\right)^2}}. \tag{3.12}$$

provided the substitutions $\omega^2 - \omega_L^2 \approx 2\omega(\omega - \omega_L)$ and $\omega\omega_L \approx \omega_L^2$ are made in the denominator and numerator respectively. For each mechanical response curve measured the lip parameters $|\mu_L|$, Q_L and $f_L = \omega_L/2\pi$ were estimated for each mode by numerically fitting equation 3.12 around local maxima, using a 5 point least squares fit routine. This approach to estimating the lip parameters is similar to that applied to the extraction of acoustic parameters from input impedance magnitude curves and the same least squares fit program was used to extract parameters from both types of resonance data. It was not possible to produce an accurate fit to strongly unsymmetrical peaks or indistinct peaks.

The mechanical response curve in figure 3.8 shows 3 distinct modes with resonance frequencies f_{L1} =223Hz, f_{L2} =260Hz and f_{L3} =393Hz. From the phase curve it is clear that the f_{L1} mode has dominant outward reed behaviour whereas modes f_{L2} and f_{L3} have dominant inward reed behaviour. There is no evidence of a strong response near the Helmholtz resonance frequency of the mouthpiece (517Hz).

Mechanical response measurements were carried out for a variety of embouchures with a large range of sub-threshold static mouth pressure values. All response measurements were performed without the trombone but with the mouthpiece, or only the mouthpiece rim, fitted to the artificial lips. Experiments were carried out to investigate whether changing the resonance properties of the mouth had any effect on the mechanical response of the lips.

3.2.4 Threshold Measurements

The apparatus used to carry out the threshold measurements is displayed in figure 3.9. To determine the threshold value for a particular embouchure setting and particular position of the trombone slide, the mouth pressure was slowly increased until a stable sound was obtained.

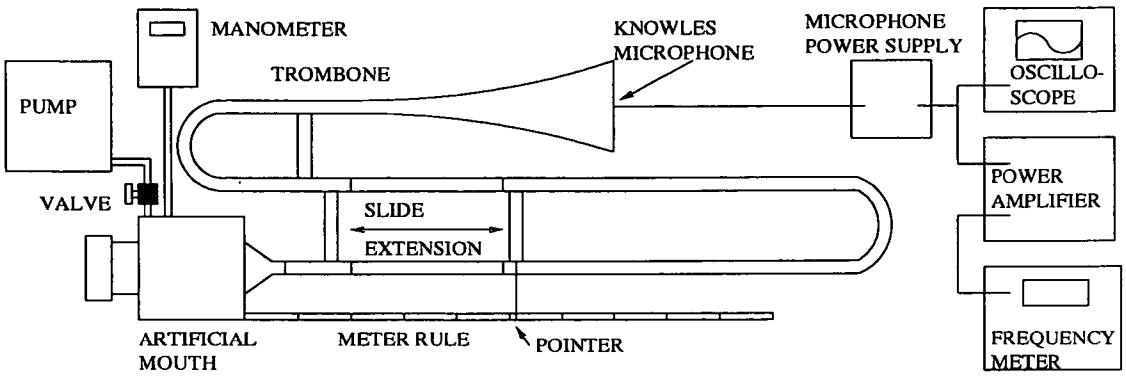

Figure 3.9: Apparatus for measuring threshold pressure and frequency.

To remove any inconsistencies in the determination of the threshold, a BT-1759 Knowles microphone was positioned just inside the bell of the trombone; the experimental threshold pressure was defined as the mouth pressure required to produce a microphone signal with a predefined (small) amplitude of 1.0V, corresponding to a SPL of 125dB. The threshold frequency was measured by a Black Star Appolo 100 digital frequency meter with a 0.1Hz precision.

Two different situations were investigated: (1) variation of threshold values as a function of slide extension, with fixed embouchure, and (2) variation of threshold values as a function of embouchure, with slide in a fixed position. Situation (1) corresponds to variation of acoustical parameters with fixed mechanical parameters while situation (2) corresponds to variation of mechanical parameters with fixed acoustical parameters. The embouchure was varied by rotating the teeth control in steps of 1/8 rotations and was always moved from tightest position to slackest position.

3.3 Comparison with Theoretical Results Obtained from Linear Stability Analysis

3.3.1 Static Mechanical Response Measurements

The results of a brief investigation into the response of the lips to a purely static mouth pressure will be presented before the dynamic mechanical response measurements described in section 3.2 are discussed. Measurements with purely static pressure were used to determine the lip parameters b and $\overline{H_0}$, and to test the assumptions regarding the pressure field surrounding the lips which were made in section 2.2.

By setting all of the alternating components to zero in the Bernoulli and volume flow relations (equations 2.4 and 2.5 respectively) and combining these equations to eliminate $\overline{U}_L$, the following relationship between static mouth pressure and volume flow was obtained

$$\sqrt{\overline{P_m}} = \left(\sqrt{\frac{\rho}{2}}\right) \frac{\overline{V}}{b\overline{H}}, \quad \overline{P_m} \geq 0. \tag{3.13}$$

A CT Platon A10HD CA232001 volume flow meter with a full scale deflection of 50l/min was inserted in the air supply pipe, between the valve and the artificial mouth. With a fixed embouchure, the volume flow was increased from 6l/min in intervals of 2l/min; for each value of volume flow the pressure in the mouth was read off from the manometer. Measurements made with 3 different embouchures are displayed in figure 3.10. In each case the plot of $\sqrt{\overline{P_m}}$ versus $\overline{V}$ is a straight line graph, indicating that the variation of $b\overline{H}$ with $\overline{V}$ is much less significant than the variation of $\overline{P_m}$ with $\overline{V}$, *i.e.* $\overline{H} \approx \overline{H_0}$, where $\overline{H_0}$ is the distance between the lips when the alternating and static mouth pressure is zero. Using equation 3.13, estimates of the lip opening area, $b\overline{H_0}$, were made from the gradients of the straight line graphs of figure 3.10.

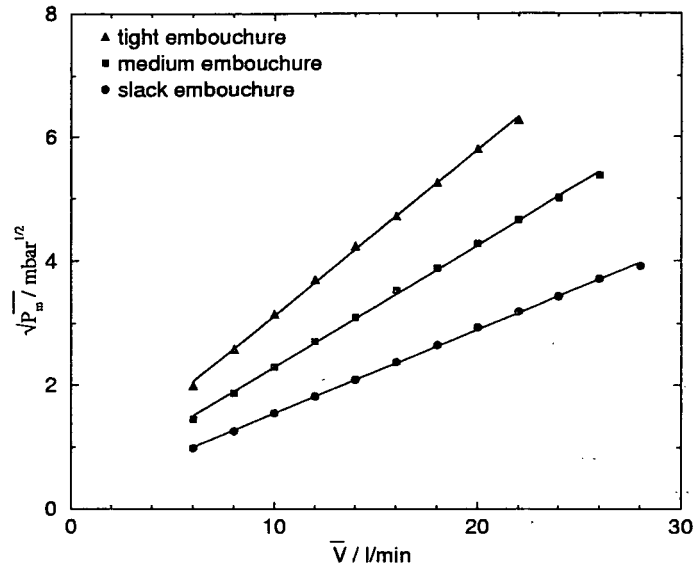

Figure 3.10: Measured variation of $\overline{\sqrt{P_m}}$ with $\overline{V}$ for 3 different embouchures.

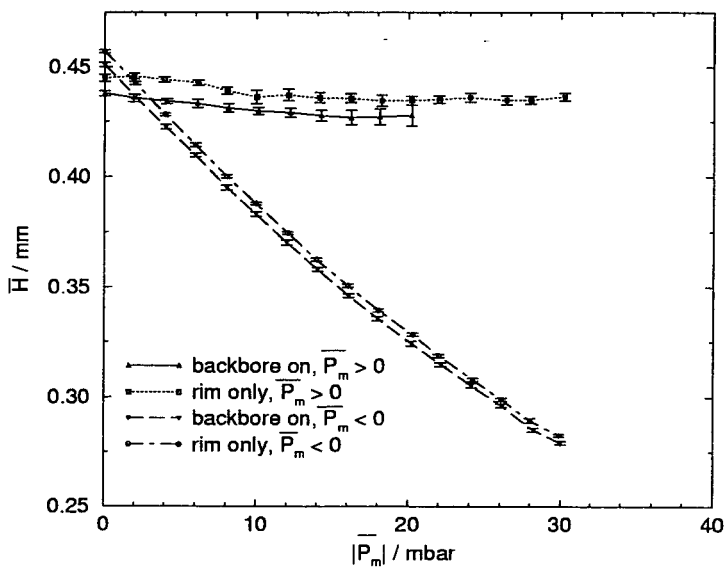

Figure 3.11: Measured variation of $\overline{H}$ with $\overline{P_m}$ for tightest embouchure. No periodic forcing of lips or self-excitation.

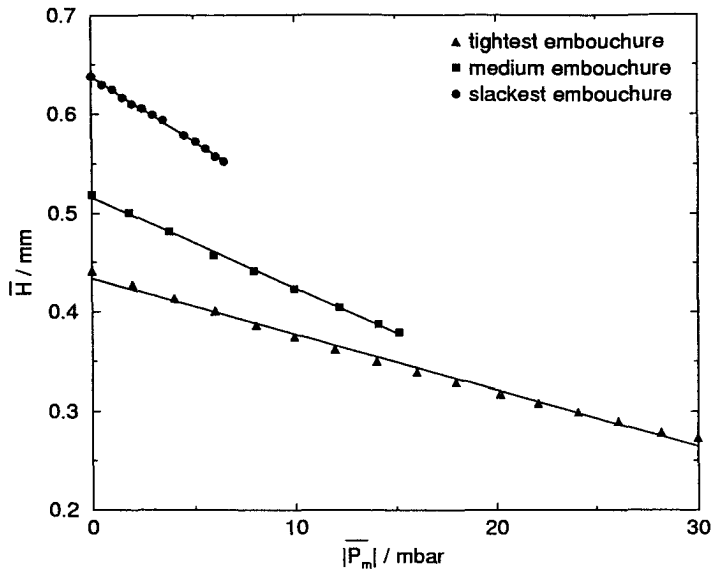

Figure 3.12: Measured variation of $\overline{H}$ with $\overline{P_m}$ for 3 different embouchures. In each case measurements were carried out with the backbore removed and with $\overline{P_m} \leq 0$.

The electronic filters were removed from the experimental set–up, allowing the (constant) distance between the lips to be deduced from the D.C. diode signal. Initial measurements, with $P_m = 0$, were carried out to determine H_0 for each of the three embouchures, 'tight', 'medium', and 'slack', considered above.

This experimental arrangement was also used to study the variation of $\overline{H}$ with $\overline{P_m}$ (figure 3.11). Notice that when the rest of the mouthpiece is added to the rim section the measured values of $\overline{H}$ are systematically reduced by about 5%. The discrepancy is due to a slight misalignment of the laser beam which resulted in the mouthpiece backbore blocking a small percentage of the beam and therefore slightly reducing the intensity of light detected by the diode. Measurements were carried out with $\overline{P_m} \geq 0$ (air flow through lips out of mouth) and with $\overline{P_m} \leq 0$ (air flow through lips into mouth). In practice a negative static mouth pressure was created by disconnecting the air inlet pipe to the artificial mouth from the output port of the pump and connecting it instead to the input port of the pump.

When $\overline{P_m} > 0$ there is little variation of $\overline{H}$ with $\overline{P_m}$, confirming the earlier observation that $\overline{H} \approx \overline{H_0}$. Following the discussion of the pressure field surrounding the lips (section 2.2), with $\overline{P_m} > 0$, it is expected that the static overpressure in the lip channel, $\overline{P_L}$, should be equal to zero because the static overpressure in the mouthpiece, $\overline{P}$, is assumed to be zero and there is assumed to be no recovery of pressure. In this case there is no Bernoulli force, $\overline{H} - \overline{H_0} = \overline{P_m}/(\omega_L^2 \mu_D)$ and so a plot of $\overline{H}$ versus $|\overline{P_m}|$ should give a straight line graph with positive gradient. With $\overline{P_m} < 0$ it is expected that $\overline{P_L} = \overline{P_m}$ and so the F_B and F_D forces both act to close the lips: $\overline{H} - \overline{H_0} = \overline{P_m}(1/(\omega_L^2 \mu_D) + 1/(\omega_L^2 \mu_B))$. Since $\overline{P_m} < 0$, a plot of $\overline{H}$ versus $|\overline{P_m}|$ should give a straight line graph with negative gradient and the magnitude of the gradient should be greater than in the $\overline{P_m} > 0$ case.

In figure 3.11, as expected, the gradient is clearly negative in the $\overline{P_m} < 0$ case. However, for the $\overline{P_m} > 0$ case the gradient is actually slightly negative for $|\overline{P_m}|$ <20mbar, indicating that the 'Bernoulli force' must be greater than the 'outward striking reed force'. Hirschberg [55] has shown that the Bernoulli force may indeed act under these conditions: the inclusion of viscous effects in the flow can lead to retarded flow separation at the exit of a diverging lip channel. As a result the velocity of the jet is less than the velocity at the entrance to the lip channel, and a pressure gradient, which acts to close the lips, is created in the lip channel.

Figure 3.12 shows that, in the $\overline{P_m} \leq 0$ case, the magnitude of the gradient of the $\overline{H}$ versus $|\overline{P_m}|$ curves increase as the embouchure is slackened. This demonstrates that the total 'static stiffness' (which is proportional to the parallel combination of $\omega_L^2 \mu_D$ and $\omega_L^2 \mu_B$) decreases as the embouchure is slackened. In the $\overline{P_m} \geq 0$ case the two forces acting on the lips oppose each other; unfortunately the measurements were insufficiently accurate to estimate 'static stiffness' in that

situation.

3.3.2 Dynamic Response Measurements for 3 Different Embouchures

The mechanical response curve presented in figure 3.8 has three distinct modes: the first mode, with resonance frequency $f_{L1} = 223$Hz, displays 'outward striking' behaviour but the higher modes, with resonance frequencies $f_{L2} = 260$Hz and $f_{L3} = 393$Hz, both demonstrate 'inward striking' behaviour. In figure 3.13 mechanical response curves, measured with $\overline{P_m} = 0$, are displayed for the three embouchures considered in section 3.3.1; each of the mechanical response measurements represented in figure 3.13 was made with the mouthpiece cup removed, leaving only the rim. The resonance frequencies increase as the embouchure is tightened. However in each case there is a strong resonance with outward character around 180–230Hz and one with inward character around 330–400Hz. The 180–230Hz and 330–400Hz resonances correspond, respectively, to the f_{L1} and f_{L3} resonances of the of the curve presented in figure 3.8. In figure 3.13, from the magnitude curve alone there is little evidence of a resonance corresponding to f_{L2}. However for the 'medium' and 'tight' embouchures the phase curve crosses the $\pi/2$ line around 250-270Hz, providing some evidence of f_{L2} resonances. There are also weaker resonances with 'outward' character around 150Hz.

The above measurements were repeated with the entire mouthpiece in place (figure 3.14). Figures 3.13 and 3.14 are of similar shape but the scale of the magnitude curves are very different; the measurements with the entire mouthpiece systematically under estimate the magnitude of the mechanical response due to the slight misalignment of the laser beam, referred to in section 3.3.1. Blocking some of the light near the edge of the beam does not greatly affect the D.C. component of the diode signal but can greatly reduce the amplitude of the A.C.

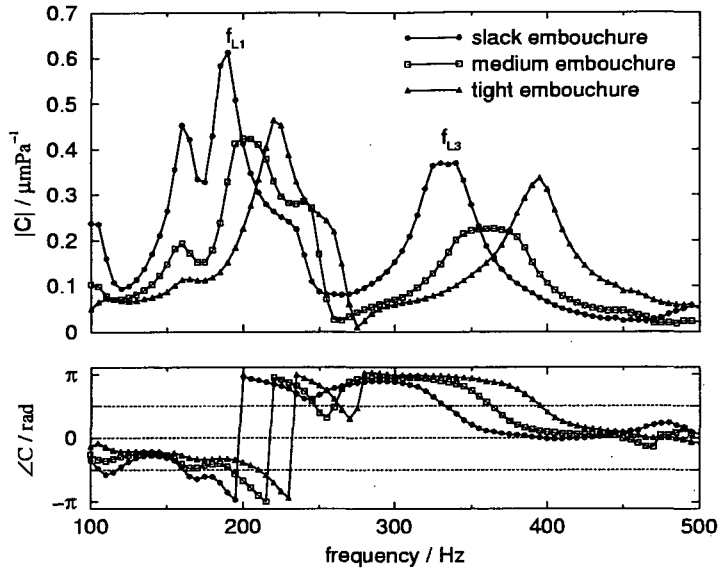

Figure 3.13: Mechanical response of the three embouchures with $\overline{P_m} = 0$ (mouthpiece cup removed).

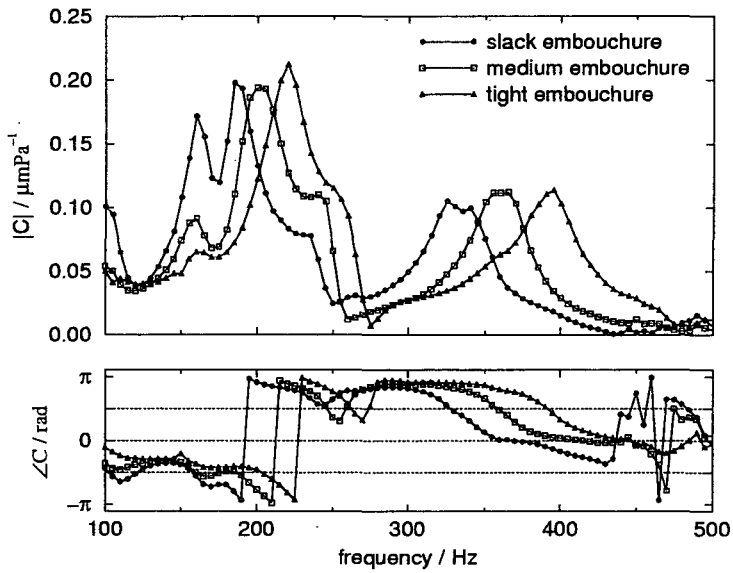

Figure 3.14: Mechanical response of the three embouchures with $\overline{P_m} = 0$ (entire mouthpiece fitted).

component, since $\overline{H} \gg h$ for mechanical response measurements.

Figure 3.15 demonstrates how the mechanical response evolves as the static mouth pressure is increased from zero to a value just below the threshold of oscillation. As $\overline{P_m}$ increases the quality factor of one or more mechanical modes increases, tending towards infinity. This suggests that as $\overline{P_m}$ increases aerodynamic coupling increases, but from figure 3.15 alone it is not clear whether the most significant aerodynamic coupling is between two mechanical modes or between one mechanical mode and one acoustical mode. Notice that in figure 3.15 the 250–270Hz resonance with 'inward' character, equivalent to the f_{L2} resonance of figure 3.8, can only be clearly distinguished when $\overline{P_m} \neq 0$.

In chapter 2 it was shown that the linearized equations which represent a system with 2 coupled modes can be arranged in the form of a matrix equation which includes a 4×4 matrix (see equation 2.11). In fact, more generally, the linearized equations which represent a system with n coupled modes can be arranged in the form of a matrix equation which includes a $2n \times 2n$ matrix. The real and imaginary parts of the mth eigenvalue, λ_m of such a $2n \times 2n$ matrix is related to the quality factor, Q_m, and natural frequency, f_m, of the mth mode: $Re[\lambda_m]/2\pi = -f_m/(2Q_m)$ and $Im[\lambda_m]/2\pi = f_m$. In general the eigenvalues, and consequently f_m and Q_m vary as a function of one or more control parameters. The experimental data from figure 3.15 was used to plot $(-f_{L1}/(2Q_{L1}), f_{L1})$ and $(-f_{L2}/(2Q_{L2}), f_{L2})$ as a function of the control parameter $\overline{P_m}$ (figure 3.16). This representation is analogous to the theoretical complex plane eigenvalue evolution (for example figure 2.4). With this representation, as $\overline{P_m}$ increases the horizontal component moves towards the vertical axis, indicating a tendency for the stability of the two mechanical modes to decrease as $\overline{P_m}$ increases.

It is interesting to compare the mechanical response measurements presented

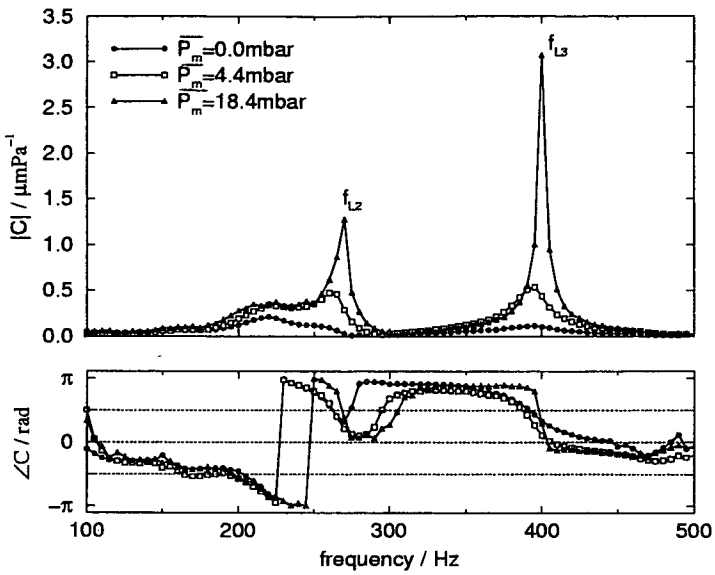

Figure 3.15: Mechanical response of tightest embouchure with different values of $\overline{P_m}$ (entire mouthpiece fitted).

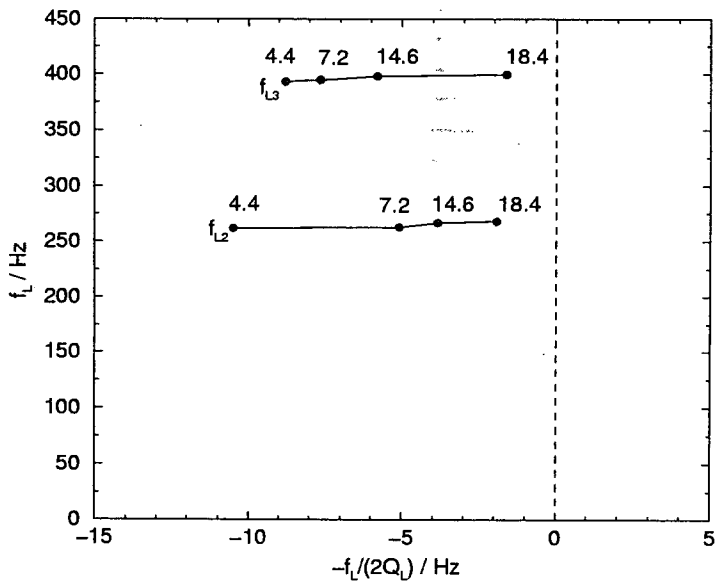

Figure 3.16: Complex plane representation of measured mechanical response of tightest embouchure (entire mouthpiece fitted). The numbers beside each point indicate $\overline{P_m}$, in mbar.

here with the preliminary measurements of Gilbert et al [44]. They used an artificial mouth of similar design but fitted with only one lip. In that study a mechanical mode with 'outward' behaviour and natural resonance frequency of approximately 200Hz was measured, but no other modes were detected above 100Hz. The 200Hz mode corresponds to the mode labelled f_{L1} in the present study. Gilbert et al pointed out that they were able to measure modes with 'outward' behaviour but not modes with 'inward' behaviour (such as the f_{L2} and f_{L3} modes in the present study), since the displacement of the lip was measured using a laser vibrometer which was sensitive only to movement of the lips in a direction perpendicular to the plane of the lips.

Figure 3.17 represents the mechanical response of the three embouchures with $\overline{P_m}$ selected to be slightly below the threshold of oscillation in each case. There is no evidence of destabilization of the f_{L1} mode, with outward character. Both modes f_{L2} and f_{L3} appear to be heading towards destabilization. The mouth pressure was then further increased until one of the modes was destabilized, resulting in self sustained oscillation. With the 'tight' embouchure the threshold playing frequency was very close to the f_{L3} resonance, indicating that it was the f_{L3} resonance which was destabilized; with the 'medium' and 'slack' embouchures the f_{L2} resonance appeared to be destabilized. As the embouchure is varied from the 'slack' position to the 'tight' position there is a bifurcation of the periodic regime associated with f_{L2} to the periodic regime associated with f_{L3}. This unexpected behaviour supports the mouthpiece playing frequency measurements of Gilbert et al [44] (figure 5); they observed two discrete oscillation regimes, one at 250Hz and one at 400Hz.

The lips of the artificial mouth did not buzz when the mouthpiece cup was removed, leaving only the rim. However, to investigate whether there was any

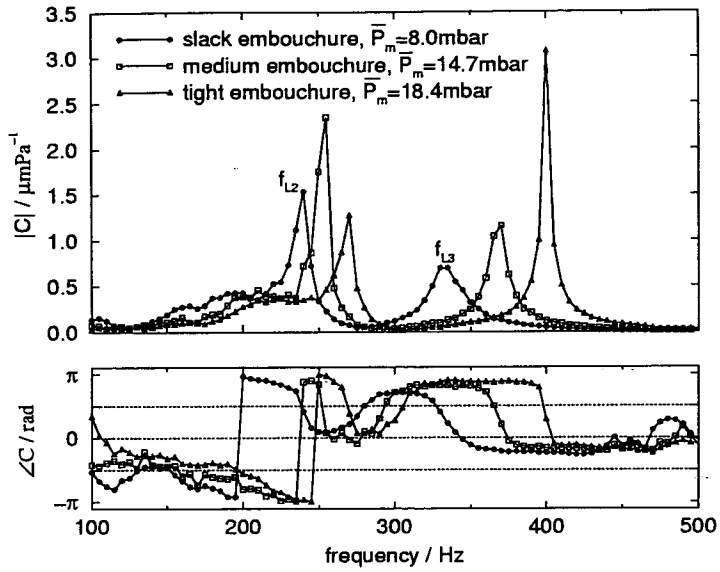

Figure 3.17: Mechanical response of the three embouchures with $\overline{P_m}$ slightly below oscillation threshold (entire mouthpiece fitted).

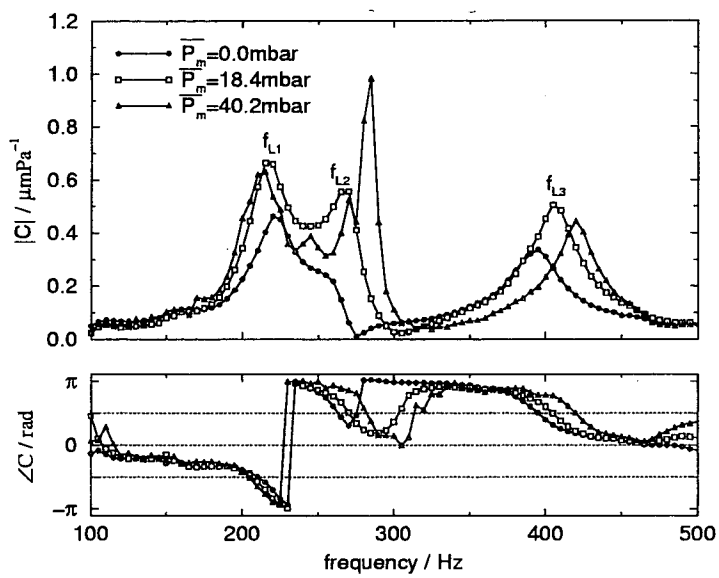

Figure 3.18: Mechanical response of the tightest embouchure with different values of $\overline{P_m}$ (mouthpiece cup removed).

evidence of a destabilizing effect even with the cup removed, mechanical response measurements were performed for increasing values of $\overline{P_m}$. In figure 3.18 the quality factor of the second mode (250Hz) increases with $\overline{P_m}$ indicating that the mode is heading towards destabilization. There is no significant increase in the quality factor of the first mode, indicating the first mode is substantially stable. With the acoustical coupling to the mouthpiece now removed, the third mode also appears stable. However its resonance frequency does increase as $\overline{P_m}$ increases, which suggests the mode could still be sensitive to airflow coupling. It is not clear if the destabilizing effect on the second mode is due to aerodynamic coupling to another mechanical mode or to aerodynamic coupling between the lips and the acoustical resonator formed by the mouth cavity [39]. It is worth noting that any possibility of flow control by the mouthpiece throat is certainly absent in the measurements with rim only.

3.3.3 Mouth Cavity Effect

To attempt to answer the question posed at the end of the previous section experiments were carried out to determine the influence of the mouth cavity on the mechanical response of the artificial lips. The mechanical response of the lips was measured with the mouth cavity in its usual state. The mouth cavity was then partially filled with solid material, reducing the volume of the cavity by approximately 30%, and the mechanical response of the lips was measured a second time. Finally, the solid material was removed and the mechanical response was measured again, with the original mouth cavity volume. Throughout the measurements the embouchure was held constant. Measurements were carried out firstly with the mouthpiece cup removed and $\overline{P_m} = 0$ (figure 3.19), and secondly with the entire mouthpiece fitted and $\overline{P_m}$ just below the threshold of oscillation (figure 3.20).

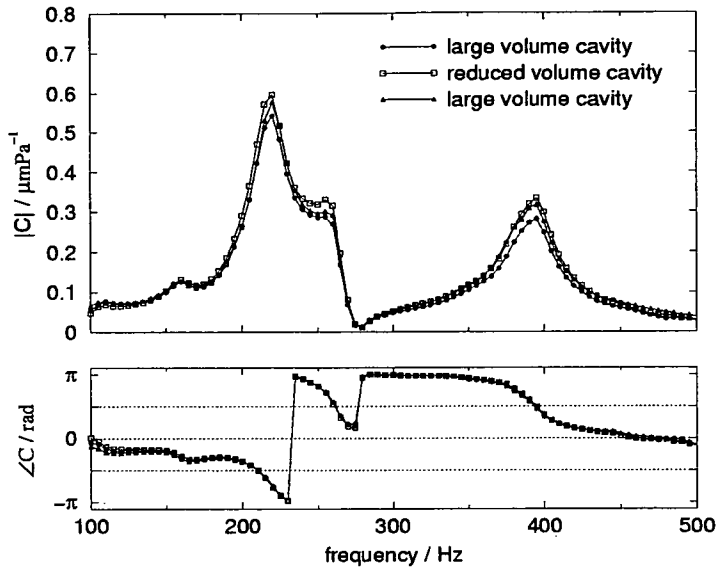

Figure 3.19: Mechanical response measurements with different mouth cavity volumes. Measurements carried out with backbore removed and $\overline{P_m} = 0$.

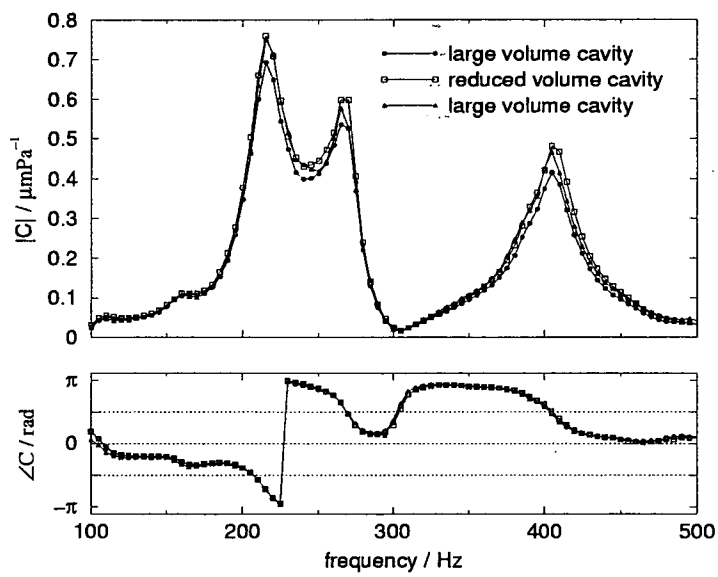

Figure 3.20: Mechanical response measurements with different mouth cavity volumes. Measurements carried out with backbore removed and $\overline{P_m} = 18.4$mbar.

There is no clear evidence that the mechanical response of the lips is significantly affected by the modification to the mouth cavity. It thus seems more probable that the incipient destabilization seen in figure 3.18 is due to coupling of two mechanical modes.

The results of the present experiment suggest the mouth cavity is not crucial for the destabilization of the lips. However, it could still have a significant effect on other aspects of brass instrument acoustics. The mouth cavity effect will be revisited in chapter 7.

3.3.4 Mechanical Response Evolution with Embouchure

The mechanical response measurements presented above were performed using only three different embouchures. The contour map (figure 3.21) indicates how the mechanical response evolves with embouchure as the embouchure varies over twenty different positions of the teeth. The contour shading indicates the decibel mechanical response ($10\log_{10}[|C(f)|/C_0]$) of a particular embouchure (indicated on vertical axis) to forcing at frequency f (indicated on horizontal axis). The lighter the shading of the map, the stronger the mechanical response. The same reference level, C_0, was used for each embouchure; C_0 was selected to be the maximum value of mechanical response magnitude. The measurements were performed with the mouthpiece cup removed and with $\overline{P_m} = 0$.

The contour map was produced using measurements performed several weeks after the measurements presented in previous sections, but examination of the resonance frequencies suggest that the early measurements with embouchures 'slack', 'medium' and 'tight' have similar mechanical response to contour map measurements with the embouchure positioned at, respectively, 3, 7 and 11 1/8 rotations from the slackest position. The new measurements have similar form to the measurements presented in previous sections but the magnitude of the

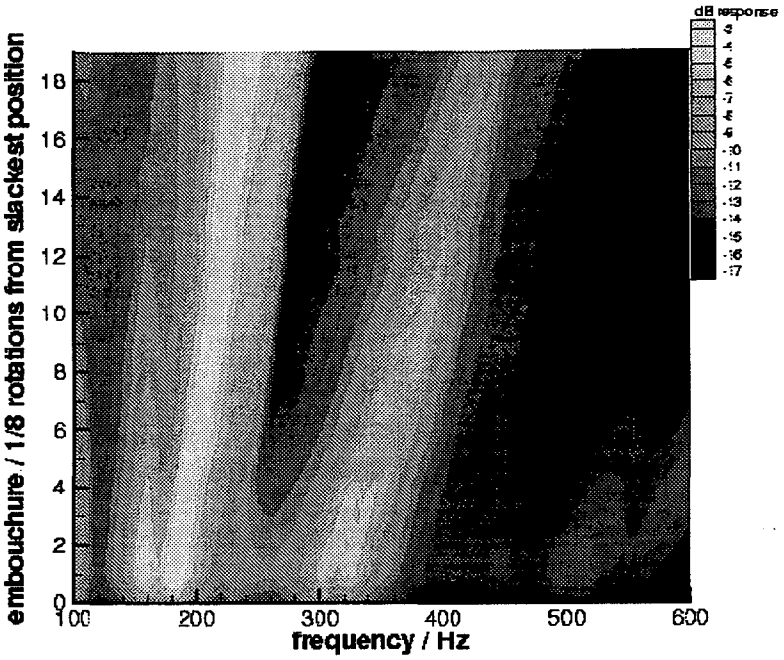

Figure 3.21: Contour map of mechanical response magnitude as a function of embouchure and frequency. Measurements performed with mouthpiece cup removed and $\overline{P_m} = 0$.

new response measurements is systematically lower. The range of parameter values extracted from the contour map response measurements are presented in table 3.2 and a complete list of the parameter values are displayed in table A.2 of appendix A. These parameters were used to select the range of f_L and Q_L for figure 2.7 and to select parameter values for additional threshold simulation measurements presented in section 3.4.

The 180–220Hz mode (previously labeled f_{L1}) and the 300–400Hz mode (f_{L3}) can be clearly distinguished on the contour map, but as $\overline{P_m} = 0$ there is no clear evidence of the intermediate f_{L2} mode. For slacker embouchures an additional mode at around 160Hz is also apparent. As the embouchure is tightened f_{L1} and f_{L3} increase in frequency.

3.3.5 Lip Parameter Values

In this chapter the mechanical response of the artificial lips has been investigated in some detail, allowing the estimation of the lip parameters required to run the one mass oscillation threshold simulations developed in chapter 2. The output from the simulations will be presented in section 3.4.

The measured lip parameters for the embouchures labelled 'slack', 'medium' and 'tight' are presented in table 3.1. Estimates for the ranges of the lip parameters are displayed in table 3.2, alongside values used by other authors. The 'present study' estimates of b and $\overline{H_0}$ are chosen to bracket the b and $\overline{H_0}$ values listed in table 3.1. The ranges of f_{L1}, Q_{L1} and $1/\mu_{L1}$ in table 3.2 were estimated from the values in table 3.1 and from the additional measurements used to generate the contour map (figure 3.21). The ranges of f_{L2}, Q_{L2}, and $1/\mu_{L2}$, in table 3.2, were estimated from the values of table 3.1 and from mechanical response measurements performed with identical embouchure positions to the contour map measurements but with $\overline{P_m}$ =3mbar. It was necessary to apply a non-zero static mouth pressure in these measurements to ensure the resonance peak of the second mode could be clearly distinguished from the resonance peak of the first mode; 3mbar was found to be the minimum static mouth pressure which ensured the second mode could be clearly distinguished over the appropriate range of embouchures. In table 3.2 only the parameter values of modes f_{L1} ('outward striking') and f_{L2} ('inward striking') are displayed because, for the acoustic resonators considered in section 3.4, initial runs of the simulation indicated that mode f_{L3} could only be destabilized with unrealistically high values of $\overline{P_m}$. The parameter estimates in the 'present study', Elliot and Bowsher [34] and Saneyoshi et al [79] were extracted from measurements with either a trombone or a euphonium mouthpiece. All of the 'present study' parameters were obtained

	slack	medium	tight
b / mm	15	12	11
$\overline{H_0}$ / mm	0.63	0.53	0.44
f_{L1} / Hz	189	203.5	222
Q_{L1}	10.5	6	9
$1/\mu_{L1}$ / $\mathrm{m^2kg^{-1}}$	0.07	0.11	0.09
f_{L2} / Hz	234	resonance	259.5
Q_{L2}	11	not clearly	10.5
$1/\mu_{L2}$ / $\mathrm{m^2kg^{-1}}$	−0.13	resolved	−0.11
f_{L3} / Hz	338.5	362	394
Q_{L3}	8	4	13
$1/\mu_{L2}$ / $\mathrm{m^2kg^{-1}}$	−0.30	−0.26	−0.14

Table 3.1: Parameters for embouchures 'slack', 'medium' and 'tight' estimated from static and dynamic mechanical response measurements.

	present study	Elliot & Bowsher [34]	Saneyoshi et al [79]
b / mm	9 – 18	13	8.8 – 10.5
$\overline{H_0}$ / mm	0.25 – 0.70	0.30 – 0.45	0.07 – 0.17
f_{L1} / Hz	182 – 237	N.A.	N.A.
Q_{L1}	6 – 12	0.5	N.A.
$1/\mu_{L1}$ / $\mathrm{m^2kg^{-1}}$	0.04 – 0.11	0.3 – 0.6	N.A.
f_{L2} / Hz	225 – 278	N.A.	N.A.
Q_{L2}	8 – 16	0.5	5
$1/\mu_{L2}$ / $\mathrm{m^2kg^{-1}}$	−0.05 – −0.13	−0.5 – −0.7	−0.19 – −0.27

Table 3.2: Comparison of parameter ranges measured in present study with parameter ranges used in previous studies. Both of the previous studies [34] [79] considered a much larger range of lip resonance frequencies than in the present study, so f_{L1} and f_{L2} have been deemed not applicable (N.A.). Also, Saneyoshi et al [79] did not consider the outward striking reed case so f_{L1}, Q_{L1} and $1/\mu_{L1}$ are not applicable (N.A.).

present study	Elliot & Bowsher [34]	Saneyoshi et al [79]
b	l	b
$\overline{H_0}$	X_0	$\overline{d}$
$\frac{1}{\mu_{L1}}$	$\frac{A}{m}$	N.A.
$\frac{1}{\mu_{L2}}$	$-\frac{A_2}{m}$	$-\frac{A}{m'}$

Table 3.3: Relationship between parameters in present study and parameters used in previous studies [34] [79].

by direct measurement, using the artificial lip reed mechanism. Not all of the parameters used by Saneyoshi et al or Elliot and Bowsher were measured directly: although some parameters were deduced from measurements with human players others were estimated using inverse calculations which assume the correctness of the one mass model.

The other authors considered a larger range of lip resonance frequencies than in the present study; the ranges of frequency dependent parameters quoted in table 3.2 are in all cases those appropriate to the range of f_{L1} and f_{L2} observed in the present study. Inevitably the various authors have used different notation. Table 3.3 indicates the relationship between the parameters used in the various studies; individual papers should be consulted for explanation of the notation.

From table 3.2 it is obvious that there is a considerable variety in the range of parameter values selected by the various authors. In particular the quality factor used by Elliot and Bowsher appears exceptionally low compared to the Saneyoshi et al and 'present study' estimates. Elliot and Bowsher based their estimate of lip quality factor not on measurements of the lips but on measurements by Ishizaka et al. [58] of the mechanical response of human neck and cheek flesh. There appears to be no experimental justification for the choice of lip quality factor adopted

by Saneyoshi et al. The ratios of effective area to effective mass ($1/\mu_{L1}$ and $1/\mu_{L2}$) measured in the present study are slightly lower than the values adopted by Saneyoshi et al., and much lower than the values used by Elliot and Bowsher.

3.4 Threshold Behaviour of Buzzing Lips Coupled to a Trombone

In this section simulated threshold behaviour is compared with the threshold behaviour measured using a trombone coupled to the artificial lips. The measured threshold pressure will be assumed to be the static mouth pressure required to obtain the permanent periodic regimes with as small an amplitude as is possible; the measured threshold frequency will be assumed to be the fundamental acoustic frequency at that value of mouth pressure. These assumptions are valid only if the characteristic variables of the permanent periodic regime (static mouth pressure and fundamental frequency) tend towards the characteristic variables of the linear threshold (threshold pressure and threshold frequency) as the amplitude of the permanent periodic regime tends to zero. This is true in the case of a direct bifurcation but not in the case of an inverse bifurcation [46]. With an inverse bifurcation the threshold mouth pressure of the permanent periodic regime is actually below the linear threshold (see for example the study by Dalmont et al [24], applied to reed instruments). In the present study it is necessary to assume that, in the case of the trombone, each bifurcation is a direct bifurcation. The experiments did not provide any evidence of inverse bifurcations.

3.4.1 Fixed Embouchure, Variable Slide Length

Immediately before conducting each set of threshold measurements, the mechanical response of each embouchure was measured with $\overline{P_m} = 0$ and the parameters f_{L1}, Q_{L1} and $1/\mu_{L1}$ were extracted. The parameters f_{L2}, Q_{L2} and $1/\mu_{L2}$ were

extracted from the $\overline{P_m}$ = 3mbar measurements. The b and $\overline{H_0}$ values were estimated from the values in table 3.1 and from extrapolation of these values. The acoustic parameters extracted from input impedance measurements are listed in table A.1 of appendix A.

Figure 3.22 demonstrates how the threshold values vary as the trombone slide is extended. The simulated behaviour was presented earlier in chapter 2 (as figure 2.6), and was discussed in some detail. It has been reproduced as figure 3.22b to allow direct comparison with the equivalent threshold measurements (figure 3.22a). The measured range of threshold pressure is similar to the range predicted by the inward striking model. The outward striking model predicts much higher threshold pressure values, but they are still within a range which a human player could easily produce. Both measurements and simulation demonstrate distinct regimes corresponding to the 4th, 5th and 6th modes of the acoustical resonator. The regimes are apparent in the variation of threshold frequency and, to a lesser extent, in the variation of threshold pressure. The experimental measurements of slide position at the transitions between regimes do not coincide with the regime transition slide positions predicted by either the inward striking or outward striking models. Figure 3.23 examines how the threshold behaviour is affected by a change of embouchure and demonstrates that the inward striking model does capture the qualitative threshold behaviour: both measurements and simulation show that tightening the embouchure increases threshold pressures and frequencies and shortens the slide extension required for the transition from acoustical mode 5 to mode 6.

With a fixed embouchure, it is found that for some slide positions the threshold frequency is above the measured acoustic resonance frequency, for others the situation is reversed. This agrees with earlier playing frequency measurements

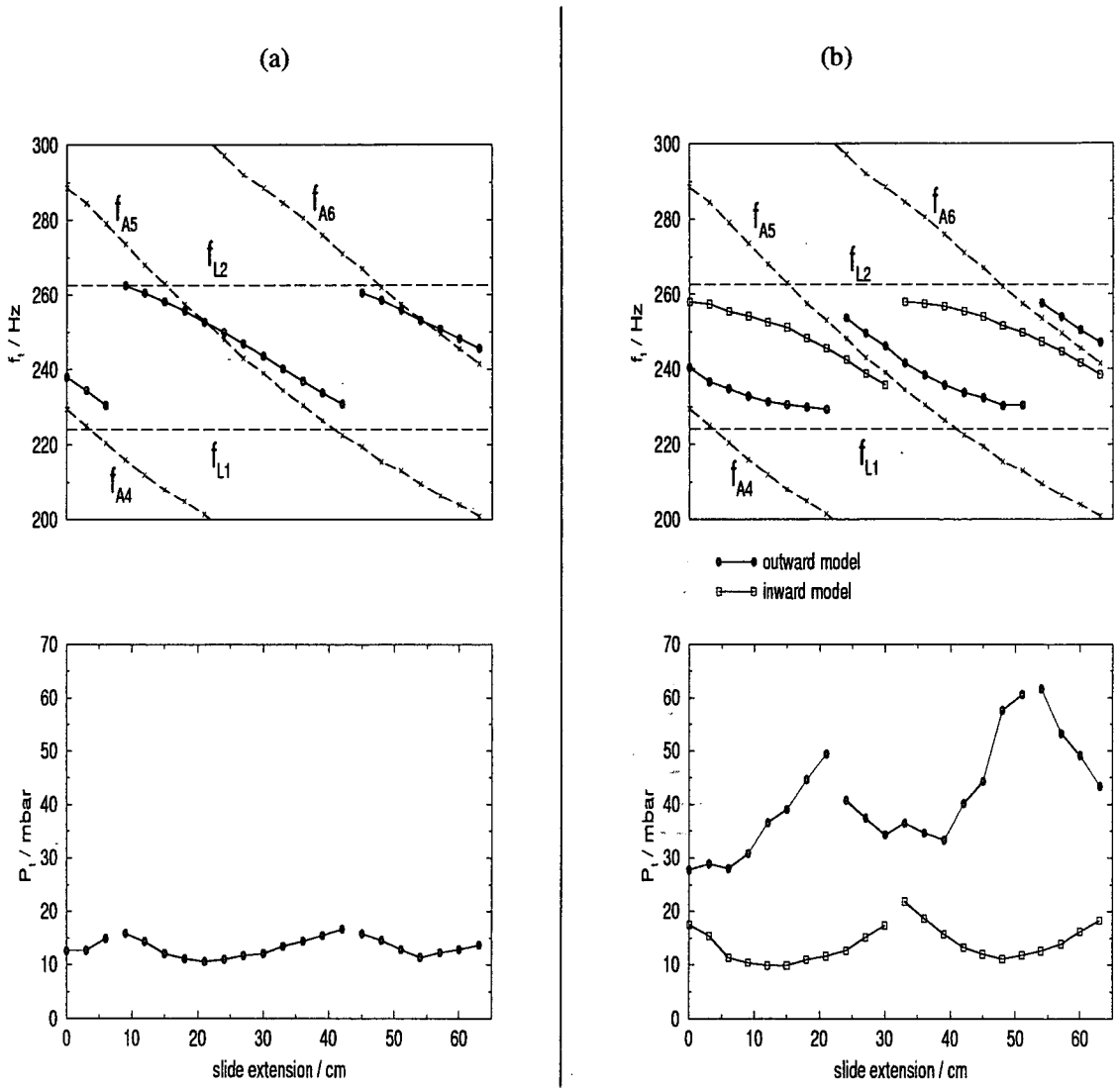

Figure 3.22: Variation of threshold values with slide position (fixed embouchure). (a) Measured threshold behaviour. (b) Threshold behaviour simulated using the inward and outward one mass models. Lip parameters used correspond approximately to the 'tight' embouchure: $f_{L1} = 224Hz$, $Q_{L1} = 9.0$, $1/\mu_{L1} = 0.09m^2Kg^{-1}$; $f_{L2} = 261Hz$, $Q_{L2} = 14.5$, $1/\mu_{L2} = -0.11m^2Kg^{-1}$.

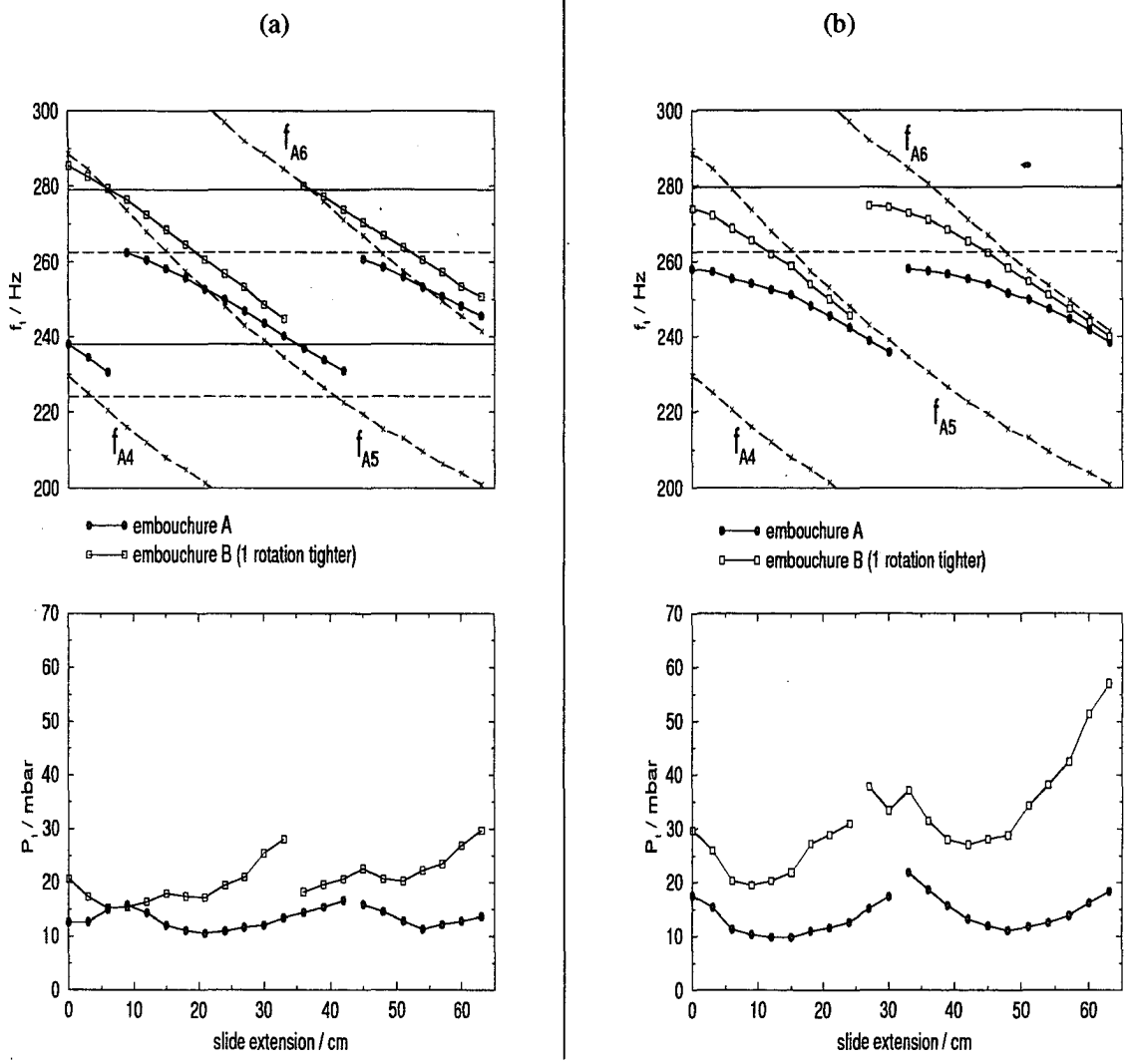

Figure 3.23: Variation of threshold values with slide position for two different embouchures. The horizontal lines indicate the lip resonance frequencies for emb ouchure A (dashed lines) and embouchure B (solid lines).(a) Measured threshold behaviour. (b) Threshold behaviour simulated using the inward one mass model. Embouchure A parameters: $f_{L2} = 261Hz$, $Q_{L2} = 14.5$, $1/\mu_{L2} = -0.11m^2Kg^{-1}$. Embouchure B parameters: $f_{L2} = 279.5Hz$, $Q_{L2} = 10.5$, $1/\mu_{L2} = -0.08m^2Kg^{-1}$.

on cup mouthpiece instruments which indicate the playing frequency may be either above or below the instrument resonance frequency, depending on playing conditions [19] [44]. Simple one mass models cannot explain this behaviour: with such models the threshold frequency is always below the acoustic resonance frequency (inward striking reed) or always above the acoustic resonance frequency (outward striking reed). A two mass model coupling the mode with outward striking characteristics, f_{L1}, to the mode with inward striking characteristics, f_{L2}, would allow the threshold frequency to lie above or below the acoustical resonance frequency, depending on the acoustic resonator conditions. Future work will include the implementation of threshold value simulations based on the two-mass model. Two-mass models have already been considered by Adachi and Sato [1]. Several additional terms, which have also been considered in previous studies, such as non-stationary flow terms [34] [79] or terms to model the effect of the mouth cavity and vocal tract [34], could also be added to the current model. Additional terms can easily be added to the one-mass model; the difficulty is in selecting realistic values for the additional parameters.

3.4.2 Fixed Slide Length, Variable Embouchure

With the trombone slide fixed in the unextended position, threshold measurements were performed as a function of embouchure position. The embouchure was set in turn to each of the twenty positions used to produce the contour plot (figure 3.21); the embouchure was varied from tightest position to slackest position. The results are shown in figure 3.24a. The experimental results may be compared with those obtained from simulations using the lip parameters listed in table A.2 (figure 3.24b).

In figure 2.7a the threshold values were calculated while varying only the lip resonance frequency, f_L. Figure 3.24b is similar to figure 2.7a, but offers a more

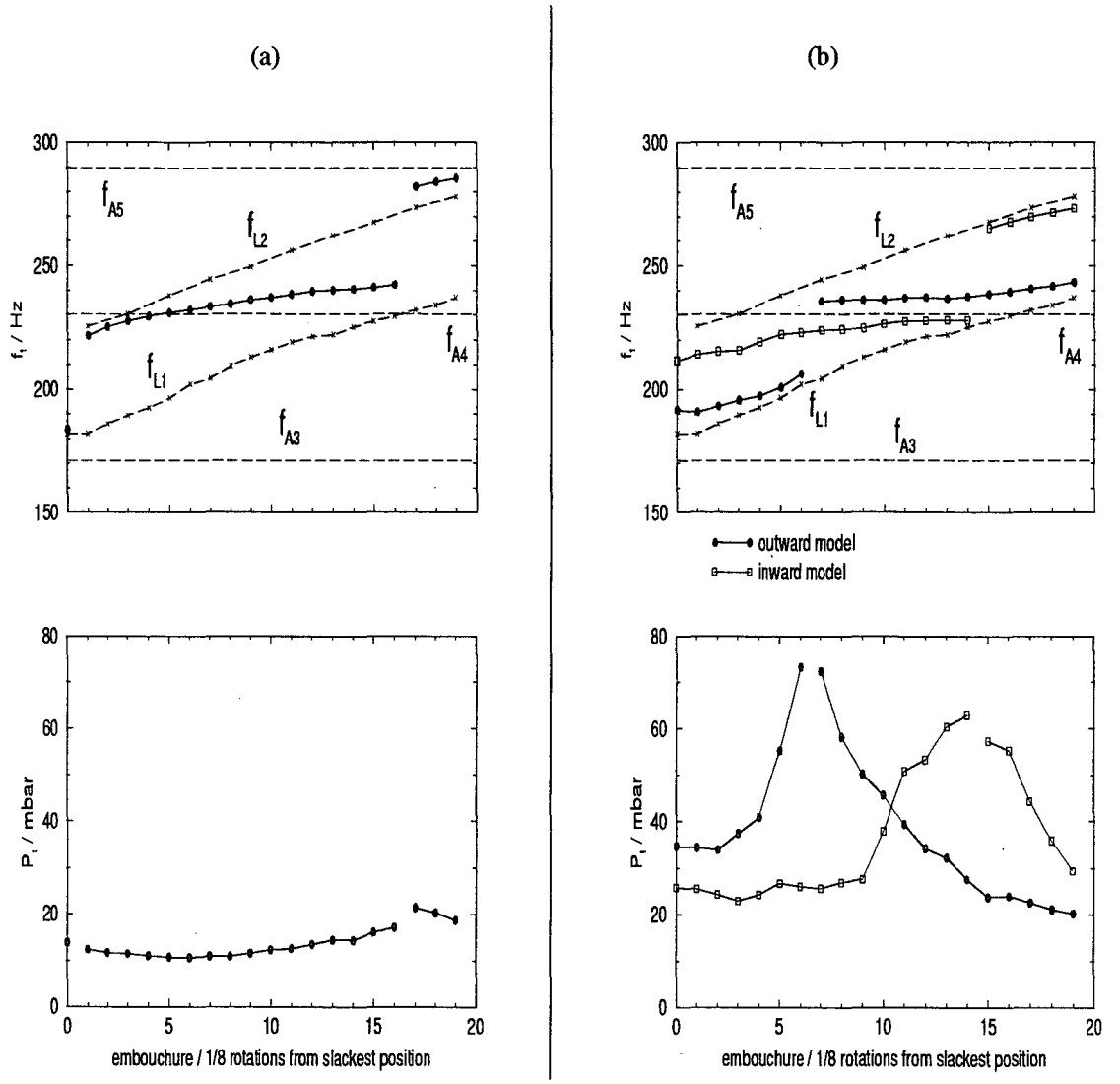

Figure 3.24: Variation of threshold values with embouchure, the trombone slide remains unextended. (a) Measured threshold behaviour. (b) Threshold behaviour simulated using the inward and outward one mass models with lip parameters estimated from mechanical response measurements (see table A.2). Acoustical parameters: $f_{A3} = 170.5Hz$, $Z_{A3} = 21M\Omega$, $Q_{A3} = 19$; $f_{A4} = 229.5Hz$, $Z_{A4} = 20M\Omega$, $Q_{A4} = 24$; $f_{A5} = 288.5Hz$, $Z_{A5} = 22M\Omega$, $Q_{A5} = 31.5$.

realistic representation since the parameters f_L, Q_L and $1/\mu_L$, extracted from experimental measurements, all vary with embouchure. In figure 2.7a the position of the local minimum in the threshold pressure curve clearly defines the 'most comfortable note'. The experimental measurements (figure 3.24a) indicate that the threshold pressure varies slowly with embouchure so the 'most comfortable note' is not so well defined. The inward striking reed model of figure 3.24b also shows a wide range of embouchures (0–9) when the threshold pressure does not vary significantly. However the outward striking model suggests that, around f_{L1}, the 'most comfortable note' is produced with an embouchure 2/8 rotations from slackest position and around f_{A4} the 'most comfortable note' will be produced with an embouchure slightly tighter than the tightest embouchure of figure 3.24b.

The experimental measurements indicate that, for the tightest embouchures, the threshold frequency lies slightly above f_{L2}, the resonance frequency of the lip mode with inward striking character. This effect cannot be explained by the simple one mass model.

3.5 Conclusions

The measurements presented in this chapter demonstrate that the mechanical response of the artificial lip mechanism is complicated and involves three strong mechanical modes, one mode with outward character and two modes with inward character. Mechanical response measurements as a function of static mouth pressure suggest that the mouthpiece 'buzz' can result from destabilization of the two modes with inward character (modes 2 and 3). However oscillation threshold measurements demonstrate that the mode with outward character (mode 1) is also important when the lips are coupled to a trombone. There is no experimental evidence that the acoustical resonance of the mouth cavity has a significant

influence on the stability of the lips.

The static and dynamic mechanical response measurements presented in this paper provide the first 'direct' measurement of lip parameters. The lip quality factors measured in this study are higher than the values which other authors have used in their simulations, while the measured ratio of effective area to effective mass is consistently lower than the values previously adopted.

The measured threshold values were compared with the theoretical threshold values predicted using linear stability analysis applied to the one-mass model. The experimental threshold pressure was considered to be the static mouth pressure required to sustain a permanent periodic regime with a predetermined small amplitude. This is a reasonable assumption provided the bifurcation is a direct bifurcation. There was found to be good qualitative agreement between the measured and simulated oscillation threshold behaviour. The discrepancies between experiment and simulation are no greater than the discrepancies encountered by Wilson and Beavers in their investigation of single reed instruments [97]. However in most instances the simulations presented in this chapter overestimate the threshold pressure and fail to accurately predict the slide/embouchure positions at the transition between different regimes. More importantly, the measurements showed that, with a fixed embouchure, for some slide positions the threshold frequency is above the measured resonance frequency; for other slide positions the situation is reversed. The one-mass model cannot explain this behaviour. The existence of two different mouthpiece buzzing regimes is also inconsistent with the one-mass model [44].

The mechanical response measurements with a non-zero static mouth pressure and the mouthpiece cup removed (figure 3.18) provide evidence of aerodynamic coupling, either between the second mechanical mode and another mechanical

mode, or between the second mechanical mode and an acoustical mode of the mouth cavity. However the mouth cavity effect measurements of section 3.3.3 suggest it is more likely that the coupling is between two mechanical modes.

Future work will include the implementation of threshold simulations based on the two-mass model, using the lip parameters presented in the current study.

Chapter 4

Theory of LDA

4.1 Introduction

In section 1.1 recent progress in understanding sound production in brass wind instruments was reviewed. It was concluded that although the acoustical behaviour of the instrument air column is well understood, further work was required to investigate firstly the behaviour of the lips and secondly the air flow into the instrument. The mechanical response measurements presented in chapter 3 do provide some added insight into the behaviour of the lips. The remainder of the thesis will be dedicated to the study of Laser Doppler Anemometry (LDA) with the ultimate aim of using the technique to measure the velocity in the mouthpiece of brass instruments, driven by the artificial lip reed mechanism.

The LDA system considered in the present study measures the component of fluid velocity in a single direction at a single point in space, the point where two laser beams intersect. In this chapter, after a brief review of other point measuring techniques available for measuring acoustic particle velocity, a more in-depth discussion of LDA and the basic principle behind the technique is presented. The LDA fringe model is introduced and used to derive mathematical expressions for the bandpass filtered photodetector signal, known as the Doppler signal. These mathematical expressions form the basis of the Doppler signal sim-

ulation programs considered in chapter 6. The instantaneous frequency of the Doppler signal is shown to be proportional to the fluid velocity. The form of the power spectral density (PSD) of the Doppler signal is studied and used to assess limitations of the LDA technique. The PSD of the instantaneous frequency of the Doppler signal is also discussed at some length because that method of presenting LDA measurements will be adopted frequently in chapters 6 and 7, especially in situations where the fluid motion is relatively complicated.

In brass instruments, during self-sustained oscillation the fluid velocity in the mouthpiece is very complicated but can notionally be divided into a steady mean flow contribution, a turbulent contribution and a multi-harmonic acoustic contribution. All three situations are considered in this chapter.

This chapter is largely a review of the theory of LDA, illustrated with some original experimental measurements. However the chapter does focus on several areas hitherto neglected, such as the consequences of applying a windowing function to the Doppler signal, periodic amplitude modulation of the Doppler signal and biasing of the PSD of the Doppler signal.

4.2 Alternative Point Measuring Techniques

In the measurement of acoustic particle velocity, the point measuring technique of LDA has proved particularly successful. However, useful measurements have also been made using other point measuring techniques. Elliot and Bowsher [34] used Hot Wire Anemometry to measure instantaneous acoustic particle speed in the throat of a trombone and Eerden, de Bree et al [32] have recently developed a new acoustic particle velocity sensor, which they have called the 'Microflown'.

4.2.1 Hot Wire Anemometry

For over a century, hot wire anemometers have been used to measure the speed of fluid flows. A typical hot wire anemometer consists of a sensor, in the form of a 1mm long wire with a diameter of approximately 5μm, arc welded to the tips of two support needles. The support needles are connected to an electronics package which supplies a heating current to the sensor. The sensor is convection cooled by the fluid passing over it. The fluid speed can be deduced from measurements of the cooling effect, using a method to be described below.

An alternative sensor, the hot film probe, consists of a thin layer of nickel or platinum deposited onto a quartz wedge and connected to the electronics package by leads attached to the film. The general term hot wire anemometry embodies hot film probes and the traditional hot wire probes.

The hot wire anemometry sensor heating current may be controlled in several different ways but it is most common to supply a heating current that varies with fluid speed to maintain a constant sensor resistance and therefore a constant sensor temperature. The electronics package of the constant temperature anemometer contains a Wheatstone bridge circuit with the sensor as one arm of the bridge. A differential feedback amplifier senses any bridge unbalance, resulting from a change in the rate of sensor cooling in response to a change of fluid speed, and adds current to hold the sensor temperature constant. The voltage difference across the bridge is related to the speed of the fluid. In fact over a particular range of fluid speeds the voltage difference across the bridge can be proportional to the fluid speed.

Hot wire anemometers have some advantages over LDA: they are less expensive and do not require the fluid to be seeded or the fluid container to be transparent. However hot wire anemometers also have several disadvantages compared

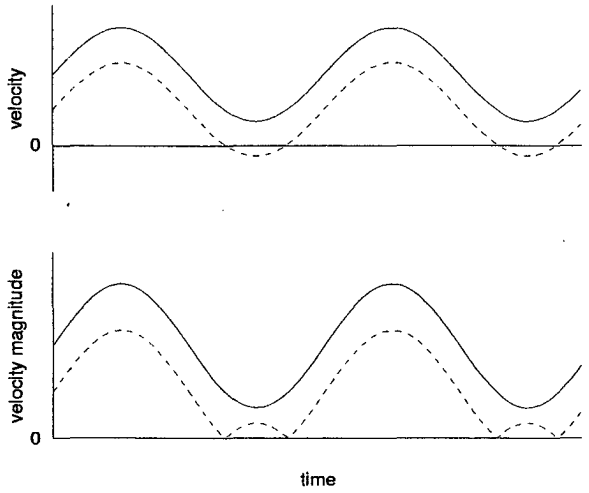

Figure 4.1: Sinusoidal variation in flow velocity and corresponding variation in magnitude of flow velocity, with mean flow greater than acoustic particle velocity amplitude (solid line) and mean flow less than acoustic particle velocity amplitude (dashed line).

with LDA: they are fragile, require calibration and physically intrude into the fluid, inevitably influencing the flow. For acoustic measurements, a major disadvantage is that the simple single sensor anemometer discussed above is capable of measuring magnitude of fluid velocity but not flow direction. With such devices the instantaneous acoustic particle velocity can only really be safely deduced from the magnitude of the instantaneous velocity if the mean flow velocity is greater than the velocity amplitude, because in that case the fluid velocity always has the same sign (solid line of figure 4.1). If the mean flow velocity is less than the velocity amplitude then the sign of the velocity changes over an acoustic cycle and the velocity amplitude magnitude curve does not have the same shape as the velocity curve (dashed line of figure 4.1). The directional ambiguity can be resolved by using two sensors, one displaced upstream from the other, provided the senors produce distinguishable signals. This can be achieved, for example, by positioning the sensors on either side of a cylinder so that the downstream

sensor is in the wake of the cylinder and therefore detects a lower velocity than the upstream sensor. Alternatively, the sensors could be arranged so that heat is convected from the upstream sensor to the downstream sensor, as is the case in a microflown (see section 4.2.2). Only a brief summary of hot wire anemometry has been presented here; Lomas discusses hot wire anemometers in some detail [63].

4.2.2 The Microflown

Unlike the hot wire anemometer, the microflown has been designed specifically to measure acoustic particle velocity. The microflown is a solid state device comprising two parallel resistive sensors of length 0.8mm positioned 40μm apart [32]. As air flow moving perpendicular to the length of the sensors passes the sensors, heat is convected from the first sensor to the second sensor. This causes a difference in temperature between the two sensors and therefore a difference in resistance which is proportional to the fluid velocity, over a particular velocity range. The differential resistance can be measured using an appropriate electronic package such as a Wheatstone bridge or the purpose developed circuit, the 'Wheatstone Gadget'. Each sensor forms one arm of the Wheatstone bridge/gadget. The output voltage of the electronic package is proportional to the differential resistance, and therefore the flow velocity [13].

The microflown is capable of resolving flow direction and thus provides a cheap alternative to LDA systems. However the microflown is fragile and physically intrusive. It also requires careful calibration as its sensitivity varies with frequency [13].

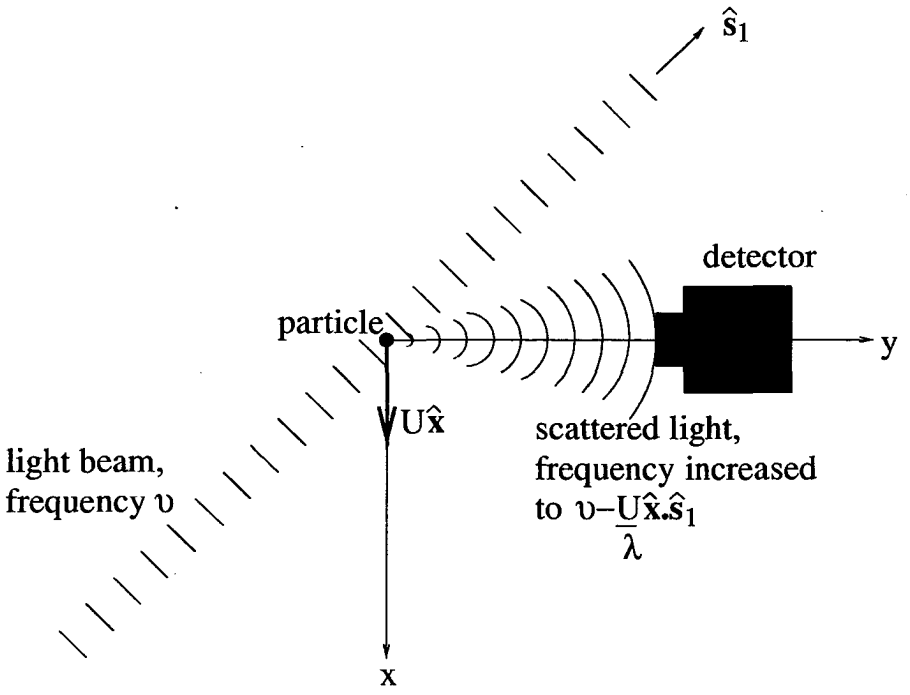

Figure 4.2: Light scattered by moving particle.

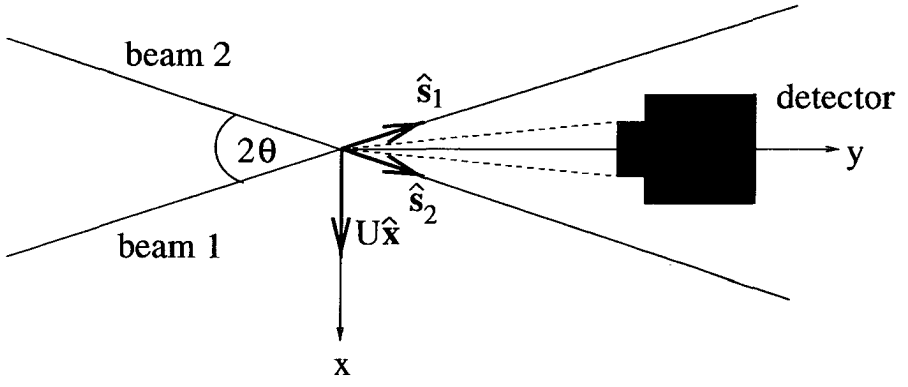

Figure 4.3: Dual beam mode.

4.3 Principle of LDA

In LDA the Doppler shift of light scattered from seeding particles is measured and used to deduce the velocity of the particles. Consider the situation illustrated in figure 4.2. A particle traveling along the x-axis with speed U crosses a plane wave light beam, with frequency ν, wavelength λ, and propagation direction with unit vector $\hat{\mathbf{s}}_1$. The component of particle velocity in the propagation direction of the plane wave is $U\hat{\mathbf{x}}\cdot\hat{\mathbf{s}}_1$, where $\hat{\mathbf{x}}$ is the unit vector in the x direction. Therefore, as the particle crosses the light beam at the origin it scatters light with Doppler shifted frequency $\nu-(U/\lambda)\hat{\mathbf{x}}\cdot\hat{\mathbf{s}}_1$. In figure 4.2 $\hat{\mathbf{x}}\cdot\hat{\mathbf{s}}_1$ is negative and so the frequency of the scattered light is greater than the frequency of the laser beam. Since the component of velocity along the y–axis is zero, if the detector is positioned on the y-axis then a particle at the origin will have no velocity component in the direction of the detector. Therefore the light scattered by the particle undergoes no further Doppler shift and the detector measures the frequency of scattered light to be $\nu-(U/\lambda)\hat{\mathbf{x}}\cdot\hat{\mathbf{s}}_1$. In principle the velocity of the particle can be deduced from the Doppler shift of the frequency of the light beam, but this is not practicable as the Doppler shift, $(U/\lambda)\hat{\mathbf{x}}\cdot\hat{\mathbf{s}}_1$, is many orders of magnitude lower than the laser light frequency, ν [45]. More elaborate systems are required to exploit the Doppler effect in order to measure the particle velocity.

There are two commonly used LDA optical systems, reference beam and dual beam [30] [45], but only the dual beam mode (represented in figure 4.3) will be considered here. The origin of the coordinate system in figure 4.3 is selected to be the point where the beams intersect. As a particle with velocity $U\hat{\mathbf{x}}$ crosses this point the particle scatters light with frequency $\nu_1 = \nu - (U/\lambda)\hat{\mathbf{x}}\cdot\hat{\mathbf{s}}_1$ from beam 1 and light with frequency $\nu_2 = \nu-(U/\lambda)\hat{\mathbf{x}}\cdot\hat{\mathbf{s}}_2$ from beam 2. The scattered light from each beam combines at the detector surface to produce an electric field

vector with magnitude proportional to $[\sin(2\pi\nu_1 t) + \sin(2\pi\nu_2 t)]$ and intensity proportional to

$$\begin{aligned}[\sin(2\pi\nu_1 t) + \sin(2\pi\nu_2 t)]^2 &= \sin^2(2\pi\nu_1 t) + \sin^2(2\pi\nu_2 t) \\ &\quad +2\sin(2\pi\nu_1 t)\sin(2\pi\nu_2 t) \qquad (4.1) \\ &= \sin^2(2\pi\nu_1 t) + \sin^2(2\pi\nu_2 t) \\ &\quad + \cos[2\pi(\nu_1 + \nu_2)t] + \cos[2\pi(\nu_1 - \nu_2)t]. \qquad (4.2)\end{aligned}$$

The detector output signal is proportional to the light intensity detected at the detector surface, but the frequencies ν_1 and ν_2 are much higher than the frequency response of any available detector, therefore the frequency of the detector signal is actually equal to the frequency of the final term on the right hand side of equation 4.2. This frequency,

$$F_D = \nu_1 - \nu_2, \qquad (4.3)$$

is known as the Doppler frequency.

$$F_D = \frac{U}{\lambda}\hat{\mathbf{x}} \cdot (\hat{\mathbf{s}}_2 - \hat{\mathbf{s}}_1) \qquad (4.4)$$

therefore

$$F_D = \frac{2U\sin\theta}{\lambda} \qquad (4.5)$$

where θ is the angle each beam makes with the y-axis. It can be shown that equation 4.5 gives the detected Doppler frequency for any detector position, on or off the y-axis [45].

4.4 Fringe Model

The Doppler shift of light provides one representation of the operation of a dual beam anemometer. An alternative perspective is provided by the fringe model,

proposed by Rudd [78]. Rudd considered masked beams with rectangular cross-section, but the principle can also be applied to unmasked beams with a Gaussian profile. The fringe model has the advantage of being easily visualised. Where the two beams intersect interference fringes are formed. As seeding particles cross the fringes the scattered light intensity, observed at the detector, is modulated at the Doppler frequency. In this section the fringe model will be used to derive expressions for the intensity of the photodetector signal as a function of fluid velocity. Several different flow conditions will be considered.

4.4.1 Intensity Distribution of Fringe Pattern

In appendix B it is shown that at point $\mathbf{x} = (x, y, z)$ in the fringe pattern, formed by the intersection of the two beams represented in figure 4.3, the intensity at time t can be expressed as

$$i(\mathbf{x}, t) = W(\mathbf{x}) \cosh\left(\frac{8xy\sin(2\theta)}{d_{e^{-2}}^2}\right) + W(\mathbf{x})\cos[2\pi F_s t + K\mathbf{x}] \tag{4.6}$$

where

$$W(\mathbf{x}) = I_0 \exp\left[-\frac{8(x^2\cos^2\theta + y^2 sin^2\theta + z^2)}{d_{e^{-2}}^2}\right], \tag{4.7}$$

$$K = \frac{4\pi\sin\theta}{\lambda}, \tag{4.8}$$

I_0 is the maximum intensity of each beam, $d_{e^{-2}}$ is the diameter of each beam at $1/e^2$ maximum intensity and F_s is the frequency of light in beam 1 minus the frequency of light in beam 2. Deliberately introducing a known frequency difference between the two beams is a common experimental technique used to shift the mean frequency of the detector signal. The frequency shift and its advantages will be discussed further at the end of this section.

The first term on the right hand side of equation 4.6 is known as the pedestal intensity. It describes the intensity which would be observed if there was no

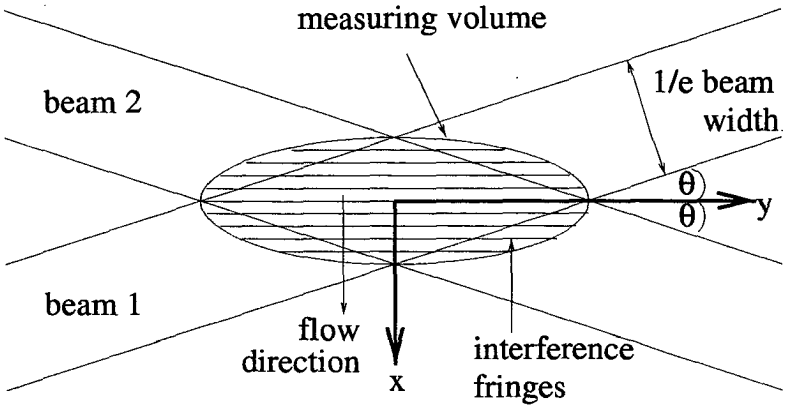

Figure 4.4: Beam intersection region in xy plane. The elliptical measuring 'volume' is defined by the locus of points at which the weight function, $W(\mathbf{x})$, falls to e^{-2} of its maximum value, $W(\mathbf{0})$. Adapted from figure 2.6.3 of [30].

interference of the beams. The remaining term on the right hand side, known as the Doppler intensity, does describe the interference of the beams. The weighting term, $W(\mathbf{x})$, defines an ellipsoidal measurement volume within which the intensity of each fringe maxima is greater than $1/e^2$ of the maximum possible value, I_0. The calculation of the dimensions of the measurement volume from equation 4.7 is trivial [45]. The cosh term describes how the two discrete beams merge to form the measuring volume as y increases from a negative value to zero and how the combined beams divide into two separate beams again as y increases from zero.

With F_s set equal to zero the Doppler intensity term describes a series of interference fringe planes parallel to the yz plane, contained within an ellipsoidal measuring volume (see figure 4.4). The spacing between the fringes is $\Lambda = 2\pi/K$. By substituting equation 4.8 for K the following expression is obtained for fringe spacing

$$\Lambda = \frac{\lambda}{2\sin\theta}. \tag{4.9}$$

A particle moving parallel to the x-axis with a speed U crosses interference planes

with a frequency

$$F_D = \frac{U}{\Lambda} = \frac{2U \sin\theta}{\lambda} \tag{4.10}$$

This frequency is the Doppler frequency of the signal; it is identical to the expression obtained by considering the Doppler shift of light (equation 4.5).

When F_s is non-zero the fringes move through the stationary ellipsoidal measuring volume with constant speed $F_s\Lambda$ and the Doppler frequency becomes

$$F_D = F_s + \frac{U}{\Lambda}. \tag{4.11}$$

If F_s is positive the fringes move in the opposite direction to the flow but if F_s is negative the fringes move in the same direction as the flow. In practice both beams are produced from the same source and so have originally the same frequency, ν. However a Bragg cell [30] [31] is often used to shift the frequency of one of the beams to $\nu + F_s$. This shift frequency acts as an additional artificial constant velocity. It resolves the directional ambiguity and extends the range of velocities which may be measured.

4.4.2 Doppler Signal Produced by Single Particle

Over the linear range of the photodetector the photodetector current, and hence the photodetector voltage, is proportional to the light intensity integrated over the detector surface [30]. This is in turn proportional to the light intensity at the position of the particle. Therefore a single particle, p, at position $\mathbf{x}_p$ produces a photodetector voltage signal

$$V_p(t) = A_p i(\mathbf{x}_p, t) \tag{4.12}$$

where A_p is a constant which is dependent on the constant load resistance of the detector, the quantum efficiency of the detector and the scattering efficiency of particle p.

If the particle is restricted to move parallel to the x-axis then it is convenient to rewrite the weight function as the product of a time dependent term (a function of the x-coordinate of particle position, $x_p(t)$) and a time independent term, w_p (dependent on the maximum intensity of a single beam and on the fixed y and z coordinates of the particle, y_p and z_p respectively).

$$W(\mathbf{x}) = w_p e^{-8x_p^2(t)/d^2} \tag{4.13}$$

where

$$w_p = I_0 \exp\left[-\frac{8(y_p^2 \sin^2\theta + z_p^2)}{d_{e^{-2}}^2}\right] \tag{4.14}$$

and

$$d = \frac{d_{e^{-2}}}{\cos\theta}. \tag{4.15}$$

By combining equations 4.6, 4.12 and 4.13, the following expression is obtained for the photodetector signal produced by light scattered from a single particle at position $(x_p(t), y_p, z_p)$

$$V_p(t) = A_p w_p e^{-8x_p^2(t)/d^2}\left\{\cosh\left[\frac{8x_p(t).y_p \sin(2\theta)}{d_{e^{-2}}^2}\right] + \cos[2\pi F_s t + K x_p(t)]\right\}. \tag{4.16}$$

In practice the Doppler signal, $V_{Dp}(t)$, is obtained by high pass filtering the detector signal, $V_p(t)$, to remove the pedestal term.

$$V_{Dp}(t) = A_p w_p e^{-8x_p^2(t)/d^2} \cos[2\pi F_s t + K x_p(t)] \tag{4.17}$$

The Doppler signal consists of a cosine wave with a time varying amplitude $A_p w_p e^{-8x_p^2(t)/d^2}$. Notice that the amplitude of the signal is independent of the shift frequency, F_s. The instantaneous frequency of the Doppler signal, *i.e.* the Doppler frequency F_D, is the rate of change of the argument of the cosine term divided by 2π.

The form of the Doppler signal will now be considered for two very different situations: a seeding particle following a laminar fluid flow with constant velocity; and a seeding particle moving with alternating velocity under the influence of a sinusoidal sound field.

Constant Velocity

If the seeding particle moves in the direction indicated in figure 4.4, with constant speed $\overline{U}$, then

$$x_p(t) = x_p(0) + \overline{U}t \tag{4.18}$$

and the resulting Doppler signal is

$$V_{Dp}(t) = A_p w_p\{\exp[-8(x_p(0) + \overline{U}t)^2/d^2]\} \cos\left[2\pi F_s t + K\overline{U}t + Kx_p(0)\right]. \tag{4.19}$$

This equation for the Doppler signal is plotted in figure 4.5 with the same time scale as the particle displacement, x_p (equation 4.18). The form of the weight function (equation 4.13) is also plotted on this diagram, against the same displacement scale as the particle displacement. Obviously there is only a significant signal while the particle is traversing the measuring volume, *i.e.* while the weight function is not negligible. The signal amplitude reaches a maximum at $t = -x_p(0)/\overline{U}$ when the x coordinate of particle displacement is zero. From the argument of the cosine term of equation 4.19 it is clear that as the particle crosses the fringe volume the Doppler frequency remains at the constant value indicated by equation 4.11.

Alternating Velocity

If a sinusoidal sound field causes the seeding particle to oscillate back and forth along a path which is parallel to the x-axis then the particle has displacement

$$x_p(t) = x_p(0) + x_m \sin(2\pi f_m t + \psi_m) \tag{4.20}$$

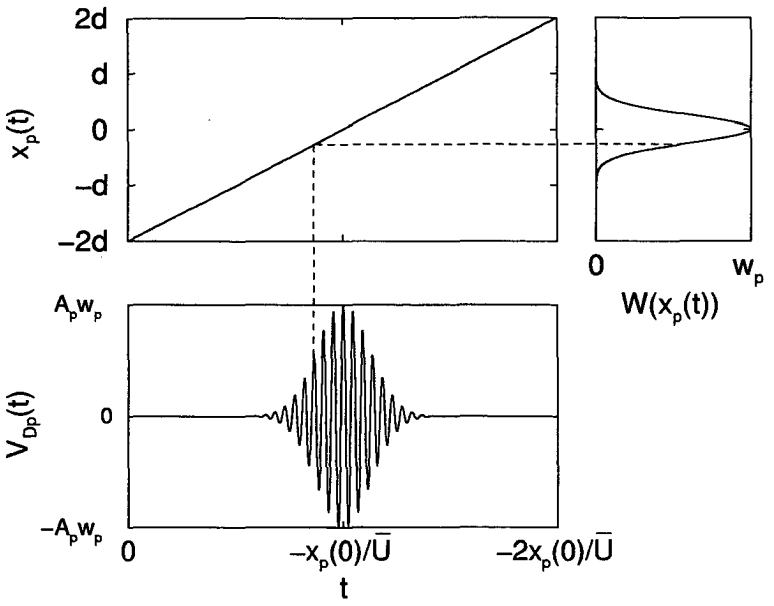

Figure 4.5: Simulated Doppler signal for single seeding particle with constant speed $\overline{U}$ and initial particle position $x_p(0) = -2d$. No frequency shift was applied *i.e.* $F_s = 0$. The particle displacement and the weight function are also displayed.

where $x_p(0)$ is the position of particle p at $t = 0$, x_m is the displacement amplitude of the sound field, f_m is its acoustic frequency and ψ_m is its phase constant. In this case the Doppler signal is

$$\begin{aligned} V_D(t) = \; & A_p w_p \{\exp[-8(x_p(0) + x_m \sin(2\pi f_m t + \psi_m))^2/d^2]\} \\ & \times \cos\left[2\pi F_s t + K x_m \sin(2\pi f_m t + \psi_m) + K x_p(0)\right]. \end{aligned} \tag{4.21}$$

and the Doppler frequency, the rate of change of the argument of the cosine term in equation 4.21 is

$$F_D = F_s + \Delta F_m \cos(2\pi f_m t + \psi_m) \tag{4.22}$$

where

$$\Delta F_m = \frac{2\pi f_m x_m}{\Lambda}. \tag{4.23}$$

The cosine term of equation 4.21 represents a frequency modulated wave with carrier frequency F_s, modulation frequency f_m and peak frequency deviation ΔF_m.

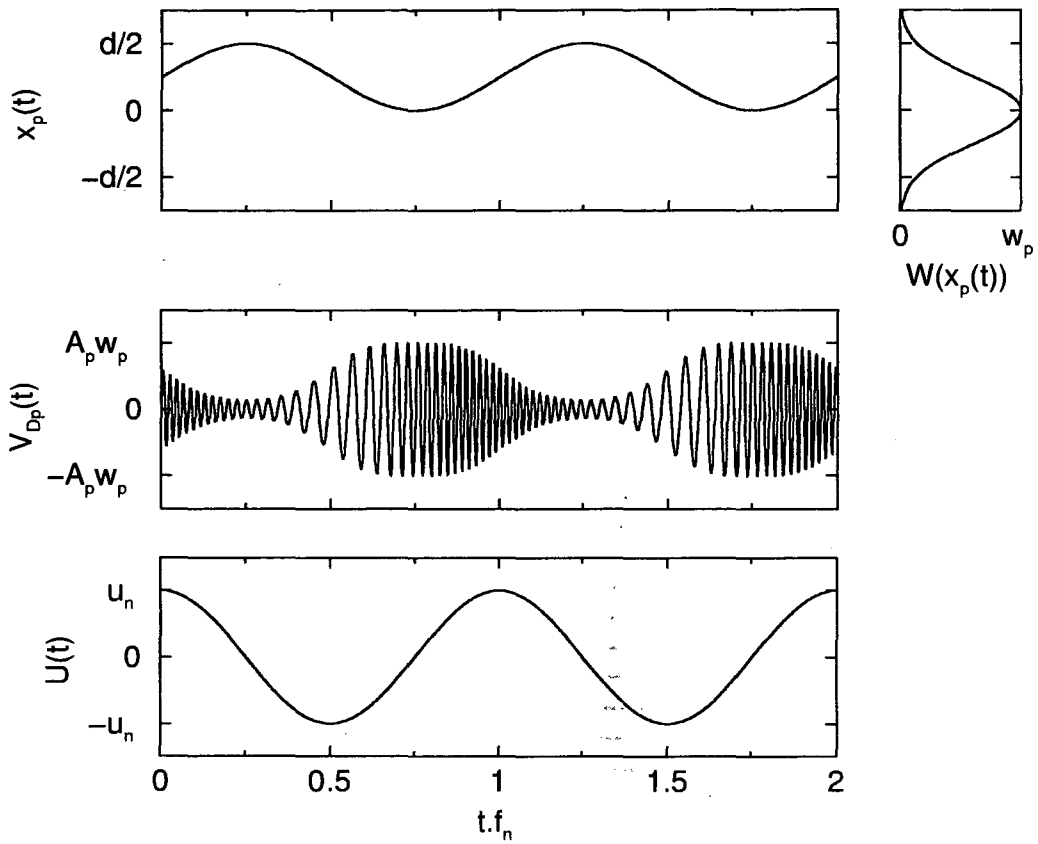

Figure 4.6: Simulated Doppler signal for single seeding particle in sinusoidal sound field with acoustic particle displacement amplitude $x_m = d/4$ and initial particle displacement, $x_p(0) = d/4$. The frequency shift, $F_s = 2u_m/\Lambda$. The particle displacement, weight function and acoustic particle displacement are also displayed.

Since the acoustic particle velocity amplitude is $u_m = 2\pi f_m x_m$ the peak frequency deviation is directly proportional the acoustic particle velocity amplitude,

$$\Delta F_m = \frac{u_m}{\Lambda}. \tag{4.24}$$

Notice that the amplitude of the Doppler signal also varies periodically at the acoustic frequency. This effect is demonstrated in figure 4.6 where the Doppler signal of equation 4.21 is plotted against the same time scale as the particle displacement (equation 4.20) and velocity. As the particle oscillates back and forth about the same point it never escapes from the measuring volume so the signal does not disappear. This figure also demonstrates frequency modulation of the Doppler signal.

4.4.3 Multiple Particle Doppler Signal

The total Doppler signal is just the sum of the Doppler signals produced by each particle. Therefore, from equation 4.17 it is clear that the Doppler signal at time t, is simply

$$V_D(t) = \sum_p A_p w_p e^{-8x_p^2(t)/d^2} \cos[2\pi F_s t + K x_p(t)]. \tag{4.25}$$

The summation extends over all particles in the flow. The particle displacement of particle p can be written as

$$x_p(t) = X(t) + x_p(0) \tag{4.26}$$

where $X(t)$ depends only on the fluid velocity, $U(t)$,

$$X(t) = \int_0^t U(\tau) d\tau. \tag{4.27}$$

Using the technique proposed by Durrani and Greated [30], by substituting equation 4.26 into the cosine argument of equation 4.25 and making use of a trigono-

metric identity, equation 4.25 can be reduced to the form

$$V_D(t) = a(t)\cos[2\pi F_s t + KX(t)] - b(t)\sin[2\pi F_s t + KX(t)] \tag{4.28}$$

where

$$a(t) = \sum_p A_p w_p[\cos(Kx_p(0))]e^{-8x_p^2(t)/d^2} \tag{4.29}$$

$$b(t) = \sum_p A_p w_p[\sin(Kx_p(0))]e^{-8x_p^2(t)/d^2}. \tag{4.30}$$

Equation 4.28 can easily be arranged into the form

$$V_D(t) = E(t)\cos[2\pi F_s t + KX(t) + \phi(t)] \tag{4.31}$$

where

$$E(t) = (a^2(t) + b^2(t))^{1/2} \tag{4.32}$$

and

$$\phi(t) = \tan^{-1}\frac{b(t)}{a(t)} \tag{4.33}$$

It is instructive to examine the form of the envelope term, $E(t)$. The $e^{-8x_p^2(t)/d^2}$ term in equations 4.29 and 4.30 describes the variation in amplitude due to particle motion within a Gaussian intensity distribution. The $\cos(Kx_p(0))$ and $\sin(Kx_p(0))$ terms indicate the relative positions of the particles within the fringe pattern. If every particle is initially located at the centre of a bright fringe, a Doppler signal with large amplitude is generated because all particles cross the fringe maxima in phase. If however the initial particle distribution is altered by displacing alternate particles by half a fringe width a signal with much lower amplitude will be detected.

Equation 4.31 may be rewritten in the form

$$V_D(t) = E(t)\cos\Phi(t) \tag{4.34}$$

where

$$\Phi(t) = 2\pi F_s t + KX(t) + \phi(t) \tag{4.35}$$

The Doppler frequency, F_D, is expressed in equation 4.36:

$$F_D = \frac{1}{2\pi}\frac{d\Phi}{dt} = F_s + \frac{U(t)}{\Lambda} + \frac{d\phi}{dt}. \tag{4.36}$$

Notice that this expression for the Doppler frequency contains an additional term which is not present when the Doppler signal is generated by a single seeding particle (see for example equation 4.11). Using multiple seeding particles introduces an error term, $d\phi/dt$, known as ambiguity noise. This uncertainty in the Doppler frequency occurs because the Doppler signal is the superposition of many sub-signals, each with a random phase related to the initial position of the particle which generated the sub-signal.

The above expressions hold for a fluid with general velocity U(t) in the x direction. The two specific flow situations considered in section 4.4.2 will now be revisited.

Constant Velocity

There are N particles in the measuring volume at time t; the pth particle has displacement, $x_p(t)$, given by equation 4.18. Each of the N particles has a different random initial displacement $x_p(0)$. This introduces ambiguity noise with causes the Doppler frequency to vary randomly about $F_s + \overline{U}/\Lambda$, the Doppler frequency produced by a single seeding particle subjected to identical flow conditions.

If the seeding density is sufficiently high there are always seeding particles in the measuring volume at any instant in time and a continuous Doppler signal is produced. However the amplitude varies randomly because the random distribution of particles within the fringe volume is constantly being replaced by

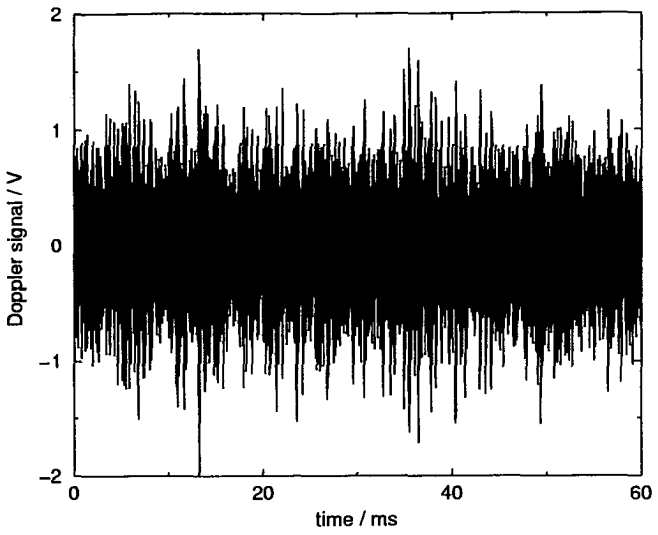

Figure 4.7: Measured Doppler signal for laminar flow with constant velocity. The signal suffers from random amplitude modulation.

a new random particle distribution. On occasion, for a short time interval, the seeding particle distribution can produce a Doppler signal with zero amplitude or a very small amplitude. In this case it becomes impossible to extract the Doppler frequency from the signal and the signal is said to suffer from signal 'dropout'. A measured Doppler signal, free from signal dropout, is displayed in figure 4.7. Details of the experimental method used to capture this signal can be found in the next chapter.

Alternating Velocity

If the seeding particles were subjected to the sound field considered in section 4.4.2, ambiguity noise would cause the Doppler frequency of the multiple particle signal to vary randomly about the Doppler frequency produced by a single particle, as indicated by equation 4.22.

Since the displacement of each particle varies periodically, there is a tendency for the amplitude of the Doppler signal, $E(t)$, to vary quasi-periodically at the

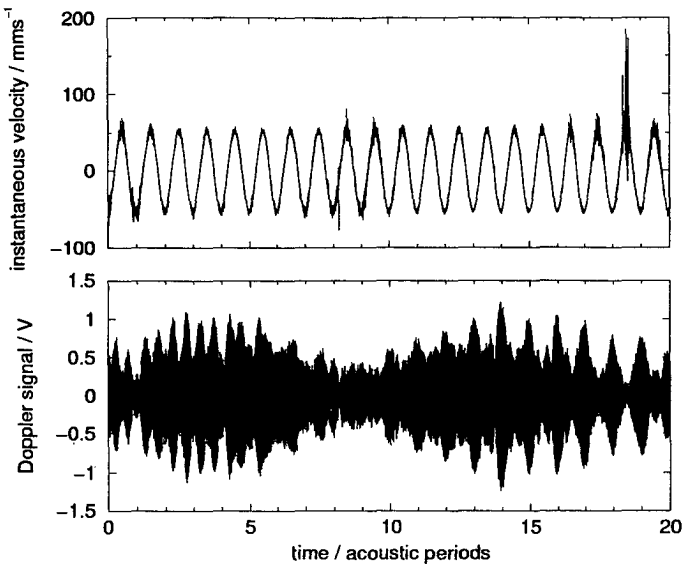

Figure 4.8: Doppler signal measured in sound field with frequency 323Hz. The instantaneous velocity extracted from this signal is also displayed. The Doppler signal suffers from quasi-periodic amplitude modulation.

acoustic frequency. This effect is demonstrated in figure 4.8 where a typical Doppler signal is plotted with the same time scale as the instantaneous velocity extracted from the signal. Notice that over the first 5 acoustic periods the Doppler signal reaches a local maximum twice per acoustic period but over the last 5 acoustic periods there is a local maximum only once per acoustic period. The periodic amplitude modulation occurs because the inhomogeneous particle distribution is swept back and forth across the fringe volume at the acoustic frequency. The amplitude modulation evolves slowly over time as the particle distribution changes.

Other researchers have observed quasi-periodic amplitude modulation of the Doppler signal [52] [91] but have not examined the phenomenon in any detail. The results of a systematic study of amplitude modulation are presented in chapter 6.

4.5 Power Spectral Density of Doppler Signal

Spectrum analysis was one of the first signal processing techniques to be applied to LDA signals. In many cases all of the required flow information can be deduced from the measured power spectra. In this section the form of the power spectral density[i] (PSD) of Doppler signals will first be considered for three different flow conditions: a uniform steady laminar flow; a turbulent flow and a sound field. Finally the power spectra will be used to demonstrate the limitations of digital analysis of LDA signals.

4.5.1 Power Spectra and Window Functions

In practice the Doppler signal is sampled over a finite time interval, T. In order to reduce signal leakage [82] the Doppler signal is multiplied by a window function, $h(t)$, and the power spectral density, $\hat{S}(F)$, of the windowed Doppler signal, $\hat{V}_D(t) = h(t)V_D(t)$ is computed using equation 4.37

$$\hat{S}(F) = \frac{|\mathcal{F}\{\hat{V}_D(t)\}|^2}{TP_W} \tag{4.37}$$

where $\mathcal{F}\{\ \ \}$ denotes the Fourier transform operation and P_W is the average power of the window function:

$$P_W = \frac{1}{T}\int_0^T h^2(t)dt. \tag{4.38}$$

Multiplying the Doppler signal by a window function reduces the power of the Doppler signal. Inclusion of the factor P_W in equation 4.37 ensures that the integral of $\hat{S}(F)$ over all frequencies is equal to the integral of the unwindowed Doppler signal, $S(F)$, over all frequencies. However at a particular frequency, F, $\hat{S}(F)$ is unlikely to be equal to $S(F)$.

[i]The term 'power spectral density' is somewhat misleading as the PSD of the Doppler signal has dimensions of [volts]^2[time], not [power][time].

If the bandwidth of the window function is less than the frequency interval between peaks in the spectrum of $V_D(t)$ then cross harmonic terms can be neglected and

$$\hat{S}(F) = \frac{1}{TP_W}|H(F)|^2 * |\mathcal{F}\{V_D(t)\}|^2 \tag{4.39}$$

where $H(F) = \mathcal{F}\{h(t)\}$.

4.5.2 Constant Velocity

The form of $|\mathcal{F}\{V_D(t)\}|^2$ will be examined for the particular situation in which the Doppler signal, $V_{Dp}(t)$, is produced by a single particle. In this case the signal is said to be a single Doppler burst.

A single particle moving parallel to the x-axis with constant velocity $\overline{U}$ and displacement defined by equation 4.18 generates the Doppler burst described by equation 4.19. By substituting the frequency

$$\overline{F} = \frac{\overline{U}}{\Lambda} \tag{4.40}$$

for $\overline{U}$ in equation 4.19 the following expression for the Doppler signal is obtained.

$$V_{Dp}(t) = A_p w_p\{\exp[-8(x_p(0) + \overline{U}t)^2/d^2]\} \cos\left[2\pi(F_s + \overline{F})t + Kx_p(0)\right] \tag{4.41}$$

If the bandwidth of the spectrum of the Gaussian term is less than half the frequency interval between the two peaks in the spectrum of the cosine term then

cross terms can be ignored [30] and

$$
\begin{aligned}
|\mathcal{F}\{V_{Dp}(t)\}|^2 &= A_p^2 w_p^2 |\mathcal{F}\{\exp[-8(x_p(0)+\overline{U}t)^2/d^2]\}|^2 \\
&\quad * |\mathcal{F}\{\cos\left[2\pi(F_s+\overline{F})t + Kx_p(0)\right]\}|^2 \qquad (4.42) \\
&= A_p^2 w_p^2 \left\{ \frac{\sqrt{\pi}\ d}{2\sqrt{2}\ \overline{U}} \exp\left[-\left(\frac{\pi d F}{2\sqrt{2}\ \overline{U}} \right)^2 \right] \right\}^2 \\
&\quad * \frac{1}{4}\{\delta[F-(F_s+\overline{F})] + \delta[F+(F_s+\overline{F})]\} \qquad (4.43) \\
&= \frac{A_p^2 w_p^2}{16\pi\sigma_F^2} \left\{ \exp\left[-\frac{(F-F_s-\overline{F})^2}{2\sigma_F^2} \right] + \exp\left[-\frac{(F+F_s+\overline{F})^2}{2\sigma_F^2} \right] \right\} \qquad (4.44)
\end{aligned}
$$

where

$$\sigma_F = \frac{\sqrt{2}\ \overline{U}}{\pi d} \qquad (4.45)$$

and δ is the Kronecker delta. This spectrum of the Doppler signal consists of Gaussian peaks with centre frequency $F = \pm(F_s + \overline{U}/\Lambda)$ and standard deviation σ_F. The standard deviation is inversely proportional to the transit time, $d/\overline{U}$, the time it takes the particle to cross the Gaussian measuring volume. The frequency spread in the spectrum is a consequence of the finite duration of the Doppler burst and is often referred to as transit time broadening. The term ambiguity broadening is also frequently used. The ambiguity noise contribution to the Doppler frequency, $d\phi/dt$, is also a consequence of finite transit time. The shorter the transit time, the quicker the rate of change of the particle population within the measuring volume and therefore the greater the ambiguity noise, $d\phi/dt$. Section 4.6.3 discusses how transit time broadening of the PSD of the Doppler signal can be quantitatively related to ambiguity noise.

It can be shown [45] that the Doppler signal produced by the summation of Doppler bursts from several individual particles (equation 4.31) has a spectrum with peaks at identical frequencies to the peaks of the spectrum of the Doppler

burst from only one of the particles (equation 4.44). If the multiple burst Doppler signal is captured over a finite time T and multiplied by the window function $h(t)$, the power spectral density of the windowed signal has the following form:

$$\hat{S}(F) \propto |H(F)|^2 * \left\{ \exp\left[-\frac{(F - F_s - \overline{F})^2}{2\sigma_F^2} \right] + \exp\left[-\frac{(F + F_s + \overline{F})^2}{2\sigma_F^2} \right] \right\}. \quad (4.46)$$

Since the signal is symmetric about $F = 0$ it is sufficient to consider only the positive frequency power spectral density, $\hat{S}_+(F)$, defined as

$$\hat{S}_+(F) = \begin{cases} 0 & F < 0 \\ \hat{S}(F) & F = 0 \\ 2\hat{S}(F) & F > 0 \end{cases} \quad (4.47)$$

From equation 4.46 it is clear that the positive frequency power spectral density of the Doppler signal is of the form

$$\hat{S}_+(F) \propto |H(F)|^2 * \exp\left[-\frac{(F - F_s - \overline{F})^2}{2\sigma_F^2} \right] \quad (4.48)$$

The Hanning window is defined in the time domain as

$$h(t) = \begin{cases} \sin^2\left(\frac{\pi t}{T}\right) & 0 \leq t < T \\ 0 & t \geq T. \end{cases} \quad (4.49)$$

Matovic and Tropea [66] observed that the Fourier transform of the Hanning window can be approximated by the central lobe of a cosine squared function. Unfortunately they did not specify the exact form of the cosine squared function but it can be deduced to be

$$H(F) = \begin{cases} \frac{T}{2}\cos^2\left(\frac{\pi T F}{4}\right) & |F| \leq \frac{2}{T} \\ 0 & |F| > \frac{2}{T}. \end{cases} \quad (4.50)$$

In the frequency domain, near the centre of the window, the relationship

$$\cos^2\alpha = e^{-\alpha^2} + O(\alpha^4) \quad (4.51)$$

can be used to approximate equation 4.50 by an unnormalized Gaussian

$$H(F) \approx \frac{1}{\pi\sigma_W} \exp[-\frac{F^2}{4\sigma_W^2}] \quad (4.52)$$

where

$$\sigma_W = \frac{2}{\pi T}. \tag{4.53}$$

By substituting equation 4.52 into equation 4.48 and observing that variances add under convolution [11], an approximation to the positive frequency power spectral density can be obtained:

$$\hat{S}_+(F) \approx \epsilon \exp\left[-\frac{(F - F_s - \overline{F})^2}{2\sigma^2}\right] \tag{4.54}$$

where

$$\sigma^2 = \sigma_F^2 + \sigma_W^2 \tag{4.55}$$

and ϵ is a constant. This approximation is only valid near the centre of the peak but the approximation is sufficient because in practice the variance of the peak is estimated using an interpolation method which only requires data points near the maximum value of the spectrum. Equations 4.54 and 4.55 demonstrate that the window function contributes to the width of the spectral peak. The ratio of standard deviation due to transit time broadening to the standard deviation due to the effect of the window function is proportional to the ratio of total sample time to transit time:

$$\frac{\sigma_F}{\sigma_W} = \frac{T}{\sqrt{2}}\frac{\overline{U}}{d}. \tag{4.56}$$

This equation indicates that broadening due to the window function is significant only for relatively low flow speeds.

4.5.3 Turbulent Flow

In a turbulent flow the instantaneous velocity may be written as the vector sum of mean velocity and fluctuations from the mean. Even if the mean velocity

is entirely in the x direction (as defined in figure 4.3) there will in general be turbulent velocity fluctuations in the x, y and z directions. However the dual beam anemometer measures only the x component of velocity and therefore the measured velocity is

$$U(t) = \overline{U} + u_T(t) \tag{4.57}$$

where $U(t)$ is the x component of instantaneous velocity, $\overline{U}$ is the mean velocity in the x direction and $u_T(t)$ is the x component of turbulent velocity fluctuations. The turbulent intensity, u'_T, is the root mean square (RMS) value of u_T:

$$u'_T = \sqrt{\overline{u_T^2(t)}}, \tag{4.58}$$

where overline denotes time average. A turbulent velocity flow with an RMS value of u'_T contributes σ_T^2 to the variance of the Doppler frequency, where

$$\sigma_T = \frac{u'_T}{\Lambda}. \tag{4.59}$$

If turbulent eddies with length scales of a comparable or smaller size than the measuring volume exist then spatial averaging occurs in the measuring volume and the turbulent intensity is underestimated by the LDA technique [42]. The smallest eddies have a length scale of the order of the Kolmogorov microscale [86].

4.5.4 Other Sources of Broadening

Velocity gradient broadening is another possible source of spectral broadening. This occurs if particles traversing the volume have a range of velocities as a result of a mean velocity gradient in the flow. The contribution of the velocity gradient broadening to the total broadening of the peak is only significant if the variation in velocity across the fringe volume is significant.

The waist of a laser beam is defined as the point where the beam has minumum diameter. Unless the beam waist of each beam lies precisely at the focal

point of the lens which converges the beams, there will be some curvature of the interference fringes [31]. Consequently, there will be some variation in the Doppler frequency as particles cross the interference volume. This variation in Doppler frequency will result in additional broadening of the peak in the PSD of the Doppler signal. This broadening, due to inprecise focusing of the laser beam, can often be considered negligible.

However if broadening due to velocity gradients, inprecise focusing and the window function are neglected then the total variance of the spectral peak of positive frequency power spectral density of the Doppler signal is

$$\sigma^2 = \sigma_F^2 + \sigma_T^2. \tag{4.60}$$

Since $\overline{U}$ and therefore σ_F may be deduced from the central frequency of the single peak in the power spectrum it is possible to deduce σ_T by measuring the standard deviation of the peak in the power spectrum.

4.5.5 Sinusoidal Velocity

Review of Taylor's Work

In 1976 Taylor reported the first LDA measurements of acoustic particle velocity amplitude [84], which he deduced from the frequency spectrum of a Doppler signal. As the frequency spectrum was used to extract velocity information he was only able to perform measurements in situations where the mono-frequency sinusoidal sound field did not change with time. Taylor's analysis apparently ignored ambiguity noise and assumed that the Doppler signal had a constant amplitude. With these gross simplifications equation 4.31 reduces to

$$V_D(t) = E\cos(2\pi F_s t + KX(t)) \tag{4.61}$$

where E is a constant. If the alternating acoustic field is characterized by

$$X(t) = x_m \sin(2\pi f_m t) \tag{4.62}$$

then equation 4.23 may be used to rearrange equation 4.61 into the form

$$V_D(t) = E\cos\left(2\pi F_s t + \frac{\Delta F_m}{f_m}\sin(2\pi f_m t)\right) \tag{4.63}$$

This frequency modulated (FM) wave [82] can be expanded to form the series

$$\begin{aligned} V_D(t) = \; & J_0\left(\tfrac{\Delta F_m}{f_m}\right)\sin(2\pi F_s t) + \textstyle\sum_{n=1}^{\infty} J_n\left(\tfrac{\Delta F_m}{f_m}\right)\sin[2\pi(F_s + nf_m)t] \\ & +(-1)^n \textstyle\sum_{n=1}^{\infty} J_n\left(\tfrac{\Delta F_m}{f_m}\right)\sin[2\pi(F_s - nf_m)t] \end{aligned} \tag{4.64}$$

where $J_n(\;\;)$ denotes an nth order Bessel function of the first kind. Therefore the positive frequency spectrum of the FM signal is of the form

$$\begin{aligned} |\mathcal{F}\{V_D(t)\}|^2 \propto \; & J_0^2\left(\tfrac{\Delta F_m}{f_m}\right)\delta(F - F_s) \\ & + \textstyle\sum_{n=1}^{\infty} J_n^2\left(\tfrac{\Delta F_m}{f_m}\right)[\delta(F - F_s + nf_m) + \delta(F - F_s - nf_m)]. \end{aligned} \tag{4.65}$$

The PSD of the FM signal comprises a spectral component centered on the shift frequency, F_s, with symmetrically spaced side lobes, each separated from its neighbour by the acoustic frequency f_m. Technically there are an infinite number of sidebands but only the sidebands nearest the centre of the spectrum are significant. Carson's rule [82] states that the effective bandwidth of the FM signal is approximately $2(\Delta F_m + f_m)$. The accuracy of the approximation increases with the ratio $\Delta F_m/f_m$. The PSD of the idealised Doppler signal (equation 4.65) is plotted in figure 4.9 with $F_m = 5f_m$. The figure serves as a useful illustration of equation 4.65 but is not representative of the high intensity sound field measurements of the present study (*e.g.* figure 4.10) where $F_m \gg f_m$.

Taylor [84] estimated acoustic particle velocity amplitude by measuring the relative magnitudes of various peaks in the Doppler signal spectrum and then finding the values of ΔF_m at which they best fit the Bessel functions in the

spectrum of the ideal Doppler signal. Unfortunately the PSD of the Doppler signal often departs significantly from this ideal case, largely because the complete description of the Doppler signal (equation 4.31) is more complex than the simplified form which Taylor seemed to consider (equation 4.63). Accurate results can only be obtained by averaging several measurements. By averaging 130 LDA velocity measurements Taylor was able to calibrate a microphone with an error of ± 0.03dB [85].

Further Complications

Some of the complications neglected by Taylor will now be discussed.

To avoid leakage, before calculating the PSD of the Doppler signal the signal must first be windowed. By applying equation 4.39 to equation 4.65 it follows that the positive frequency power spectral density of a windowed Doppler signal can be as expressed as

$$\begin{aligned}\hat{S}_+(F) \propto \; & J_0^2\left(\tfrac{\Delta F_m}{f_m}\right) H^2(F - F_s) \\ & + \textstyle\sum_{n=1}^{\infty} J_n^2\left(\tfrac{\Delta F_m}{f_m}\right) [H^2(F - F_s + nf_m) + H^2(F - F_s - nf_m)].\end{aligned} \tag{4.66}$$

Each spectral peak has a finite width, determined by the window function. The acoustic particle velocity amplitude does not influence the width of the spectral peaks.

If a mean velocity with speed $\overline{U}$ is superimposed on the acoustic velocity, the variance of each spectral peak becomes $\sigma_F^2 + \sigma_W^2$, where σ_F and σ_W are defined by equations 4.45 and 4.53 respectively. If the mean velocity is in the opposite direction to the fringe motion, the spectrum becomes centered on $F_s + \overline{U}/\Lambda$ but if mean velocity is in the same direction as the fringe motion the spectrum is centered on $F_s - \overline{U}/\Lambda$.

In section 4.4.3 it was shown that there can be significant quasi-periodic am-

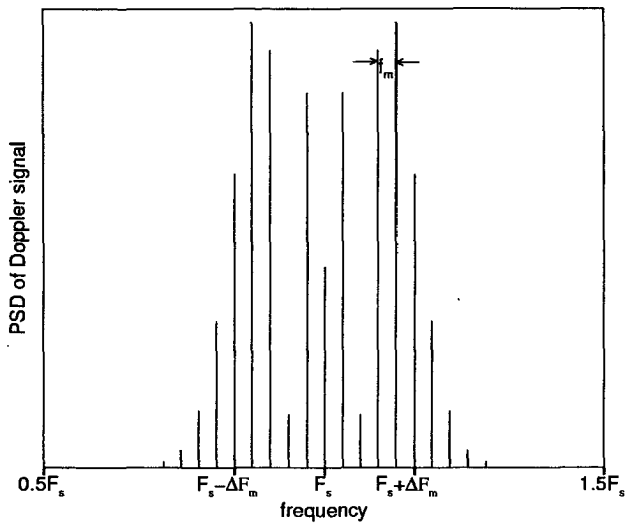

Figure 4.9: PSD of ideal Doppler signal (equation 4.61) for sinusoidal acoustic field with $\Delta F_m = 5f_m$.

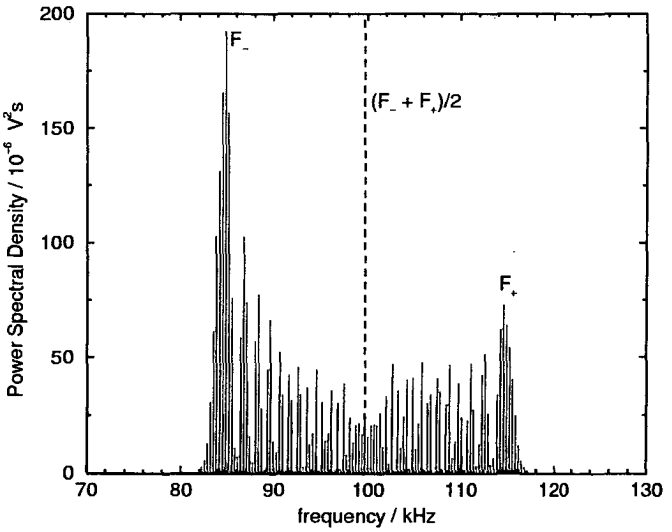

Figure 4.10: PSD of the measured Doppler signal displayed in figure 4.8

plitude modulation of the Doppler signal. This amplitude modulation affects the power spectrum. The power spectrum of the measured Doppler signal of figure 4.8 is displayed in figure 4.10. Over the last 10 acoustic cycles of figure 4.8, local maxima in the Doppler signal occur at local minima of the instantaneous velocity. That is, when the estimated instantaneous frequency lies below the mean value of instantaneous frequency, the amplitude of the Doppler signal is generally greater than the amplitude when the instantaneous frequency lies above its mean value. This biasing of the Doppler signal power towards low frequencies results in an asymmetric Doppler signal PSD. The PSD may be biased towards either low frequencies or high frequencies, depending on the form of the quasi-periodic amplitude modulation.

Extracting Information from the PSD

The mean value of the instantaneous frequency can be calculated from F_- and F_+, the frequency positions of the highest peaks to the left and right, respectively, of the shift frequency F_s. The mean velocity can then be extracted using the relation

$$\overline{U} = \Lambda \left(\frac{F_- + F_+}{2} - F_s \right). \tag{4.67}$$

Since the acoustic frequency, f_m, is the frequency interval between adjacent peaks, the error in measuring $\overline{U}$ using this method is $\pm f_m$.

Carson's rule states that the peak frequency deviation is approximately equal to $B/2 - f_m$, where B is the bandwidth of the PSD. Since B is very slightly greater than $(F_+ - F_-)$, a very crude estimate of the bandwidth of the signal can be obtained using F_- and F_+. Equation 4.68 provides a first approximation to the acoustic particle velocity amplitude, u_m:

$$u_m \approx \Lambda \left(\frac{F_+ - F_-}{2} \right) \tag{4.68}$$

This relation underestimates u_m by several times f_m but it does provide a quick estimation of u_m which can be reasonably accurate in intense, low frequency sound fields.

So far only sinusoidal sound fields have been considered. Complex sound fields containing several harmonic components can be measured using LDA. However alternative methods of analysis must be used since the PSD of the Doppler signal becomes very complex. In chapter 6 frequency tracking methods will be used to measure complex sound fields.

4.5.6 Limitations of Digital Analysis

If the analogue signal from the photodetector is bandwidth limited to frequencies below F_{LP} then it can be sampled without aliasing distortion only if the sampling frequency, $1/\Delta t$, exceeds $2F_{LP}$. This is known as the Nyquist criterion [70]. Δt is the time interval between successive samples. In practice digital analysis of LDA signals is limited by the maximum available sampling frequency.

Steady and Turbulent Flow

The Doppler signal is extracted from the photodetector signal by passing the photodetector signal through a bandpass filter. Before the photodetector signal is bandpass filtered there is a second Gaussian peak in the spectrum of the photodetector signal, due to the pedestal term, centered on $F = 0$ (see figure 4.11). Both Gaussians have the same standard deviation, σ, defined by equation 4.60. It is important to select a shift frequency which ensures there is no significant overlap of the two Gaussians. The frequency of the high pass filter, F_{HP}, must then be carefully selected to remove the pedestal signal without attenuating significant low frequency components of the Doppler signal. Furthermore the frequency of the low pass filter, F_{LP} must be selected to ensure that the Nyquist criterion is sat-

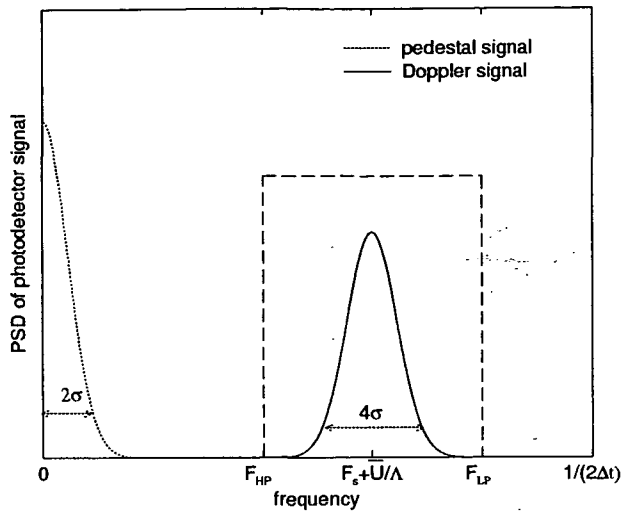

Figure 4.11: Diagram of PSD of photodetector signal. This signal is passed through an ideal filter, with bandwidth indicated by the dashed lines, to extract the Doppler signal.

isfied. The shift frequency, F_s, must also be sufficiently low to ensure significant high frequency components of the Doppler signal are not attenuated by the low pass filter. In summary the sampling conditions are: $F_{HP} > 2\sigma$, $F_{LP} < 1/(2\Delta t)$ and $(F_{HP} + 2\sigma) < F_s < (F_{LP} - 2\sigma)$. These three conditions imply

$$\sigma < \frac{1}{12}\frac{1}{\Delta t} \tag{4.69}$$

This places a limit on the maximum turbulent intensity which can be measured using digital techniques.

Alternating Velocity

If the mean and turbulent components of velocity are negligible then the bandwidth of the signal can be approximated by Carson's rule. In this case, with suitable choice of shift frequency, the maximum frequency of the Doppler signal is $2\Delta F_m$ and the limiting condition is

$$\Delta F_m < \frac{1}{4}\frac{1}{\Delta t} \tag{4.70}$$

or

$$u_m < \frac{\Lambda}{4}\frac{1}{\Delta t}. \tag{4.71}$$

Equation 4.71 is the theoretical upper limit to the acoustic particle velocity amplitude which can be measured. Of course ideal filters with infinitely steep cut-offs do not actually exist and therefore in practice the maximum value of u_m is somewhat lower than the value indicated by equation 4.71.

4.5.7 Shot Noise

LDA measurements were carried out using a photomultiplier tube (PMT) as a photodetector. When photons strike the cathode of the PMT electrons are emitted from the material. A strong electric field accelerates the electrons towards a dynode chain. Electrons from the cathode strike the first dynode in the chain, causing the dynode to emit electrons: more electrons than it absorbs. The electric field accelerates electrons from the emitting surface of each dynode to the absorbing surface of the next. The number of electrons multiplies at each dynode in the chain. The electrons emitted by the final dynode in the chain are collected at the anode to produce an anode current which is then filtered and passed through a load resistor. The Doppler signal, $V_D(t)$, is the voltage measured across this load resistor.

The time at which the nth photoelectron is emitted from the cathode is a random variable. This randomness introduces 'shot noise' into the Doppler signal. Shot noise can be considered to be white noise and therefore contributes a constant noise floor to the PSD of the Doppler signal. Shot noise is easily distinguished from ambiguity noise as ambiguity noise has the effect of broadening peaks in the PSD of the Doppler signal and does not contribute to the noise floor. Shot noise can be reduced by minimising the amount of background light

inadvertently captured by the photomultiplier and maximising the intensity of light scattered from the measuring volume.

4.6 Power Spectral Density of Instantaneous Frequency

In the previous section it was shown that the PSD of the Doppler signal can be used to measure mean flow velocity, turbulent intensity and the frequency and amplitude of a sinusoidal sound field. However the phase of the acoustic wave cannot be deduced from the PSD of the Doppler signal and neither can the Fourier series components of a complex sound field. To make such measurements it is necessary to extract the instantaneous frequency, or Doppler frequency, F_D, of the signal. In section 4.4.3 it was shown that, after removal of the frequency shift, the Doppler signal is proportional to the instantaneous flow velocity (neglecting ambiguity noise). Methods of extracting the Doppler frequency from the Doppler signal will be outlined in the next chapter. In this section it will be shown that useful data can be extracted from the PSD of the Doppler frequency, including the magnitude of each of the Fourier series components of a complex sound field.

The PSD of the **instantaneous frequency** should not be confused with the PSD of the **Doppler signal**. The PSD of the instantaneous frequency has dimension [time]$^{-1}$ whereas the PSD of the Doppler signal has dimension [Volts]^2[time]. Furthermore the bandwidth of the instantaneous frequency is usually at least one order of magnitude smaller than the bandwidth of the Doppler signal. To avoid confusion the symbol f will be used to indicate the frequency at which the instantaneous frequency, F_D, fluctuates.

Consider the complex situation in which the fluid velocity has simultaneously mean velocity, $\overline{U}$, turbulent velocity fluctuations $u_T(t)$ and acoustic particle ve-

locity $u_A(t)$. In this case, if a shift frequency of F_s is applied, the instantaneous frequency takes the form

$$F_D(t) = F_s + \frac{1}{\Lambda}\left(\overline{U} + u_T(t) + u_A(t)\right) + \frac{d\phi}{dt}, \tag{4.72}$$

which becomes

$$\tilde{F}_D(t) = \frac{1}{\Lambda}\left(u_T(t) + u_A(t)\right) + \frac{d\phi}{dt} \tag{4.73}$$

after removal of the D.C. part. The positive frequency PSD of the alternating part of instantaneous frequency, $S_{\tilde{F}_D+}$ can be written as the sum of the positive frequency PSDs of turbulent velocity, S_{T+}, acoustic particle velocity, S_{A+}, and ambiguity noise, $S_{\dot{\phi}+}$:

$$S_{\tilde{F}_D+} = S_{T+} + S_{A+} + S_{\dot{\phi}+}. \tag{4.74}$$

Each contribution to the PSD of the instantaneous frequency will be considered individually.

4.6.1 Turbulence

Parseval's theorem [82] states that the mean squared value, $\overline{u_T^2(t)}$, of a fluctuating signal, $u_T(t)$, can be obtained by integrating the PSD of the signal over all frequencies. However in turbulence theory the turbulent kinetic energy, $\overline{u_T^2(t)}$, of a flow with turbulent velocity, $u_T(t)$, can be obtained by integrating the so called energy spectrum, $E(f)$, over all frequencies. The energy spectrum and PSD of turbulent velocity fluctuations are in fact one and the same. To clarify the terminology; what is known as the the energy spectrum in turbulence theory literature has been labeled the 'power spectrum of instantaneous fluid velocity' in LDA literature [30]. The PSD of instantaneous fluid velocity is the PSD of instantaneous frequency multiplied by Λ^2. Therefore the PSD of instantaneous fluid velocity

(also known as the energy spectrum) has dimensions of [length]^2[time]$^{-1}$ and not [power][time] or [energy][time].

The energy spectrum of a turbulent flow can be divided into three different ranges. At very low wavenumbers and frequencies the flow supplies energy to large scale eddies and this is reflected in the energy spectrum by an initial rapid increase in energy as the wavenumber/frequency increases from zero. At slightly higher wavenumbers/frequencies the energy spectrum models the cascade of energy from large scale eddies (small wavenumber/frequency) to small scale eddies (large wavenumber/frequency). This range is known as the inertial range. At still higher wavenumbers/frequencies small scale eddies dissipate their energy through viscosity. This highest wavenumber/frequency range is known as the viscous range [88].

An approximate expression for the form of the energy spectrum in the inertial range can be obtained by applying Taylor's Hypothesis [67] to the Kolmogorov wavenumber spectrum [68], resulting in the relation

$$E(f) = \gamma f^{-5/3} \tag{4.75}$$

where γ is a constant related to the dissipation rate and the mean velocity, $\overline{U}$. It follows that the positive frequency PSD of the turbulent component of instantaneous frequency is

$$S_{T+} = \frac{\gamma}{\Lambda^2} f^{-5/3} \tag{4.76}$$

The PSD of the turbulent component of instantaneous velocity is represented in figure 4.12.

4.6.2 Acoustic Particle Velocity

In a periodic acoustic wave with several harmonic components the acoustic particle velocity, $u_A(t)$, can be represented by the Fourier series expansion

$$u_A(t) = \sum_m u_m \cos(2\pi m f_0 t + \psi_m) \tag{4.77}$$

where u_m, mf_0 and ψ_m are respectively the acoustic particle velocity amplitude, frequency and phase of the mth harmonic component of the acoustic wave. An expression for the positive frequency PSD of an infinitely long instantaneous frequency signal, S_{A+}, can be obtained by appropriate scaling of the square of the Fourier transform of equation 4.77:

$$S_{A+} = \frac{1}{\Lambda^2} \sum_m \frac{1}{2} u_m^2 \delta(f - mf_0). \tag{4.78}$$

In calculating the PSD of the turbulent velocity fluctuations the effect of the window function could be safely neglected since the bandwidth of the turbulence spectrum is much wider than the bandwidth of the window function. However since the spectrum of the acoustic velocity consists of a series of delta functions, the effect of the window function must be considered in this case.

If the instantaneous velocity signal is multiplied by the Hanning window, with time domain representation defined by equation 4.49 and frequency domain representation as approximated by equation 4.50, then the PSD of the windowed instantaneous frequency spectrum is of the form

$$\hat{S}_{A+} = \frac{H^2(f)}{TP_W\Lambda^2} * \sum_m \frac{1}{2} u_m^2 \delta(f - mf_0) \tag{4.79}$$

$$= \frac{1}{2TP_W\Lambda^2} \sum_m u_m^2 H^2(f - mf_0) \tag{4.80}$$

$$\approx \frac{T}{8P_W\Lambda^2} \sum_m u_m^2 \cos^4\left[\frac{\pi T}{4}(f - mf_0)\right], \quad mf_0 - \frac{2}{T} \le f \le mf_0 + \frac{2}{T}. \tag{4.81}$$

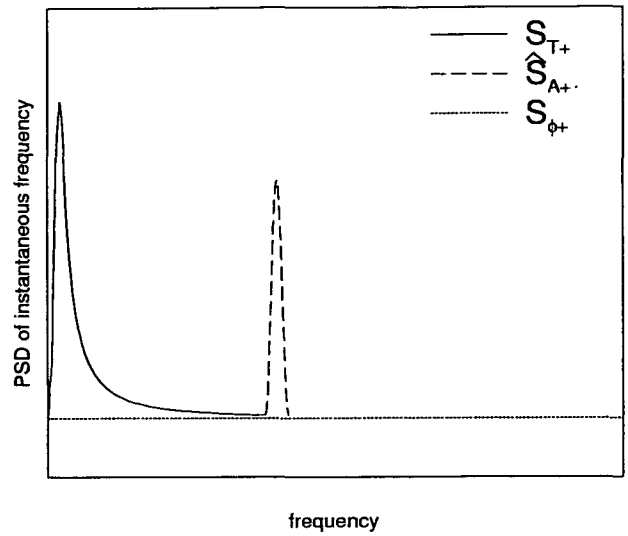

Figure 4.12: Diagram of PSD of instantaneous frequency for a sinusoidal sound field superimposed on turbulent flow.

By substituting equation 4.49 into equation 4.38 it can be shown that the average power of the Hanning window, $P_W = 3/8$. Substitution of $P_W = 3/8$ into equation 4.81 yields

$$\hat{S}_{A+} \approx \frac{T}{3\Lambda^2} \sum_m u_m^2 \cos^4 \left[\frac{\pi T}{4} (f - m f_0) \right], \quad m f_0 - \frac{2}{T} \leq f \leq m f_0 + \frac{2}{T} \tag{4.82}$$

4.6.3 Ambiguity Noise

Durrani and Greated [30] showed that the positive frequency PSD of the ambiguity noise, $S_{\dot{\phi}+}$, can be considered to be approximately constant. Using equation 3.3.74 of their book it is easy to show that

$$S_{\dot{\phi}+} \approx \frac{\sigma_F}{2\sqrt{\pi}} \tag{4.83}$$

where the standard deviation of the finite transit time broadening, σ_F, is defined by equation 4.45.

Figure 4.12 demonstrates how the positive frequency PSDs of turbulent fluctuations, acoustic particle velocity and ambiguity noise all contribute to the positive

frequency PSD of the alternating part of the instantaneous frequency.

4.6.4 Fourier Series Coefficients

Although the Fourier series amplitude coefficients, u_m, can be deduced from the PSD of the Doppler frequency, it is more convenient to plot a velocity amplitude spectrum, $|\hat{G}_+(f)|$, where the height of each peak is equal to u_m. If the complex valued spectrum $\hat{G}_+(f)$ is defined by

$$\hat{G}_+(f) = \frac{4}{T}\mathcal{F}\{h(t)u_A(t)\}, \quad f > 0, \tag{4.84}$$

then the amplitude spectrum, the magnitude of the complex valued spectrum, has the required form:

$$|\hat{G}_+(f)| \approx \sum_m u_m cos^2\left[\frac{\pi T}{4}(f - nf_0)\right], \quad nf_0 - \frac{2}{T} \leq f \leq nf_0 + \frac{2}{T}. \tag{4.85}$$

The Fourier series phase terms, ψ_m, can also be extracted using the relation

$$\psi_m = \tan^{-1}\left(\frac{\Im\{\hat{G}_+(mf_0)\}}{\Re\{\hat{G}_+(mf_0)\}}\right) \tag{4.86}$$

where $\Im\{\hat{G}_+(mf_0)\}$ and $\Re\{\hat{G}_+(mf_0)\}$ are respectively the imaginary and real values of $\hat{G}_+(mf_0)$.

4.7 Seeding Particles

In previous sections of this chapter it has been assumed that the seeding particles faithfully follow the flow; however this is not always the case. The relationship between the acoustic fluid particle velocity, $\mathbf{u_a}$, and the alternating velocity of a seeding particle suspended in the fluid, $\mathbf{u_p}$, can easily be deduced if it is assumed that the seeding particle is a sphere with diameter d_p and density ρ_p, subjected to a Stokes viscous drag force [89] of magnitude $3\pi d_p \eta_a(\mathbf{u_a} - \mathbf{u_p})$, where η_a is the

viscosity of the air. In this case, since the particle mass is $(\pi/6)\rho_p d_p^3$, the equation of motion of the particle [12] is

$$\frac{\pi}{6}\rho_p d_p^3 \frac{d\mathbf{u_p}}{dt} = 3\pi d_p \eta_a (\mathbf{u_a} - \mathbf{u_p}). \tag{4.87}$$

Using this expression it can be shown that if a seeding particle is suspended in an acoustic field with acoustic particle velocity amplitude $|u_a|$, frequency f, and phase angle $\angle\mathbf{u_a}$, then the velocity amplitude of the seeding particle is

$$|u_p| = \frac{|u_a|}{\sqrt{1 + 2\pi f \tau_p}} \tag{4.88}$$

and the phase angle of the seeding particle velocity is

$$\angle\mathbf{u_p} = \angle\mathbf{u_a} - \tan^{-1}(2\pi f \tau_p), \tag{4.89}$$

where the relaxation time is

$$\tau_p = \frac{d_p^2 \rho_p}{18\eta_a}. \tag{4.90}$$

Brandt et al [12] derived a similar expression for the amplitude ratio but added a small correction factor to compensate for observed discrepancies between experimental measurements of viscous drag force and the theoretical expression for Stokes drag. Vignola et al [94] derived a model for the motion of seeding particles in a sound field in which the force imparted on the seeding particle by the pressure gradient around the micro-particle is considered in addition to the viscous drag force. However they found the viscous drag force dominates at frequencies below $1/(2\pi\tau_p)$. For the seeding particles used in the present study $1/(2\pi\tau_p)$ is equal to 2kHz with water droplet seeding and 135kHz with smoke particle seeding. As the present study considered only acoustic frequencies below 2kHz the effect of the pressure gradient force may be neglected.

Equations 4.88 and 4.89 imply that water droplet seeding particles with density 1000Kgm^{-3} and diameter 5μm lag a 2kHz acoustic air flow by 45^o and oscillate with an amplitude equal to only 71% of the acoustic particle velocity amplitude. Clearly such seeding particles do not faithfully follow the acoustic flow.

Many of the LDA measurements presented in this study were made using smoke seeding from incense sticks. The density and diameter of these seeding particles were not measured but it is reasonable to assume the particles have similar properties to cigarette smoke particles, which have diameters of less than $0.6\mu m$ [60]. Keith and Derrick [60] pointed out that it is difficult to estimate the density of smoke particles but did suggest an approximate value of 1g/cc ($1000kgm^{-3}$). These values imply smoke particles lag a 2kHz acoustic air flow by less than 1^o and oscillate with an amplitude of 99.3% of the acoustic particle velocity amplitude. Therefore the viscous drag of smoke particles can safely be ignored in most measurements at frequencies below 2kHz.

4.8 Summary

Alternative point measuring techniques to LDA were briefly discussed. Both microflowns and hot wire anemometers have the disadvantage that they are physically intrusive, require calibration, and are fragile. In addition, single probe hot wire anemometers cannot resolve directional ambiguity.

The underlying principle behind dual beam LDA was introduced. Due to the Doppler effect, light scattered from each beam has a slightly different frequency. At the detector surface light scattered from each beam mixes to produce a photodetector signal which oscillates at the difference frequency.

The fringe model for the photodetector signal was also introduced. Where

the beams intersect interference fringes are formed. As seeding particles cross the fringes the scattered light intensity, observed at the detector, is modulated at the Doppler frequency. An expression for the intensity distribution of the interference fringes was presented and used to derive a mathematical expression for the Doppler signal produced by a single particle. With a steady flow the single particle produces a constant frequency Doppler signal of finite extent; if a sound field is applied the single particle produces a frequency modulated Doppler signal of infinite duration. The analysis was extended to include Doppler signals produced by several particles. With a steady flow the amplitude of the multiple particle Doppler signal varies randomly in time; this is a manifestation of ambiguity noise. If a sound field is applied the amplitude of the frequency modulated Doppler signal varies quasi-periodically at the frequency of the sound field.

The PSD of the Doppler signal was considered. Particular emphasis was placed on the influence of window functions as this effect is not covered in any of the standard texts on LDA. With a steady flow the spectrum consists of a single peak at a frequency which is proportional to the mean flow velocity. In a turbulent flow the width of the single peak is determined by the turbulent intensity. If a sinusoidal sound field is applied the power spectrum consists of a number of peaks, each separated from its neighbour by the acoustic frequency. In this case the bandwidth of the spectrum is proportional to the acoustic particle velocity amplitude. If a steady flow is superimposed on the sound field the spectrum is translated along the frequency axis in proportion to the mean flow velocity. It was shown that the Nyquist criterion limits the maximum intensity of the sound field which can be digitally sampled.

In general the PSD of the instantaneous frequency of the Doppler signal contains contributions from turbulent velocity fluctuations, acoustic particle velocity

and ambiguity noise. Turbulent velocity fluctuations contribute a decay function; acoustic particle velocity contributes peaks at the partials of the acoustic particle velocity and ambiguity noise contributes a constant noise floor.

Finally, Stokes drag law was used to assess how successfully seeding particles follow an acoustic air flow. Smoke particles should faithfully follow the flow, at least at frequencies below 2kHz.

Chapter 5

LDA Apparatus and Signal Processing

5.1 Introduction

In this chapter, the LDA apparatus is introduced and two methods of analysing the Doppler signals (the digital Hilbert transform method and the analogue frequency tracker method) are discussed. The advantages and disadvantages associated with each method are considered.

Several preparatory measurements are presented including studies of the signal-to-noise ratio (SNR) of the LDA system, the phase response of the analogue tracker and the magnitude and phase response of the probe microphones.

5.2 Experimental Arrangement

The LDA apparatus consisted of three main parts: **transmitter optics** to produce the interference fringes, **detector optics** to detect the scattered light, and **processing electronics** to process the signal detected by the detector optics. The optical components used in the apparatus were all Disa 55X series components.

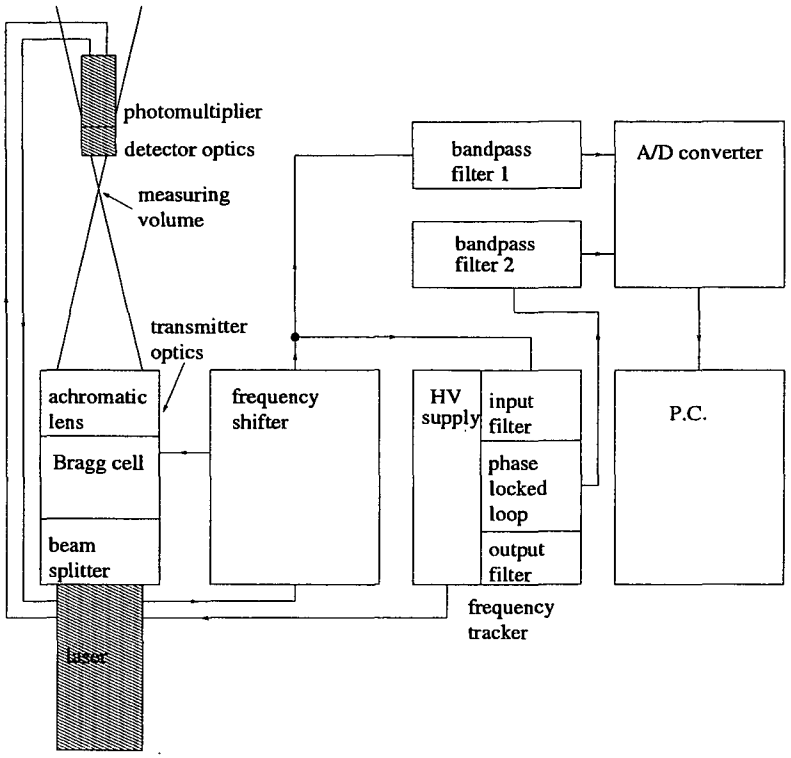

Figure 5.1: Experimental apparatus for simultaneous capture of LDA Doppler signal and output of frequency tracker.

Transmitter Optics

Incorporated into the transmitter optics was a Spectra-Physics 106-1 He-Ne 10mW laser which produced a 633nm wavelength beam with an unfocused e^{-2} beam diameter of 0.68mm. This beam was passed through a beam splitter. One of the resulting beams was passed through a Bragg cell [30], which shifted the frequency of the beam through 40MHz, while the other beam was passed through a compensating rod. The two beams were then passed through a 310mm focal length achromatic lens which caused the beams to intersect, forming a fringe volume with a focussed beam diameter $d_{e^{-2}} = 0.31$mm and a fringe separation $\Lambda = 3.3\mu$m. The number of fringes in the fringe volume, $N_f = d/\Lambda = 94$. The acute angle between the two beams was 22.1° [25].

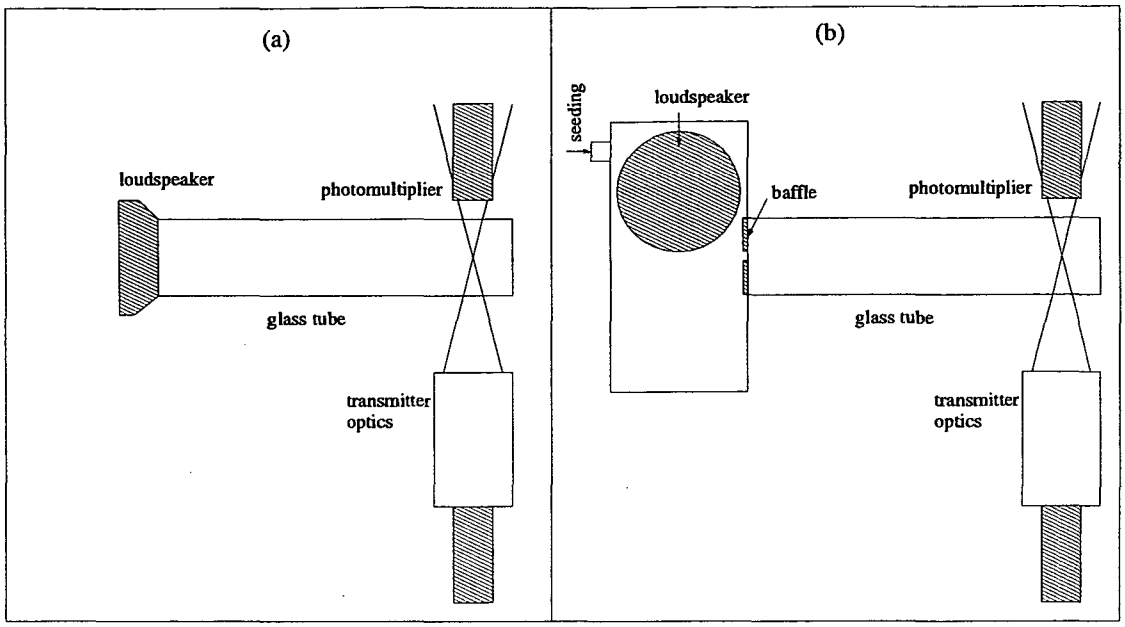

Figure 5.2: Arrangement of loudspeaker and glass tube for LDA measurements. In (a) the loudspeaker is attached directly to the tube; in (b) the loudspeaker is attached through a box of volume 1.3l.

Detector Optics

A photomultiplier was used to detect the scattered light. The optics for the photomultiplier were adapted by positioning a 150mm focal length convex lens immediately in front of the standard 150mm focal length lens. This alteration increased the image of the measuring volume in the plane of the photomultiplier cathode, and thus increased the intensity of scattered light captured by the photomultiplier. The photomultiplier was provided with a pin hole, positioned between the standard lens and the cathode, to reduce the background light imaged onto the cathode. The standard pin hole had a diameter of 0.1mm, but this was increased to 1.0mm to allow for the increased image size resulting from the addition of the convex lens. The photomultiplier was mounted at an angle of 15° to the horizontal beam plane to avoid detecting light from the direct beams.

Processing Electronics

The photomultiplier signal was sent to a Disa 55N12 frequency shifter which electronically down shifted the photomultiplier signal, reducing the 40MHz optical frequency shift to a selected lower frequency. This effective frequency shift could be varied from 10kHz to 100kHz in intervals of 10kHz, from 100kHz to 1MHz in intervals of 100kHz, or from 1MHz to 10MHz in intervals of 1MHz.

Two different methods were used to process the electronically down shifted photomultiplier signal. Figure 5.1 illustrates the apparatus required to simultaneously apply both methods. One method was to pass the signal through bandpass filter 1 (a DISA 55D26 signal conditioner) to remove the pedestal value [45] and prevent aliasing. The resulting Doppler signal was then sampled at a sample rate of 1MHz, or lower, using an A/D converter (IOtech WaveBook 512) connected to a PC. The signal could then be demodulated later using digital techniques such as the Hilbert transform. Alternatively, the electronically down shifted photomultiplier signal could be passed through a Disa 55N20 frequency tracker for demodulation. If required the demodulated signal could be passed through bandpass filter 2 (a Kemo VBF/3 filter) and then sampled using the A/D converter. Simultaneously capturing both the Doppler signal and the demodulated Doppler signal permitted direct comparison of the analogue frequency tracker and the digital Hilbert transform.

Overall Arrangement

All of the measurements presented in chapters 5 and 6 were performed inside a cylindrical glass tube with internal diameter 24mm and wall thickness 2mm. An acoustic field was generated within the tube using a FANE HF100 8Ω loudspeaker located at one end of the tube. Depending on the seeding conditions

the loudspeaker was either attached directly to the end of the tube by means of a flange with a rubber seal (figure 5.2a), or mounted in a box with volume 1.3l which was coupled to the tube through a baffle with a small hole in the centre (figure 5.2b). The box was in fact the artificial mouth and the artificial lips formed the baffle. The other end of the tube could be stopped with a rubber bung (in which case the tube had length 530mm) or left open (in which case the tube had length 545mm). A probe microphone could be inserted into the end of the tube opposite the loudspeaker to enable the acoustic pressure to be measured. The microphone signal could be sampled simultaneously with the Doppler signal or frequency tracker output signal. The entire arrangement of glass tube, loudspeaker and probe microphone was mounted on a translational table to allow measurements to be made along the length of the tube without adjustment to the optics.

5.3 Signal to Noise Ratio of Doppler Signal

5.3.1 Experimental Method

The signal to noise ratio (SNR) of the Doppler signal was measured firstly to quantify the performance of the experimental arrangement, and secondly to investigate the relative merits of various seeding methods. The SNR could not be measured directly during acoustic measurements as it is difficult to separate out the signal from the noise in the large bandwidth Doppler signals produced in such measurements. SNR measurements were performed inside the glass tube described in section 5.2, but no acoustic field or mean flow was applied. The sinusoidal Doppler signals studied were produced purely by applying a 100kHz frequency shift, F_s. As the positive frequency PSDs of such Doppler signals consist of a single peak (the signal) and a noise floor, the SNR can be calculated

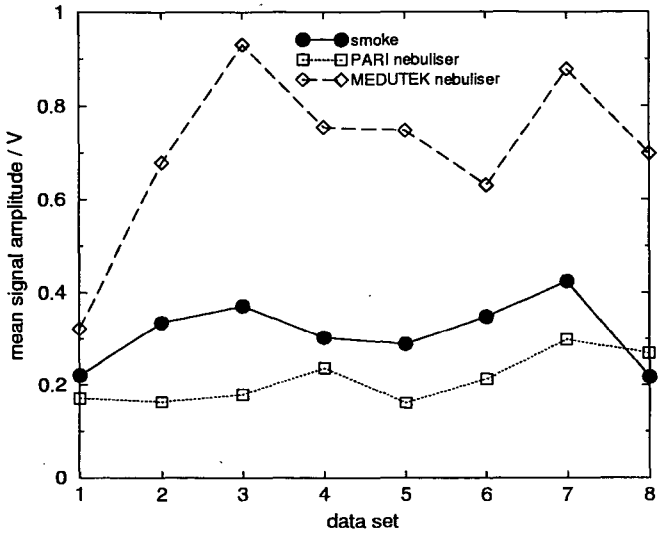

Figure 5.3: Measured mean amplitude of Doppler signals produced by applying a 100kHz frequency shift.

easily.

The photomultiplier signals were passed through a 31.5-315kHz bandpass filter (a DISA 55D26 Signal Conditioner) before they were sampled at 0.5MHz using the A/D converter connected to the PC. A 32768 point sample was made of each signal.

Measurements were made using three different methods of seeding. Two atomisers were tried: a MEDUTEK Medusonic nebuliser which produced water droplets with diameter 0.5-5μm and a PARI LC Plus nebuliser with TurboBoy compressor which produced water droplets with 4μm diameter. Smoke particles from burning incense sticks were also used to seed the air. In chapter 4 it was explained that these particles were thought to have a diameter of less than 0.6μm. Eight signals were recorded for each method of seeding.

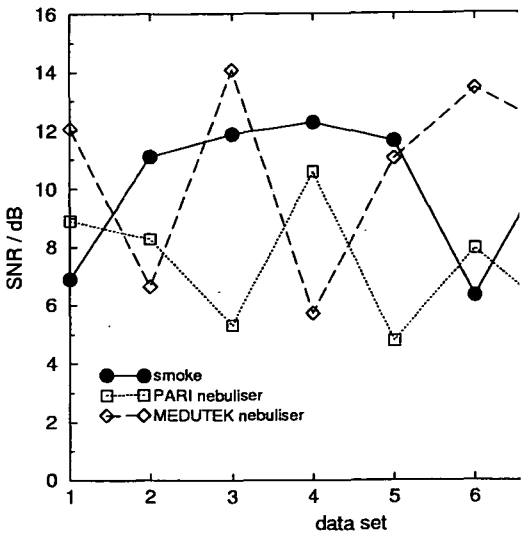

Figure 5.4: Measured SNR of Doppler signals produced
frequency shift.

5.3.2 Signal Analysis

A program based on the spectral peak interpolation algori
tovic and Tropea [66] was used to calculate both the mea
of the captured Doppler signals. The results are illustrate
The interpolation program divides a 32768 point signal
ments, applies Matovic and Tropea's routine to each of
averages the 8 results to produce just one of the 8 points
The interpolation program was tested using a Doppler sig
which can simulate additive noise. The interpolation prog
lation program 'simul.c' are described in more detail in a
respectively and program listings are provided in appendi

5.3.3 Results and Discussion

Although figure 5.3 clearly indicates that the MEDUTE
larger amplitude signal than either the PARI nebuliser or

rt transform of the Doppler signa

$$V_{D\perp}(t) = \mathcal{F}^{-1}\{\mathcal{H}\{V$$

enotes the inverse Fourier transf
apter 4,

$$\mathcal{H}\{V_D(t)\} = \begin{cases} -j\mathcal{F}\{V_D(\\ j\mathcal{F}\{V_D(\end{cases}$$

cy component of $V_{D\perp}(t)$ is in phas
component of $V_D(t)$[82] and the
signal is

$$\Phi(t) = \tan^{-1}\left(\frac{V_{D\perp}}{V_D}\right.$$

t was shown that the instantaneo
the instantaneous velocity of th
phase of the Doppler signal (see
gram developed by Hann and Gr
rithm listed above. The Doppler
ity (PSD) of the windowed signa
elect the limits of a bandwidth fi
processing. This manual inspec
der to maximise the signal-to-noi
rogram applies equation 5.2 and
iltered Doppler signal, before d
by the window function. Final
rentiated and scaled to produce
al.

sented in figure 5.4 show that in
similar to that of the smoke see
easurements presented in figure 5.4
was measured to be 7.5±2dB. Th
one seeding method to be signific

buliser particles produce greater a
ing particles because the MEDUT
ter and so scatter the most light.
because the shot noise of the ph
light incident on the cathode.

Signal Analysis

sure the instantaneous frequency, o
instantaneous acoustic particle ve
ncy using equation 4.36. The ampl
ts of a complex sound field can in
Frequency tracking requires a ne
high seeding density. There are s
ly two will be considered here: di
and the analogue phase locked loo

lbert Transform

ichius [47] first applied the Hilbe
Doppler signals in 1996. In the
sing a Hilbert transform program

There are a couple of problems associated with the Hilbert
gram. Division of the signal by the window function creates nume
because, in the time domain, window functions must take sma
beginning and end of the sample. Dividing by the window functi
degrade the quality of the instantaneous frequency curve at the
end of the sample (see for example figure 6.14).

Also, each point in the instantaneous frequency curve calcula
gram is influenced, to some extent, by every single point in the fr
and each of these points in turn depends on every point in the
signal. Therefore each point in the output instantaneous freque
fluenced, to some extent, by every single point in the input Do
a portion of the Doppler signal is degraded, for example by sig
affects to some extent the entire instantaneous frequency curve
sample time.

5.4.2 Analogue Frequency Tracker

Principle of Operation

The Disa 55N20 tracker is represented schematically in figure 5.5.
tiplier signal is first passed through an amplifier which can be cont
GAIN adjustment knob. The amplified signal is then passed thr
bandpass filter with a pass band which is selected using the RAN
pass band selection must ensure that the signal pedestal is remov
signal is then sent to a discriminator that converts the input sign
wave, available at the MONITOR OUT BNC terminal.

The square wave representation of the Doppler signal is also
a phase locked loop which consists of a phase detector, a loop filte
controlled oscillator (VCO) which produces a square wave. The

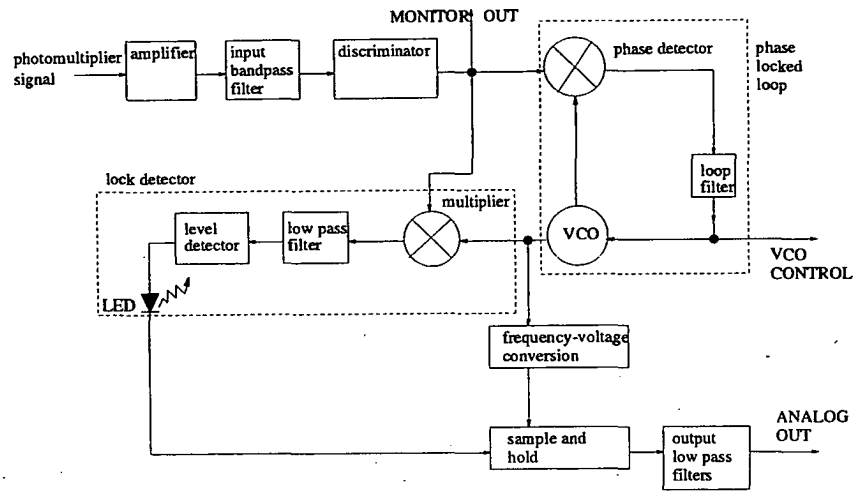

Figure 5.5: Simplified block diagram of Disa 55N20 frequency tracker.

compares the phase of the input signal with the phase of the VCO and outputs a signal related to the phase difference between the two [41]. The phase detector signal is then passed to the loop filter, which averages the phase detector output signal over a period of time in order to reduce its noise content. The transfer function of the loop filter is given on page 14 of the Disa manual [28]. The output signal from the loop filter is used to control the VCO by adjusting the frequency of the VCO in such a way as to reduce the phase difference between the input signal and the VCO output signal. The VCO output signal can be described as a cleaned up version of the Doppler signal as it has the same frequency as the Doppler signal but has a much lower noise content.

The VCO control voltage, available at the VCO CONTROL BNC terminal, is actually proportional to the instantaneous frequency of the Doppler signal. However the VCO control voltage is a very noisy signal and a much cleaner signal is available at the ANALOG OUT BNC terminal. This ANALOG OUT signal is obtained by passing the VCO output signal, a cleaned up version of the square wave Doppler signal, through a frequency to voltage converter which

operates after the charge pump principle [28].

The tracker is equipped with a lock detection mechanism which multiplies the square wave Doppler signal with the output of the VCO and averages the result by passing the product signal through a low pass filter. If the phase locked loop is in perfect lock then the output of the VCO is in phase quadrature with the square wave Doppler signal and the averaged product of the two signals is zero. In practice, the lock detector considers the phase locked loop to be in lock provided the level of the product signal is less than a predetermined drop-out level. The lock detector outputs a logic signal which indicates whether the loop is in lock. A green LED is also illuminated whenever the loop is in lock.

The tracker is further equipped with a sample and hold circuit. If the phase locked loop is in lock the circuit stores the output voltage of the frequency to voltage converter while allowing the signal to proceed towards the ANALOG OUT terminal. However, if the loop is out of lock the sample and hold circuit replaces the current converter output with the value stored immediately before the loop lost lock. The loop often loses lock when the Doppler signal suffers from signal drop-out. This results in an ANALOG OUT signal in which the drop-out regions are replaced by horizontal lines.

At the final stage the demodulated signal is passed through a low pass filter. The cut off frequency of the filter depends on the settings of both the RANGE and FILTER knobs. The filter can be disabled by turning the FILTER knob to OUT.

It is important to understand that in normal operation of the Disa tracker it is the frequency to voltage converter which demodulates the signal; the primary purpose of the phase locked loop is to remove noise from the signal. The phase locked loop acts as an adaptive filter. There is no analogous adaptive filter in the

Hilbert transform program which uses only a bandpass filter and a Savitzy-Golay time domain smoothing function. The addition of an adaptive filter to the Hilbert transform program could significantly improve its performance.

Phase Lag of Analogue Tracker

The Disa tracker described above contains several filters, each with an associated time constant. As it is the aim of this work to study the phase of the acoustic particle velocity in addition to the magnitude it was necessary to examine the phase lag introduced by the filter circuits of the tracker.

A Black Star LDO100 signal generator was used to produce a sinusoidal signal with frequency f. This signal was applied as a sweep signal to a second signal generator (a Thandor TG501 5MHz Function Generator) which output an FM signal with carrier frequency F and modulation frequency f. The FM signal was fed into the photomultiplier terminal of the tracker to simulate a Doppler signal from an LDA measurement in an acoustic field. The ANALOG OUT tracker signal was passed through a 3kHz low pass anti-aliasing filter (a Kemo VBF/3 filter) and the ANALOG OUT and sweep signals were simultaneously captured using an A/D converter connected to a PC. The experimental arrangement is represented schematically in figure 5.6. The phase difference between the two signals was measured using the frequency response program, 'auto.c' employed previously in chapter 3. The program is listed in appendix D and described in appendix C.3. Two different experiments were performed.

In the first experiment, the output filters were disabled and the phase responses of the six input filters with widest bandwidth were examined. The filter with narrowest bandwidth was not investigated as it is too narrow to be useful for LDA measurements in acoustic sound fields. For each filter, the carrier frequency, F, was set to approximately half the maximum frequency of the pass band and

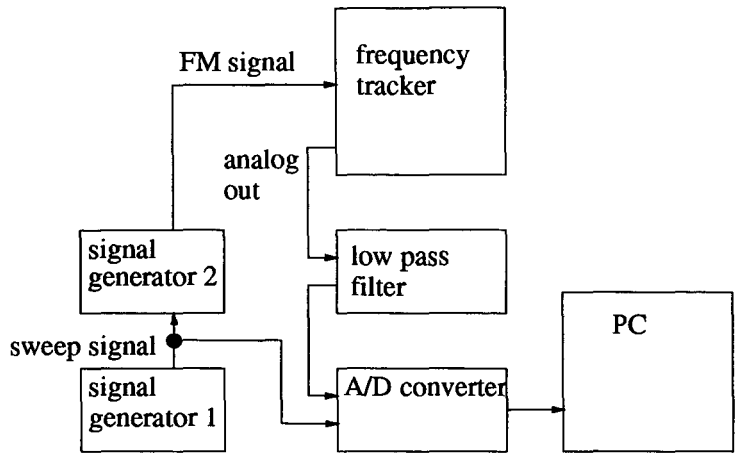

Figure 5.6: Apparatus for measuring phase lag of tracker.

phase was measured at 100Hz intervals between 100Hz and 1200Hz. Finally, the phase response of the anti-aliasing low pass filter was measured.

The second experiment was concerned with the tracker's output low pass filters. The internal output filters were reconnected and the external anti-aliasing filter was short circuited. It was anticipated that only the filters with the two highest cut off frequencies, 590Hz and 1.9kHz, would be relevant for subsequent acoustic LDA measurements. Throughout the second experiment the input filter was set to the 0.33-3.33MHz position, and the carrier frequency, F, was set to 1.5MHz. The phase response of each of the two above low pass filters was investigated by taking phase measurements at 100Hz intervals in f over a frequency range greater than the bandwidth of the filter.

The phase measurements from the first experiment are plotted in figure 5.7. Only measurements from the 3.3-33kHz, 10-100kHz, 33-333kHz and 0.1-1MHz filters are plotted as the phase responses of the 0.1-1MHz, 0.33-3.33MHz and 1-10MHz filters are so similar it would not have been possible to distinguish them if they were all plotted on the same graph. The phase response of the anti-aliasing filter is also plotted for comparison. The phase lag of the tracker is the phase

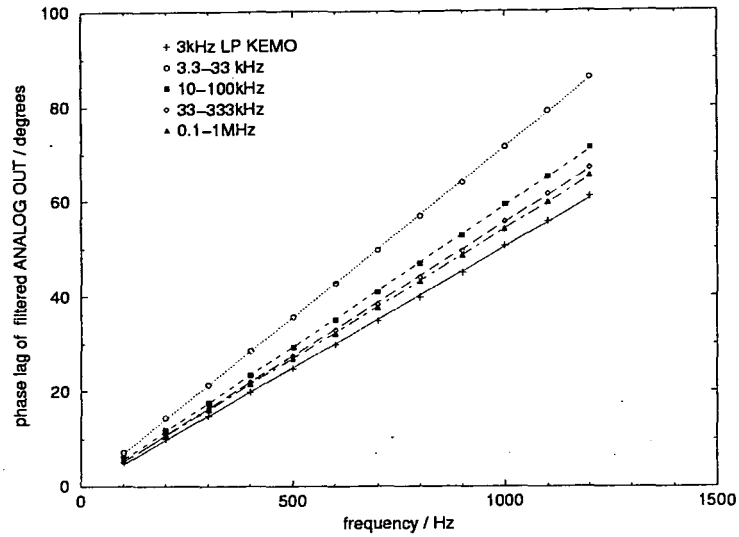

Figure 5.7: Phase response of tracker input bandpass filters.

input filter	time delay / $\mu s \pm 1\mu s$
3.3-33kHz	58
10-100kHz	24
33-333kHz	14
0.1-1MHz	10
0.33-3.33MHz	10
1-10MHz	9

Table 5.1: Time delays introduced by tracker with output filter disabled.

difference between the phase response of the anti-alias filtered ANALOG OUT signal and the phase response of the anti-alias filter.

Least square fit straight lines were fitted to each set of measurements and the time delay introduced by each filter (listed in table 5.1) was estimated from the gradient of the straight line fit. If any of the three widest bandwidth filters are used the time delay introduced by the tracker is largely independent of the choice of filter, suggesting that in this case it is not the input filter, but other elements of the tracker which are introducing the bulk of the time delay. The Disa instruction manual [28] states that the frequency to voltage converter introduces

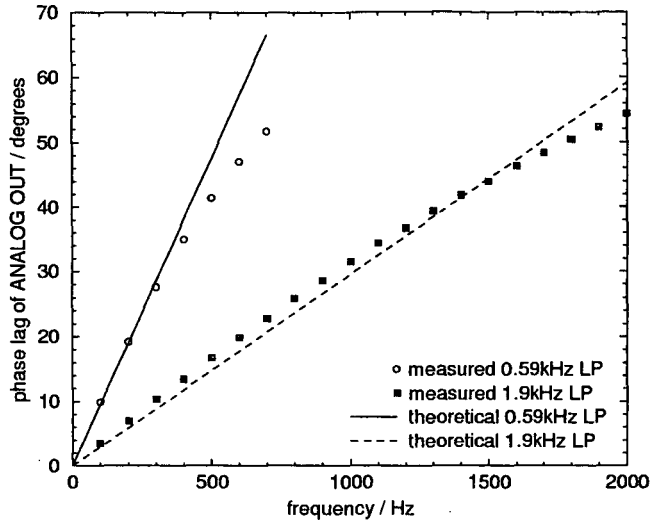

Figure 5.8: Phase response of tracker output low pass filters.

a $6\mu s$ delay. It is not clear which element or combination of elements introduces the remaining $3\pm1\mu s$ delay. The measurements indicate that the four input filters with largest bandwidth should be used in LDA acoustic measurements if possible. This ensures that, provided the output filters are disabled, the greatest time delay introduced by the tracker is limited to $14 \pm 1\mu s$ which, with a 2kHz modulation frequency, corresponds to a phase lag of approximately 10^o.

The results of the second experiment, designed to study the tracker's output filters, are displayed in figure 5.8. The gradients of the straight line graphs were calculated from the filter time constants listed in the Disa service manual [29]. Similar information was not available for the input filters. The measurements clearly demonstrate that the internal output filters must be disabled if the phase of the tracker signal is required; with only a 1kHz modulation frequency the 1.9kHz filter introduces a 30^o phase lag. In future experiments identical external filters will be applied to both the tracker signal and any reference signals. This will enable the tracker signal to be filtered without introducing any additional

phase lag to the small error inevitably introduced in the main body of the tracker.

5.5 Microphone Calibration

In chapter 6, LDA measurements of acoustic particle velocity amplitude and phase are compared with the velocity predicted by applying simple theory to pressure measurements. The pressure is measured using probe microphone attachments from a Brüel and Kjaer UA0040 probe microphone kit. The probe microphone attachments permit measurement in confined regions inaccessible to standard microphones. Unfortunately the magnitude and phase response of the probe microphones are non-linear and they require careful calibration.

5.5.1 Method

The probe microphones comprise a probe microphone attachment, a Brüel and Kjaer type 4134 1/2 inch condenser microphone cartridge and type 2619 preamplifier. Two different probes were calibrated: a short probe of length 4.7cm and a longer probe of length 24.3cm. The apparatus used to calibrate the probe microphones is illustrated in figure 5.9. The probe microphone was inserted into a coupling device supplied with the probe microphone kit. The coupling device also contained a second Brüel and Kjaer 1/2 inch microphone, which acted as a reference microphone, and an ear-piece, which acted as a sound source. The voltage from the probe microphone was amplified by a Brüel and Kjaer type 2603 measuring amplifier while the voltage from the reference microphone was amplified by a Brüel and Kjaer type 2609 measuring amplifier. The output voltages from the two amplifiers were simultaneously sampled by a WaveBook 512 A/D converter connected to the PC. The PC also supplied a sine wave signal to the sound source of the coupling device, enabling the frequency response of the probe

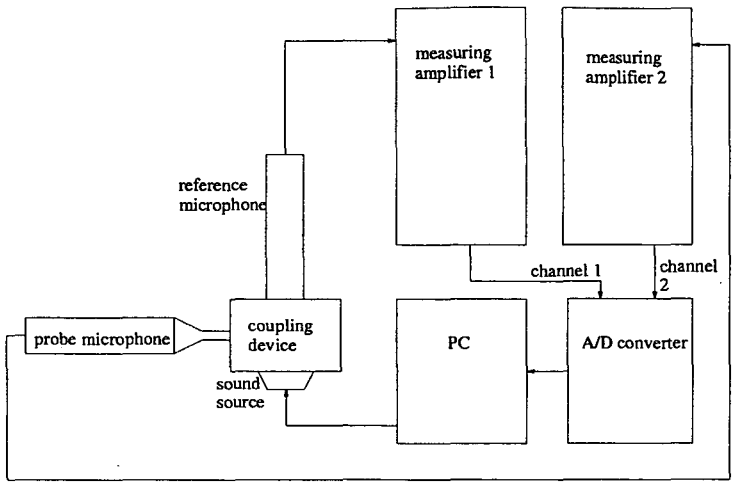

Figure 5.9: Microphone calibration apparatus.

microphone to be automatically measured at 5Hz intervals over the frequency range 50-2000Hz.

The frequency response of the probe microphone was calculated from the two microphone signals using the same frequency response program, 'auto.c' that was used to analyse the mechanical response of the lips in chapter 3 and the phase response of the tracker earlier in this chapter. The program is listed in appendix D and described in appendix C.3. The equations evaluated by the program will be derived below in order to clarify the definition of microphone response.

5.5.2 Theory

When measuring amplifier 1 displayed a full scale deflection of 20dB the RMS value of the signal voltage output by the amplifier, V_r', was $\sqrt{10}$V. Therefore, if the gain control of the amplifier is set to G_rdB and the reference microphone consistently underestimates the sound pressure level by U_rdB then the actual

sound pressure level at the position of the reference microphone is

$$SPL = 20\log_{10}(V_r'\sqrt{10}) + G_r + U_r \tag{5.4}$$

$$= 20\log_{10}(V_r') + G_r + U_r + 10. \tag{5.5}$$

U_r was determined by using the reference microphone and measuring amplifier 1 to measure a 94.0dB 1kHz sound produced by a Brüel and Kjaer Sound Level Calibrator, type 4200.

When measuring amplifier 2 displayed a full scale deflection of 20dB the RMS value of the signal voltage output by the amplifier, V_p', was however 10V. Therefore, if the gain control of the amplifier is set to G_pdB the probe microphone measures the sound pressure level to be

$$SPL_p = 20\log_{10}(V_p') + G_p \tag{5.6}$$

The magnitude response of the probe microphone and amplifier 2 combination is

$$R_p = SPL_p - SPL \tag{5.7}$$

$$= 20\log_{10}\left(\frac{V_p'}{V_r'}\right) + G_p - G_r - U_r - 10 \tag{5.8}$$

$$= 20\log_{10}\left(\frac{|V_p|}{|V_r|}\right) + G_p - G_r - U_r - 10 \tag{5.9}$$

where $|V_r|$ and $|V_p|$ are the amplitudes of output signals from amplifiers 1 and 2 respectively.

As the Brüel and Kjaer 1/2 inch microphones are reverse biased (see page 70 of the Brüel and Kjaer [14] manual) the actual phase of the pressure measured by the reference microphone is equal to the phase of the microphone signal, α_r, minus π. If the phase of the probe microphone signal is measured to be α_p then the phase response of the probe microphone is defined to be $\alpha_p - \alpha_r + \pi$.

5.5.3 Results

The frequency response of the short and long probe microphones is displayed in figure 5.10. In the case of the long probe the wavelength λ_1 corresponding to the frequency of the first local maximum in the frequency response magnitude curve is such that $\lambda_1/4$ is only slightly greater than the length of the probe. Similarly the wavelengths λ_2 and λ_3 corresponding to the frequencies of the second and third maxima respectively are such that $3\lambda_2/4$ and $5\lambda_3/4$ are each only slightly greater than the length of the probe. The response of the long probe is thus similar to the pressure response which would be measured at a closed end of a cylindrical pipe, if the opposed end was open.

In the case of the short probe there is only one single local maximum in the frequency response magnitude curve. The short probe thus appears to behave more as a Helmholtz resonator [61], with the elongate narrow bore cylindrical section of the probe acting as the neck of the resonator and the volume enclosed between the end of said elongate section and the microphone cartridge acting as the cavity volume. This Helmholtz resonator behaviour is to be expected since, over the frequency range considered (50Hz–2kHz), the wavelength is far greater than the length of the short probe.

The frequency response data displayed in figure 5.10 is now automatically called by LDA analysis programs which use the data to convert probe microphone signals into measurements of pressure amplitude (in Pascals) and pressure phase.

5.5.4 Knowles Microphone

The mechanical response measurements presented in chapter 3 were performed using a Knowles microphone, type BT–1759. If a suitable coupling device had

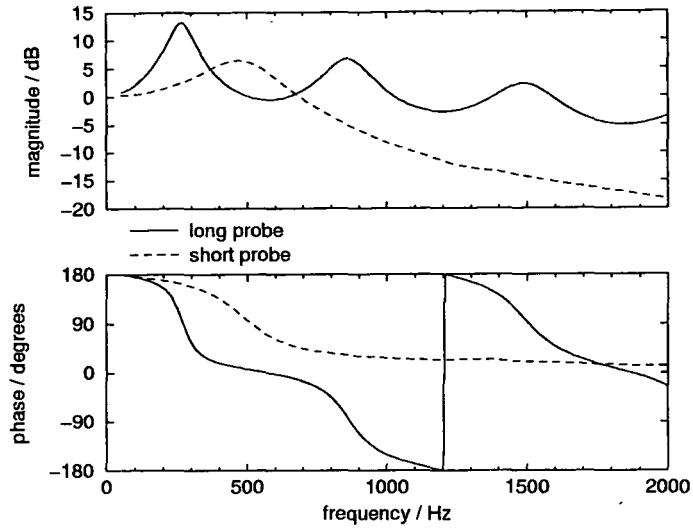

Figure 5.10: Measured frequency response of probe microphones.

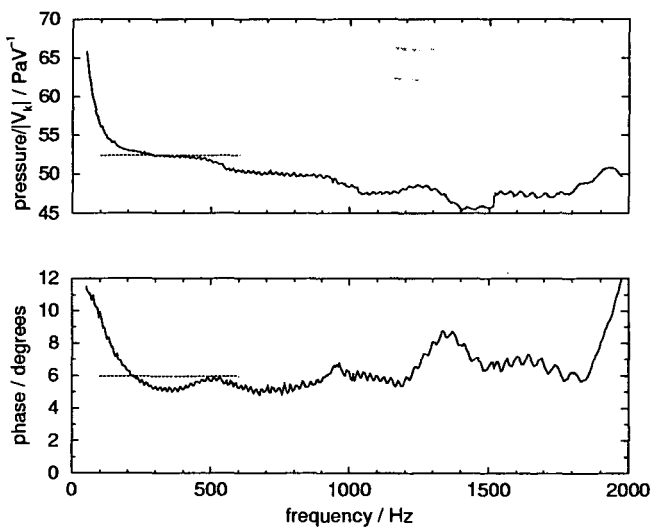

Figure 5.11: Measured frequency response of Knowles microphone.

been available it would have been desirable to calibrate the Knowles microphone using a 1/2 inch Brüel and Kjaer microphone as the reference, using an identical method to that employed for the probe microphone calibration. However as a suitable coupling device was not readily available the coupling device used in the probe microphone calibrations was adapted. The Knowles microphone was sealed into the device, in place of the 1/2 in microphone, using blue-tak, and the calibrated probe microphone was used as the reference microphone. This time the probe microphone's measuring amplifier signal was sent to channel 1 of the A/D converter, while the Knowles microphone was connected directly into channel 2 of the A/D converter, without amplification. The code of the frequency response program was altered slightly for these calibrations. The program converted the probe microphone signal into measurements of pressure amplitude (in Pascals) and pressure phase and then used these measurements, combined with simultaneous measurements of the voltage, V_k, output from the Knowles microphone, to calculate the magnitude response of the Knowles microphone (in Pascals/Volt) in addition to the phase response.

The results are displayed in figure 5.11. Notice that over the 100-600Hz range there is not a great variation in either the magnitude or phase response of the Knowles microphone. It was decided that sufficiently accurate mechanical response measurements could be obtained by using the average values indicated by the horizontal lines in figure 5.11.

5.6 Conclusions

The experimental arrangement of the LDA system was presented. The SNR of the LDA system was then investigated; measurements established that a SNR of approximately10dB could be obtained using either the MEDUTEK nebuliser or

burning incense sticks as the method of seeding.

The general principle of the Hilbert transform demodulation routine was outlined and the specific program employed in the present study was discussed. Discussions also focused on the alternative method of analysis used in the present study, *i.e.* the Disa analogue frequency tracker. Experimental measurements of the phase response of this apparatus were presented. The measurements indicate that the tracker's output filters introduce a significant phase lag and should therefore not be used in LDA measurements where the phase of the acoustic particle velocity is required. With the output filter disabled, provided the 33-333kHz or larger bandwidth filters are used, the phase lag introduced by the main body of the filter is less than 10^o for acoustic frequencies below 2kHz.

The probe microphones were calibrated in preparation for the simultaneous LDA velocity and probe microphone pressure measurements presented in chapter 6. The short probe appeared to behave as a Helmholtz resonator whereas the longer probe had a similar frequency response to a long cylinder. The phase response of the Knowles microphone used in chapter 3 was also presented. Over the 100-600Hz frequency range used in the mechanical response measurements, there is no significant variation in either the phase or magnitude of the Knowles microphone frequency response; therefore average calibration values are sufficient.

Chapter 6

LDA Measurement of Sound

In this chapter the problem of quasi-periodic amplitude modulation of the Doppler signal is investigated and the seeding methods most susceptible to this effect are identified. Using the optimal seeding method, LDA velocity measurements carried out in mono-frequency sound fields are used to assess the relative merits of the digital Hilbert transform and analogue frequency tracking signal analysis techniques. The mono-frequency sound field measurements are also used to determine the dynamic range of the measuring technique and to demonstrate that LDA can be used to measure the phase of acoustic particle velocity. The chapter continues with a study of the application of LDA to the measurement of multi-harmonic sound fields. Finally, simultaneous LDA and probe microphone measurements are used to determine specific acoustic impedance in a cylindrical tube as a function of frequency.

6.1 Amplitude Modulation of Doppler Signals

6.1.1 Introduction

In chapter 4 it was shown that for a steady air flow with a high seeding density, the Doppler signal takes the form of a sine wave with an amplitude which varies randomly in time. The random amplitude reflects the fact that the random

distribution of particles within the Gaussian envelope fringe volume is constantly being replaced by a new random particle distribution. The random distribution of particles within the measuring volume also results in random fluctuations in the frequency of the Doppler signal and therefore a broadening of the single peak in the power spectrum of the Doppler signal.

Chapter 4 also demonstrated that seeding particles in air subjected to a mono-frequency acoustic field generate a Doppler signal in the form of a frequency modulated wave with carrier frequency equal to the shift frequency, modulation frequency equal to the acoustic frequency and peak frequency deviation proportional to the acoustic particle velocity amplitude. The amplitude of the signal varies quasi-periodically at the acoustic frequency as demonstrated in figure 4.8. The periodic amplitude modulation occurs because the inhomogeneous particle distribution is swept back and forth across the fringe volume at the acoustic frequency. The amplitude modulation evolves slowly over time as the particle distribution changes.

Amplitude modulation could present a serious obstacle to LDA measurement of sound fields in air as it can result in periodic signal dropout, so that velocity information is always degraded at the same point in the acoustic cycle. Amplitude modulation of the Doppler signal is most significant when the acoustic particle displacement amplitude is high, *i.e.* when the acoustic particle velocity amplitude is high and the acoustic frequency is low. Amplitude modulation is likely to represent less of a problem in water measurements, where the natural seeding particles have a more homogeneous distribution than the seeding particles introduced in air measurements.

6.1.2 Experimental Method

Experimental Apparatus

Measurements were performed using the LDA setup described in section 5.2 and illustrated in figure 5.1, with loudspeaker and tube arrangement as illustrated in figure 5.2b. In this arrangement one end of the glass tube is attached to the artificial mouth and the sound field is generated using a loudspeaker positioned in the artificial mouth. In some experiments the other end of the tube was terminated with a rubber bung, in others it was left open.

With the open ended tube all measurements were carried out 5cm from the open end, close to the velocity anti-node but far enough away from the end to prevent the seeding escaping from the tube. With the closed ended tube all measurements were carried out at the velocity anti-node in the centre of the tube.

For this experiment the analogue frequency tracker signal was displayed on an oscilloscope and was used only to obtain an approximate but immediate estimate of the acoustic particle velocity amplitude; there was no need to capture the frequency tracker signal. After the down shifted photomultiplier signal was passed through a 31.5-315kHz bandpass filter it was sampled at 1MHz by the A/D converter. A 65536 point sample was made of each signal.

Seeding Procedure

The PARI and MEDUTEK nebulisers and the burning incense stick methods of seeding, previously explored in chapter 5, were used again in the present experiment. The diameter of the smoke seeding particles ($< 0.6\mu m$) was less than the fringe separation ($3.3\mu m$) and less than the acoustic particle displacement amplitudes considered in the experiments ($3\mu m - 23\mu m$). The maximum diameter of the water droplets ($5\mu m$) was slightly greater than the fringe separation and

within the range of acoustic particle displacement amplitudes encountered in the experiment.

Measurements with smoke particle seeding had to be conducted inside the closed tube to ensure sufficient seeding density, but it was not necessary to renew the seeding between measurements. With nebuliser seeding the nebuliser was switched on for 5s, then switched off, and after a short time interval the Doppler signal was captured. This procedure was followed for every nebuliser measurement. It was necessary to provide water droplet seeding before every measurement to provide sufficient signal strength. Nebuliser measurements were usually conducted in an open tube because the water droplets were reluctant to enter the tube when the opposite end was closed. In order to provide a direct comparison with smoke seeding, a series of nebuliser measurements were conducted inside the closed tube with the rubber stopper terminating the tube removed to allow seeding particles to enter, but replaced before signal capture.

Signal Processing

A simple computer program was written to calculate the positive frequency power spectral density of the envelope of each captured Doppler signal. The program first detects every local maximum of the sampled Doppler signal to yield the signal envelope sampled at non-uniform time intervals (see figure 6.1). Linear interpolation is then employed to re-sample this signal so it is defined at times $n\Delta t$ where the integer n takes values $0 \leq n < N$, $N = 8192$ and $\Delta t = 5\mu s$. This re-sampled Doppler signal envelope $E(n\Delta t)$ is then divided into constant and alternating components, $\overline{E}$ and $e(n\Delta t)$ respectively (see figure 6.2). The positive frequency power spectral density of the alternating component, $S_{e+}\left(\frac{n}{N\Delta t}\right)$ is defined over the range $0 \leq n < N/2$. The program calculates $S_{e+}\left(\frac{n}{N\Delta t}\right)$ from the discrete Fourier transform of $e(n\Delta t)$. Finally the program divides

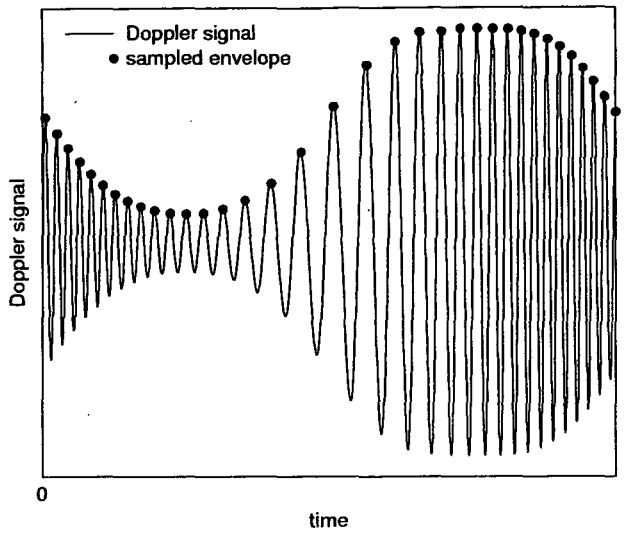

Figure 6.1: Diagram of short section of Doppler signal demonstrating how the envelope is extracted from the signal. The envelope is sampled at irregular time intervals.

$S_{e+}\left(\frac{n}{N\Delta t}\right)$ by $\overline{E}^2$ to produce a normalised PSD of the envelope of the Doppler signal, $S_{E+}(\frac{n}{N\Delta t}) = (1/\overline{E}^2)S_{e+}\left(\frac{n}{N\Delta t}\right)$.

From initial experiments it was clear that there was significant variation in harmonic content of the normalised PSD envelope spectra when measurements were repeated. Therefore each measurement was carried out 12 times and the normalised PSD envelope spectra were averaged to produce the spectra plotted in section 6.1.3.

The instantaneous particle velocity was extracted from the sampled Doppler signals using the Hilbert transformation demodulation routine described in section 5.4.1. The velocity curve in figure 4.8 was obtained using this routine. The acoustic particle velocity amplitude was calculated from the amplitude spectrum of these velocity signals. Although it is the acoustic particle velocity which is of particular interest, when seeding particles are emitted from the nebuliser they inevitably have a small constant velocity component parallel to the axis of the tube.

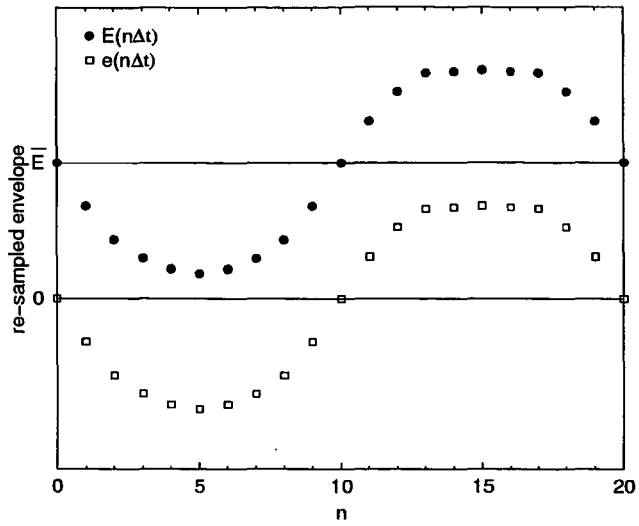

Figure 6.2: Envelope of Doppler signal of figure 6.1 re-sampled with regular time interval, Δt. The alternating and steady components of the envelope, $e(n\Delta t)$ and $\overline{E}$ respectively, are also displayed.

The magnitude of this mean flow velocity depends on the nebuliser compressor. It can theoretically be extracted simply by calculating the mean value of the estimated instantaneous acoustic particle velocity deduced from the demodulated Doppler signal. However the Doppler signal suffers from amplitude modulation which periodically reduces signal strength and as a result either the minima or maxima in the instantaneous velocity curve extracted from the Doppler signal are systematically corrupted (see for example the 17th-19th local maxima in figure 4.8). This has the effect of biasing the estimate of mean flow velocity. A more reliable estimate was obtained from the PSD of the Doppler signal using equation 4.67.

6.1.3 Results and Discussion

Only the low frequency regions of the envelope spectra are displayed because negligible power is contained above the tenth harmonic of the acoustic frequency. The envelope spectra of figure 6.3 were measured inside a closed tube. In nebuliser

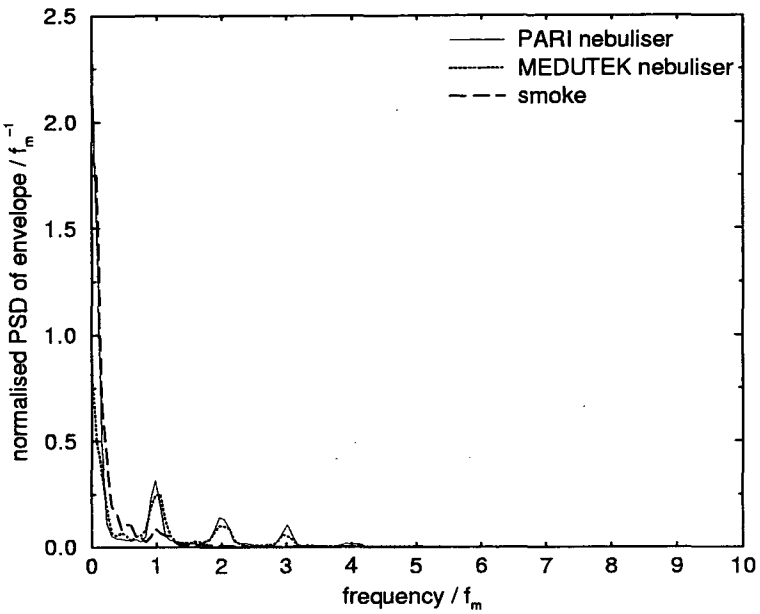

Figure 6.3: Normalised PSD from measured Doppler signal envelopes with 3 different seeding conditions. In each case f_m =323Hz and u_m=153mms^{-1}.

measurements the signal was captured 10s after the nebuliser was switched off. Each measurement was made under identical acoustical conditions i.e. with constant acoustic particle velocity amplitude, u_m, and constant acoustic frequency f_m; only the seeding method was altered. The low frequency peak in each spectrum indicates a random variation in the Doppler signal envelope due to a very slow mean flow with an associated finite transit time. The peaks at the harmonics of the acoustic frequency indicate periodic amplitude modulation. The spectra from the two nebulisers are very similar, both displaying a significant low frequency peak and significant peaks at the first three harmonics of the acoustic frequency. In the smoke seeding spectrum, however, there is only a significant low frequency peak. Figure 6.3 demonstrates that negligible amplitude modulation is observed when smoke particles are used to seed the flow.

The envelope spectra of figure 6.4 were obtained from measurements inside

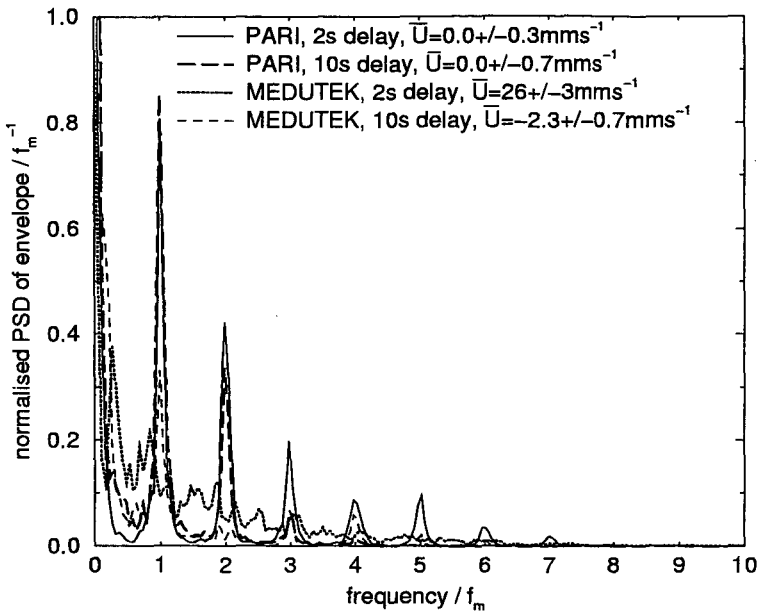

Figure 6.4: Normalised PSD from measured Doppler signal envelopes with 4 different seeding conditions and consequently different u_0. In each case f_m = 467Hz and u_m =68mms^{-1}.

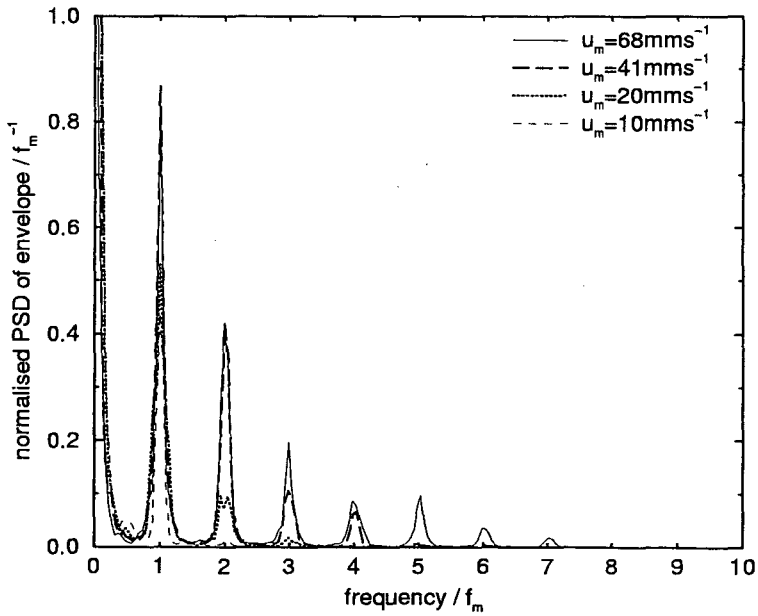

Figure 6.5: Normalised PSD from measured Doppler signal envelopes with 4 different values of u_m. In each case f_m = 467Hz and seeding is provided by the PARI nebuliser with a 2s delay.

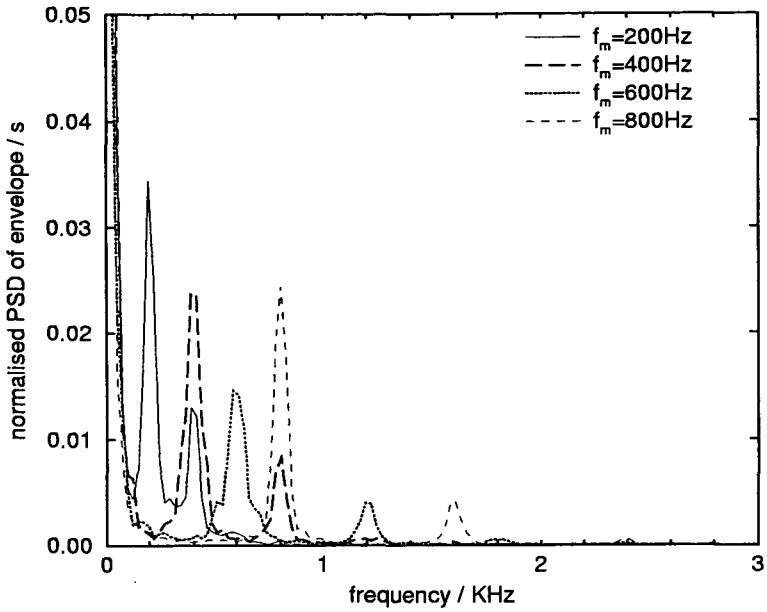

Figure 6.6: Normalised PSD from measured Doppler signal envelopes with 4 different values of f_m. In each case u_m =19mms^{-1} and seeding is provided by the PARI nebuliser with a 2s delay.

the open tube. The vertical scale on this and the following graphs has been expanded to show the peaks at harmonics of the acoustic frequency; the low frequency peaks are off scale. As before, each measurement was made under identical acoustical conditions. The graph contrasts spectra from signals captured 2s after the nebuliser was switched off with spectra from signals captured 10s after the nebuliser was switched off. Comparing the two spectra from PARI nebuliser measurements, it is clear that with a 2s delay there is a much richer harmonic content than with a 10s delay, but the power contained in the peak at the fundamental acoustic frequency is not significantly altered. With only a 2s delay the MEDUTEK envelope spectrum provides no evidence of amplitude modulation. This is not surprising because the mean flow velocity generated by the nebuliser is 40% of the acoustic particle velocity amplitude, so at any instant in time the seeding particle distribution within the fringe volume is completely

different to the particle distribution exactly one acoustic cycle earlier. It is surprising however that MEDUTEK measurements with a 10s delay indicate a slow mean flow towards the loudspeaker box and that only the first harmonic is significant when the first 2 harmonics are strong in the equivalent PARI spectrum. Further investigation is required to determine if the small negative velocity in the MEDUTEK 2s delay measurements is genuine or represents a systematic error in the frequency shift.

The envelope spectra of figure 6.5 were obtained using the PARI nebuliser with a 2s delay between switching off the nebuliser and signal capture. A 467Hz sound wave was used for each of the measurements but the acoustic particle velocity amplitude was varied. It is clear from this graph that the number of harmonic components of the signal envelope decreases with the acoustic particle velocity amplitude. There also appears to be some reduction in the power of the fundamental component as the velocity amplitude is decreased.

The envelope spectra of figure 6.6 were obtained using exactly the same seeding procedure as was used to obtain the spectra in figure 6.5. The acoustic particle velocity amplitude was maintained at 19mms^{-1} while the frequency of the sound field was varied. Each spectrum contains significant peaks only at the first and second harmonics of the acoustic frequency; the number of significant harmonic components does not appear to vary with acoustic frequency.

6.1.4 Computer Simulation of Envelope

Equation 4.32 with equations 4.29 and 4.30 were used to simulate the envelope of the Doppler signal. To provide direct comparison with measured envelopes the simulated envelope was evaluated at $5\mu s$ intervals in time, and 8192 point samples were produced. The normalised PSD of the envelope was then calculated using the same software as was used for experimentally measured envelopes. In

the simulation d was set equal to 0.36mm, corresponding to the focused beam diameter of the experimental set up [25] and A_p was set equal to 1 for every particle. The simulations were run with

$$X(t) = \overline{U}t + x_m sin(2\pi f_m t). \tag{6.1}$$

The simulation program 'simul.c' is described further in appendix C.5 and a complete listing is provided in appendix D.

The simulation program requires a list of the initial positions of all the particles. Such a list was generated randomly using a second program, 'rand_part.c' described in appendix C.6 and listed in appendix D. The program randomly assigns the initial positions, $x_p(0)$, of $2MR$ particles to any of the $(1+2R\times 10^6)$ 1D lattice sites between $x = -Rd$ and $x = Rd$. Each site has an equal probability of being occupied. The simulation allows M, the number of particles per length d to be varied, but $M = 4$ was used in most simulations. In each simulation the value of R was selected to ensure that seeding particles would always be present in the measuring volume for the duration of the sample. In selecting a suitable value for R it was necessary to consider both $\overline{U}$ and x_m. For each set of acoustical parameters both of the above programs were run 12 times, and the 12 normalised PSDs were averaged.

6.1.5 Analytical Expression for Envelope

The envelope spectra of figure 6.4 resemble PSDs of frequency modulated (FM) signals with a carrier frequency of zero. This suggests that it may be possible to develop an analytical expression which could be fitted to envelope spectra. Using equation 4.51, equation 4.29 can be approximated as

$$a(t) \approx \sum_{|x_p(t)|<d/2} A_p w_p[\cos(K x_p(0))] \cos^2\left(\frac{2\sqrt{2}}{d} x_p(t)\right). \tag{6.2}$$

The Gaussian measuring volume is replaced with the central lobe of a $\cos^2$ function. The summation extends only over particles which at time t are within $d/2$ of the centre of the measuring volume. Although this is a poor approximation when $x_p(t)$ is slightly less than $d/2$ the approximation is sufficient to describe the qualitative variation of $a(t)$. Particles with $x_p(t) > d/2$ can be considered to make negligible contribution to the Doppler signal and therefore equation 6.2 is valid even for large values of x_m. Using a trigonometric identity, equation 6.2 can be rearranged in the form

$$a(t) \approx \sum_{|x_p(t)|<d/2} \frac{A_p}{2}[\cos(Kx_p(0))][1+\cos(\kappa x_p(t))] \tag{6.3}$$

where

$$\kappa = \frac{4\sqrt{2}}{d}. \tag{6.4}$$

Just as equation 4.25 was written in the form of equation 4.31, equation 6.3 can be written in the form

$$a(t) \approx E_0(t) + E_A(t)\cos(\kappa X(t) + \phi_A(t)) \tag{6.5}$$

where E_0, E_A and ϕ_A all depend on the $t = 0$ displacement of each of the seeding particles within the measuring volume at time t. Therefore in general E_0, E_A and ϕ_A are functions of time since the seeding particles present in the measuring volume at one instant are constantly being replaced by new seeding particles, each with different $x_p(0)$ from the particles of an earlier population. However if $\overline{U} = 0$ and x_m is small, say $x_m \leq d/(2\sqrt{2})$, the occupation of the measuring volume does not change significantly with time and E_0, E_A and ϕ_A are approximately constant. In this case, if $X(t) = x_m \sin(2\pi f_m t)$ and $\beta = \kappa x_m$, then

$$a(t) \approx E_0 + E_A \cos[\beta \sin(2\pi f_m t) + \phi_A]. \tag{6.6}$$

This represents a FM signal with a carrier frequency of zero, a modulation index β and phase constant ϕ_A. Technically this expression is only valid if $\beta \leq 2$ but it is found to be in reasonable agreement with the results of the simulation described in section 6.1.4 even for higher values of β. A similar expression to equation 6.6 could be derived for $b(t)$. It should be stressed that all of the simulation results presented in this study were produced using the exact model described in section 6.1.4. However the approximation to the model, derived in this section, provides an analytical method of estimating the form of the envelope spectrum.

6.1.6 Comparison of Computer Simulation with Experimental Observations

Variation of Acoustic Particle Displacement Amplitude

Comparing the simulated spectra of figure 6.7 with measured spectra of figure 6.5, notice that the low frequency peak in the simulated spectra is absent because the mean velocity was set to zero. As with the experimental data, as u_m is decreased the number of significant peaks in the simulated spectra decrease. In fact the number of significant harmonics in the simulated spectra is approximately $\beta + 1$, as predicted by Carson's rule for the number of sidebands of an FM signal [82]. However notice that the values of u_m in the simulation are significantly higher than the values of u_m measured experimentally. The harmonic content of the measured spectra would agree with Carson's rule only if d was much smaller than the calculated value.

The 1D simulation assumes that each particle travels the same distance, d, through the interference pattern. However, from figure 6.8 it is clear that with a 2D or 3D fringe pattern some particles travel a shorter distance through the fringe pattern than others. The value of d used in the simulation should therefore

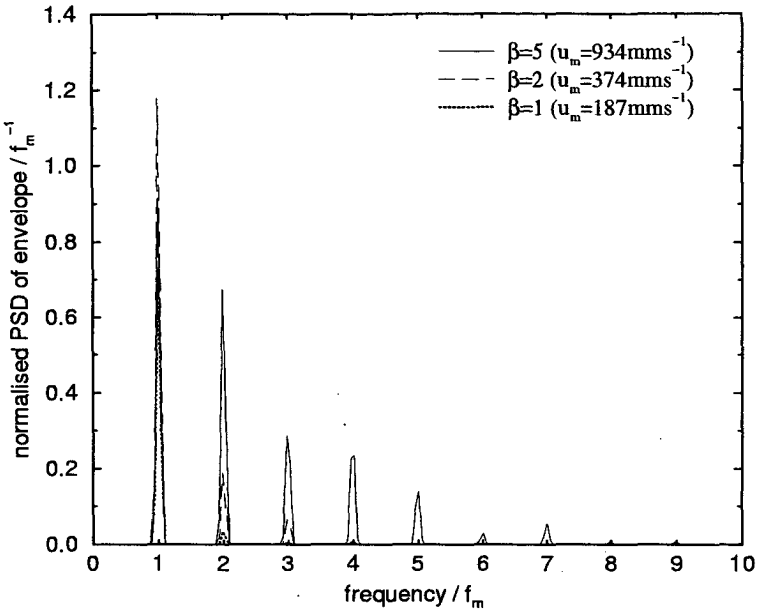

Figure 6.7: Normalised PSD from simulated Doppler signal envelopes with 4 different values of u_m. In each case $u_0 = 0$, f_m =467Hz and $M = 4$.

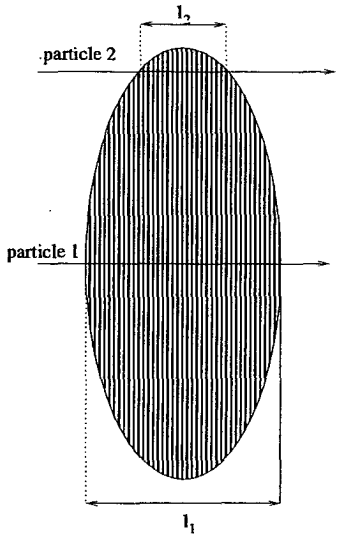

Figure 6.8: Trajectories of 2 particles moving through fringe pattern. Particle 1 travels a distance l_1 through the fringe pattern; particle 2 travels the shorter distance l_2.

be replaced with a smaller effective fringe pattern width. Approximate calculations suggest that this effect cannot completely explain the discrepancy between measured and simulated values of u_m.

In figure 6.9 u_m is fixed and β is varied by altering f_m. The frequency bandwidth of the spectra remains largely constant and the number of significant peaks is again correctly predicted by Carson's rule. This behaviour is in direct contrast to the equivalent measured spectra (figure 6.6) which always have two significant peaks, and therefore a bandwidth which varies with f_m.

Variation of Seeding Particle Density

The particle density is varied in figure 6.10. Although the A.C. power of the signal was found to increase with particle density the ratio of A.C. power to D.C. power, as indicated by the normalised spectra, actually decreases as particle density is increased and a more homogeneous particle density is created. This suggests that amplitude modulation effects can be minimised by arranging homogeneous seeding.

The fact that smoke was found to demonstrate little evidence of amplitude modulation suggests smoke seeding has a higher particle density than water droplets from the nebulisers. This is highly probable since the smoke seeding appears to produce similar D.C. photomultiplier currents to the water droplet seeding despite the much smaller diameter of the smoke particles. Also notice from figure 6.10 that, in the simulation, the number of significant components does not vary as the particle density is varied. This does not appear to agree with experimental measurements which demonstrate that the number of significant components depends on the seeding conditions. When the seeding conditions are altered, by changing the nebuliser or changing the time delay between switching the nebuliser off and commencing signal capture, the size distribution of the

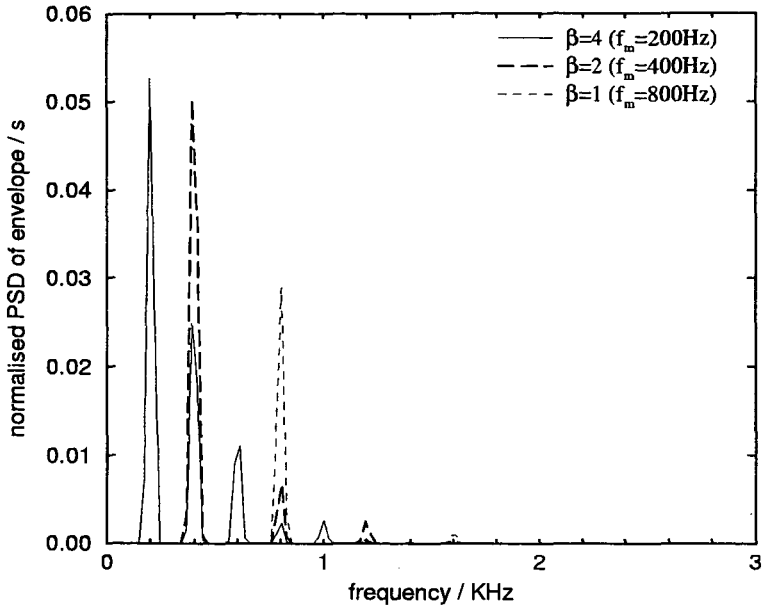

Figure 6.9: Normalised PSD from simulated Doppler signal envelopes with 3 different values of f_m. In each case $u_0 = 0$, u_m =273mms^{-1} and $M = 4$.

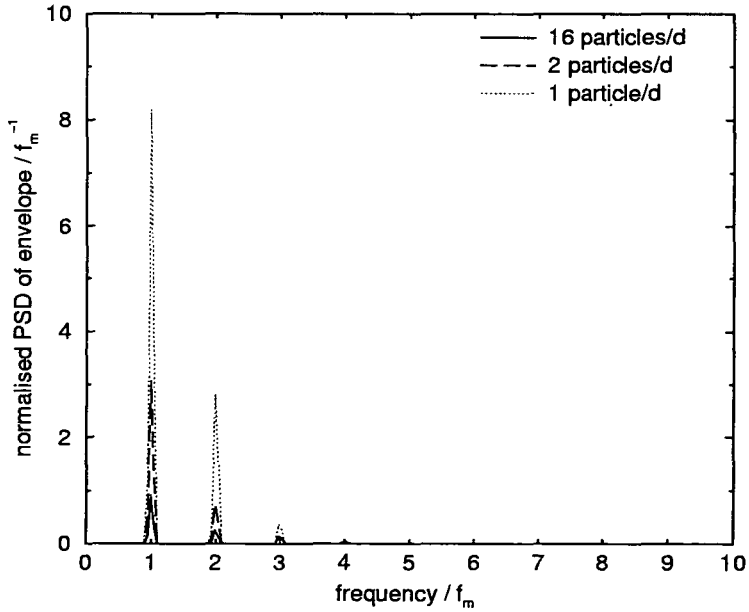

Figure 6.10: Normalised PSD from simulated Doppler signal envelopes with 3 different values of M. In each case f_m =467Hz and u_m =187mms^{-1}.

seeding particles is altered in addition to the particle density. It could be that the variation in particle size distribution affects the number of significant components in the PSD of the Doppler signal envelope. This effect was not investigated in the simulations. Unfortunately the particle size distribution could not be easily measured. In future investigations synthetic seeding particles could be used to ensure a small variation in particle size.

Variation of Mean Flow

In figure 6.11 non-zero mean flow velocities are introduced, creating low frequency components. As the mean flow velocity is increased the peak at the acoustic frequency splits into smaller sidebands on either side of the acoustic frequency. This occurs because the carrier frequency is no longer zero and so the negative frequency peaks are no longer folded exactly onto the positive frequency peaks. The power around the second harmonic of acoustic frequency actually appears to increase when u_0 is increased providing a possible explanation for the anomalously large number of significant peaks in measured spectra. As u_0 is further increased all evidence of amplitude modulation disappears.

Phase Considerations

In figure 6.12 two contrasting envelopes are compared. The envelopes were generated using identical acoustical parameters but different random particle distributions. The mean flow was set to zero so, unlike the measured Doppler signals presented in figure 4.8, the envelopes do not change with the number of acoustic cycles. The envelopes represent 2 of the 12 envelopes used to obtain the $\beta = 1$ spectrum of figure 6.7. Consider first the envelope with one local maximum per cycle. It is easy to understand how this envelope could be produced by just one particle initially positioned slightly to one side of the centre of the fringe volume

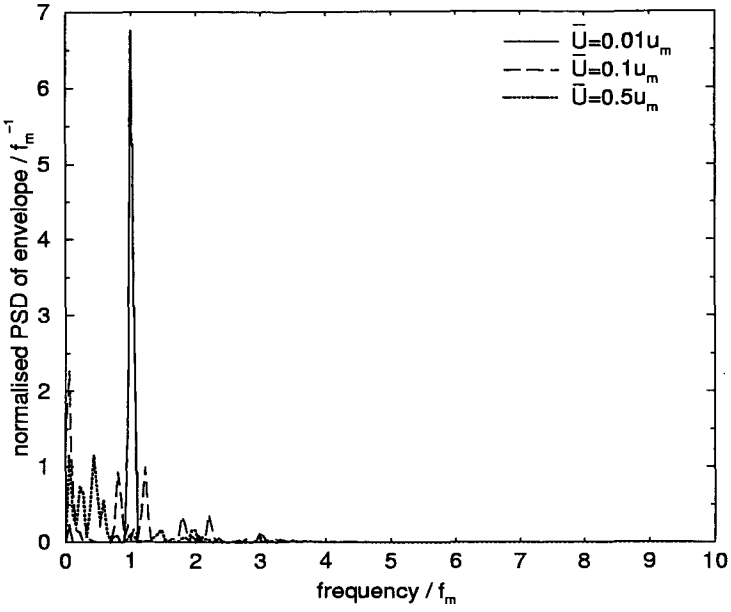

Figure 6.11: Normalised PSD from simulated Doppler signal envelopes with 3 different values of u_0. In each case u_m=187mms^{-1}, f_m =467Hz and $M = 4$.

and periodically moving towards then away from the centre of the fringe volume, under the influence of the acoustic field. In this way signal envelope maxima and minima would be produced when the particle was maximally displaced from its initial position i.e. at velocity zeros. At first it would appear that the other envelope could also be explained by the motion of one single particle provided it was initially placed at the centre of the fringe volume. On closer inspection, however, it becomes apparent that this would result in an incorrect phase relationship between the envelope and instantaneous velocity curve; this envelope curve could only be produced by at least two particles, each one initially placed on opposite sides of the centre of the fringe volume.

Notice that for the envelope produced using particle distribution 2 of figure 6.12, maxima and minima occur at velocity zeros. However, over the last 5 acoustic cycles, maxima and minima of the Doppler signal displayed in fig-

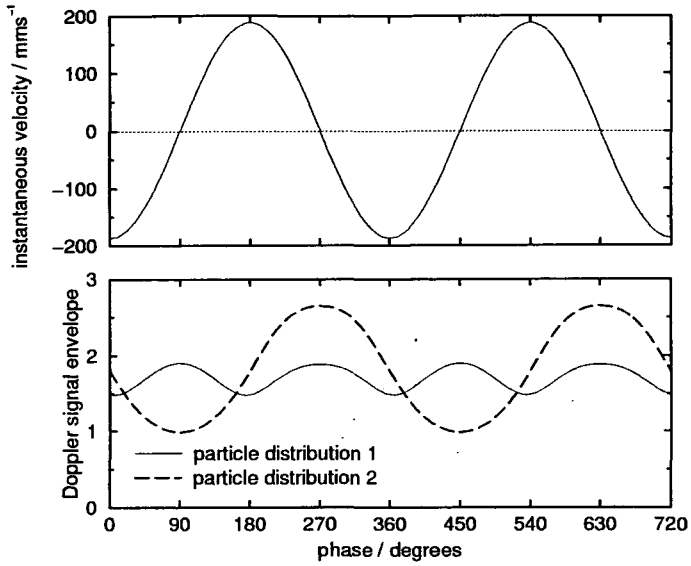

Figure 6.12: Simulated Doppler signal envelopes for two different random seeding distributions. The envelopes are displayed over two complete acoustic periods. In each case $u_0 = 0$, u_m =187mms^{-1}, f_m =467Hz and $M = 4$. The instantaneous velocity is also plotted.

ure 4.8 occur at velocity minima and maxima. This phase relationship between captured Doppler signals and extracted velocities is typical of all sections of measured Doppler signal envelopes in which there is only one clear local maximum per acoustic cycle. No explanation can at present be offered for the 90° difference between the phase relationship demonstrated in measurements and the phase relationship indicated by simulation.

6.1.7 Exploiting Amplitude Modulation

Both measurements and simulations suggest that the ratio of A.C. power to D.C. power in Doppler signal envelopes decreases as the particle density increases. This effect could possibly be exploited to measure the density of microparticles suspended in air.

There is experimental evidence that the frequency bandwidth of the envelope

spectra is proportional to the amplitude of the acoustic oscillation, although the precise relationship between bandwidth and acoustic particle velocity amplitude appears to depend on the seeding conditions. However, with suitable calibration, the envelopes of the Doppler signal could be used to estimate the frequency and acoustic particle velocity amplitude of mono-frequency sound fields provided there was negligible mean flow. In fact similar envelopes will be produced by particle oscillation in a single Gaussian beam with no interference fringes. This would offer a significant reduction in equipment costs compared to conventional LDA apparatus as the only equipment required for a basic acoustic anemometer would be a laser, a photomultiplier and a P.C. with an ordinary 44kHz A/D card. Of course the absolute experimental error in the measured acoustic particle velocity amplitude would be larger than the absolute error associated with LDA measurements as the bandwidth of the amplitude modulation signal is theoretically $4\sqrt{2}u_m/d$ compared with a Doppler signal bandwidth of u_m/Λ. However for very intense acoustic fields the relative error associated with measurements made using the proposed anemometer would be acceptable. In fact the proposed acoustic anemometer could be more appropriate than LDA for the measurement of intense sound fields because in this situation the large bandwidth of the LDA signal can cause signal processing problems.

6.1.8 Conclusions

In this section experimental evidence has been produced to show the periodic amplitude modulation of Doppler signals from LDA measurements in sound fields. As a result, at certain points in the acoustic cycle, it can become impossible to accurately extract instantaneous velocity from the Doppler signal. The amplitude modulation is a result of the periodic motion of inhomogeneous particle distributions across the fringe volume. An experimental investigation into dif-

ferent seeding methods has shown that smoke seeding shows little evidence of Doppler signal amplitude modulation, but water droplet seeding can produce significant amplitude modulation. This contrasting behaviour may be explained by differences in particle density. All measurements presented in the remainder of this study were performed using the preferred burning incense stick method of seeding.

Experiments have also shown that the periodic amplitude modulation is replaced by random amplitude modulation when a mean flow velocity of about 40% of the the acoustic particle velocity is applied. Loizeau and Gervais [62] conducted a series of LDA acoustic velocity measurements using a mean convection flow velocity of approximately $3u_{\tilde{m}}$ to improve signal quality. The price to pay for the disappearance of the periodic amplitude modulation is an increase in the random amplitude modulation. However acoustic velocity measurements suffering from signal dropout due to random amplitude modulation can often be effectively treated by ensemble averaging over several acoustic periods (see section 6.3.1).

A 1D simulation was developed to study how the amplitude modulation of the Doppler envelope depends on acoustical parameters. The simulation suggests that if PSD from repeated envelope measurements are averaged they can be used to predict the acoustic particle velocity amplitude and acoustic frequency of mono-frequency acoustic fields.

There is disagreement between experimental results and simulation output which requires further study. In particular the 90° phase discrepancy between the position of measured and simulated envelope maxima should be investigated and the simulations should be repeated using 3D models.

6.2 Mono-frequency Sound Field

6.2.1 Introduction

The measurements presented in this section are used to determine the best signal analysis method, the range of acoustic particle velocities which can be measured with the present LDA system and the accuracy of the LDA measurements. LDA measurements of acoustic particle velocity will be compared with the acoustic particle velocity deduced by applying simple theory to probe microphone pressure measurements.

Measurements were performed using the LDA setup described in section 5.2 and illustrated in figure 5.1 with loudspeaker, tube and probe microphone arrangement as illustrated in figure 6.13. The loudspeaker was driven by an amplified sine wave generator signal. In all experiments the end of the tube opposite the loudspeaker was stopped with a rubber bung. This end of the tube will subsequently be referred to as the 'rigid end' since it is certainly stiffer than the loudspeaker end. A long probe microphone was inserted through the centre of the bung and arranged such that the receptive end of the probe was flush with the circular end wall of the bung inside the tube. Whenever additional seeding was required the rubber bung/probe microphone assembly was removed and a burning incense stick was inserted into the tube for a period of approximately 20 seconds.

6.2.2 Standing Wave Theory

Consider an air filled tube driven at $x = L$ by a loudspeaker and terminated at $x = 0$ (see figure 6.13). The loudspeaker diaphragm vibrates sinusoidally at (angular) frequency ω and at time t produces the plane wave

$$p_i = Ae^{j(wt+kx)} \tag{6.7}$$

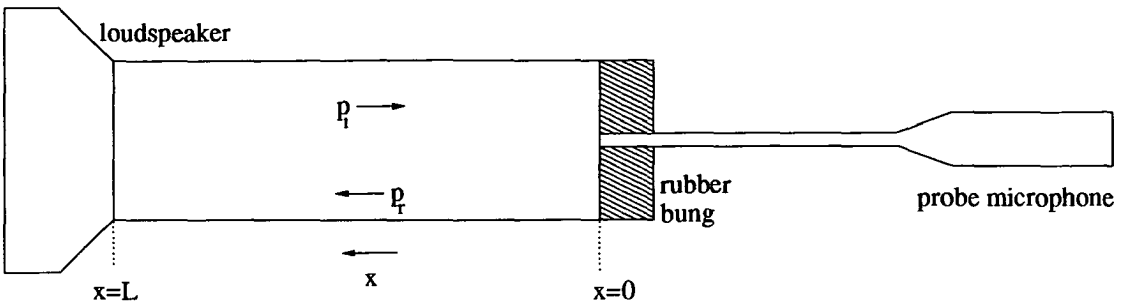

Figure 6.13: Loudspeaker, tube and probe microphone arrangement for standing wave pressure and velocity measurements.

with wavenumber k propagating towards the rubber bung [61]. For simplicity, the phase of the wave is chosen to be zero, so the amplitude can be represented by a real number, A. The wave is reflected from the termination at $x = 0$, suffering partial attenuation and also a phase change θ. The reflected wave has the form

$$p_r = Be^{j(wt-kx+\theta)}, \tag{6.8}$$

where B is the (real) amplitude. The interaction of the incident and reflected waves produces a standing wave in the tube. The total pressure at a point x is

$$\begin{aligned} p(x,t) &= p_i + p_r & (6.9)\\ &= e^{j(wt+\theta/2)}[Ae^{j(kx-\theta/2)} + Be^{-j(kx-\theta/2)}] & (6.10)\\ &= e^{j(wt+\theta/2)}[(A+B)\cos(kx-\theta/2) \\ &\qquad +j(A-B)\sin(kx-\theta/2)] & (6.11)\\ &= (A+B)e^{j(wt+\theta/2)}\left[\cos(kx-\theta/2) + \frac{j}{\mathrm{SWR}}\sin(kx-\theta/2)\right] & (6.12) \end{aligned}$$

where the standing wave ratio

$$\mathrm{SWR} = \frac{A+B}{A-B}. \tag{6.13}$$

From equation 6.12 it is clear that the pressure amplitude is

$$|p(x)| = (A+B)\sqrt{\cos^2(kx-\theta/2) + \frac{1}{\mathrm{SWR}^2}\sin^2(kx-\theta/2)}. \tag{6.14}$$

For a plane wave travelling towards the rubber bung the acoustic impedance is ρc, but for a plane wave traveling in the opposite direction the acoustic impedance is $-\rho c$ [61], where ρ is the density of air and c is the speed of sound in air. Therefore the acoustic particle velocity of a wave traveling towards the rubber bung is $p_i/(\rho c)$, the acoustic particle velocity of a wave traveling away from the rubber bung is $-p_r/(\rho c)$ and the velocity at a point x in the resulting standing wave is

$$u(x,t) = \frac{1}{\rho c}(p_i - p_r) \tag{6.15}$$

$$= \frac{(A+B)}{\rho c} e^{j(wt+\theta/2)} \left[\frac{1}{\mathrm{SWR}} \cos(kx - \theta/2) + j \sin(kx - \theta/2) \right] \tag{6.16}$$

In several experiments the probe microphone was retained at the end of the tube, at position $x = 0$, while the LDA measuring volume was positioned at x. Evaluating equation 6.12 at $x = 0$ yields

$$p(0,t) = (A+B)e^{j(wt+\theta/2)} \left[\cos(\theta/2) - \frac{j \sin(\theta/2)}{\mathrm{SWR}} \right] \tag{6.17}$$

$$\approx (A+B)e^{j(wt+\theta/2)}. \tag{6.18}$$

Using equations 6.16 and 6.18 it is easy to show that the ratio of acoustic particle velocity at x to pressure at $x = 0$ is

$$\frac{u(x)}{p(0)} = \frac{1}{\rho c} \left[\frac{1}{\mathrm{SWR}} \cos(kx - \theta/2) + j \sin(kx - \theta/2) \right]. \tag{6.19}$$

The magnitude of this ratio is

$$\left| \frac{u(x)}{p(0)} \right| = \frac{1}{\rho c} \sqrt{\frac{1}{\mathrm{SWR}^2} \cos^2(kx - \theta/2) + \sin^2(kx - \theta/2)}, \tag{6.20}$$

and the phase lead of the velocity at x relative to the pressure at $x = 0$ is

$$\angle u(x) - \angle p(0) = \tan^{-1} \left[\mathrm{SWR} \frac{\sin(kx - \theta/2)}{\cos(kx - \theta/2)} \right]. \tag{6.21}$$

Velocity anti-nodes occur when

$$kx - \theta/2 = \pi(n + 1/2) \tag{6.22}$$

where n is zero or a positive integer. At such points

$$\left|\frac{u(x)}{p(0)}\right| = \frac{1}{\rho c} \tag{6.23}$$

and

$$\angle u(x) - \angle p(0) = \begin{cases} \pi/2 & \text{if } n \text{ is even} \\ -\pi/2 & \text{if } n \text{ is odd.} \end{cases} \tag{6.24}$$

Both ρ and c are dependent on temperature. To allow comparison of velocity measurements with pressure measurements it is necessary to derive an expression for the temperature dependency of the characteristic impedance of air, ρc. The ideal gas law can be written in the form

$$\rho = \frac{MP}{RT_K} \tag{6.25}$$

where M is the mass of 1 mole of air, P is atmospheric pressure, R is the gas constant and T_K is the Kelvin temperature. Substituting $M = 0.029\text{Kg mol}^{-1}$, $P = 1.013 \times 10^{-5}\text{Pa}$ and $R = 8.315\text{J mol}^{-1}\text{Kg}^{-1}$ into equation 6.25 yields

$$\rho = \frac{353.3}{T_K} \quad \text{Kg m}^{-3}. \tag{6.26}$$

Kinsler et al [61] quote the speed of sound in air to be

$$c = 331.6\sqrt{\frac{T_K}{273}} \quad \text{ms}^{-1}. \tag{6.27}$$

Multiplying together both sides of equations 6.26 and 6.27 yields

$$\rho c = \frac{7090}{\sqrt{T_K}} \quad \text{Pa s m}^{-1}. \tag{6.28}$$

6.2.3 Comparison of Digital Hilbert Transform and Analogue Frequency Tracking Methods

Figure 6.14 displays a Doppler signal, $V_D(t)$, and the instantaneous frequency signals $F_{HT}(t)$ and $F_{AT}(t)$ extracted from the Doppler signal using the digital Hilbert transform routine and analogue tracker respectively. The Doppler signal was recorded with the measuring volume positioned at a velocity anti-node of a 445Hz sinusoidal acoustic standing wave; a 100kHz frequency shift was applied. As shown in figure 5.1, one of the frequency shifter output signals was sent to the analogue frequency tracker and the instantaneous frequency signal from the tracker's ANALOG OUT terminal was passed through bandpass filter 2 before being sampled by the A/D converter. The other identical frequency shifter output signal was sent to the A/D converter via bandpass filter 1 (see figure 5.1). To arrange as similar conditions as possible for both methods of analysis the input filter of the analogue tracker was set to 33-333kHz and bandpass filter 1 was set to 31.5-315kHz. The output of the analogue tracker was passed through bandpass filter 2 which was set to have bandwidth 75-750Hz. The Doppler signal and the $F_{AT}(t)$ signal were sampled simultaneously at 0.5MHz. A 32768 point sample of each signal was produced.

Even with smoke seeding the Doppler signal is still affected by quasi-periodic amplitude modulation which introduces significant noise around the $F_{HT}(t)$ local maxima. At several points e.g. around $36s$, $45s$ and $53s$ the reduction in Doppler signal amplitude is sufficient to produce large spikes in the $F_{HT}(t)$ signal and can result in an underestimation in the amplitude of the $F_{AT}(t)$ signal. However, the analogue tracker is clearly more robust than the digital Hilbert transform routine and gives a much cleaner signal due to the various filtering operations outlined in the previous chapter. Notice that there is a phase discrepancy between the

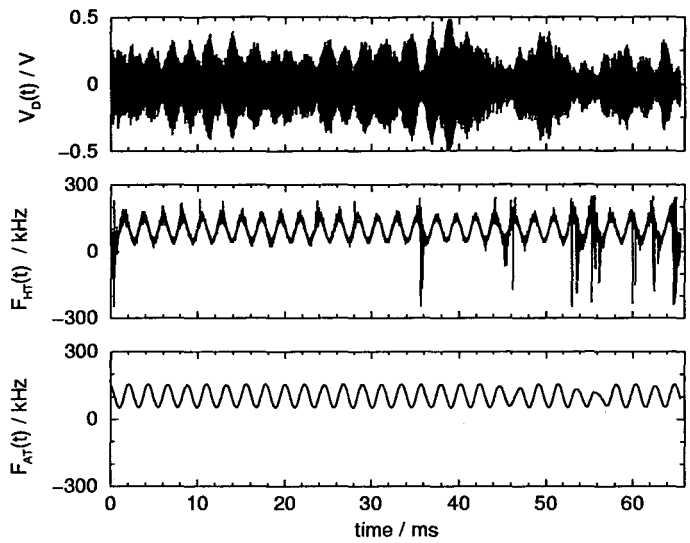

Figure 6.14: Doppler signal, $V_D(t)$, from measurement at a sinusoidal standing wave velocity anti-node and instantaneous frequency signals $F_{HT}(t)$ and $F_{AT}(t)$ extracted from the Doppler signal using the digital Hilbert transform routine and analogue tracker respectively.

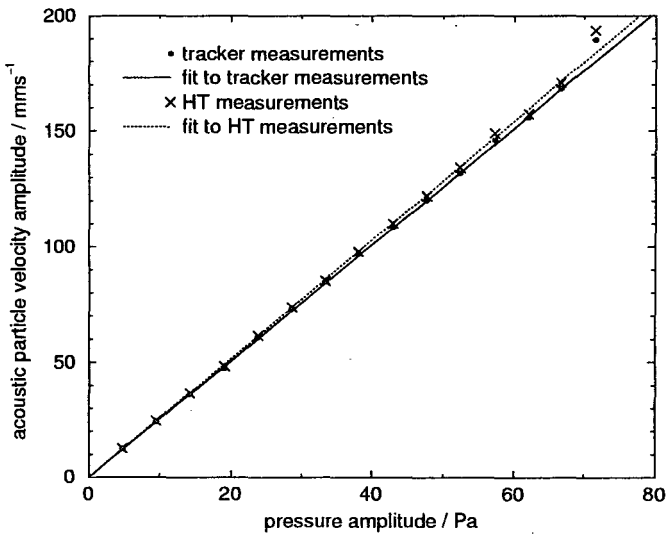

Figure 6.15: LDA measurement of acoustic particle velocity amplitude at a velocity anti-node versus probe microphone measurement of acoustic pressure amplitude at a pressure anti-node. Small amplitude measurements.

$F_{AT}(t)$ and $F_{HT}(t)$ curves. This is a consequence of passing the $F_{AT}(t)$ signal through bandpass filter 2.

The amplitude of the acoustic particle velocity was estimated by applying the signal to noise ratio program 'spec.c' used in section 5.3 to instantaneous frequency curves rather than Doppler signals. The SNR program is described in appendix C.4 and listed in appendix D. Figure 6.15 is a plot of acoustic particle velocity amplitude versus pressure amplitude for a range of acoustic pressures. The measurements were performed with LDA, filter and acoustic conditions identical to those used to produce the signals presented in figure 6.14, except that the gain of the loudspeaker was increased in steps to provide a range of acoustic pressure.

Acoustic pressure amplitude, $|p|$, was deduced from the RMS value of the output signal, V_p', from the probe microphone's measuring amplifier using the relation

$$|p| = \sqrt{2} V_p' 10^{\frac{G_p - R_p - 94}{20}} \tag{6.29}$$

where G_p is the gain setting of the measuring amplifier and R_p is the amplitude response of the probe microphone/measuring amplifier combination as indicated in figure 5.10. Equation 6.29 can be derived by substituting equation 5.6 into equation 5.7 along with the definition of sound pressure level [61]:

$$SPL = 20 \log_{10} \left(\frac{p'}{20 \mu \text{Pa}} \right) \tag{6.30}$$

where p' is the RMS Pascal pressure.

A digital voltmeter was used to measure the RMS value of the probe microphone measuring amplifier signal. This enabled the Doppler signal and $F_{AT}(t)$ signal to be captured simultaneously with the pressure amplitude measurement. The microphone signal was not recorded using the A/D converter because if 3

input channels are used the sample rate of the WaveBook 512 must be reduced below 0.5MHz, requiring a reduction in the frequency shift, thus resulting in a reduction in the dynamic range.

The reciprocal of the gradient of each of the straight line graphs in figure 6.15 is effectively a measure of the average value of the ratio of pressure amplitude measured at a pressure anti-node to acoustic particle velocity measured at a velocity anti-node and is therefore theoretically equal to ρc (see equation 6.23). With either analysis method, at acoustic particle velocity amplitudes below 170mms^{-1} there is no significant departure of the measured points from their respective best fit straight line graphs, indicating that there is very little random error in the measurements. In fact the relative error in the gradients of each graph is only 0.4% which corresponds to a random error in the measurement of acoustic particle velocity amplitude of only 0.03dB. However, comparison of the gradients of the two straight line graphs in figure 6.15 indicates the discrepancy between the amplitudes of the instantaneous frequency signals extracted using the two different methods of analysis is 0.2dB on average, much greater than the random error of each individual analysis method. The gradients of analogue tracker and Hilbert transform derived straight line graphs correspond to characteristic impedances of respectively $391 \pm 2\,\text{Pa s m}^{-1}$ and $397 \pm 2\,\text{Pa s m}^{-1}$. However the measurements were performed at a temperature of 22.5°C which corresponds theoretically (see equation 6.28) to a characteristic impedance of $412\,\text{Pa s m}^{-1}$. The LDA/probe microphone measurements systematically underestimate the characteristic impedance by 0.5dB in the worst case (Hilbert transform analysis).

With the particular filter settings listed above, LDA measurements are only successful if the acoustic particle velocity amplitude is less than or equal to 170mms^{-1}. For example, figure 6.15 illustrates that the points with acous-

tic particle velocity amplitudes of approximately 190mms^{-1} do not lie close to the best fit straight lines. With a 100kHz shift and a 33-333kHz ideal filter it should be possible to measure acoustic particle velocity amplitudes of up to (100-33)kHz$\times$3.3μm=221mm s^{-1} [i]. However with real filters it appears to be safer to limit measurements to sound fields with acoustic particle velocity amplitudes of less than or equal to 75% of the theoretical limit calculated by considering the frequency shift and the theoretical cut-off frequencies of the filters.

Figure 6.15 presents the measured amplitudes of 15 different $F_{AT}(t)$ signals and 15 different $F_{HT}(t)$ signals. The signal-to-noise ratio (SNR) of each of these signals was also measured. The average SNR of the 15 different $F_{AT}(t)$ signals (25dB) is significantly higher than the average SNR of the 15 Hilbert transform routine signals (13.5dB), confirming the earlier qualitative observation that signals extracted using the Hilbert transform method have a higher noise content.

6.2.4 Dynamic Range

This short section investigates the range of acoustic particle velocity amplitudes which can be measured using the particular LDA setup described in chapter 5. It is clear that the analogue tracker, which has a bandwidth of up to 9MHz, has a much greater dynamic range that the digital Hilbert transform method which is currently limited by the 1MHz maximum sample rate of the A/D converter. It should be noted however that in the case of the Hilbert transform routine the only real limit of the dynamic range is the sample rate of the A/D converter which in turn is limited by financial, rather than technical, constraints. As the analogue tracker has the additional advantage of having a higher SNR than the digital Hilbert transform routine, all of the LDA measurements presented in the remainder of this work were analysed using the analogue tracker.

[i] recall the fringe spacing $\Lambda = 3.3\mu$m

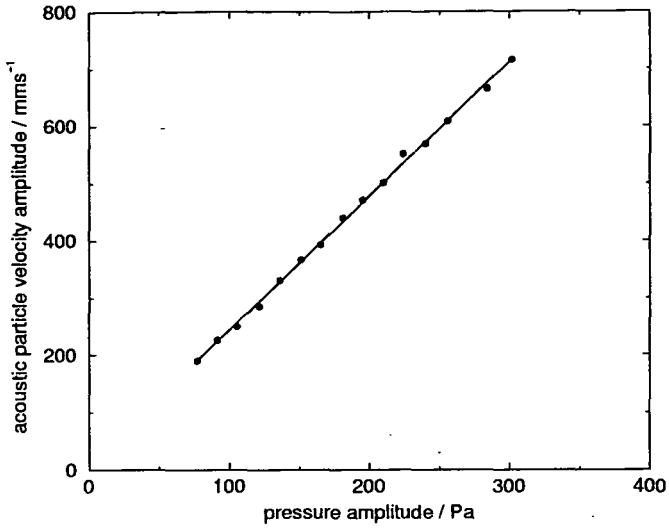

Figure 6.16: LDA measurement of acoustic particle velocity amplitude at a velocity anti-node versus probe microphone measurement of acoustic pressure amplitude at a pressure anti-node. Large amplitude measurements.

The measurements presented in this section were performed with the same acoustic frequency (445Hz) as the measurements presented in figure 6.15, with the LDA measuring volume positioned at the same point in the tube (the velocity anti-node nearest the rubber bung). In this case however an increased frequency shift of 1MHz was applied and the input filter of the tracker was set to 0.3-3.33MHz. Also, since there was no need to sample the Doppler signal, the $F_{AT}(t)$ and probe microphone signals were sampled simultaneously and the amplitude of each signal was extracted using the 'single burst' option of the frequency response program, 'auto.c', described in appendix C.3. The anti-nodal pressure amplitude was varied from approximately 70Pa to 300Pa (140dB SPL) but was not increased any further as that would probably have resulted in the introduction of significant non-linear effects such as acoustic streaming [48].

In figure 6.16 the gradient of the best fit straight line to the measured data points corresponds to a characteristic impedance of 427Pa s m^{-1} suggesting that

LDA/probe microphone measurements have overestimated the acoustic particle velocity amplitude by 0.3dB compared to figure 6.15's underestimate of 0.3dB. It is not clear why one set of measurements should systematically underestimate the impedance whilst the other set systematically overestimates the impedance. It is unlikely that such a large variation could be explained by a fluctuation in temperature as the temperature was carefully monitored and even a significant decrease in temperature of 1°C would only increase the characteristic impedance by approximately 0.01dB. It is even more unlikely to be caused by positioning the measuring volume slightly to one side of the velocity anti-node as a 2mm error would overestimate the characteristic impedance by only 0.001dB. It is probable that the amplitude of the tracker's ANALOG OUT signal is slightly dependent on the range setting of the tracker. This is a reasonable assumption as the range control not only selects the range of the input filter, and hence the noise content, but also controls the operation of the phase locked loop [28].

The measurements presented in figures 6.15 and 6.16 demonstrate that the analogue frequency tracker may be used to measure sinusoidal sound fields in air with acoustic particle velocity amplitudes in the range 12-700mm s^{-1} (SPL 105-140dB) with an accuracy of ±0.3dB.

6.2.5 Measurement of Standing Wave Pressure and Velocity as a Function of Displacement from Rigid End

Introduction

In the previous subsection all velocity measurements were conducted at the same point in the tube. In this subsection velocity amplitude, $|u(x)|$, and phase, $\angle u(x)$ will be measured along the length of the tube. Simultaneous measurement of

pressure amplitude, $|p(0)|$, and phase, $\angle p(0)$, at the rigid end will also be performed. The measured values of $|u(x)|/|p(0)|$ and $\angle u(x) - \angle p(0)$ will be compared with the theoretical values listed in equations 6.20 and 6.21 respectively. There is very little published material relating to LDA measurement of acoustic particle velocity phase [81].

Pressure Measurements

It is sensible to perform measurements at natural resonance frequencies of the tube because at such frequencies there is the greatest possible variation in amplitude as the probe microphone is moved from anti-node to node. To determine the natural resonance frequencies, the probe microphone was fixed in position at the end of the tube (as shown in figure 6.13) and a 50-2000Hz frequency sweep was applied to the loudspeaker using the same software as was used to generate the frequency sweep for the microphone calibration. The output signal from the probe microphone's measuring amplifier was captured by the A/D converter and analysed using option 4 of the mechanical response program 'auto.c' described in appendix C.3 and listed in appendix D.

The resulting anti-nodal pressure measurements are displayed in figure 6.17. The vertical lines in the figure represent the theoretical resonance frequencies if the tube had been rigidly terminated at each end. If most of the resonance peaks had aligned close to the vertical lines then the loudspeaker could have been described as a heavy driver [61]; if most of the anti-resonance troughs had aligned close to the vertical lines then the loudspeaker could have been described as a light driver. The measurements demonstrate that neither classification applies to the loudspeaker used in the measurements, *i.e.* it does not behave like a rigid termination or an open end. It was decided to perform initial measurements in a 1740Hz standing wave because 1740Hz is a resonance of the loudspeaker-pipe

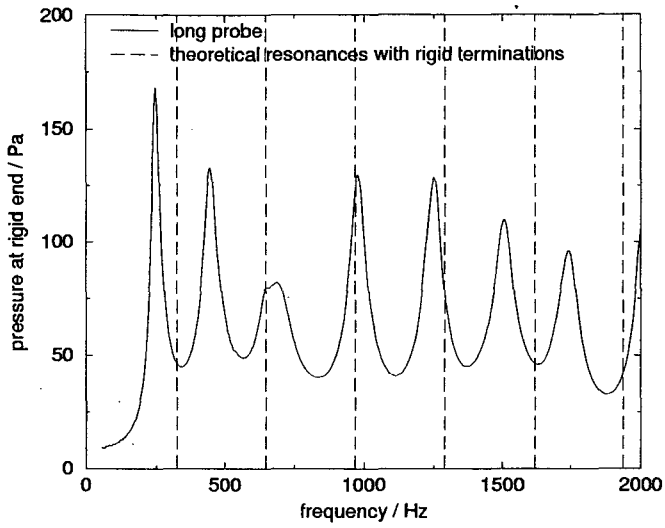

Figure 6.17: The anti-nodal pressure amplitude for the rigidly terminated loudspeaker-pipe system. The sweep signal to the loudspeaker had a constant amplitude.

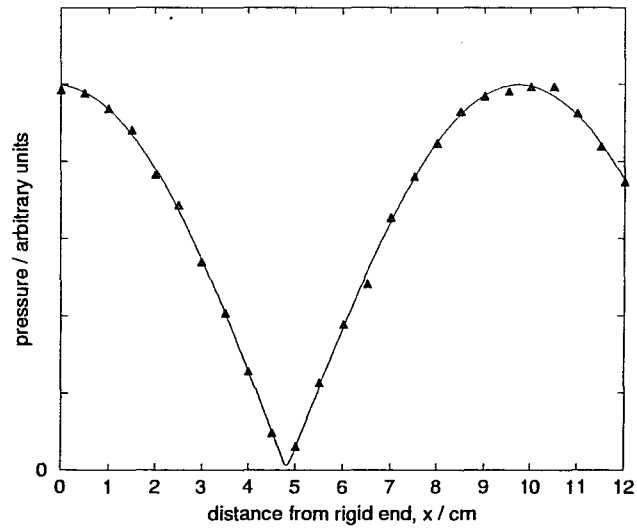

Figure 6.18: Pressure amplitude measured in a 1740Hz standing wave.

system and is also a relatively high frequency and as a result would be sensitive to any phase lag problems.

Before performing the measurements described in the above introduction it was necessary to carry out pressure measurements to determine the SWR. The probe microphone was inserted further into the tube and measurements of acoustic pressure amplitude were carried out at 1cm intervals from the end of the tube. The results are displayed in figure 6.18. A least squares fit routine, 'lsf_sw.c', was written to fit equation 6.14 to the pressure amplitude measurements by selecting values of $(A + B)$, SWR and θ which optimize the fit. The program is described further in appendix C.7 and listed in appendix D.

In determining SWR and θ it is only the relative values of pressure amplitude which are required. All of the pressure measurements presented in figure 6.18 were carried out at the same frequency (1740Hz), therefore there was no need to apply the calibration data to the probe microphone signal. The vertical scale of figure 6.18 is actually the RMS voltage of the output signal from the microphone's measuring amplifier which is directly proportional to pressure amplitude in Pascals (see equation 6.29).

Velocity Measurements

A 1740Hz standing wave was set up in the tube and the probe microphone was positioned at the end of the tube, as shown in figure 6.13. The temperature inside the tube was 20°C, identical to the temperature experienced in the above pressure measurements. LDA measurements were performed at 1cm intervals along the axis of the tube. The position of the LDA system was fixed throughout the measurements but the tube, loudspeaker and probe microphone assembly was moved on a translational table. The values $|u(x)|/|p(0)|$ and $\angle u(x) - \angle p(0)$ presented in figure 6.19 were extracted from $F_{AT}(t)$ and probe microphone signals

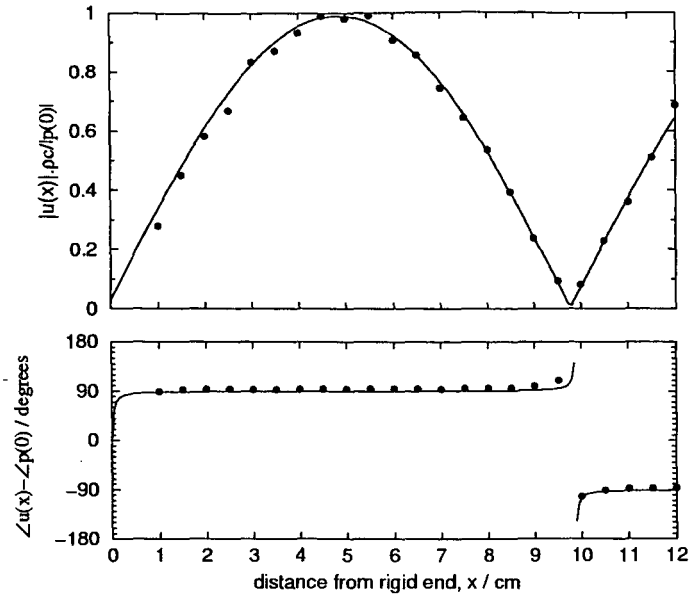

Figure 6.19: Velocity amplitude, $|u(x)|$, and phase, $\angle u(x)$, measured in a 1740Hz standing wave. The results are presented relative to anti-nodal pressure amplitude, $|p(0)|$, and phase, $\angle p(0)$.

using the single burst option of the mechanical response program. The solid curves in figure 6.19 represent equations 6.20 and 6.21. The magnitude curve was fitted to the data points using the least squares fit routine which was used to fit the pressure curve. However, with the velocity measurements only $(A + B)$ and θ were optimized; the SWR was set equal to the value deduced from the earlier pressure measurements. The theoretical phase curve is simply a plot of equation 6.21 using parameter values from the magnitude curve.

In the magnitude graph of figure 6.19 the vertical axis is scaled by ρc. Therefore at the velocity anti-node the scaled ratio of velocity amplitude to anti-nodal pressure amplitude should be equal to 1 (see equation 6.23). The maximum value of the fitted curve is in fact 0.99. The phase measurements are also close to the theoretical values, although the measured phase lead of the velocity is generally overestimated by approximately 5^o. Most of the measured magnitude and phase

points also lie very close to the fitted curves.

6.2.6 Conclusions

The instantaneous frequency signal extracted from a Doppler signal using the analogue frequency tracker is very similar to the instantaneous frequency signal produced by applying the Hilbert transform routine to the same Doppler signal. However the analogue tracker is preferable to the Hilbert transform due to a far better SNR and a greater dynamic range.

When using the frequency tracker, acoustic particle velocity can be accurately measured provided the amplitude of the signal is less than 75% of the theoretical limit calculated by considering the frequency shift and the bandwidth of the input filter to the tracker. It appears that the amplitude of the instantaneous frequency signal produced by the tracker is influenced to a small extent by the range of the input filter. Nevertheless the anti-nodal velocity and pressure measurements indicate that the LDA system can be used to measure acoustic particle velocity amplitudes in air with an error of only ± 0.3dB over a velocity range corresponding to SPLs in the range 105-140dB.

Anti-nodal pressure measurements indicate that the loudspeaker behaves neither as a light driver nor as a heavy driver. LDA measurements along the axis of the tube show that the technique can be used in air to measure acoustic particle velocity amplitude, even at frequencies as high as 1740Hz. The measurements also demonstrate that LDA can successfully provide phase information in addition to amplitude information.

6.3 Multi-harmonic Sound Fields

All LDA measurements previously presented in this work have been performed in simple mono-frequency standing waves. LDA measurements in more complex sound fields with several harmonic components have been carried out by other researchers [49] but such measurements are at a preliminary stage. To the best of the author's knowledge the measurements presented below form the most comprehensive study to date of the application of LDA to the measurement of multi-harmonic sound fields. It is important to establish whether LDA can be used in such sound fields before attempting measurements in lip driven brass instruments, where the sound fields usually contain many harmonic components [16].

6.3.1 Experimental Method

A .wav file was written to produce a signal with three harmonically related Fourier series components at 323, 646 and 969Hz; each component had equal amplitude. The .wav file was played out using the PC's sound card and the resulting output signal was amplified and then applied to the loudspeaker to produce a multi-harmonic standing wave in the tube. Although all three components of the .wav file do have the same amplitude, each component of the standing wave in the tube has a different amplitude, due to the resonance properties of the loudspeaker-tube system (see figure 6.17).

Measurements were performed using the method applied in section 6.2.5. Velocity was measured along the length of the tube while the pressure at the rigid end was simultaneously monitored. As before, the ANALOG OUT and probe microphone measuring amplifier signals were sampled by the A/D converter. However the signals could not be processed using the frequency response program because each signal consists of several harmonic components, and the frequency

response program considers only the strongest frequency component. A new program, 'phaseav.c' was written to process the more complex signals.

The program simultaneously analyses the velocity and pressure signal. It detects signal dropout portions in the velocity signal (completely horizontal portions) and removes them. It then extracts the fundamental frequency from the pressure signal and uses this information to individually ensemble average both pressure and velocity signals. The process of ensemble averaging velocity signals can be explained as follows: each measurement of velocity has a time coordinate associated with it which is used to assign a phase coordinate such that any two velocity measurements separated by one acoustical period become separated in phase by 2π. The velocity values associated with all phase values in the range $2(m-1)\pi/n$ to $2m\pi/n$ are then averaged, where n is the number of phase bins per acoustic period and m is an integer between 1 and n. This process is repeated for all values of m to provide a smoothed velocity versus phase curve. The top right graph of figure 6.20 is an example of such an ensemble averaged curve. The graph is plotted over two acoustic periods. The information contained in the 360-720 degree range is identical to the information contained in the 0-360 degree range but it is useful to observe the curves over at least two complete periods. Ensemble averaging is a common technique in LDA and has previously been applied to the measurement of periodic phenomena such as air jets in flue organ pipes [73] and simulated ocean waves [71].

The program also performs a FFT over one acoustic period of the ensemble averaged data and extracts the amplitude and phase of all harmonic components (see figure 6.20). Since the transform is performed over only one acoustic period the frequency resolution of the amplitude and phase spectra is equal to the fundamental frequency and the program cannot therefore be applied to inharmonic

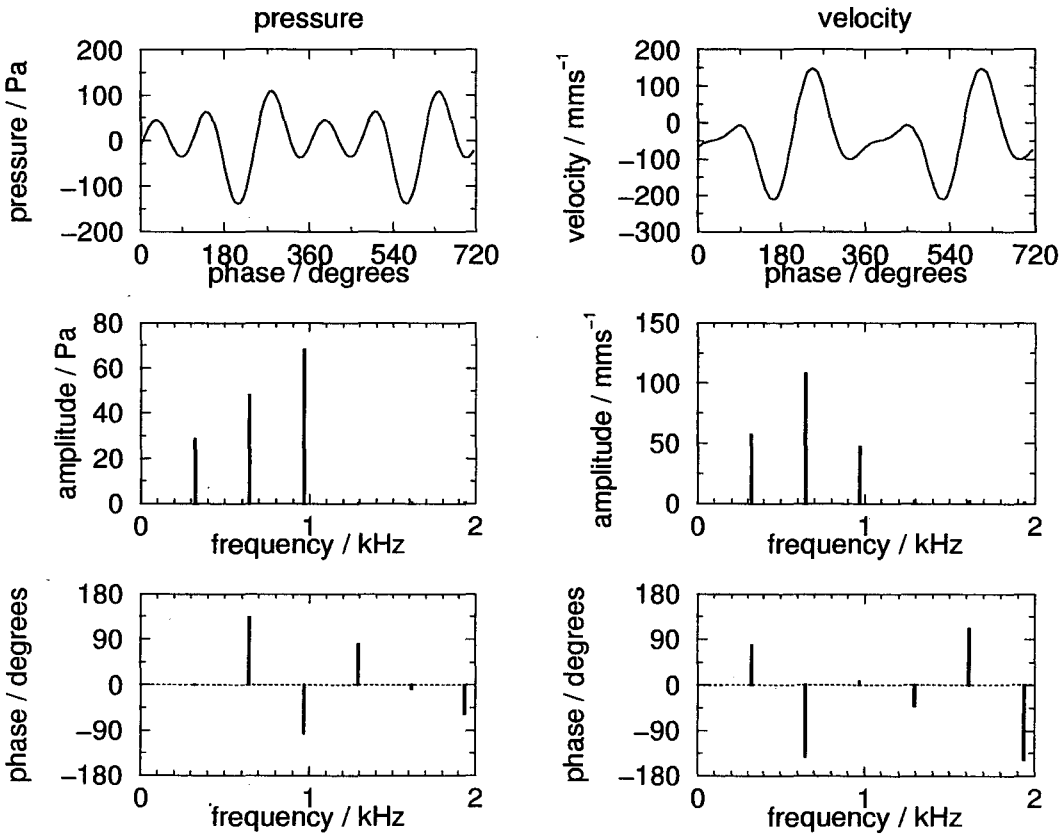

Figure 6.20: Pressure and acoustic particle velocity measurements made in a standing wave with harmonic components at 323, 646 and 969Hz. Pressure was measured at the rigid end while velocity was measured 16cm from the rigid end. Pressure measurements are set out in the left column and velocity measurements in the right column. The graphs display ensemble averaged pressure (or velocity) and the amplitude and phase of the harmonic components of the ensemble averaged signals.

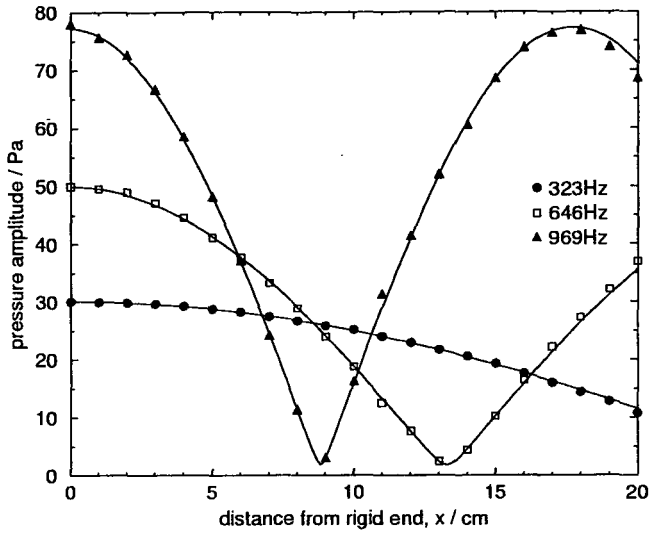

Figure 6.21: Pressure amplitude of each of the frequency components of a standing wave with three harmonic components.

sound fields. However it should be possible to apply the program to many useful situations, including velocity measurement in wind instrument air columns, where the sound fields are harmonic in any case. Performing the FFT over only one acoustic period has the advantage that signal leakage is eliminated, therefore no window function is required. The ensemble averaging program is described in greater detail in appendix C.8 and is listed in appendix D.

Before making the LDA measurements the multi-harmonic sound field was set up in the tube and pressure measurements were performed along its length. The ensemble averaging program was then applied to the resulting probe microphone signals and used to extract the pressure amplitude of each of the three harmonic components. These components are plotted in figure 6.21. The 63 points in this graph were extracted from just 21 probe microphone signals. As in section 6.2.5 the solid curves were fitted to each set of amplitude points using the least squares routine in order to determine the SWR associated with each harmonic component.

Acoustic particle velocity was then measured along the axis of the tube. At

the same time the pressure at the end of the tube was measured. Pressure and velocity signals were analysed using the ensemble averaging program. The ratio of velocity amplitude to anti-nodal pressure amplitude of the first, second and third harmonics are presented in figures 6.23, 6.24 and 6.25 respectively; the phase lead of velocity relative to pressure is also plotted. As in section 6.2.5 the least square fit routine was employed to fit the solid curves to the data points using the SWRs deduced from the earlier pressure measurements.

6.3.2 Results and Discussion

Figure 6.22 demonstrates how the harmonic content of the acoustic particle velocity varies along the length of the tube. In figures 6.24 and 6.25 the curves fitted to the amplitude data have maxima very close to 1, as required by equation 6.23. Furthermore there is good agreement between the measured phase points and the theoretical phase curve. This is demonstrated in particular in figure 6.25, where the measured phase jump between $x = 17$cm and $x = 18$cm occurs at the theoretically predicted position. In figure 6.23 there is a large discrepancy between measured phase points and the theoretical phase curve, particularly near the rigid end. It is surprising that the phase error is most apparent in the lowest frequency component because a particular time delay in a filter for example would result in a smaller phase error at low frequencies than at high frequencies. Of course the phase discrepancy in figure 6.23 may be due to a problem with the probe microphone rather than the LDA system. Recall that the probe microphone was calibrated using a 1/2 inch microphone as a reference. It is difficult to verify if the reference microphone does actually provide an accurate phase reference.

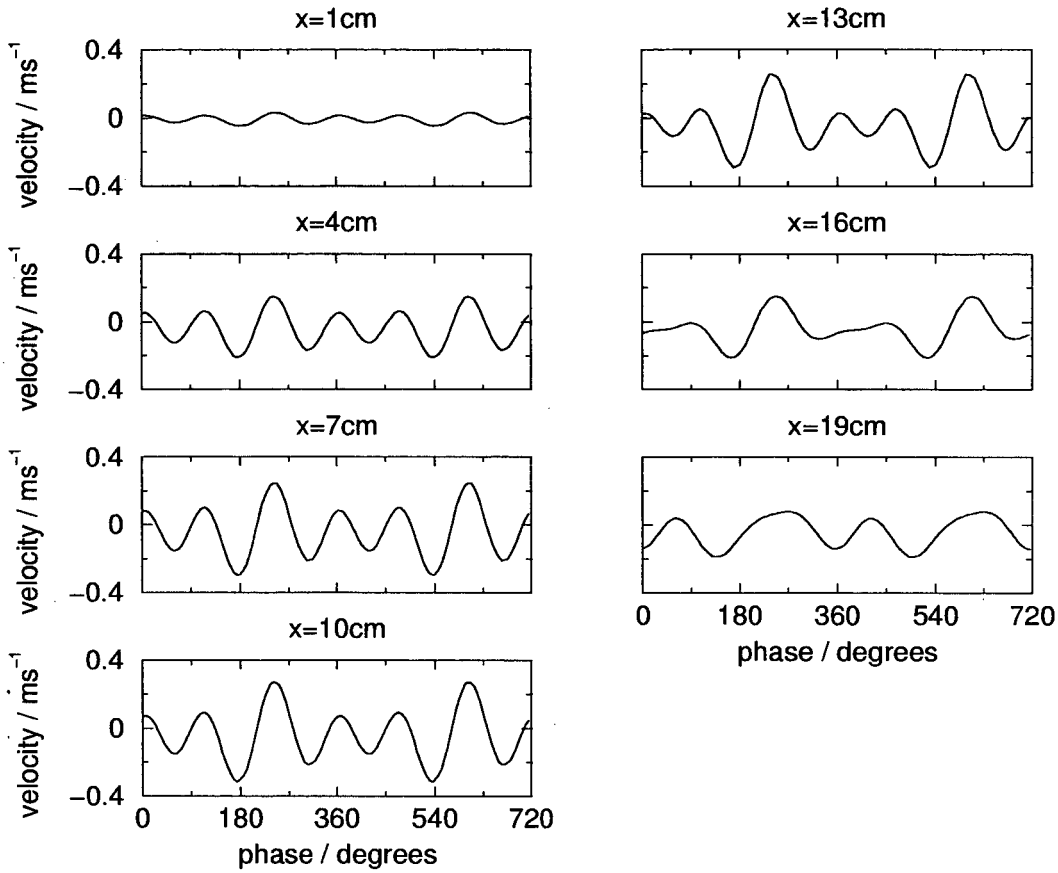

Figure 6.22: Ensemble averaged acoustic particle velocity from measurements along the axis of a tube containing a standing wave with harmonic components at 323, 646 and 969Hz. Each graph displays the velocity measured at a different position, x, in the tube where x is the distance from the rigid end.

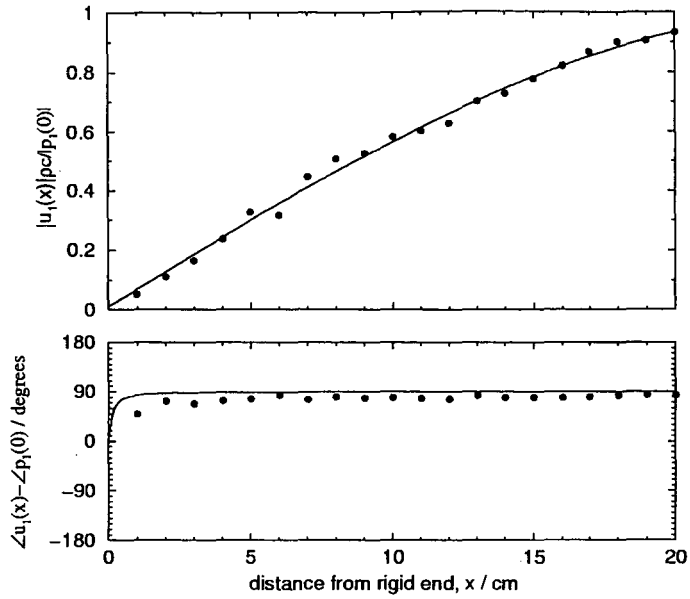

Figure 6.23: Velocity amplitude, $|u_1(x)|$, and phase, $\angle u_1(x)$, of the fundamental component of a standing wave with three harmonic components The results are presented relative to anti-nodal pressure amplitude, $|p_1(0)|$, and phase, $\angle p_1(0)$, of the fundamental.

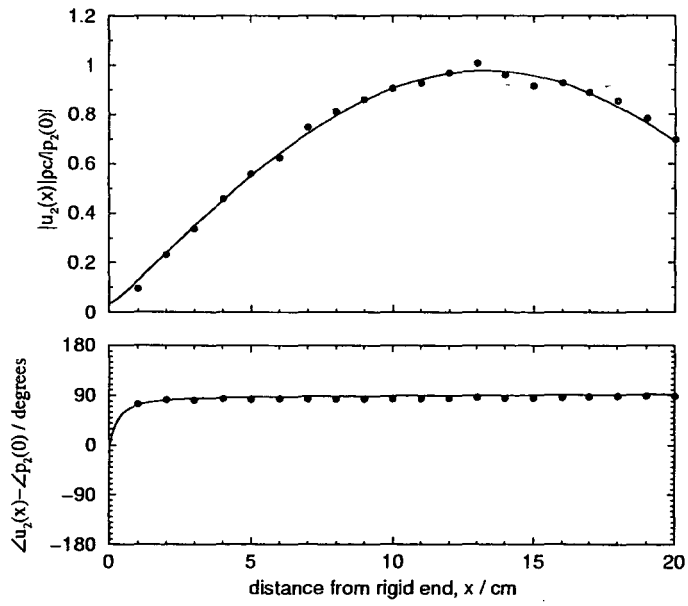

Figure 6.24: Velocity amplitude, $|u_2(x)|$, and phase, $\angle u_2(x)$, of the fundamental component of a standing wave with three harmonic components The results are presented relative to anti-nodal pressure amplitude, $|p_2(0)|$, and phase, $\angle p_2(0)$ of the second harmonic.

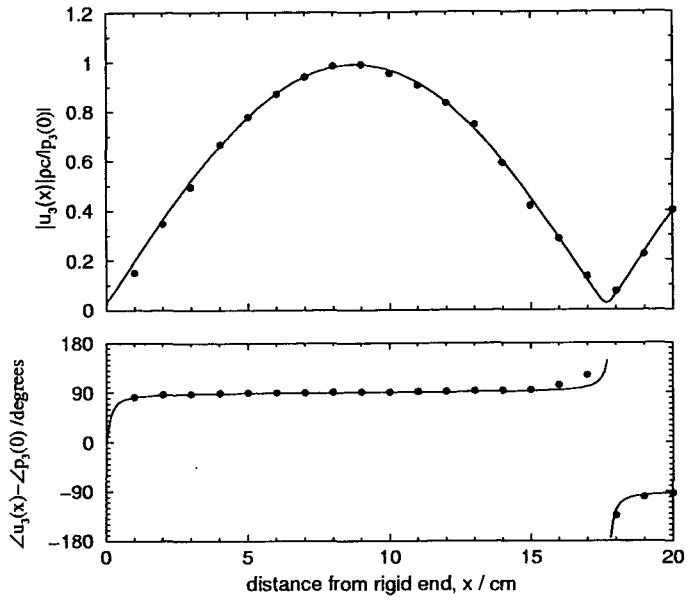

Figure 6.25: Velocity amplitude, $|u_3(x)|$, and phase, $\angle u_3(x)$, of the fundamental component of a standing wave with three harmonic components The results are presented relative to anti-nodal pressure amplitude, $|p_3(0)|$, and phase, $\angle p_3(0)$ of the third harmonic.

6.3.3 Conclusions

The measurements presented in figures 6.23, 6.24 and 6.25 demonstrate firstly that multi-frequency sound fields can be successfully measured using LDA and secondly that the ensemble averaging program is a suitable tool for smoothing the data and extracting the individual frequency components from the acoustic particle velocity.

6.4 Measurement of Acoustic Impedance

In acoustics one of the most important quantities which can be measured is acoustic impedance. Acoustic impedance is defined as the ratio of pressure to volume velocity. Acoustic impedance measurements have already been used extensively in chapter 3. The apparatus used to make these measurements applies

a constant volume velocity input to the instrument mouthpiece and measures the pressure at the entrance to the mouthpiece in order to deduce the magnitude of the impedance at the mouthpiece, known as the input impedance. However this apparatus has several disadvantages: it is capable of measuring only the input impedance and not the impedance at any other point in the instrument, it requires frequent calibration and does not provide crucial phase information. More complicated impedance rigs equipped with at least two spatially separated microphones are however able to deduce complex acoustic impedance indirectly.

In order to overcome the above disadvantages there has been some interest in the measurement of acoustic impedance using LDA [26] [81].

6.4.1 Theoretical Expression for Impedance in a Cylinder

In dealing with the transmission of acoustic radiation in pipes and wind instruments it is conventional to use the acoustic impedance. However as LDA measures acoustic particle velocity rather than volume velocity the technique naturally lends itself to the measurements of specific acoustic impedance. It is of course possible to transform specific acoustic impedance measurements into acoustic impedance measurements simply by dividing the specific acoustic impedance by the cross sectional area of the pipe (or instrument) at the point of measurement.

By making use of equations 6.7, 6.8, 6.9 and 6.15 it is easy to show that in a tube-loudspeaker system such as that illustrated in figure 6.13, the specific acoustic impedance at a distance x from the termination opposite the loudspeaker

is

$$Z_s(x) = \rho c \frac{p_i + p_r}{p_i - p_r} \tag{6.31}$$

$$= \rho c \frac{Ae^{jkx} + Be^{j\theta}e^{-jkx}}{Ae^{jkx} - Be^{j\theta}e^{-jkx}} \tag{6.32}$$

$$= \rho c \frac{(A + Be^{j\theta})\cos kx + j(A - Be^{j\theta})\sin kx}{(A - Be^{j\theta})\cos kx + j(A + Be^{j\theta})\sin kx} \tag{6.33}$$

$$= \frac{Z_r + j\rho c \tan kx}{1 + j(Z_r/\rho c)\tan kx} \tag{6.34}$$

where the specific radiation impedance of the termination at $x = 0$ is

$$Z_r = \rho c \frac{A + Be^{j\theta}}{A - Be^{j\theta}}. \tag{6.35}$$

Notice that the impedance is not influenced by acoustical conditions between the driver and the point of measurement, x.

6.4.2 Experimental Method

Impedance measurements were conducted using the tube-loudspeaker arrangement illustrated in figure 5.2a. The measurements were compared with the theoretical impedance predicted using a program written by Sharp [80] which evaluates equation 6.34 but considers the additional complication of viscous losses, as formulated by Keefe [59]. The end of the tube opposite the loudspeaker end was left unterminated in these experiments to permit the use of a theoretical expression for the radiation impedance [61] [80]. The LDA measuring volume was positioned 17cm from the unterminated end of the tube and the probe microphone was inserted into the tube and positioned with the receptive end directly below the measuring volume. The input filter of the analogue tracker was set to 0.1-1MHz and a 500kHz frequency shift was applied. The frequency was swept from 50-2000Hz using the computer's A/D card driven by software previously used in the microphone calibrations. The ANALOG OUT and probe microphone

signals were captured simultaneously by the A/D converter and then analysed using the impedance option of the frequency response program, 'auto.c', described in appendix C.3 and listed in appendix D.

6.4.3 Results and Discussion

The resulting specific acoustic impedance curves are displayed in figure 6.26. There is very good agreement between the measured and theoretical values of impedance magnitude over the entire frequency range. However there is a large discrepancy between measured and theoretical phase at low frequencies. The measured phase lead of pressure relative to velocity is consistently overestimated at frequencies below 300Hz. Recall that this discrepancy in the phase was also observed in the lowest frequency component of the multi-harmonic LDA measurements (see figure 6.23) where the phase lead of *velocity* relative to *pressure* was consistently *under*estimated. This phase discrepancy may not be limited to the measurements presented in this study; it is interesting to note that in their investigations into the performance of the microflown, van der Eerden et al [32] considered only frequencies above 400Hz. Figure 6.26 clearly demonstrates that LDA can be successfully used in impedance measurements, at least at frequencies above 300Hz.

6.5 Conclusions

The first section of this chapter investigated the best method of seeding the flow. Water droplet seeding was found to result in quasi-periodic amplitude modulation of the Doppler signal at the acoustic frequency and occasionally in periodic signal dropout. Experimental results demonstrated that the problem could be mitigated by applying smoke seeding from incense sticks rather than water droplet seeding.

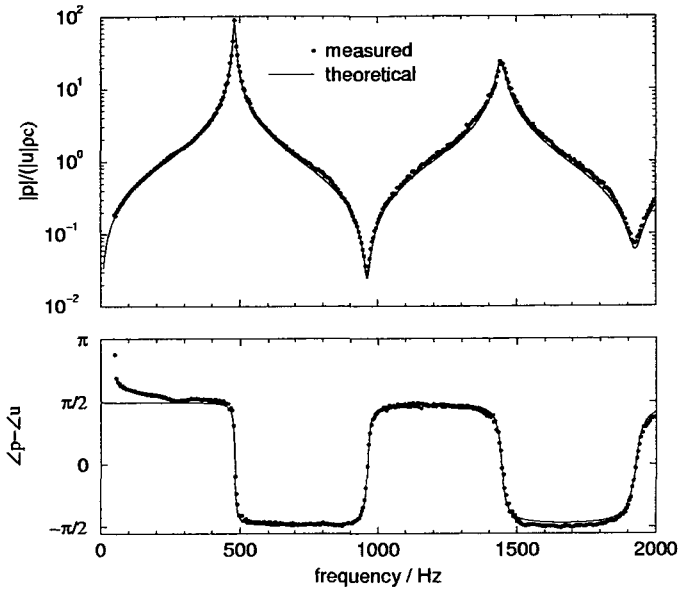

Figure 6.26: Specific acoustic impedance measured 17cm from the open end of a cylindrical tube.

A further solution is to superimpose a mean flow with a velocity greater than 40% of the acoustic particle velocity amplitude.

The second section was concerned with methods of demodulating the Doppler signal. Two methods were considered: analogue frequency tracking and digital demodulation using a Hilbert transform routine. The former method demonstrated greater SNR and dynamic range. The analogue frequency tracker was used to measure sinusoidal sound fields with an error of ± 0.3dB over a velocity range corresponding to SPLs in the range 105-140dB.

In the third section measurements were performed in a sound field containing three harmonic components. An ensemble averaging routine was used to smooth the velocity signal from the tracker before the amplitude and phase of each frequency component was extracted. The measured velocity amplitude of each frequency component compares favourably with the theoretical velocity; however only the 2nd and 3rd components demonstrate reasonable agreement between

measured and theoretical velocity phase.

In the fourth section specific acoustic impedance was measured using a combination of probe microphone and LDA. The magnitude of the impedance was accurately measured over the entire frequency range range but it appears that the phase can only be successfully measured at frequencies above 300Hz.

Chapter 7

Application of LDA to the Study of Brass Instruments

The measurements presented in section 6.4 demonstrate that LDA can be used in combination with a probe microphone to measure the specific acoustic impedance in a tube. The first section of this chapter will explain how this successful technique may be used to measure the impedance of the artificial mouth mechanism, as viewed from the instrument side.

The main aim of this chapter is to use LDA to measure the velocity in the mouthpiece of a brass instrument, excited by the artificial lip mechanism. Each of the measurements presented in chapter 6 was performed under conditions where the mean flow velocity was less than the acoustic particle velocity amplitude. In fact in most cases the mean flow velocity was negligible relative to the acoustic particle velocity amplitude. That is not the case in brass instruments sounded just above the threshold of oscillation, where the acoustic particle velocity amplitude is by definition very small, far smaller than the mean flow velocity.

Before attempting LDA measurements in artificially excited brass instruments, where a sound field coexists with a significant mean flow, LDA was first used to investigate air flows with mean volume velocities of a similar magnitude to those encountered in brass instruments under playing conditions; these mean

flow measurements are presented in the second section. Finally in the third section LDA measurements in the mouthpiece of an artificially blown trombone are presented.

7.1 Impedance of Artificial Mouth

7.1.1 Theoretical Effect of the Mouth Cavity

In the basic one-mass model of the lips developed in section 2.2 the input impedance of the mouth cavity was assumed to be zero, implying the alternating pressure, p_m, in the mouth was also zero. This assumption will soon be relaxed.

Elliot and Bowsher [34] considered the conditions, in the frequency domain, for self sustained oscillation. These conditions are often known as the Helmholtz regeneration conditions. They considered both the effect of a non zero mouth cavity input impedance and the effect of a secondary volume source. Their work will be reviewed here, but the complication of the secondary volume source will be neglected.

With a zero mouth cavity input impedance the linearized Bernoulli relation is given by equation 2.16. Substituting this equation into the linearized volume flow equation (2.17) yields

$$b\overline{U_L}\frac{h(\omega)}{p(\omega)} = \frac{b\overline{H}}{\rho\overline{U_L}} + \frac{v(\omega)}{p(\omega)}. \tag{7.1}$$

The ratio $h(\omega)/p(\omega)$ defines one possible measure of the mechanical response of the lips, $G(\omega)$, an alternative definition to that of mechanical response $C(\omega)$ used in chapter 3 (see equation 3.4). Also the ratio $v(\omega)/p(\omega)$ is simply the reciprocal of the input impedance of the instrument, $1/Z(\omega)$. Furthermore by setting all the alternating components in equations 2.4 and 2.5 to zero and combining the

two resulting equations it is easy to show that

$$\frac{b\overline{H}}{\rho\overline{U_L}} = \frac{1}{2\overline{R}} \tag{7.2}$$

where

$$\overline{R} = \frac{\overline{P_m}}{\overline{V}} \tag{7.3}$$

is the acoustic resistance of the lip channel averaged over an acoustic cycle. Substituting $G(\omega)$ for $h(\omega)/p(\omega)$, $1/Z(\omega)$ for $v(\omega)/p(\omega)$ and $1/2\overline{R}$ for $b\overline{H}/(\rho\overline{U_L})$ in equation 7.1 yields

$$b\overline{U_L}G(\omega) = \frac{1}{2\overline{R}} + \frac{1}{Z(\omega)}. \tag{7.4}$$

In the literature [1] [99], it is often said that self-sustained oscillation can theoretically occur only when (a) the phase of the left hand side of equation 7.4 is equal to the phase of the right hand side and (b) the magnitude of the left hand side is greater than or equal to the magnitude of the right hand side.

However, if the mouth cavity has non zero input impedance then the linearized Bernoulli equation becomes

$$p_m(\omega) = p(\omega) + \rho\overline{U_L}u_L(\omega), \tag{7.5}$$

the mechanical response becomes

$$G(\omega) = \frac{h(\omega)}{p(\omega) - p_m(\omega)} \tag{7.6}$$

and consequently the condition for self sustained oscillation becomes

$$b\overline{U_L}G(\omega) = \frac{1}{2\overline{R}} + \frac{v(\omega)}{p(\omega) - p_m(\omega)} \tag{7.7}$$

$$= \frac{1}{2\overline{R}} + \frac{1}{Z(\omega) + Z_{mc}(\omega)} \tag{7.8}$$

where

$$Z_{mc}(\omega) = -\frac{p_m(\omega)}{v(\omega)} \tag{7.9}$$

is the input acoustical impedance of the mouth cavity. The negative sign is required because under playing conditions the lips act as the source and a volume velocity is defined as positive if the direction of the velocity is from the lips towards the instrument; with this convention, in the instrument, air moving away from the source has positive velocity as usual but in the mouth cavity air moving from the source has negative velocity.

Elliot and Bowsher [34] showed that the effect of the mouth cavity can be included simply by adding the mouth cavity input impedance in series with the instrument input impedance. This result is reproduced in equation 7.8. Equation 7.8 also illustrates that if the instrument input impedance is much greater than the mouth cavity input impedance then the mouth cavity can have little effect.

Fletcher and Rossing [39] suggested the mouth cavity effect could provide one possible explanation for the ability of brass players to buzz their lips when the instrument and mouthpiece are removed. If the impedance of the mouth cavity is neglected and the instrument and mouthpiece are removed, so that $Z = 0$, then the right hand side of equation 7.8 becomes infinite implying that self-sustained oscillation of the lips is impossible. If the input impedance of the mouth cavity is not negligible then the right hand side of equation 7.8 remains finite, even if $Z = 0$, and there remains some possibility that self-sustained oscillation may occur. The importance of the mouth cavity effect has yet to be studied experimentally.

7.1.2 Experimental Method

The impedance of the artificial mouth could have been measured using a traditional multiple microphone impedance rig rather than the complicated LDA arrangement used in the present study. Indeed the multiple microphone rigs would introduce less noise than the present LDA system. However the geometry of the particular impedance rig used to produce the input impedance measurements of chapter 3 prevented its use in the measurement of the artificial mouth.

The apparatus used to measure the impedance of the artificial mouth is illustrated in figure 7.1. The end of one 10cm length of glass tubing was hermetically sealed into the front plate of the artificial mouth in a manner which ensured the artificial lips were in contact with the end of the tube. A realistic embouchure was then selected by blowing air into the mouth cavity and then adjusting the embouchure until a note was produced by self sustained oscillation of the artificial lips and air column. A second 10cm length of glass tubing was attached to a loudspeaker and the two tubes were joined together by a 10cm length of rubber tubing. The long probe microphone was inserted through a small hole punched in the rubber tubing. Both of the glass tubes had an internal diameter of 24mm and a wall thickness of 2mm.

In preliminary experiments the 10cm long glass tube connected to the artificial mouth was the only tube used and the loudspeaker was positioned in free space, 10cm from the open end of this tube. However with that method the SPL which could be produced in the tube was insufficient for impedance measurements.

In playing experiments air flow generated by a fan is usually blown into the artificial mouth via a 40l reservoir and a 2m length of flexible plastic tubing which connects the reservoir to the artificial mouth. In the impedance measurements the plastic tubing and reservoir were connected to the artificial mouth because they

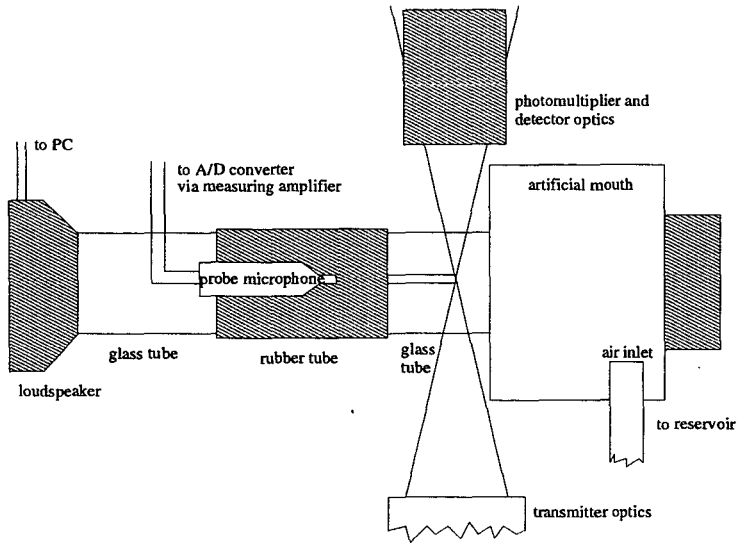

Figure 7.1: Plan view of apparatus for measuring acoustic impedance of artificial mouth.

may contribute inertance and compliance respectively to the input impedance of the artificial mouth.

As it would be very difficult to arrange the measuring volume to be positioned precisely in front of the lips, the measuring volume was positioned 3cm from the lip end of the tube, at the centre of the cross section of the tube and the receptive end of the probe microphone was positioned directly beneath the measuring volume.

Seeding was provided by removing the pipe at the air inlet and inserting a burning incense stick into the artificial mouth. This method of seeding was only partially successful as most of the smoke preferred to linger in the artificial mouth rather than disperse through the lips to enter the cavity formed by the loudspeaker and the glass and rubber tubing. In future experiments a tap could be incorporated into this cavity; the tap could be opened to encourage the seeding particles to enter the cavity.

The LDA apparatus, method of producing the sweep signals and method of

processing the instantaneous frequency signal, $F_{AT}(t)$, were arranged exactly as described in section 6.4. A 100kHz frequency shift was applied over frequency ranges where there was a significant impedance and therefore a small velocity amplitude, and a 500kHz frequency shift was applied over frequency ranges where there was smaller impedance and therefore a larger velocity amplitude. The 33-333kHz tracker input filter was used with the 100kHz shift and the 0.1-1MHz tracker input filter was used with the 500kHz shift.

The measurement of the impedance of the mouth cavity is of particular interest in the study of brass instrument acoustics since the material presented in section 7.1.1 suggests the mouth cavity could influence the sound produced. However it should be noted that the experiment described above does not strictly measure the acoustic impedance of the mouth cavity but instead measures the impedance of a 3cm length of cylindrical tubing terminated by the input impedance of the artificial mouth, which in turn is the *series* combination of the acoustic impedance of the lips Z_{lip} and the acoustic impedance of the mouth cavity Z_{mc}. The term mouth cavity and symbol Z_{mc} will be taken to mean the impedance of the entire system of mouth cavity, reservoir/lungs and pipe to reservoir/larynx. Elliot and Bowsher [34] pointed out that when there is negligible mean flow (as is the case in impedance measurements) the acoustic impedance of the lips is complex valued and very different to the purely resistive acoustic impedance (see equation 7.2) encountered when there is rapid mean flow (as is the case with self sustained oscillation). Since volume velocity is assumed to be conserved in the transition from mouth cavity to lips the impedance of the mouth cavity and lips should be considered to be connected in series. By making use of equation 6.34 it is straightforward to show that the actual impedance measured in the above experiment

is

$$Z_s = \frac{Z_{mc} + Z_{lip} + j\rho c \tan kx}{1 + j\frac{Z_{mc}+Z_{lip}}{\rho c} \tan kx} \tag{7.10}$$

where x =3cm. However in the limit $kx \rightarrow 0$

$$Z_s \approx Z_{mc} + Z_{lip} \tag{7.11}$$

which, with $x = 3cm$, may be considered a valid approximation at frequencies below 2kHz.

7.1.3 Results and Discussion

The impedance measurements of the artificial mouth are presented in figure 7.2. The measurements have a much higher noise content to those presented in figure 6.26 because of the difficulty of trying to introduce sufficient seeding in this case. Notice also that in figure 7.2 the original specific acoustic impedance measurements have been scaled by the cross-sectional area of the tube to provide acoustic impedance in acoustic ohms (or $kgm^{-4}s^{-1}$). The internal diameter of the glass tube (24mm) is very similar to the internal diameter of the mouthpiece rim (28mm) and therefore figure 7.2 can be compared with the conventional input impedance curves such as figure 3.1.

Elliot and Bowsher [34] suggested that if there is no significant mean flow the lips may be modeled as a thin slit. They used an expression for the impedance of a thin slit developed by Crandall [21]:

$$Z_{lip} = \frac{12\mu d}{bH^2} + j\omega\frac{5\rho d}{6bH} \tag{7.12}$$

where μ is the shear viscosity of air, d is the thickness of the lips (along the axis of flow), b is the width of the lip aperture, H is the height of the lip aperture, ω is the angular acoustic frequency and ρ is the density of air. Since the real part is

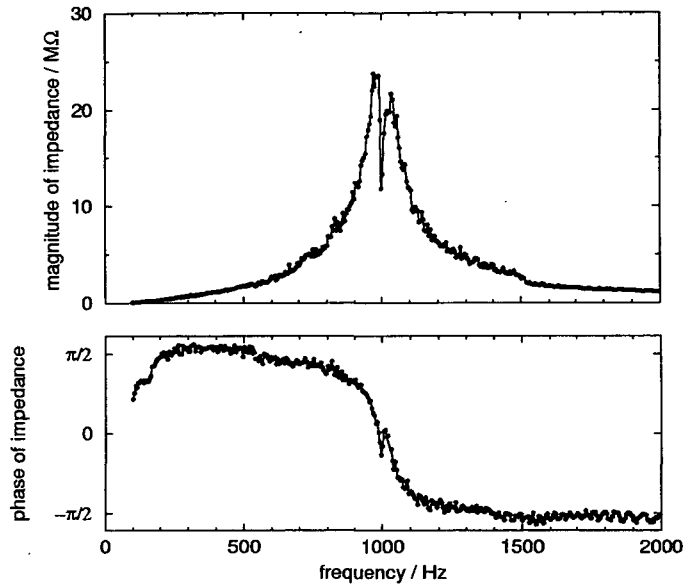

Figure 7.2: Measured acoustic impedance of a 3cm length of cylindrical tubing terminated by the artificial mouth.

a constant and the imaginary part increases with frequency the magnitude of the lip impedance is expected to increase with frequency. With the lip parameters used in Chapter 3, $Z_{lip} < 1\text{M}\Omega$ at 2kHz, and therefore over the entire measured frequency range. Figure 7.2 shows that $Z_s \gg 1$ MΩ at frequencies below 1.5kHz. Therefore since $Z_s \approx Z_{mc} + Z_{lip}$ (equation 7.11), figure 7.2 must represent Z_{mc}, at least at frequencies below 1.5kHz.

The measurements presented in figure 7.2 display a very strong resonance behaviour with a double resonance at around 1kHz indicated by the dual peaks in the magnitude curve and the triple zero crossing in the phase curve. The measurements were repeated in case the observation of a double peak was due to an error in the measurement; however the repeated measurements were almost identical to the initial measurements and confirmed the double resonance behaviour. In contrast to human mouths, the artificial mouth has rigid internal walls. The frequency of the resonance peaks suggest that the acoustical resonances result from

standing waves in the mouth cavity; the dual peaks are indicative of reflections from different rigid surfaces within the mouth cavity.

Comparison of the magnitude curve of figure 7.2 with figure 3.1 indicates that the maximum magnitude of mouth cavity impedance is of a similar magnitude to the maxima of the instrument impedance, suggesting that the mouth cavity effect could be significant, at least at frequencies near the dual peaks of the mouth cavity. However the experimental measurements presented in section 3.3.3 provide no evidence of a significant mouth cavity effect. Presumably that it is because the acoustic modes of the mouth cavity have much higher frequencies (around 1000Hz) than the mechanical modes of the lips (below 500Hz), and therefore significant aerodynamic coupling between the acoustical modes of the mouth cavity and the mechanical modes of the lips is unlikely. That is why the artificial lips were unable to 'buzz' when the mouthpiece cup was removed to leave only the rim. Decreasing the volume of the mouth cavity (as in section 3.3.3) increases the frequency of the acoustical modes of the mouth cavity, further decreasing the likelihood of them coupling with mechanical modes. Although figure 3.18 does provide some evidence of a destabilising effect it is thought that this is due to aerodynamic coupling between two mechanical modes of the lips rather than between a mechanical mode and an acoustical mode of the mouth cavity.

With the entire mouthpiece in place it was found that the lips were able to 'buzz' the mouthpiece. The artificial lips can buzz with the mouthpiece but not with the mouth cavity alone because the resonance peak of the mouthpiece occurs around 500Hz, and therefore, unlike the mouth cavity, has an acoustical mode with a frequency only slightly greater than the mechanical modes of the lips, making aerodynamic coupling more likely.

The dimensions of the artificial mouth are greater than the mouth cavity of

a human player and it is therefore dangerous to use this experiment to draw too many conclusions about the mouth cavity effect in human players. However the LDA/probe microphone method of impedance measurements could easily be applied to a human mouth in the future. Alternatively the artificial mouth could be adapted to provide means of varying the volume of the mouth cavity, and input impedance measurements could be carried out for a range of different mouth cavity volumes. It would also be interesting to study the effect of lining the mouth cavity with a porous martial.

Although the experimental measurements suggest the mouth cavity is not crucial for the destabilisation of the lips, it could still have a significant effect in other aspects of brass instrument acoustics. One famous example is the didjeridu, in which a significant variation in timbre is observed as the player performs circular breathing. The didjeridu is a primitive instrument relative to a modern orchestral brass instrument and has relatively weak acoustical resonances. The strength of any mouth cavity resonance relative to the instrument resonances is therefore expected to be greatest in the didjeridu. Variations in mouth cavity resonance behaviour resulting from variations in mouth cavity volume over the breathing cycle should therefore be accentuated in the didjeridu. Of course over the circular breathing cycle didjeridu players may well vary not only their mouth cavity but also their embouchure, consequently affecting the mechanical response and/or average lip resistance (averaged over an acoustic cycle). It could be this variation in embouchure which is principally responsible for the timbre variation and would be most noticeable in the didjeridu due to its weak resonance characteristic. When considering the mouth cavity effect with the didjeridu one should retain the perspective that all didjeridu players use circular breathing and probably consciously or subconsciously aim to maximise the timbre variation since it is

the only feature of the instrument, whereas only the most skilled orchestral brass players employ circular breathing and they aim to minimise any timbre variation.

7.2 Preliminary Steady Flow Measurements in a Pipe

In this section LDA measurements of the mean air flow in a pipe are presented. Such measurements are certainly not original but they serve as a useful preparation for LDA measurements in brass instruments excited by the artificial mouth. The results will be carefully discussed in order to understand problems which may occur in the measurement of brass instruments. This section aims to understand the relative importance of ambiguity broadening, shot noise and turbulence. A further aim is to check whether the LDA measured mean value of the air flow velocity is consistent with the volume flow rate measured using a simple flow meter with a rotary float.

7.2.1 Laminar Pipe Flow Theory

When fluid flows through a cylindrical pipe the speed at which the fluid moves in the axial direction is a function of the radial distance from the axis of the pipe. The fluid which moves along the axis has the greatest velocity, U_{max}, whilst the fluid immediately next to the walls remains at rest due to the no-slip condition. If the velocity profile of the pipe is parabolic then the flow is known as Poiseuille flow. It is easy to show [90] that in this case

$$U_{max} = \frac{2V}{S} \tag{7.13}$$

where V is the volume velocity of the fluid and S is the cross-sectional area of the pipe. When flow first enters the pipe its velocity profile is unlikely to be parabolic, but over an entry length, X, the flow develops and tends towards the parabolic

profile. The entry length, X, is the distance downstream from the entry point at which U_{max} is within 5% of its Poiseuille value [90] as defined in equation 7.13. A pipe with diameter d has entry length

$$X = \frac{Re}{30} d \tag{7.14}$$

where the Reynolds number of the pipe flow is defined to be

$$Re = \frac{\rho U_{av} d}{\mu}, \tag{7.15}$$

U_{av} is the velocity U averaged over the cross-sectional area, ρ is the density of the fluid and μ is the shear viscosity of the fluid. The critical condition

$$V = \frac{30\pi\mu X}{4\rho} \tag{7.16}$$

can be derived by substituting equation 7.15 into 7.14, rearranging and making the additional substitution $V = U_{av}\pi(d/2)^2$. Provided the volume velocity is less than the critical value indicated by equation 7.16, at a downstream distance from the entry point of X or greater, a Poiseuille velocity profile should be observed.

Poiseuille flow is one extreme case. The opposite extreme case is that in which the fluid has a uniform velocity over substantially the entire cross-section, in which case $U_{max} = V/S$. Such a uniform flow velocity profile can only exist when the fluid has just entered the pipe because the profile will immediately start to develop towards a parabolic profile as the fluid progresses down the pipe.

In conclusion, the velocity on the axis of the pipe, U_{max}, is constrained to lie between V/S and $2V/S$. Furthermore, if the velocity is measured at least a distance X from the entry point then the velocity will be within 5% of $2V/S$. The greater the volume velocity the greater the Reynolds number and the longer the entry length.

7.2.2 Experimental Method

The apparatus used in the flow measurements is illustrated in figure 7.3 and comprises a pump connected to a glass tube or pipe via a 40l reservoir. A burning incense stick was positioned inside the reservoir to seed the flow. The reservoir not only provided a means of seeding the flow but also reduced any fluctuations in the air supply to the glass pipe. Plastic tubing with an internal diameter of 10mm was initially used to connect the reservoir to the glass tube but for the later experiments this feed pipe was replaced with rubber tubing with an internal diameter of 1 inch (25.4mm). The volume flow rate was measured using a CT Platon A10HD CA232001 flow meter and controlled using a valve. The glass pipe had an internal diameter of 24mm, wall thickness 2mm and length 545mm. The measuring volume was positioned on the axis of the glass pipe, 450mm downstream from the entry point.

The LDA apparatus was arranged as described in section 5.2 and illustrated in figure 5.1 except bandpass filter 2 was removed to enable random fluctuations in the tracker output signal to be measured. The tracker's output filter was disabled, the input filter was set to 0.1-1MHz and a frequency shift of either 200kHz or 300kHz was applied. The tracker output signal was sampled at 100kHz and 8192 point samples of each signal were produced. The tracker output signals were scaled to produce instantaneous frequency signals, $F_{AT}(t)$. Recall that, after the frequency shift F_s has been removed, the instantaneous frequency is proportional to the instantaneous velocity. If the Doppler signal was required rather than the instantaneous frequency signal, bandpass filter 1 (see figure 5.1) was set to 0.31-3.1MHz, a 100kHz frequency shift was applied and the Doppler signal was sampled at 0.5MHz; in this case a 32768 point sample of the Doppler signal was recorded.

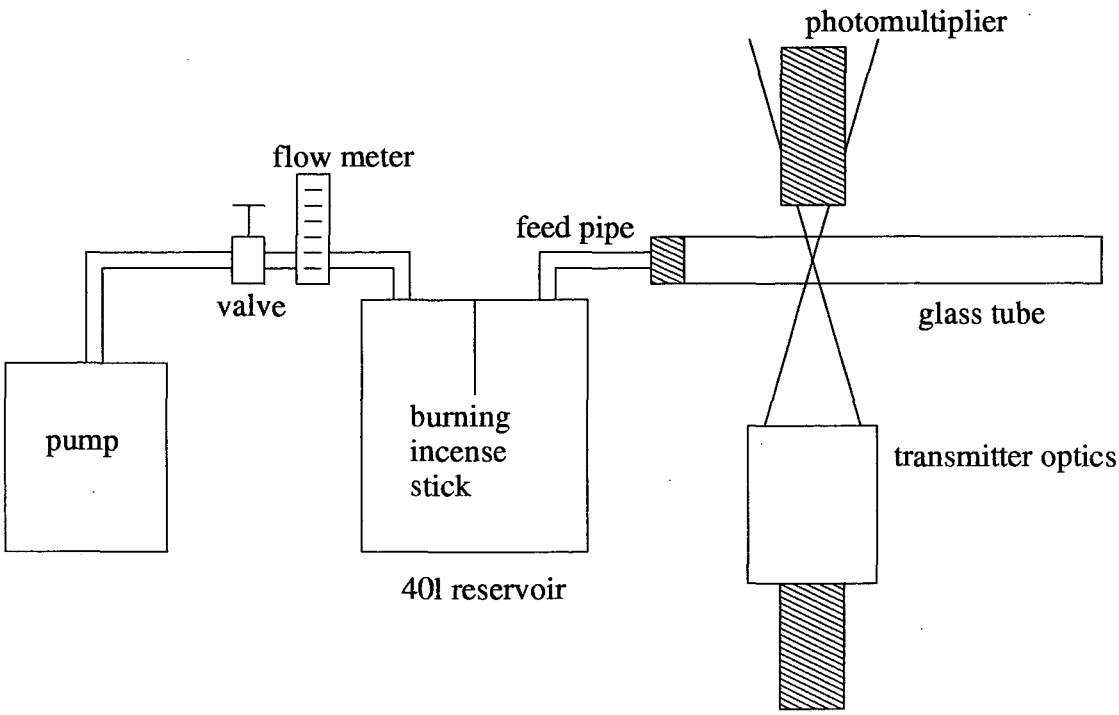

Figure 7.3: Experimental apparatus for the measurement of steady flow in a pipe.

7.2.3 Results and Discussion

The instantaneous frequency curves of three different Doppler signals are presented in figure 7.4. In a perfectly steady laminar flow with velocity U measured by a hypothetical ideal LDA system which introduces no noise, each instantaneous frequency curve would be a straight line with frequency $F_s + U/\Lambda$ (see equation 4.11). However each of the signals displayed in figure 7.4 clearly contains a significant noise content.

A volume velocity of 3.5l/min would not be sufficient to drive the artificial lips into self-sustained oscillation. Figure 7.4 illustrates that a flow with such a modest volume velocity produces a much higher noise content than the $V = 0$ signal. When the volume velocity is further increased to 30l/min, a level sufficient to drive the artificial lips into self-sustained oscillation, the high frequency noise content of the signal is not observed to increase. This can be explained as follows: with no volume flow at all seeding was provided by a burning incense stick inserted directly into the glass tube, allowing the seeding density to build up to a reasonable level and thus resulting in Doppler signals and consequently instantaneous frequency signals with a low noise content; however as soon as any non-zero flow was introduced the accumulated seeding particles were blown out of the glass tube, the seeding density within the tube was reduced to that within the reservoir and the noise content of the signals therefore increased.

In figure 7.4 there appears to be no increase in the high frequency noise content as the volume flow rate is increased from 3.5l/min to 30l/min, which suggests that the shot noise is more significant than ambiguity broadening. The V =30l/min signal does however contain random low frequency fluctuations, possibly signaling the onset of turbulence. The Reynolds number of the 10mm diameter feed pipe is 4×10^3 and therefore lies within the Reynolds number range (2×10^3 to 10^5)

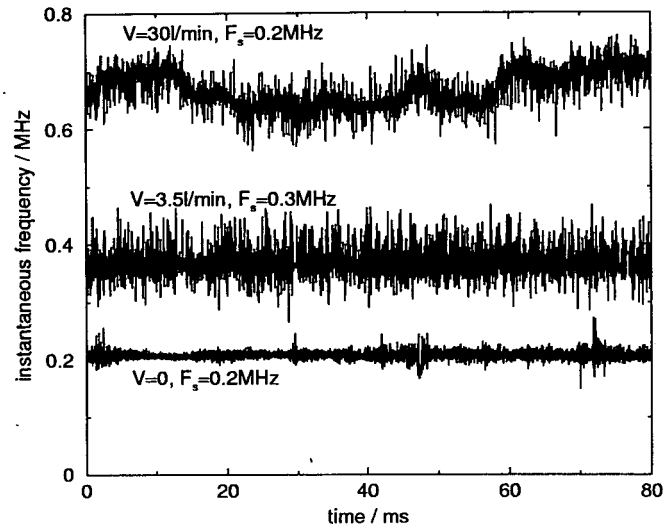

Figure 7.4: Instantaneous frequency of Doppler signal (including frequency shift F_s) with three different volume flow rates.

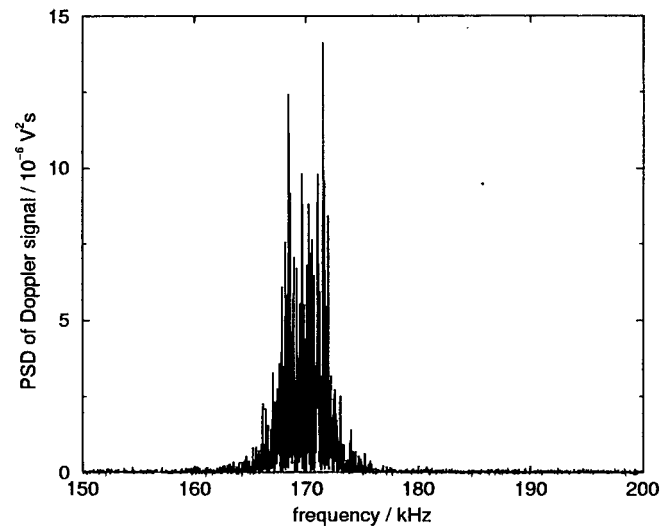

Figure 7.5: PSD of the Doppler signal resulting from a measurement in a 3.5l/min laminar flow. A 100kHz frequency shift was applied.

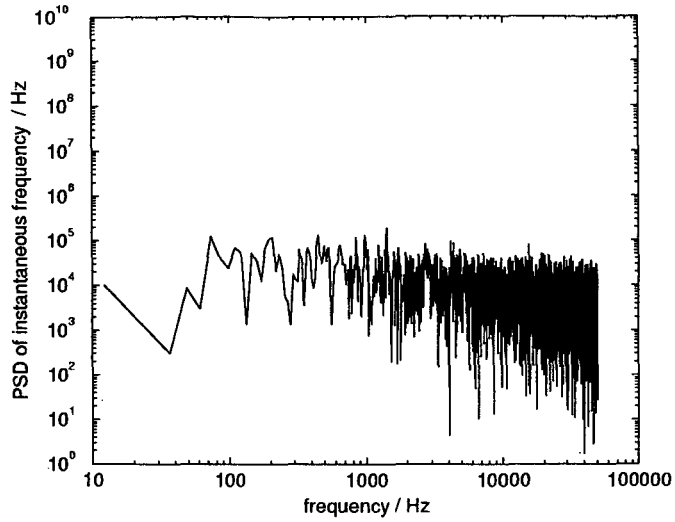

Figure 7.6: Log-log plot of the PSD of an instantaneous frequency signal recorded in a 3.5l/min flow. The feed pipe from reservoir to glass measuring tube had internal diameter 10mm.

associated with the transition to turbulent conditions [90]. Furthermore, the rapid expansion in the diameter of the fluid channel (from 10mm in the feed pipe to 24mm in the glass tube) actually encourages the growth of turbulence.

Figure 7.5 displays the PSD of the Doppler signal resulting from a measurement in a 3.5l/min laminar flow. This figure should be compared with the theoretical equivalent, the section of figure 4.11 enclosed in dashed lines. Broadening of the peak is apparent in figure 7.5. The standard deviation of the spectral peak of figure 7.5 is estimated to be 1700Hz, approximately six times the theoretical ambiguity broadening estimated using equation 4.45. The measured broadening could be greater than predicted by equation 4.45 if the laser beams were not precisely focused (see section 4.5.4).

In figures 7.6, 7.7 and 7.8 the PSD of **instantaneous frequency signals** have been plotted on a log-log scale to facilitate the study of the low frequency components. With a 10mm diameter feed pipe, the low frequency components of

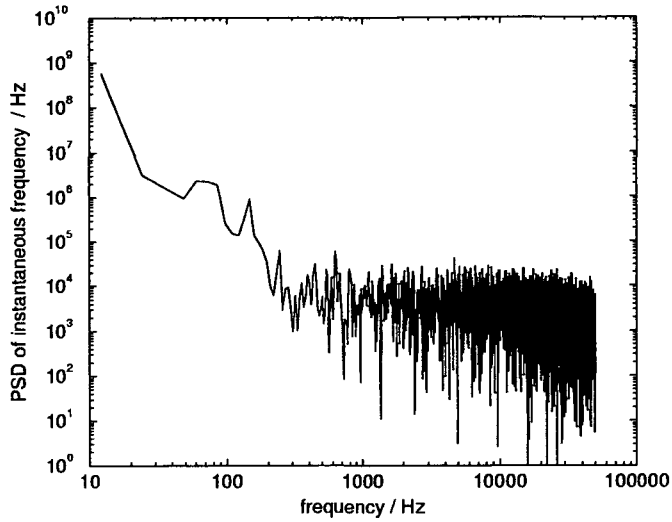

Figure 7.7: Log-log plot of the PSD of an instantaneous frequency signal recorded in a 30l/min flow. The feed pipe from reservoir to glass measuring tube had internal diameter 10mm.

the PSD resulting from a 30l/min flow (figure 7.7) are much stronger than the low frequency components of the PSD resulting from a 3.5l/min flow (figure 7.6), which merely confirms the earlier time domain observation (see figure 7.4). When the feed pipe was replaced with a larger 1 inch (25.4mm) diameter pipe the low frequency components of the PSD resulting from a 30l/min flow were found to decrease. Increasing the diameter of the feed pipe removes the rapid expansion in flow channel diameter resulting in a decrease in the turbulent intensity.

Figure 7.9 is a plot of the LDA measured velocity on the axis of the tube (the axial velocity) versus the volume velocity indicated by the the rotary float meter. All measurements were performed 450mm from the entry end of the glass tube using the 1 inch (25.4mm) diameter feed pipe. As predicted in section 7.2.1, nearly all of the velocity measurements lie within the range V/S to $2V/S$ and the velocity tends to develop from $2V/S$ towards V/S as the volume velocity, V, is increased. Furthermore figure 7.9 indicates that the flow measured 450mm from the entry

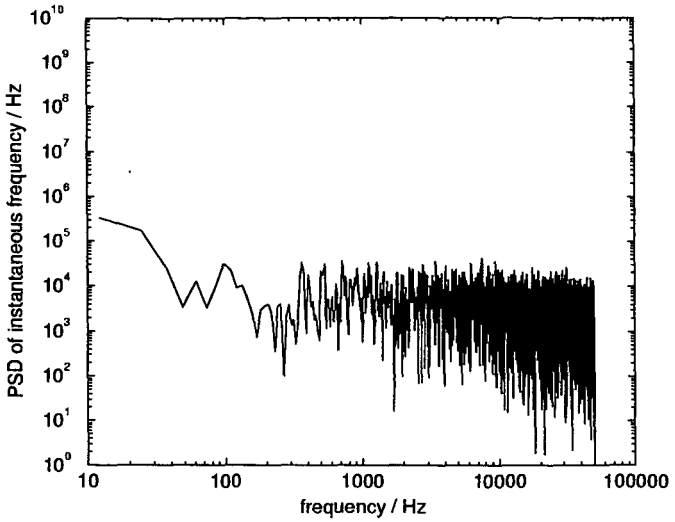

Figure 7.8: Log-log plot of the PSD of an instantaneous frequency signal recorded in a 30l/min flow. The feed pipe from reservoir to glass measuring tube had internal diameter 1 inch (25.4mm).

end of the glass tube loses its Poiseuille nature when V exceeds 10l/min, which compares favourably with the theoretical value of 9.5l/min obtained by setting $X = 450$mm in equation 7.16. However it is possible that a larger estimate of the entry length, X, should have been used to allow for the possibility that at least a portion of the flexible feed pipe may act to extend the glass tube, in which case it would be reasonable to expect Poiseuille flow to remain at slightly higher volume velocities than 10l/min. Figure 7.9 does demonstrate that the LDA system can be used to measure rapid air flows with velocities as high as 1.7ms^{-1} at least.

The measurements of apparent RMS velocity presented in figure 7.10 were extracted from the same instantaneous frequency signals which were used to produce figure 7.9. Due to shot noise and ambiguity broadening this apparent RMS velocity is expected to be much greater than the actual RMS velocity.

When the axial velocity is increased from a zero value there is a sudden increase in the RMS velocity due to the associated change in seeding conditions.

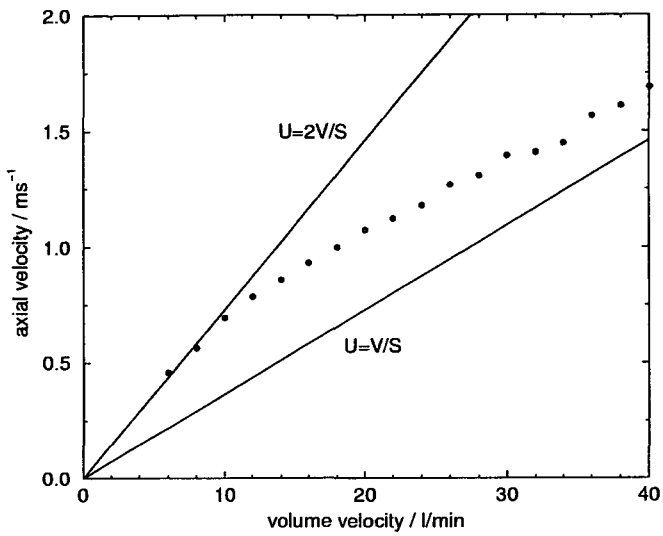

Figure 7.9: Measured velocity versus volume velocity. The solid lines indicate the theoretical velocity versus volume velocity relationship for Poiseuille flow and for uniform flow.

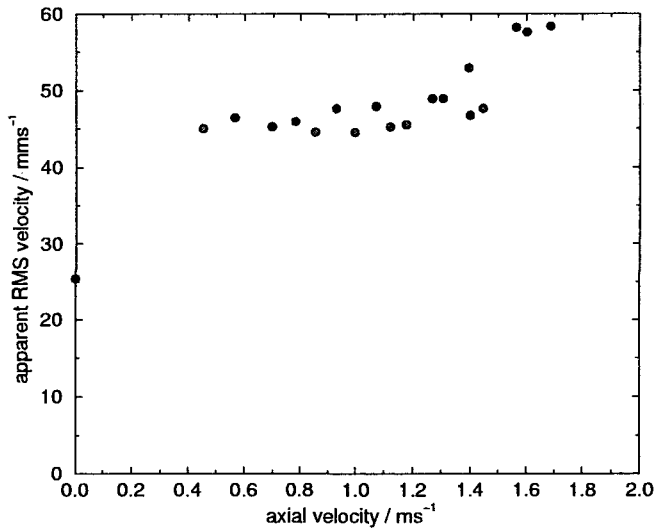

Figure 7.10: Measured apparent RMS velocity deduced from the same instantaneous frequency signals as were used to extract the mean velocities plotted in figure 7.9. For comparison, the RMS velocity deduced from a zero velocity measurement is also included.

With axial velocities between 0.4 and 1.3ms^{-1} the major contribution to the apparent RMS velocity is shot noise and there is therefore no significant variation in the RMS value. However when the axial velocity is further increased it appears that the transition to turbulence begins and there is an increase in the apparent RMS velocity.

7.3 Measurements in Transparent Trombone Mouthpiece

This section presents LDA measurements performed in a specially designed transparent trombone mouthpiece coupled to the artificial mouth. The experimental apparatus, including the transparent mouthpiece, will first be described. The measurements presented in subsection 7.3.2 are limited to the situation where the mouth pressure is below the threshold value, so that self-sustained oscillation does not occur. This initial investigation is an extension of the work presented in section 7.2 but although the range of volume velocities used in section 7.3.2 are similar to those employed in section 7.2 the small dimensions of the trombone mouthpiece and lip aperture result in greater mean velocities and turbulent intensities, respectively. Subsection 7.3.3 presents LDA measurements performed while the lips and air column are in a state of self-sustained oscillation.

7.3.1 Experimental Apparatus

Transparent Mouthpiece

During initial LDA trials in cylindrical glass tubes with small diameter it was found that a significant proportion of the laser light incident on the curved outer wall of the glass tube was reflected and failed to enter the cylinder. Any transparent mouthpiece based on a conventional design would also suffer from this problem. It was therefore decided to design a completely new trombone mouth-

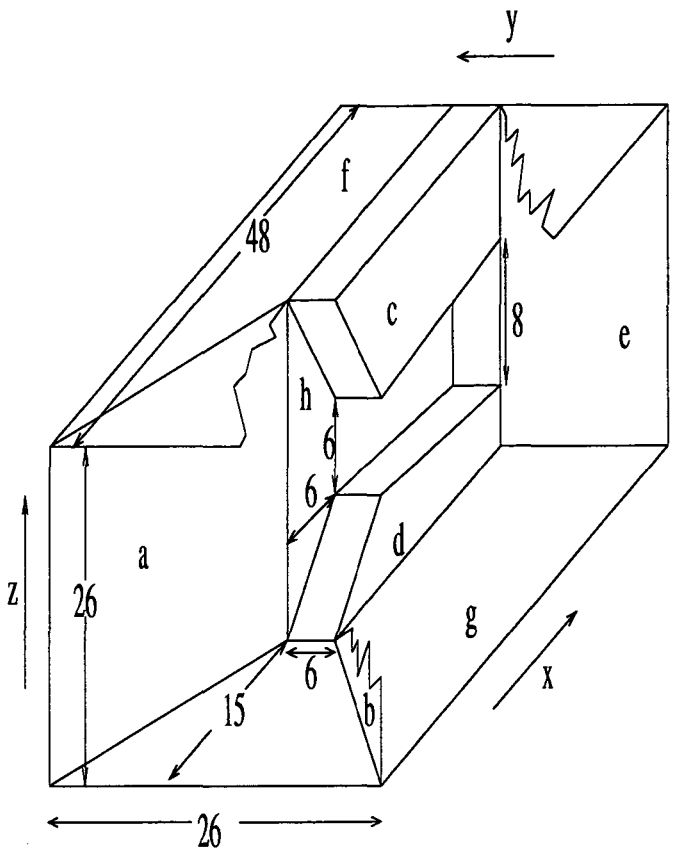

Figure 7.11: Design of the transparent portion of the transparent trombone mouthpiece. The numbers indicate dimensions in mm whereas the letters label the various parts of the mouthpiece and are referenced in the main text.

piece consisting almost entirely of planar surfaces. Figure 7.11 is an illustration of this design; the mouthpiece rim and a portion of the backbore are not shown in this figure.

The transparent mouthpiece comprises left and right perspex walls (a,b), two identical vertically spaced perspex wedges (c,d), rear perspex wall (e), two mutually parallel horizontal glass walls (f,g) and two mutually parallel vertical glass walls (h,i). The letters in brackets refer to elements of figure 7.11. In this figure sections of the upper horizontal glass wall (f) and right perspex wall (b) have been cut away and the right vertical glass wall (i) has been omitted entirely. The

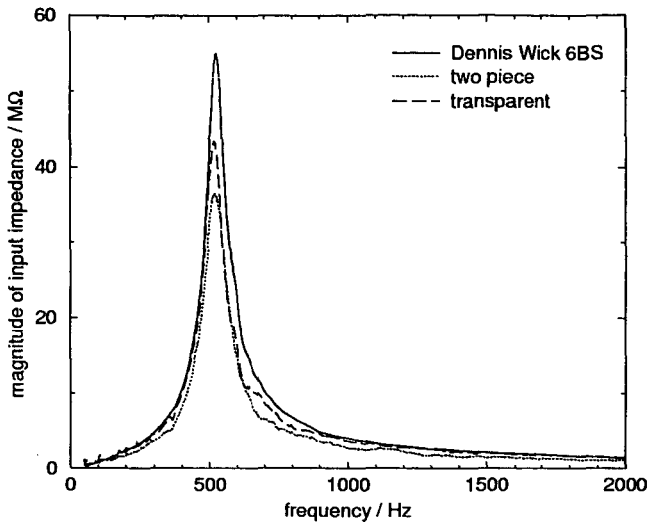

Figure 7.12: Input impedance of three mouthpieces: a Dennis Wick 6BS, the transparent mouthpiece of figure 7.11 and the two-piece mouthpiece used in chapter 3.

glass walls (f,g,h,i) were made from 1mm thick microscope slides and the perspex walls (a,b,e) were cut from 3mm thick perspex sheets. The area between the lowermost edge of the upper perspex wedge (c) and the uppermost edge of the lower perspex wedge (d) may be considered to be the throat of the mouthpiece. The volume downstream of the throat bounded by the two perspex wedges (c,d), the two vertical glass walls (h,i) and the rear wall (e) defines a portion of the backbore of the mouthpiece. A first trapezoid upstream of the throat is also bounded by the two perspex wedges (c,d) and the two vertical glass walls (h,i). A second trapezoid is defined by left and right perspex walls (a,b) and horizontal glass walls (f,g). The first and second trapezoids together form the majority of the mouthpiece cup.

The mouthpiece further comprises a square frame rim (not shown) with external dimension 36mm×36mm, internal dimension 26mm×26mm and thickness 3mm. The rim was glued onto the front of the section of the mouthpiece drawn

in figure 7.11 so as to complete the mouthpiece cup and provide a comfortable surface for human or artificial lips. The mouthpiece additionally comprises a backbore member in the form of a brass truncated cone with axial length 28mm, internal upstream diameter 9mm and internal downstream diameter 11mm. The backbore member was glued in place through a circular hole in the centre of the rear perspex wall (e). The backbore member is the only part of the mouthpiece with circular symmetry; it enables the mouthpiece to be fitted to a standard trombone.

The dimensions of the mouthpiece are indicated in the above paragraph and in figure 7.11. The mouthpiece was designed with the aim that it should have internal cross sectional areas at the rim, throat and instrument end of the backbore identical to the respective cross sectional areas in the common Dennis Wick 6BS trombone mouthpiece. The axial lengths and volumes of both the cup and the backbore sections were also constrained to be equal to those of the 6BS mouthpiece. As expected, the input impedance of the transparent mouthpiece is very similar to that of the Dennis Wick 6BS (see figure 7.12). In fact the transparent mouthpiece is more successful in its emulation of the Dennis Wick impedance curve than the two piece mouthpiece used in chapter 3, even although a design requirement of the two piece mouthpiece was that internally it should be as close as possible to the Dennis Wick mouthpiece. Human players found the transparent mouthpiece satisfactory but did express a preference for traditional circular rimmed mouthpieces.

The transparent mouthpiece couples to the artificial mouth using a specially designed artificial mouth front plate with a square aperture in the centre to receive the transparent mouthpiece. The rim of the mouthpiece is contained within the mouth cavity and the lips are arranged to press against the rim. Much

of the second trapezoid (defined by walls a,b,f,g) lies within the thickness of the artificial mouth front plate, thus restricting LDA access. The mouthpiece design was originally intended to permit some LDA access to the second trapezoid, provided the mouthpiece was orientated within the front plate with glass wall (f) normal to the laser beams. However the LDA measuring volume could only be positioned within the second trapezoid if the acute angle between the LDA beams was reduced or if the transmitter and receiver optics were angled so that both made an angle of less than 90^o with the x axis of figure 7.11. However with such optical arrangements the performance of the LDA system proved unsatisfactory. LDA access was therefore effectively restricted to the volume in between the perspex wedges (c,d), with the mouthpiece orientated in a manner which ensured the laser beams were normal to the vertical glass walls (h,i).

Entire Apparatus

The experimental arrangement is illustrated in figure 7.13. The set up is very similar to that used in section 7.2 and illustrated in figure 7.3 but in this section the artificial mouth and transparent mouthpiece replace the glass tube. One pipe of the inner slide section of a trombone was coupled to the mouthpiece to form the acoustical resonator.

The LDA measuring volume was always positioned on the axis of the mouthpiece. The artificial mouth, mouthpiece and inner trombone slide were arranged on a translatable table to permit measurement along the entire length of the vertical glass walls (h,i) of the mouthpiece. In fact the measurements presented here were limited to three discrete points, x_1, x_2 and x_3, where x_2 is precisely at the throat, x_3 is 20mm downstream from the throat (in the backbore) and x_1 is 3mm upstream from the throat (in the first trapezoidal section of the mouthpiece cup). The cross-sectional area at x_1 is 96mm^2, the cross-sectional area at x_2 is 36mm^2

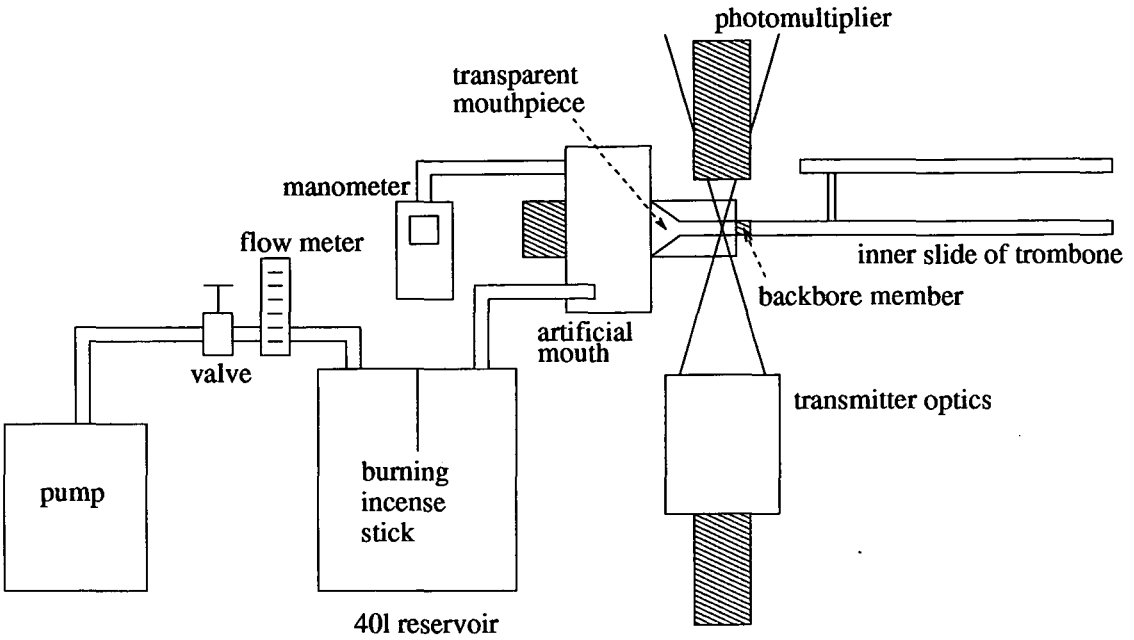

Figure 7.13: Plan view of experimental apparatus for the measurement of velocity within a transparent trombone mouthpiece using LDA.

and the cross-sectional area at x_3 is 45mm^2. Holes were made in the mouthpiece upper horizontal glass plate (f) and the mouthpiece upper perspex wedge (c) at positions x_2 and x_3 to accommodate the short probe microphone. The probe microphone and LDA system were used to simultaneously measure pressure and velocity at the same point within the mouthpiece.

The velocities encountered in the mouthpiece are very turbulent and result in Doppler signals with very large bandwidths, excluding the possibility of Doppler signal capture due to the limited sample rate (1MHz) of the A/D converter. However the narrower bandwidth instantaneous frequency signal from the tracker was recorded on the PC as usual. Unless otherwise stated the output filter of the tracker was disabled and bandpass filter 2 was removed.

During the self-sustained oscillation measurements the input filter of the tracker was set to its maximum range (1-10MHz) and a 100kHz frequency shift

was applied. In fact the frequency shift was applied in this case only because the LDA system is incapable of providing a zero frequency shift. During the sub-threshold measurements both the 0.33-3MHz and 1-10MHz tracker input filters were used and for each measurement the frequency shift setting was selected to ensure the mean frequency of the Doppler signal was as close as possible to the centre frequency of the tracker input filter.

7.3.2 Sub-threshold of Oscillation

The measuring volume was first positioned in the mouthpiece cup at x_1. The mean velocity through the mouthpiece was set to 3 l/min and the resulting instantaneous frequency signal from the tracker was recorded on the PC. The mean and RMS values of the signal were then extracted and scaled to yield respectively the mean velocity at x_1 and the apparent RMS velocity at this point, as indicated in figure 7.14. The measurements were repeated with higher volume velocities of 6 and 9l/min. At position x_1 it was impossible to carry out LDA measurements with volume velocities greater than 9l/min because the resulting Doppler signals had prohibitively large bandwidths.

The measuring volume was relocated to position x_3 and again mean and apparent RMS velocity were measured as a function of volume velocity. The bandwidth of the Doppler signal is generally narrower at x_3 than at x_1 and so at position x_3 it was possible to extend the measurements to include greater volume velocities. When the volume velocity was increased beyond 15l/min self-sustained oscillation was induced. The x_1 and x_3 measurements are compared in figure 7.14.

In figure 7.14 the apparent RMS velocity is observed to increase as the volume velocity increases; this behaviour in the mouthpiece should be contrasted with that observed in the glass tube (see figure 7.10), where the apparent RMS velocity remains reasonably constant at least at non-zero volume velocities less than or

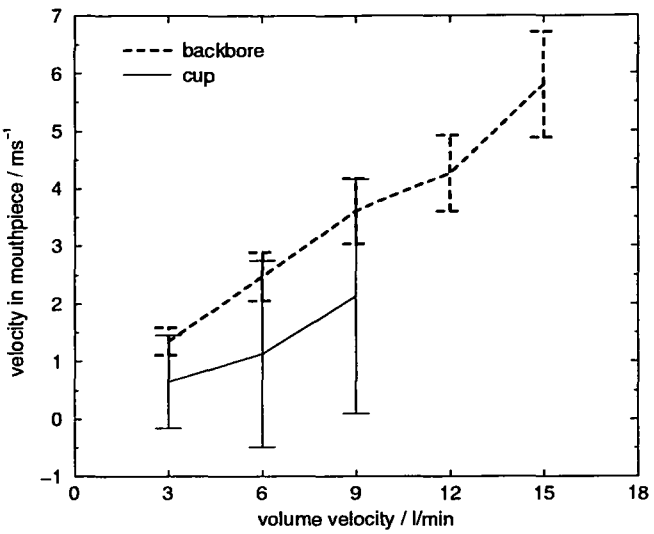

Figure 7.14: Measured velocity at positions x_1 (cup) and x_3 (backbore) of the transparent mouthpiece. The error bars indicate the apparent RMS velocity. The mouth pressure was kept below the threshold of oscillation.

equal to 15l/min. Furthermore the apparent RMS velocities measured in the mouthpiece are much greater than the apparent RMS velocities measured in the glass tube. In fact the average value of the apparent RMS velocity in the glass tube is less than 10% of the minimum apparent RMS velocity measured in the mouthpiece. In section 7.2 it was noted that the apparent RMS velocity in the glass tube of less than 50mms^{-1} was probably due mainly to shot noise. Since both the glass tube and the mouthpiece experiments employ identical seeding methods and similar ranges of volume velocity it is reasonable to assume that shot noise also contributes less than 50mms^{-1} to the apparent RMS velocity measured in the mouthpiece, which leaves more than 90% of the RMS velocity unaccounted for. The RMS velocity deficit cannot be explained by ambiguity broadening: it has already been shown in section 7.2 that ambiguity broadening makes a negligible noise contribution relative to the shot noise.

It must be concluded that the apparent RMS velocity measured in the mouth-

piece is mainly due to turbulence and therefore the apparent RMS velocity provides a reasonable approximation to the turbulent intensity, overestimating the turbulent intensity by less than 10% due to the shot noise contribution to the apparent RMS velocity. It is not surprising that turbulence is so dominant in the mouthpiece measurements because immediately before entering the mouthpiece the air must pass through the lip aperture which has a cross-sectional area estimated (using the 'medium' values of $\overline{H_0}$ and b of table 3.1) to be typically only 3% of the cross-sectional area of the 1 inch (25.4mm) diameter feed pipe used to supply air to the glass tube, and a jet will be formed at the exit of the lips.

Other interesting observations can be made from figure 7.14. Firstly, the mean velocity is consistently higher in the backbore than in the cup, which is to be expected since the cross-sectional area of the backbore is approximately half that of the cup. Secondly, the turbulent intensity measured in the cup is consistently higher than the turbulent intensity in the backbore. In measurements under conditions of self-sustained oscillation there is a danger that any acoustical information in the velocity signal will be masked by the turbulence, but it appears that this effect could be minimised by performing measurements at the downstream end of the backbore rather than in the cup.

7.3.3 Self-sustained Oscillation

Experimental Method

The apparatus was arranged as illustrated in figure 7.13. The probe microphone was inserted into the rear backbore hole x_3 and the measuring volume was aligned immediately below the probe. The valve was gradually opened, increasing the mean volume velocity and static mouth pressure, until the lips and air column entered into a state of self-sustained oscillation. At this point the instantaneous frequency and probe microphone signals were captured using the A/D converter.

This process was repeated several times, both with bandpass filter 2 short circuited and with the filter set to pass 50-500Hz signals only. When the filter was used both microphone and ANALOG OUT signals were passed through identical filters to ensure no phase error was introduced. The cleanest signals were selected for processing using various different techniques. At the threshold of oscillation the static mouth pressure was around 18mbar, the mean volume velocity was around 18l/min, the acoustic frequency was 297Hz, and therefore the acoustic period was 3.37ms.

Results and Discussion

Figure 7.15 presents an LDA measurement of the velocity in the backbore during self-sustained oscillation of the lips. The velocity trace was obtained by scaling the ANALOG OUT signal appropriately. The velocity trace demonstrates some periodicity but is unfortunately dominated by higher frequency random fluctuations, probably due to turbulence.

It is easier to distinguish the individual components of the velocity trace of figure 7.15 from a frequency domain representation such as figure 7.16. Figure 7.16 is a log-log plot of the PSD of the velocity trace of figure 7.15. In figure 7.16 there is a peak at the acoustic frequency, 297Hz. There is only one significant acoustic component because the static mouth pressure was set to a level only very slightly above the threshold of oscillation.

In section 4.6 it was shown that the PSD of instantaneous velocity is equivalent to the energy spectrum. In figure 7.16 the negative gradient of the graph at frequencies above 500Hz indicates dissipation of energy. Recall from section 4.6 that in the inertial range the energy decay is theoretically proportional to $f^{-5/3}$ so that with a log-log representation points in the energy spectrum are expected to lie on a straight line with gradient -5/3.

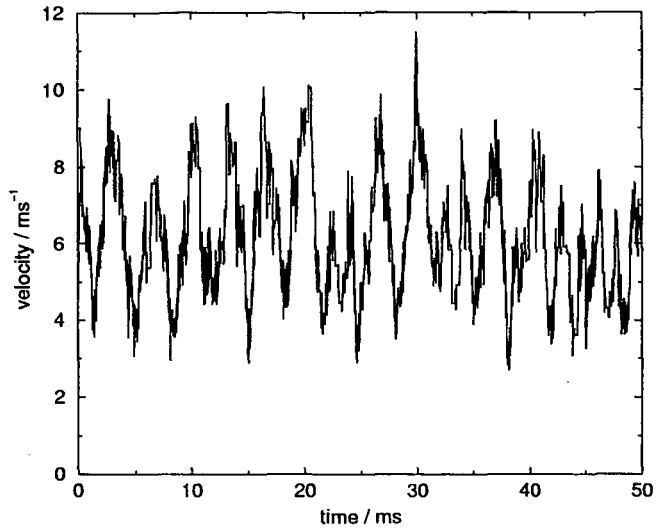

Figure 7.15: LDA measurement of the velocity in the backbore of the transparent mouthpiece during self-sustained oscillation. Bandpass filter 2 was short circuited. The static mouth pressure was only slightly greater than the threshold of oscillation.

The large fluctuations in the spectrum of figure 7.16 make it difficult to fit a straight line to the data points. To reduce the fluctuations the spectrum of figure 7.17 was produced by applying a running average routine to the data used to plot figure 7.16. The best fit straight line in figure 7.17 has gradient -1.7±0.1, which supports the hypothesis that the energy spectrum follows at $f^{-5/3}$ decay.

It is important to view this apparently positive result in the correct perspective. Frisch [40] pointed out that when a power law is fitted to data, the value of the exponent changes somewhat with the choice of the fitting region. The solid line of figure 7.17 was fitted to data points lying in the range 500-2000Hz. This frequency range was selected because at higher frequencies there is a danger that the measured spectrum may not provide an accurate representation of the true spectrum, due to ambiguity broadening or spatial averaging of small scale eddies within the measuring volume (see sections 4.5.2 and 4.5.3 respectively).

It should also be noted that the Taylor hypothesis, which in section 4.6 was

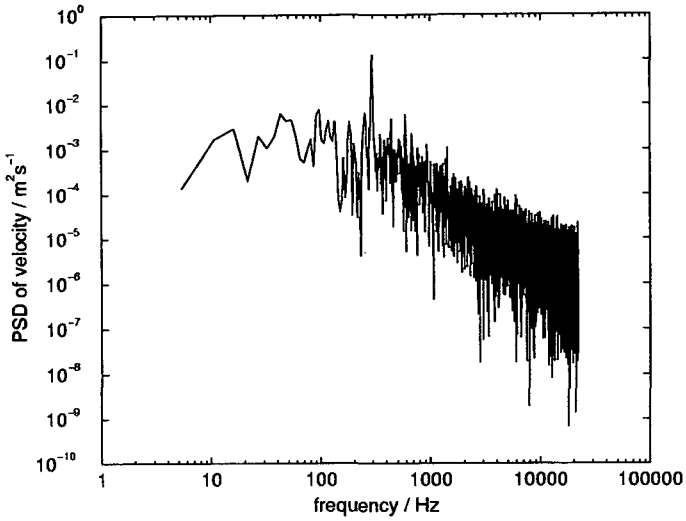

Figure 7.16: PSD of velocity trace presented in figure 7.15.

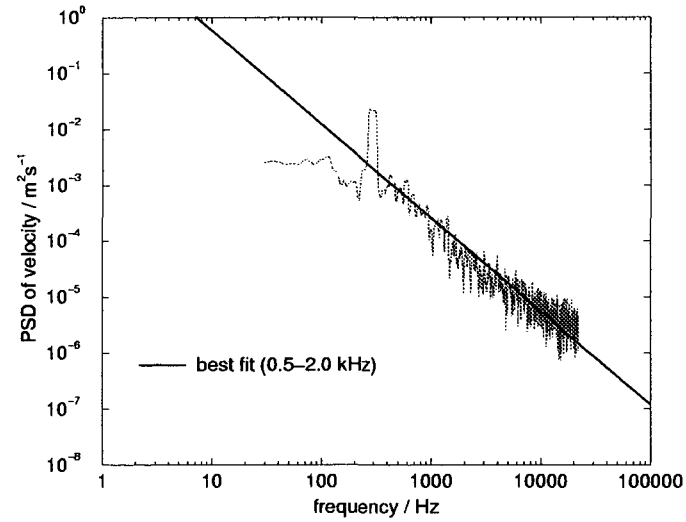

Figure 7.17: Running average over 10 points, of the data points presented in figure 7.16. The gradient of the best fit straight line is -1.7±0.1.

used in the derivation of the $f^{-5/3}$ decay law, is only strictly valid when the RMS velocity of turbulent fluctuations is significantly less than the mean velocity [40]. In the present situation, with a mean volume velocity of 15l/min the ratio of RMS velocity of the turbulent fluctuations to the mean velocity is actually approximately 1:6 (see figure 7.14).

Figure 7.18 presents an LDA measurement at position x_3, performed under very similar conditions to those encountered when acquiring the velocity trace of figure 7.15, except bandpass filter 2 was applied to the ANALOG OUT signal used to produce figure 7.18. As expected the effect of the filter is to remove high frequency noise but clearly the filtered signal is still significantly affected by turbulent fluctuations.

The velocity traces displayed in figures 7.15 and 7.18 were each passed through an ensemble averaging routine, together with simultaneously recorded probe microphone signals; the resulting ensemble averaged signals are displayed in figure 7.19. The ensemble averaging routine, 'phaseav.c', has been discussed previously in section 6.3.1 and is also considered in appendix C.8 and listed in appendix D. The ensemble averaging routine successfully smoothes out fluctuations remaining in the filtered velocity signal but partially fails in the case of the unfiltered velocity signal where some fluctuations remain.

Figure 7.20 presents similar measurements to those displayed in figure 7.19 except all measurements presented in figure 7.20 were made in the mouthpiece throat (position x_2) rather than in the backbore (position x_3). The pressure in the throat region is complex and contains several harmonic components, even although the static mouth pressure was set to a value barely above the threshold of oscillation. Of course the higher harmonic components were not passed by bandpass filter 2 and so are only evident in the unfiltered pressure signal of

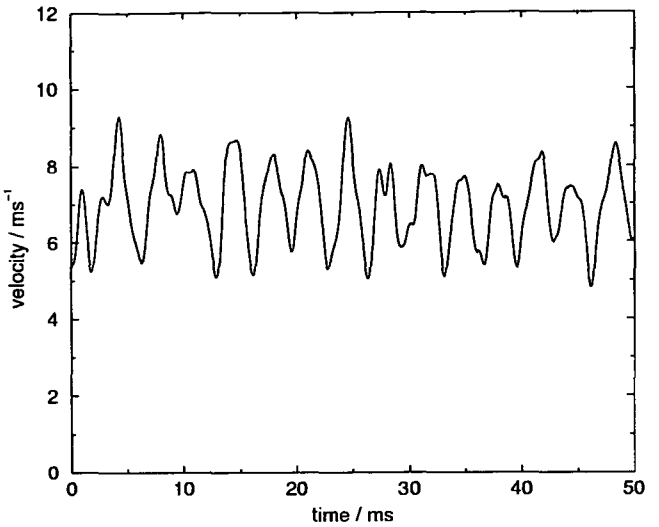

Figure 7.18: LDA measurement of the velocity in the backbore of the transparent mouthpiece during self-sustained oscillation. Bandpass filter 2 was applied. The static mouth pressure was only slightly greater than the threshold of oscillation.

figure 7.20. Even after ensemble averaging both filtered and unfiltered velocity signals are significantly affected by the turbulence. It is therefore difficult to determine whether higher harmonic acoustic components are present in the unfiltered velocity signal.

It is not surprising that turbulent intensities have been observed to be higher in the throat than in the backbore. In section 2.2 it was assumed that an air jet is produced as air exits the lips and that after traveling a short distance in the cup it rapidly expands to produce a region of turbulent mixing in the mouthpiece cup. The turbulent intensity is expected to decrease with distance downstream from the expansion region. Figure 7.14 demonstrates that the turbulent intensity in the cup is greater than the turbulent intensity in the backbore.

It would be extremely useful to measure the air flow in the mouthpiece cup rather than limit measurements to the throat and backbore. However, as already stated, there was no LDA access to the second trapezoid section of the

cup, the section nearest the lips, and although the LDA measuring volume could be positioned in the first trapezoid section of the cup, the section adjacent the throat, the turbulent intensity experienced at that point resulted in Doppler signals with extremely large bandwidths which could not be processed using the frequency tracker. Theoretically, if the tracker input filters are set to 1-10MHz and a frequency shift is applied which minimises the frequency difference between the carrier frequency of the Doppler signal and the centre frequency of the filter bandwidth, it should be possible to measure signals with a bandwidth of 8MHz. However in section 6.2.3 it was shown that it is advisable to apply Doppler signals with bandwidths of only 75% of the theoretical limit, *i.e.* the maximum bandwidth is 6MHz in this case. Such a bandwidth corresponds to a fluid velocity with a turbulent intensity of $7ms^{-1}$ or an acoustic particle velocity amplitude of $10ms^{-1}$.

In practice it was found that the tracker was not able to operate successfully over the entire 1-10MHz input filter range. To test this filter range sinusoidal Doppler signals were produced by applying frequency shifts only; no mean flows or acoustic fields were applied. When the input filter was set to the 1-10MHz range the tracker could only track Doppler signals with frequency 2MHz and 3MHz; with higher frequencies the phase locked loop was unable to lock onto the signal. This behaviour is surprising as the measurements presented in chapter 5, which involved feeding FM signals from frequency generators to the tracker, indicated that the tracker was capable of tracking a signal with a carrier frequency of 5MHz. It must be concluded that when the tracker input filter is set to 1-10MHz the tracker cannot track signals with frequency components in the range 4-10MHz unless the signal has a very low noise content. Measurements presented in section 5.3 showed that a typical SNR for a sinusoidal Doppler signal was

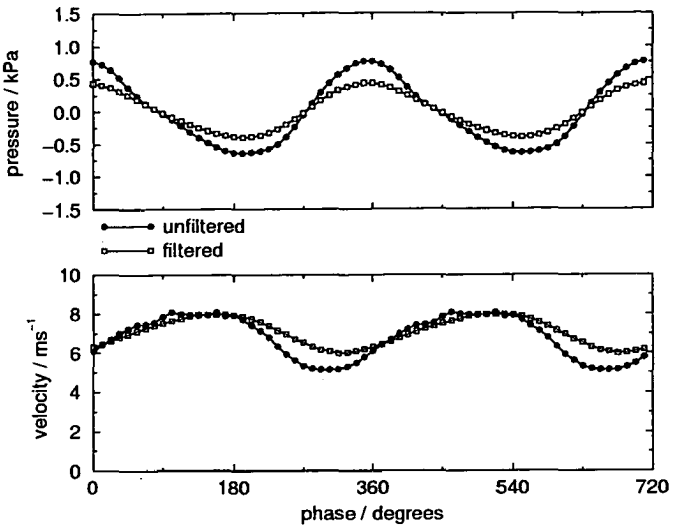

Figure 7.19: Ensemble averaged pressure and velocity in the backbore of the transparent mouthpiece during self-sustained oscillation. Both filtered (hollow squares) and unfiltered (filled circles) are considered.

about 10dB, therefore the SNR must be at least greater than 10dB, and probably higher, if the 4-10MHz range of the tracker is to be used.

With LDA measurements effectively constrained to situations where no frequency components of the Doppler signal can lie outside the 1-4MHz range, only flows with turbulent intensities of less than 3.5ms^{-1} can be measured. This lower limitation on the turbulent intensity prevented measurements in the mouthpiece cup, where the turbulent intensity is greater, and also prevented high static mouth pressure measurements in the backbore because the turbulent intensity tended to increase with the velocity of the air flow.

It is interesting to compare the velocity measurements presented in figure 7.20 with Elliot and Bowsher's [34] hot wire anemometry velocity measurements in the throat of a trombone mouthpiece (figure 19 of their paper). In Elliot and Bowsher's measurements the mean flow is generally around 10ms^{-1} and is therefore only slightly greater than the mean flow velocity of approximately 8ms^{-1} in

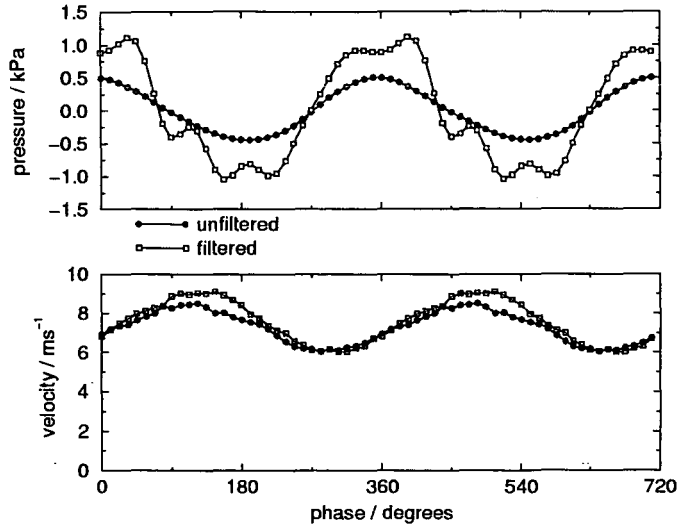

Figure 7.20: Ensemble averaged pressure and velocity in the throat of the transparent mouthpiece during self-sustained oscillation. Both filtered (hollow squares) and unfiltered (filled circles) are considered.

the present study, and yet the acoustic particle velocity amplitude in Elliot and Bowsher's measurements is in some cases around 10ms^{-1}, far greater than the amplitude of less than 1ms^{-1} measured in the present study. Furthermore in Elliot and Bowsher's measurements the turbulent intensity is small, relative to the acoustic particle velocity amplitude, whereas in the present study the acoustic nature of the velocity trace could only be distinguished from the random turbulent fluctuations after ensemble averaging was applied to smooth out the random fluctuations.

Of course the studies are not strictly directly comparable because Elliot and Bowsher:

1. fitted an entire trombone to the mouthpiece, not just the inner section of the slide;

2. used a human player rather than an artificial mouth;

3. used a conventional mouthpiece rather than a transparent mouthpiece with square cross-section and

4. performed their measurements at a higher dynamical level (mf) than in the present study (ppp).

Each of the above points will be addressed in turn.

1. The fundamental frequency of the measurements presented in figure 7.20 was around 300Hz which corresponds approximately to the note D_4 in pitch, in between the $B_3^\flat$ and F_4 notes considered by Elliot and Bowsher.

2. Comparing a human player with the artificial mouth, it is possible that the human would be better able to reduce turbulent intensity in the mouthpiece, possibly by reducing the threshold pressure and consequently the mean flow velocity. However it would be almost impossible to measure the performance of a human player using the LDA system due to the difficulty of introducing seeding into the flow at a sufficient rate.

3. A mouthpiece with a transparent portion is of course necessary for LDA measurements but it is possible the square cross section of the transparent mouthpiece might act in a way which increases turbulent intensity even although there is little acoustical difference between the square cross-section mouthpiece and a conventional mouthpiece.

4. As indicated above, due to the limitations of the LDA system, the static mouth pressure could not be increased above a level only slightly greater than the threshold of oscillation and therefore the measurements presented in figure 7.20 were effectively carried out at a dynamic level of ppp. Elliot and Bowsher's measurements do suggest that if the static mouth pressure

is increased significantly above the threshold value then the ratio of turbulent intensity to acoustic particle velocity amplitude actually decreases. Unfortunately as a consequence of the increase in static mouth pressure the acoustical particle velocity amplitude increases to a level which would prohibit analysis of the resulting Doppler signal using the currently available LDA apparatus.

7.4 Conclusions

The first section of this chapter was concerned with the mouth cavity effect. The literature suggests the mouth cavity can theoretically influence the pitch and timbre of notes produced on a brass instrument and can also provide an explanation for the ability of players to buzz their lips even when the instrument and mouthpiece are absent. Following Elliot and Bowsher [34], the mouth cavity effect was modeled by considering the input impedance of the mouth cavity to act in series with the input impedance of the instrument. Simultaneous LDA and probe microphone measurements were used to measure the input impedance of the artificial mouth, which is a good approximation to the input impedance of the mouth cavity. The artificial mouth input impedance curve displays dual resonance peaks around 1kHz which are similar in magnitude to trombone input impedance peaks, indicating the mouth cavity of the artificial mouth probably influences the sound produced, particularly the frequency components in the region of 1kHz. However the frequency of the resonance peaks is much greater than the frequency of the mechanical modes of the lips, therefore the mouth cavity effect is unlikely to be crucial for the destabilisation of the lips, thus confirming the observations of section 3.3.3. It was acknowledged that the artificial mouth impedance measurements cannot be extrapolated to deduce the influence of a human player's mouth

cavity, but the measurements certainly do not impugn Fletcher and Rossing's estimation of the importance of the mouth cavity effect [39].

Preliminary LDA measurements of the velocity of air rapidly moving through a glass tube revealed that shot noise makes a far greater contribution to the noise content of the instantaneous frequency signal than ambiguity broadening. It was also shown that when any non-zero flow is applied the noise content of the instantaneous frequency signal is significantly higher than if no flow is present (and a non-zero instantaneous frequency results purely from a frequency shift) because with non-zero fluid flow the seeding particles do not have the opportunity to accumulate. However with non-zero volume flows less than 30l/min the noise content of instantaneous frequency signals did not appear to increase with velocity. With large volume velocities turbulence was observed, but could be eliminated by increasing the diameter of the feed pipe connecting the source reservoir to the glass tube. Measurements of velocity, U_{max}, on the axis of a glass tube with cross-sectional area S were compared with the volume velocity, V, measured using a rotary float flow meter. At low volume velocities Poiseuille flow was observed ($U_{max} = 2V/S$) but at higher velocities the velocity profile tended towards, but never attained, a uniform profile ($U_{max} = V/S$).

The transparent mouthpiece employed in the third section of the chapter was described in some detail. Initial measurements in the mouthpiece limited the static mouth pressure to a range below the threshold of oscillation. Velocity signals with large random fluctuations resulted; the random fluctuations were mainly due to turbulence. Subsequent studies were carried out with static mouth pressures slightly greater than the threshold of oscillation so that the lips and air-column (formed by the inner slide of a trombone) entered into a state of self-sustained oscillation. Velocity could be measured in the throat and backbore of

the mouthpiece, but the high turbulent intensity in the cup prevented LDA measurement in that interesting region. In time domain representations of throat and backbore signals it was difficult to distinguish the acoustic signal from the turbulent fluctuations, although ensemble averaging did help to clean up the signals. In the frequency domain representations of the velocity curves a peak at the fundamental acoustic frequency could be clearly distinguished from the turbulence. The PSD of the backbore velocity signal demonstrated a decay consistent with the Kolmogorov spectrum. The operational bandwidth of the frequency tracker was found to be significantly less than the bandwidth of the widest input filter, which made LDA measurements during self-sustained oscillation very difficult. Comprehensive velocity measurements in the mouthpiece will only be possible using an analysis system with a significantly broader bandwidth than the Disa tracker.

Chapter 8

Summary and Conclusions

8.1 Achievement of Aims

The initial research aims set out in section 1.3 have all been achieved. In this chapter each aim is restated and the extent to which the aim was fulfilled is discussed.

8.1.1 Development of Artificial Lip Reed Mechanism

The first aim was to develop an improved artificial lip reed mechanism.

The present study used an artificial mouth comprising water filled latex rubber lips. The apparatus is a development of the design introduced by Gilbert and Petiot [43]. Their prototype design was improved upon to provide means of adjusting the volume of water in the lips while the lips are in situ in the artificial mouth, thus achieving a greater control of the embouchure.

With the artificial mouth used in the present study only a small portion of the mouthpiece lies within the mouth. This improvement over the prototype design was achieved by fixing the mouthpiece to the front plate of the artificial mouth and providing 'teeth', which could be moved to adjust the embouchure. If a transparent mouthpiece is used with this arrangement LDA measurements can be made inside the mouthpiece. Furthermore the design permits the cup portion

of the mouthpiece to be removed; this feature was used during the measurement of the mechanical response of the lips.

The artificial mouth was found to perform well when the lips and teeth were arranged so that, with a static mouth overpressure of zero, the lips were slightly separated from each other at the centre but remained together at the mouthpiece rim. Artificial mouth embouchures could be reproduced over a period of about two weeks, but over longer periods of time the embouchure properties were found to vary slightly. The artificial mouth could be used to play notes on a tenor trombone and during threshold measurements produced notes with fundamental frequencies in the range 230-380Hz [22], corresponding approximately to the notes $B_3^\flat$ to $F_4^\sharp$ in the equal tempered scale.

8.1.2 Measurement of Mechanical Response of Artificial Lips

The second aim was to develop apparatus and software for automatically measuring the mechanical response of artificial lips over an appropriate frequency range and to use this arrangement to systematically measure the mechanical response with a variety of different embouchures and other conditions.

In this study mechanical response was defined in the frequency domain as the ratio of lip separation to mouth cavity acoustic pressure. The apparatus developed to measure the mechanical response of the lips included a laser beam which was shone through the aperture between the lips of the artificial mouth, and a diode which measured the intensity of the beam. It was shown that the voltage of the diode signal was proportional to the lip separation. The lips were driven by a loudspeaker positioned inside the artificial mouth. Software was written to provide a swept sound wave signal to the loudspeaker and to extract the mechanical response from the diode signal and the signal produced by a Knowles

microphone positioned inside the artificial mouth. With this arrangement the mechanical response of the lips could be measured over the frequency range 100-500Hz in approximately 2 minutes.

The measurements presented in chapter 3 demonstrate that the mechanical response of the artificial lip mechanism is complicated and involves three strong mechanical modes, one mode with outward striking character and two higher frequency modes, each with inward striking character. Mechanical response was measured for a range of static mouth overpressures. These measurements showed that the quality factors of the two modes with inward character increased with static mouth overpressure. As a mechanical mode tended towards destabilisation the quality factor of the mode tended towards infinity. With a sufficient static mouth pressure one or other of the two modes with inward character was destabilised (depending on embouchure) resulting in a mouthpiece 'buzz'. The measurements were repeated with the mouthpiece cup removed. In this case the quality factors of the first and second resonances were found to increase with static mouth overpressure, providing some evidence of aerodynamic coupling between mechanical modes; this coupling was however too weak to result in complete destabilisation.

It was concluded that the mouth cavity could not significantly effect the destabilisation of the lips because (1) when the mouth cavity volume was reduced no significant variation in the mechanical response of the lips was observed, even when a substantial static overpressure was applied; and (2) input impedance measurements of the mouth cavity revealed acoustical resonances only around 1000Hz, far above the mechanical resonance frequencies of the lips.

The static and dynamic mechanical response measurements presented in chapter 3 provide the first 'direct' measurement of each of the lip parameters required

by a simple one-mass model. Mechanical response was measured for a range of embouchures and the lip parameters characterising each of these embouchures were extracted. The lip quality factors measured in this study are higher than the values which other authors have used in their simulations, while the measured ratio of lip effective area to lip effective mass is consistently lower than the values previously adopted.

8.1.3 Development of Lip Vibration Model

The third aim was to develop software which models the oscillation threshold behaviour of a trombone by applying linear stability analysis to a one–mass model of the lips.

In the one–mass physical model of this study the lips and the resonator were each represented by simple harmonic oscillators. Several assumptions were made regarding the pressure field around the lips, permitting a relatively simple representation of the air flow through the lips. The basic equations describing the system were linearized about the equilibrium position of the lips and arranged to from a matrix equation involving a 4×4 matrix. A computer program was written to evaluate the eigenvalues of the 4×4 matrix, and hence deduce oscillation threshold pressure and frequency. The simulation program was run using lip parameters extracted form mechanical response measurements with the artificial mouth, and acoustical parameters extracted from input impedance measurements of a trombone.

8.1.4 Measurement of Oscillation Threshold Behaviour and Comparison with Theoretical Behaviour

The fourth aim was to measure the oscillation threshold behaviour of a trombone driven by the artificial mouth, with several different embouchures and several

different acoustical conditions, and to compare the measured behaviour with that predicted by the above computational model.

The experimental threshold pressure was considered to be the static mouth pressure required to sustain a permanent periodic regime with a predetermined small amplitude, and the threshold frequency was considered to be the frequency of said periodic regime. The threshold values were measured (1) as a function of trombone slide extension (with fixed embouchure) and (2) as a function of embouchure (with fixed trombone slide extension). The measured threshold behaviour was compared with the threshold behaviour predicted by the one-mass model. In each case the one-mass model was run firstly using lip parameters extracted from the first resonance of the mechanical response curves (a mode with outward striking character) and secondly using lips parameters extracted from the second resonance of mechanical response curves (a mode with inward striking character).

The threshold measurements are divided into three distinct regimes corresponding to the 4^{th}, 5^{th} and 6^{th} acoustical modes. The regimes may be distinguished from one another in both the threshold pressure and threshold frequency measurements but are most apparent in the frequency measurements. Both the inward striking and outward striking models also demonstrate such distinct regimes; however the models fail to accurately predict the slide positions (or embouchures positions) at the transition between different regimes. Furthermore in most instances the one-mass models overestimate the threshold pressure. The measurements showed that, with a fixed embouchure, for some slide positions the threshold frequency is above the measured acoustic resonance frequency; for other slide positions the situation is reversed. The one-mass model cannot explain this behaviour: with the outward striking model the threshold frequency

is consistently above the acoustic resonance frequency whilst with the inward striking model the threshold frequency is consistently below the acoustic resonance frequency. It may be concluded that an accurate theoretical description of the interaction of player's lips with an instrument air column requires at least a two-mass model of the lips, incorporating one mechanical mode with outward character and a higher frequency mechanical mode with inward character.

The work of chapters 2 and 3 has been accepted for publication in *Acustica*.

8.1.5 Investigation of Different Techniques for Processing Doppler Signals

The fifth aim was to investigate different techniques for processing Doppler signals, writing new software as required.

Two different methods were investigated. The first method involved digitally sampling the Doppler signal and then applying a Hilbert transform demodulation routine (written by Hann and Greated [49]) to the sampled signal. The second method involved passing the Doppler signal through a Disa analogue frequency tracker and then sampling the resulting demodulated signal. Both methods provide the instantaneous frequency of the Doppler signal, which is proportional to the instantaneous velocity of the fluid.

It was found that the Disa tracker provided the velocity signals with the greatest SNR. The superior performance of the tracker is probably due largely to the provision of adaptive filtering means. In the measurement of high intensity sound fields, the dynamic range of the tracker is greater than the dynamic range of the digital sampling/Hilbert transform method which can be obtained using currently available A/D converters.

A program was written to ensemble average velocity signals to reduce noise content. The program also ensemble averages a simultaneously recorded alter-

nating pressure signal and calculates the Fourier series amplitude and phase coefficients of each component of the pressure and velocity signals.

The program 'auto.c', which was originally written to extract the mechanical response of the lips from diode and microphone signals, was adapted to extract the specific acoustic impedance from simultaneously recorded probe microphone and LDA instantaneous velocity signals. Another program was written to calculate the power spectrum of LDA signals and, in the case of sinusoidal Doppler signals, the SNR of the Doppler signal.

8.1.6 Investigation of Flow Seeding Methods

The sixth aim was to investigate different methods of seeding the flow.

LDA measurements in sound fields using water droplet seeding were found to suffer from quasi-periodic amplitude modulation of the Doppler signal at the acoustic frequency, and occasionally in periodic signal dropout. An experimental study of Doppler signal envelopes demonstrated that the problem could be mitigated by replacing the water droplet seeding with smoke seeding from incense sticks.

Stokes drag law was used to theoretically assess how successfully seeding particles follow an oscillating air flow. It was found that smoke particles should faithfully follow the flow at frequencies less than or equal to 2kHz, whereas water droplet seeding particles theoretically lag an acoustic flow oscillating with frequency 2kHz by 45°.

The SNR of the Doppler signals resulting from LDA measurements using MEDUTEK nebuliser water droplets as seeding particles was found to be similar to the SNR of the Doppler signals resulting from measurements using incense stick smoke particles as seeding particles (approximately 10dB for a sinusoidal Doppler signal generated by applying a frequency shift). However the amplitude

modulation experiments and theoretical study of Stokes drag suggest that smoke from burning incense sticks provides a better method of seeding the flow than water droplets produced by nebulisers.

8.1.7 LDA Measurements in Sound Fields

The seventh aim was to verify that a particular LDA system correctly measures instantaneous acoustic particle velocity by performing LDA measurements in mono-frequency and multi-frequency standing waves and comparing results with the velocity predicted by applying basic acoustic theory to pressure measurements.

LDA measurements were carried out in a mono-frequency standing wave set up in a loudspeaker driven glass pipe. Using the analogue frequency tracker, acoustic particle velocity amplitude could be measured with an accuracy of ± 0.3dB over a velocity range corresponding to SPLs in the range 105-140dB.

A sound field containing three harmonic components was also set up in the tube and the ensemble averaging routine was applied to velocity measurements made along the length of the tube. The measured velocity amplitude of each frequency component compares favourably with the theoretical velocity; however the measured velocity phase agreed with the theoretical velocity phase measurements only in the case of the second and third harmonic components, but not in the case of the fundamental.

This low frequency phase discrepancy was also apparent in probe microphone/LDA measurements of the acoustic impedance of a cylinder: there was found to be good agreement between theoretical and measured velocity phase only at frequencies above 400Hz, even although there is excellent agreement between the measured and theoretical magnitudes of the impedance of the cylinder, over the entire measured frequency range.

8.1.8 LDA Measurements Inside a Trombone Mouthpiece

The eighth aim was to assess the feasibility of applying LDA to the measurement of air flow velocity inside a trombone mouthpiece when the trombone is excited using an artificial lip reed mechanism.

The bandwidth of the Doppler signal is proportional to the acoustic particle velocity amplitude and therefore the maximum acoustic particle velocity amplitude which can be measured is determined by the maximum bandwidth of the frequency tracker. In theory the maximum bandwidth of the frequency tracker is 9MHz but in practice it was found that the bandwidth of the frequency tracker was only 3MHz, unless the SNR was very low. With the LDA setup of the present study, such a bandwidth restricts the maximum acoustic particle velocity amplitude to less than $3ms^{-1}$, corresponding to an SPL of 153dB. Such an SPL is greater than that encountered at the mouthpiece throat of a trombone, at least if the trombone is played softly. However during self-sustained oscillation the dynamic range is unfortunately reduced below this level, due to several complications, which will be discussed below.

Before carrying out LDA measurements under conditions of self-sustained oscillation LDA was first used to measure rapid mean flows in a cylindrical pipe. It was found that as soon as any significant mean flow was introduced there was a reduction in seeding density and the shot noise content of the velocity signal consequently increased. The shot noise was found to make a far greater contribution to the noise content than ambiguity broadening. Further increasing the mean flow velocity had no effect until a critical level was reached, at which point low frequency random fluctuations appeared in the velocity signal, signifying the onset of turbulence.

Further mean flow measurements were performed within a specially designed

transparent trombone mouthpiece with a square cross-section, coupled to the artificial mouth. With static mouth pressure below the threshold of oscillation velocity signals from measurements within the mouthpiece were found to contain random fluctuations, considered to be mainly due to turbulence. The static mouth overpressure was then increased until the lips and air column (a cylindrical tube) participated in self-sustained oscillation. During self-sustained oscillation velocity could be measured in the throat and backbore of the mouthpiece, but the high turbulent intensity in the cup prevented LDA measurements in that interesting region. In time domain representations of throat and backbore signals it was difficult to distinguish the acoustic signal from the turbulent fluctuations, although ensemble averaging did help to clean up the signals. In the frequency domain representations of the velocity curves a peak at the fundamental acoustic frequency could be clearly distinguished from the turbulence.

Using the present apparatus LDA measurements in the mouthpiece are very difficult to carry out because, unless the threshold mouth pressure is maintained at a level only very slightly above the threshold of oscillation, the turbulent intensity increases to a level where the bandwidth of the Doppler signal is greater than the effective bandwidth of the analogue frequency tracker. Comprehensive velocity measurements in the mouthpiece of a brass instruments will only be possible if the apparatus is improved. Possible areas of improvement are discussed at the end of section 8.2.

8.2 Further Work

There are several ways in which the work of this thesis could be extended.

The implementation of a threshold simulation program based on a two-mass model of the lips should be straight forwards as it would merely involve extend-

ing the existing 'matrix.c' program to evaluate the eigenvalues of a 6×6 matrix, rather than just a 4×4 matrix; the only perceived difficulty would be in adapting the function 'filter()' so that it correctly assigns each of the randomly ordered eigenvalues to the correct array (see Appendices C.1 and D). A two-mass model simulation could be run using the lip parameters and acoustical parameters measured in the present study. The simulation could alternatively be extended by adding perturbation terms to the one-mass model to take into account effects such as a secondary volume source. However it is difficult to envisage an experiment which could provide suitable parameters for such perturbation terms and so it is probably more worthwhile to concentrate on the two-mass model initially.

In this study the mechanical response of the lips has been investigated in some detail but no effort has been made to investigate the relationship between lip displacement and mouthpiece pressure during self-sustained oscillation. It would be easy to perform such measurements using substantially the apparatus adopted in the mechanical response measurements. The resonator could comprise a fixed pipe and a sliding pipe arranged to slide snugly over the fixed pipe, thus creating a resonator of variable length. The pipes could be coupled to the artificial lips through a mouthpiece or alternatively, if the pipes were of sufficient diameter, could be placed in direct contact with the lips. Either arrangement would permit the lip illuminating laser beam to pass along the axis of the resonator. A probe microphone could be positioned in the resonator, immediately downstream from the lips. The pipe lengths and fixed embouchure could be arranged so that the playing frequency lies below the acoustical resonance frequency of the nearest acoustical mode when the sliding pipe is unextended, but above the resonance frequency when fully extended. To some degree such an experiment would repeat the threshold measurements presented in chapter 3 (*e.g.* in figure 3.22), but

would provide additional information: the phase difference between lip displacement and pressure immediately downstream from the lips. As the slide extension is increased and the playing frequency evolves from being below the acoustical resonance frequency to above the acoustical resonance frequency it is expected that outward striking behaviour should take over from inward striking behaviour, resulting in a significant shift in the phase difference between lip displacement and mouthpiece pressure.

It is predicted that the work suggested in previous paragraphs could be carried out easily and quickly. Longer term goals will now be described.

Additional LDA velocity measurements in the mouthpiece would be of great interest, particularly if the measurements could be made in the cup section, very close to the lips because then the air jet could be studied. One could also use the LDA apparatus in conjunction with the sliding tube apparatus described above, to provide the phase of the acoustic particle velocity and the phase of the pressure immediately downstream from the lips. One possible experiment could involve tracing the acoustic particle velocity along the axis of the resonator from immediately in front of the lips to a short distance downstream of the lips, whilst holding the slide at a fixed position; the measurements could then be repeated with several different slide positions.

The phase behaviour observed in such an experiment could be compared with the corresponding theoretical phase behaviour which would occur with plane wave propagation, as outlined below. When the standing wave sustained in a lip driven instrument has a frequency equal to the resonance frequency of the instrument then a pressure anti-node occurs precisely at the input end of the instrument (the end which is driven) whilst a velocity node occurs at this same position. If however the standing wave has a frequency slightly greater than the resonance frequency

then the pressure anti-node and velocity node will occur slightly downstream of the input end. Using equation 6.34 it is possible to show[i] that at a point slightly upstream of a velocity node/pressure anti-node the pressure lags the velocity in phase by approximately $\pi/2$, whereas slightly downstream of a velocity node/pressure anti-node the pressure leads the velocity in phase by approximately $\pi/2$. Thus in the experiment described above, if the sliding pipe and artificial mouth embouchure are arranged so that the playing frequency is slightly greater than the acoustic resonance frequency then as the measuring volume is moved downstream from the lips the phase interval between the pressure immediately downstream of the lips and the LDA measured acoustic particle velocity should undergo a phase change of around π as the velocity node is traversed. If the sliding pipe was then adjusted so that the playing frequency was slightly less than the acoustic resonance frequency then there would be no velocity anti-node near to the downstream side of the lips and so one would expect there to be no significant change in the phase.

The above experiment could be carried out using narrow bore pipes coupled to the lips through a transparent mouthpiece or wider bore transparent pipes coupled directly to the lips. The second method has the advantage that the resonance characteristics of the resonator can easily be calculated theoretically. Furthermore, for a given acoustic volume velocity, the acoustic particle velocity in a wide bore tube is less than the acoustic particle velocity in the throat of a mouthpiece. However preliminary measurements indicate that greater levels of turbulence would be experienced if the pipes were coupled directly to the lips.

If lip separation was studied in addition to the acoustic particle velocity and pressure immediately downstream from the lips then the Helmholtz regeneration

[i]It is helpful to consider the extremely idealised case where $Z_r = 0$ and therefore $Z_s(x) = j\tan(kx)$

condition (equation 7.1) could be tested experimentally.

Unfortunately considerable additional development work will be required before LDA measurements can be made immediately in front of the lips. This work could include: (1) constructing a third generation artificial mouth with the lips outside of the mouth cavity, so as to permit LDA measurements immediately in front of the lips; (2) investigating if the turbulent intensity in the mouthpiece could be reduced by replacing the transparent square cross-section mouthpiece with a conventional shaped mouthpiece provided with glass windows to permit optical access for LDA; (3) extending the dynamic range of the LDA system by increasing the fringe spacing in the measuring volume; or (4) extending the dynamic range of the LDA system by replacing the Disa analogue tracker with demodulating apparatus with a larger bandwidth.

Additional longer term projects could involve video recording the motion of the artificial lips during self-sustained oscillation and comparing the footage with video recordings of human players, such as the video recordings produced by Ayers [4]; measuring the input impedance of the mouth cavity for a range of mouth cavity volumes; or removing one lip from the artificial mouth and measuring the mechanical response of the single remaining lip.

Appendix A

Tables of Measured Acoustical and Mechanical Parameters

slide extension /cm	f_{A4} /Hz	Z_{A4} /MΩ	Q_{A4}	f_{A5} /Hz	Z_{A5} /MΩ	Q_{A5}	f_{A6} /Hz	Z_{A6} /MΩ	Q_{A6}
0	229.5	20	24.0	288.5	22	31.5	343.0	19	29.5
3	225.0	18	26.5	284.5	20	28.5	335.0	17	23.5
6	220.5	20	26.5	279.0	21	25.0	329.0	20	29.0
9	216.0	20	26.5	273.5	21	25.0	322.5	19	26.0
12	212.0	19	26.0	268.0	21	25.0	317.0	20	33.0
15	208.0	20	25.0	263.0	21	28.0	311.0	20	33.5
18	205.0	19	23.5	257.5	19	24.0	306.5	18	33.5
21	201.5	20	24.0	253.0	20	24.5	302.0	19	26.5
24	197.0	21	25.0	248.0	21	27.0	297.0	20	26.5
27	194.0	20	25.0	243.0	19	25.5	292.0	20	28.5
30	190.5	19	23.5	239.0	18	26.5	288.5	21	33.5
33	187.5	13	24.0	234.5	14	27.5	284.5	15	27.5
36	184.0	14	22.5	230.5	14	29.5	280.5	15	28.0
39	180.5	14	21.5	226.5	15	32.0	276.0	15	28.5
42	177.5	15	25.5	222.5	13	28.0	271.0	15	28.5
45	174.5	15	22.0	219.5	13	28.0	267.0	15	27.5
48	171.0	15	22.0	215.5	13	31.0	262.0	16	26.5
51	168.5	15	22.5	213.0	12	24.5	257.5	15	28.0
54	165.5	16	23.0	209.5	13	27.5	253.5	15	27.5
57	163.0	15	20.5	206.5	12	27.5	249.5	15	28.0
60	160.5	15	23.0	204.0	12	28.5	245.5	14	27.5
63	158.0	15	22.0	201.0	12	27.5	241.5	14	27.0

Table A.1: Acoustical parameters of modes 4, 5 and 6, extracted from input impedance measurements of trombone. These parameters were used to produce figures 2.6/3.22b and 3.23b.

embouchure	$\overline{H_0}$ /mm	b /mm	f_{L1} /Hz	Q_{L1}	$1/\mu_{L1}$ /m^{2}kg^{-1}	f_{L2} /Hz	Q_{L2}	$1/\mu_{L2}$ /m^{2}kg^{-1}
0	**0.70**	**18**	182.0	9.5	0.044	**223.0**	**9.2**	**−0.065**
1	**0.68**	**17**	182.0	10.0	0.041	225.5	10.5	−0.059
2	**0.65**	**16**	186.0	10.5	0.042	**228.0**	**9.8**	**−0.066**
3	0.63	15	189.5	10.5	0.042	230.5	8.0	−0.084
4	**0.61**	**14**	192.5	11.5	0.039	**234.2**	**10.2**	**−0.069**
5	**0.58**	**13**	196.5	10.0	0.044	238.0	12.5	−0.058
6	**0.56**	**13**	202.0	8.5	0.053	**241.2**	**11.8**	**−0.065**
7	0.53	12	204.5	7.0	0.063	244.5	11.0	−0.073
8	**0.51**	**12**	209.5	7.5	0.064	**247.0**	**10.8**	**−0.073**
9	**0.48**	**12**	213.0	8.5	0.059	249.5	10.5	−0.074
10	**0.46**	**11**	216.0	9.5	0.056	**252.8**	**13.2**	**−0.059**
11	0.44	11	219.0	9.5	0.059	256.0	16.0	−0.048
12	**0.41**	**11**	221.5	10.5	0.056	**259.0**	**15.8**	**−0.049**
13	**0.39**	**10**	222.0	11.0	0.057	262.0	15.5	−0.050
14	**0.37**	**10**	225.0	12.0	0.056	**264.8**	**14.8**	**−0.052**
15	**0.34**	**10**	227.5	12.0	0.059	267.5	14.0	−0.053
16	**0.32**	**9**	229.5	11.5	0.064	**270.5**	**13.0**	**−0.059**
17	**0.30**	**9**	232.0	11.5	0.067	273.5	12.0	−0.067
18	**0.27**	**9**	234.0	11.5	0.070	**275.8**	**12.2**	**−0.068**
19	**0.25**	**9**	237.0	12.0	0.072	278.0	12.5	−0.069

Table A.2: Lip parameters extracted from mechanical response measurements. Numbers in bold font indicate parameters which were estimated from extrapolating or interpolating neighbouring measured parameter values (standard font). The lip parameters in this table were used to produce figure 3.24.

Appendix B

Derivation of Intensity Distribution of Fringe Pattern

If both the beams represented in figure 4.3 are coherent and have wave number k and polarization direction $\hat{\mathbf{p}}$ then at position $\mathbf{x}$ and time t the electric field vector of beam m is

$$\mathbf{E}_m(\mathbf{x},t) = \sqrt{I_m(\mathbf{x})}(\exp[j(\omega_m t - k\hat{\mathbf{s}}_m \cdot \mathbf{x})])\hat{\mathbf{p}}, \quad m = 1,2 \tag{B.1}$$

where $I_m(\mathbf{x})$ is the Gaussian intensity of beam m and ω_m is the angular frequency of beam m. The intensity distribution of the interference pattern formed by combining to the two beams is

$$\begin{aligned} i(\mathbf{x},t) &= |\mathbf{E}_1(\mathbf{x},t) + \mathbf{E}_2(\mathbf{x},t)|^2 \\ &= |\mathbf{E}_1(\mathbf{x},t)|^2 + |\mathbf{E}_2(\mathbf{x},t)|^2 + \mathbf{E}_1(\mathbf{x},t)\mathbf{E}_2^*(\mathbf{x},t) + \mathbf{E}_1^*(\mathbf{x},t)\mathbf{E}_2(\mathbf{x},t) \end{aligned} \tag{B.2}$$

The total intensity, $i(\mathbf{x},t)$, can be related to the intensity of beams 1 and 2 by substituting equation B.1 into the above expression:

$$\begin{aligned} i(\mathbf{x},t) &= I_1(\mathbf{x}) + I_2(\mathbf{x}) + 2\sqrt{I_1(\mathbf{x})I_2(\mathbf{x})}\cos[(\omega_1 t - k\hat{\mathbf{s}}_1 \cdot \mathbf{x}) - (\omega_2 t - k\hat{\mathbf{s}}_2 \cdot \mathbf{x})] \\ &= I_1(\mathbf{x}) + I_2(\mathbf{x}) + 2\sqrt{I_1(\mathbf{x})I_2(\mathbf{x})}\cos[(\omega_1 t - \omega_2 t) + k\mathbf{x} \cdot (\hat{\mathbf{s}}_2 - \hat{\mathbf{s}}_1)] \\ &= I_1(\mathbf{x}) + I_2(\mathbf{x}) + 2\sqrt{I_1(\mathbf{x})I_2(\mathbf{x})}\cos[2\pi F_s t + K\mathbf{x}] \end{aligned} \tag{B.3}$$

where

$$F_s = \frac{\omega_1 - \omega_2}{2\pi}, \tag{B.4}$$

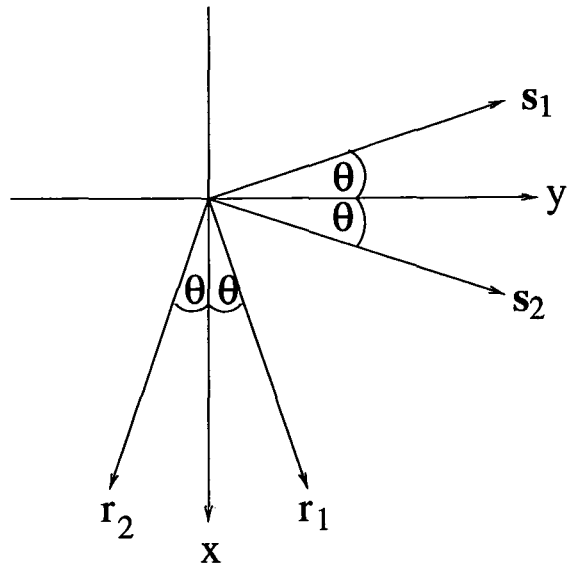

Figure B.1: Relation of coordinate systems.

$$K = k\hat{\mathbf{x}} \cdot (\hat{\mathbf{s}}_2 - \hat{\mathbf{s}}_1) = \frac{4\pi \sin\theta}{\lambda}, \tag{B.5}$$

and x is the magnitude of $\mathbf{x}$. The Gaussian intensity of beam 1 can easily be described in a Cartesian coordinate system (r_1, s_1, z) formed by rotating the original coordinate system of figure 4.3 anti-clockwise about the z-axis through the angle θ so that one axis of the new coordinate system is coincident with the beam direction (see figure B.1). Similarly a coordinate system (r_2, s_2, z) can be defined for beam 2 so that the beams lie along the s_1 and s_2 axes and the intensity of beam m at position (r_m, s_m, z) depends only on the radial distance from the centre of the beam:

$$I_m(r_m, s_m, z) = I_0 \exp\left[-\frac{8(r_m^2 + z^2)}{d_{e^{-2}}^2}\right], \quad m = 1, 2 \tag{B.6}$$

where I_0 is the maximum intensity of each beam and $d_{e^{-2}}$ is the diameter of each beam at $1/e^2$ maximum intensity. By performing the appropriate transformations

from the (r_m, s_m, z) coordinate systems to the (x, y, z) coordinate system [2] expressions for $I_1(\mathbf{x})$ and $I_2(\mathbf{x})$ can easily be derived from equation B.6. Substitution of these expressions for $I_1(\mathbf{x})$ and $I_2(\mathbf{x})$ into equation B.3 finally gives

$$i(\mathbf{x}, t) = W(\mathbf{x}) \cosh\left(\frac{8xy \sin(2\theta)}{d_{e^{-2}}^2}\right) + W(\mathbf{x}) \cos[2\pi F_s t + K\mathbf{x}] \tag{B.7}$$

where

$$W(\mathbf{x}) = I_0 \exp\left[-\frac{8(x^2 \cos^2\theta + y^2 sin^2\theta + z^2)}{d_{e^{-2}}^2}\right] \tag{B.8}$$

Appendix C

Structure and Operation of Computer Programs

C.1 Simulation of Threshold Behaviour

The program 'matrix.c' requires the parameters associated with one mechanical mode of the lips and the parameters associated with one acoustical mode of the trombone. It outputs threshold pressure and frequency as a function of slide position of the trombone. To run the program on a unix machine the user must enter the command line input:

```
matrix mechanical.mec acoustical.aco mode
```

where 'matrix' is the name of the executable file, 'mechanical.mec' is the name of the file containing the mechanical parameters, 'acoustical.aco' is the name of the file containing the acoustical parameters and 'mode' is the acoustic mode number.

The mechanical files should be created by editing the numerical values in the sample file listed below. The variable names and the required units are explained in commented sections of the source code at lines 31-42 of the main() function (see appendix D).

```
f_L: 238.0
Q_L: 11.5
1/mu: 0.08
b: 0.009
h_0: 0.00025
temp_of_threshold: 18.3
temp_of_impedance: 18.3
min_P_m: 0.0
max_P_m: 10000
no_p_steps: 2000
```

The acoustical file must characterise the development of a particular acoustical mode of the trombone as a function of slide extension. It should consist of four columns, with one line for every trombone slide position. Columns 1 to 4 should list respectively slide extension (in any units), frequency of input impedance local maximum (in Hz), magnitude of input impedance at the local maximum (in acoustic Ohms) and quality factor of the resonance peak.

For each trombone slide position the program loops through a range of mouth pressures, incrementing the mouth pressure with each execution of the loop until the program detects the threshold pressure associated with the particular slide position. One pass through the pressure loop will now be described. The 4×4 matrix of equation 2.21 is evaluated and its eigenvalues are calculated using the function eigenval(), which returns the two complex conjugate pairs of eigenvalues in a random order. The two eigenvalues with negative imaginary parts are neglected but the eigenvalues with positive imaginary parts are assigned to arrays. The arrays are then passed to the function filter() which swaps the array assignment if it detects the array elements differ significantly from the elements stored in the previous execution of the pressure loop. This step is required because unfortunately the eigenval() function returns eigenvalues in a seemingly random order. Finally the real parts of the correctly ordered eigenvalues are passed to the function thresh() which compares the real part of the eigenvalue to the value

stored on the previous execution of the loop. An increase from a value less than zero to a value greater than zero indicates the transition from stability to instability, in which case the threshold pressure lies between its current value and its value on the previous execution of the loop. Similarly the threshold (angular) frequency lies between the current imaginary part of the eigenvalue and its value on the previous execution of the loop.

The program automatically generates output filenames which combine the name of the input mechanical filename and the input mode number; if the mechanical filename 'mechanical.mec' and the mode number 'mode' are input then filenames of the form 'mechanical_mode.ext' will be generated, where '.ext' is one of several possible extensions. The most useful output files generated by the program include 'mechanical_mode.pre' which lists slide extension in the first column and threshold pressure (in mbar) in the second, and 'mechanical_mode.fre' which lists slide extension in the first column and threshold frequency in the second. These files were used to produce figure 2.6 for example. If the 'acoustical' file consists of only a single line then the files 'mechanical_mode.co1' and 'mechanical_mode.co2' are generated. Each of those files is a parametric representation of the evolution of one eigenvalue with increasing threshold pressure; the real parts of the eigenvalue are listed in the first column while the imaginary parts are listed in the second and final column. The files 'mechanical_mode.co1' and 'mechanical_mode.co2' were used to produce figure 2.4 for example. Lesser used files are described in the commented section of the source code at lines 14-23.

C.2 Least Squares Fit to Resonance Curve

The program 'lsf_reson' fits resonance curves to each of the resonances of a mechanical response or input impedance curve and outputs the frequency, quality

factor and maximum value of each of the fitted curves.

In response to screen prompts the user should enter the filename of a two column input file which lists frequency in the first column and either mechanical response or input impedance in the second column. The program can process either 5Hz resolution mechanical response measurements stored in files of length 97 lines, or 1Hz resolution input impedance measurements stored in files of length 950 lines. The length of the files can of course be altered by changing the value assigned to the variable 'length' at line 24 or 31 of the main() function of the source code.

If 1Hz resolution data is to be processed the program temporarily reduces the resolution to 5Hz. Local maxima of the 5Hz resolution input impedance or mechanical response curves are identified using the function peakfind(). The reduction in resolution avoids the false identification of local maxima, which could otherwise occur due to signal noise in the input impedance data. After the local maxima have been identified the lsf() function is applied around each local maxima. The lsf() function calculates the square of the difference between the mechanical response (or input impedance) data from the input file and the theoretical resonance curve

$$A(f) = \frac{A_0}{\sqrt{1 + \frac{4Q_0^2(f-f_0)^2}{f_0^2}}} \tag{C.1}$$

which has maximum value A_0 at frequency f_0 and quality factor Q_0. In the case of the 1Hz resolution input impedance measurements the squared difference is calculated for the point which peakfind() identified as a local maximum, and for the 5 points on either side of the local maximum. An iterative process is then employed to find the values of A_0, f_0 and Q_0 which minimise the squared difference summed over the 11 points. In the case of the lower resolution mechanical response measurements the least squares difference is minimised using only 5

points.

The program outputs the optimum values of A_0, f_0 and Q_0 to the screen and also evaluates equation C.1 in the vicinity of local maxima and outputs f and $A(f)$ to a two column output file.

C.3 Frequency Response

The frequency response program 'auto.c' was written to analyse data from experiments which involve driving a sound source with a swept sine wave signal produced by a PC sound card. The program is arranged for use with .wav files which produce swept sine waves consisting of 97 individual 1s segments, each segment having a constant frequency which is higher than the frequency of the proceeding segment. A further requirement is that resulting microphone or LDA ANALOG OUT signals fed to the program must be sampled at 4096Hz. The program may also be used to analyse individual 1s segments. Of course the program can be adapted for use with various swept sound waves by changing the values of the macros at the beginning of the source code.

The program can be used to calculate (a) the mechanical response of the lips, in which case the microphone signal and diode signal should be stored respectively in the first and second columns of the input file; (b) microphone calibration curves, in which case the reference microphone and the microphone which requires calibration should be stored respectively in the first and second columns of the input file; (c) acoustical impedance, in which case the LDA ANALOG OUT signal and the probe microphone signal should be stored respectively in the first and second columns of the input file; and (d) the acoustic pressure, in which case the microphone signal should be stored in a single column file. The structure of the program is illustrated in figure C.1.

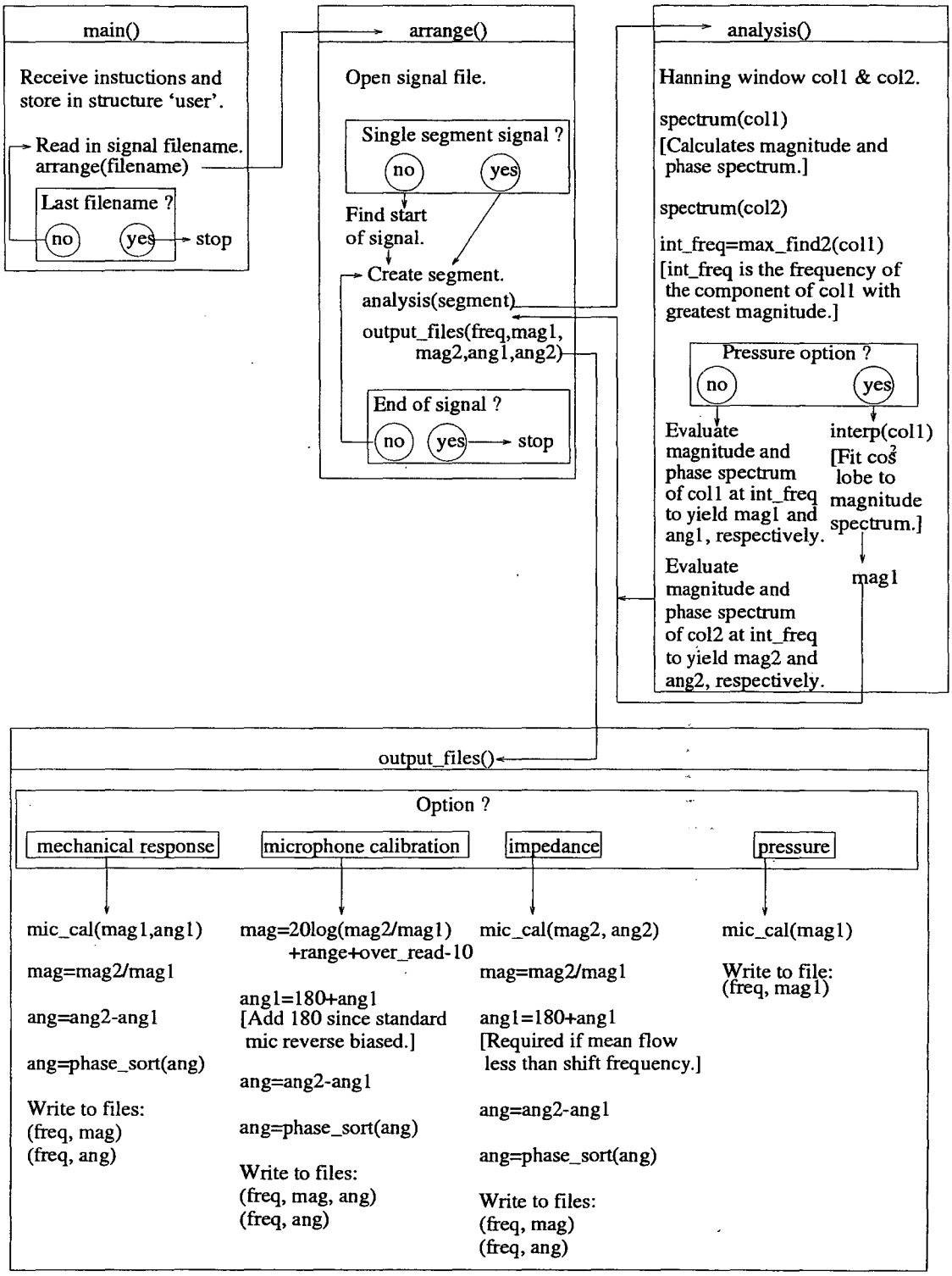

Figure C.1: Structure of the frequency response program.

Provided the program is run using a unix operating system several input files may be batch processed. To use this facility each of the input files should be stored in a directory which is otherwise empty. The input file names can be listed using the 'ls' command and the group of input files can then be copied and, in response to the appropriate screen prompt, pasted as a group into the terminal window which is being used to run the program. If the input files are labelled 'input1.txt' to 'inputn.txt' the program will output files 'input1.ang' to 'inputn.ang' each listing frequency in the first column and phase of frequency response in the second. Generally the program will also output files 'input1.mag' to 'inputn.mag' listing frequency in the first column and magnitude of frequency response in the second column. However if the microphone calibration option is selected, frequency, magnitude of microphone response and phase of microphone response are output to respectively the first, second and third columns of the '.mag' file.

C.4 Signal to Noise Ratio

If a single column file containing a 32768 point sample of a **sinusoidal** Doppler signal is input into the SNR program 'spec.c' it will write the SNR to the screen and also return a single column file listing the PSD of the Doppler signal.

The program first divides the Doppler signal up into 8 equal segments and then calculates the PSD and SNR of each segment individually before averaging the 8 values of SNR. Dividing the signal into segments has the effect of increasing the frequency interval between neighbouring points in the frequency domain, which consequently reduces random fluctuations in the spectrum around the crucial single peak.

Each of the segments is passed to the function snr() which windows the

segments with a Hanning window and then passes the data to the function spectrum() which calculates the FFT of the windowed segment. The function max_find2() finds the spectral coefficient with maximum amplitude and this central point and its two immediate neighbours are passed to the function interp(). Matovic and Tropea [66] observed that the Fourier transform of a Hanning window can be approximated by the central lobe of a cosine squared function (see section 4.5.2). The function interp() finds the unique cosine squared function which fits the three points passed from the function snr() and returns the fitting parameters to the function snr(). The signal power is calculated from the amplitude of the cosine squared lobe. The noise power is calculated by squaring all spectral components and then taking the sum of those squared components which lie outside the central lobe of the cosine squared function; the noise power is also adjusted to account for power loss due to the window function (see the source code at line 50 of snr()).

C.5 Simulation of Doppler Signal

The program 'simul.c' offers the option of either simulating Doppler signals by evaluating equation 4.25 or simulating only the the envelopes of Doppler signals by evaluating equation 4.32. The program assumes a simplified one-dimensional model in which seeding particles lie only on the x axis.

To run the program on a unix machine the user should enter the command line

```
simul param
```

where 'simul' is the name of the executable file and 'param' is the name of the file containing all the parameters for the simulation. The 'param' file can be created by editing the numerical values in the file below.

```
Particle_filename:                                  test
Doppler_signal(0)_or_envelope(1):                   0
Number_of_samples:                                  32768
Sample_rate(in_kHz):                                500
Acoustic_frequency(in_kHz):                         0.5
Amplitude_of_instantaneous_frequency(in_kHz):       20
Frequency_shift(in_kHz):                            100
Frequency_due_to_mean_flow(in_kHz):                 0
Number_of_particles:                                1
Noise_power                                         0.05
```

The 'Particle_filename' field stores the name of a file which lists the initial position of every seeding particle. The file should consist of a single column list of floats which describe the initial particle positions relative to the centre of the measuring 'volume' as a non-integer multiple of d, where d is the length of the one dimensional measuring 'volume'.

In the 'Noise_power' field the user should enter the desired noise power as a fraction of the signal power produced by a single particle positioned at the centre of the measuring 'volume' for the entire duration of the signal. Of course generally the seeding distribution is more complicated and is time varying, and therefore the SNR depends not only on the value of 'Noise_power', but also on the seeding distribution, as is the case in physical experiments. The program adds to the simulated Doppler signal random noise with a Gaussian probability distribution; the added noise simulates white shot-noise.

C.6 Random Distribution of Seeding Particles

The program 'rand_part.c' produces a single column output file listing the random initial positions of a group of seeding particles. The output file can be used as the input particle distribution file for the Doppler signal simulation program discussed above. A different random distribution is created each time the program is run.

C.7 Least Squares Fit to Standing Wave

The program 'lsf_sw.c' fits theoretical expressions for standing waves to experimental measurements carried out along the length of a tube terminated by an (almost) rigid end. The program provides the option of fitting equation 6.14 to probe microphone measurements of pressure amplitude or fitting equation 6.20 to LDA measurements of velocity amplitude scaled by the pressure amplitude at the rigid termination.

In response to an on screen prompt the user must provide the name of a two column input file which lists in the first column displacement from the rigid end, x, and lists in the second column either pressure or velocity amplitude scaled by the pressure amplitude at the rigid termination.

When used to process pressure measurements the program finds the set of $(A + B)$, θ and SWR values which minimise the sum of squared **relative** errors, where the squared relative error is defined as the difference between the square of the right hand side of equation 6.14 and the square of the measured pressure amplitude, all divided by the square of the measured pressure amplitude. Whereas with scaled velocity measurements the user must provide SWR and the program finds the $(A + B)$ and θ values which minimise the sum of squared **absolute** errors, where the squared absolute error is defined as the difference between the square of the right hand side of equation 6.20 and the square of the measured ratio of velocity amplitude at position x to pressure amplitude at the rigid termination. The range of possible values of $(A + B)$, θ and SWR can be altered at lines 8-14 of the function main().

The program outputs the optimum value of $(A + B)$, θ and SWR and also outputs a two column file listing in the first column displacement from the rigid termination and listing in the second column the best fit curve obtained by sub-

stituting the optimum values into either equation 6.14 or 6.20. In the case of scaled velocity measurements a second output file is produced listing in the first column displacement from the rigid end, x, and listing in the second column the phase of the velocity at x minus the phase of the pressure at the rigid termination.

C.8 Ensemble Average

The program 'phaseav.c' simultaneously ensemble averages velocity and microphone signals over an acoustic period. Of the programs written as part of this work the ensemble averaging program is the most complex; its structure is illustrated in figure C.2. The program can be run on a unix machine by entering the command line

```
ensembleav filename.txt paramfile shift sense
```

where 'ensembleav' is the name of the executable file, 'filename.txt' is a two column file listing a sampled LDA ANALOG OUT signal in the first column and a simultaneously sampled probe microphone signal in the second column, 'paramfile' is the name of a file containing parameters required by the program, 'shift' is a float equal to the frequency shift (in MHz) and 'sense' should equal '1' if the shift frequency is greater than the mean instantaneous frequency of the Doppler signal but should equal '0' if the shift frequency is less than the mean instantaneous frequency of the Doppler signal. Reversing the 'sense' setting changes the phase of the ensemble averaged LDA signal by π.

```
calibration_file:       longb.cal
no_pts:                 4096
convention(1=u,2=F):    1
filter_max/MHz:         1.0
scale(ms^-1/MHz):       3.29
sample_rate/KHz:        16.384
dB_range:               140
```

```
approx_freq/Hz:        320
no_phase_points:       64
threshold:             0.001
```

A suitable 'paramfile' can be produced by editing the numerical values in the file listed above. The entries in the 'paramfile' require some explanation. In the 'calibration_file' field the user should enter the name of the appropriate 3 column probe microphone calibration file; the calibration file can be produced using the frequency response program described in appendix C.3. The 'no_pts' field should be equal to the number of lines in the 'filename.txt' file. If the 'convention' field is set to '1' the program will output ensemble averaged acoustic particle velocity curves and data but if the field is set to '2' the same information will be presented as instantaneous frequency rather than velocity. The low pass cut off frequency of the tracker input filter should be entered in the 'filter_max' field. In the 'scale' field the user should enter the velocity to instantaneous frequency conversion factor dictated by the fringe spacing. The 'dB_range' is the gain setting of the probe microphone's measuring amplifier. The 'approx_freq' need not be known very accurately but should provide a rough indication of the acoustic frequency; the program accurately calculates the acoustic frequency from the averge time interval between negative gradient zero crossings and so it is important for the program to be aware of the approximate frequency because otherwise it would overestimate the fundamental frequency of a multi-harmonic pressure signal if the signal exhibited more than one negative gradient zero crossing per acoustic period. The 'no_phase_pts' is the number of phase bins (see section 6.3.1). The 'threshold' field is used to set the sensitivity of the signal dropout filter: if the square of the voltage difference between consecutive samples of the ANALOG OUT signal is less than the square of the value stored in the 'threshold' field then the function time_filter1() considers the signal to have suffered from signal

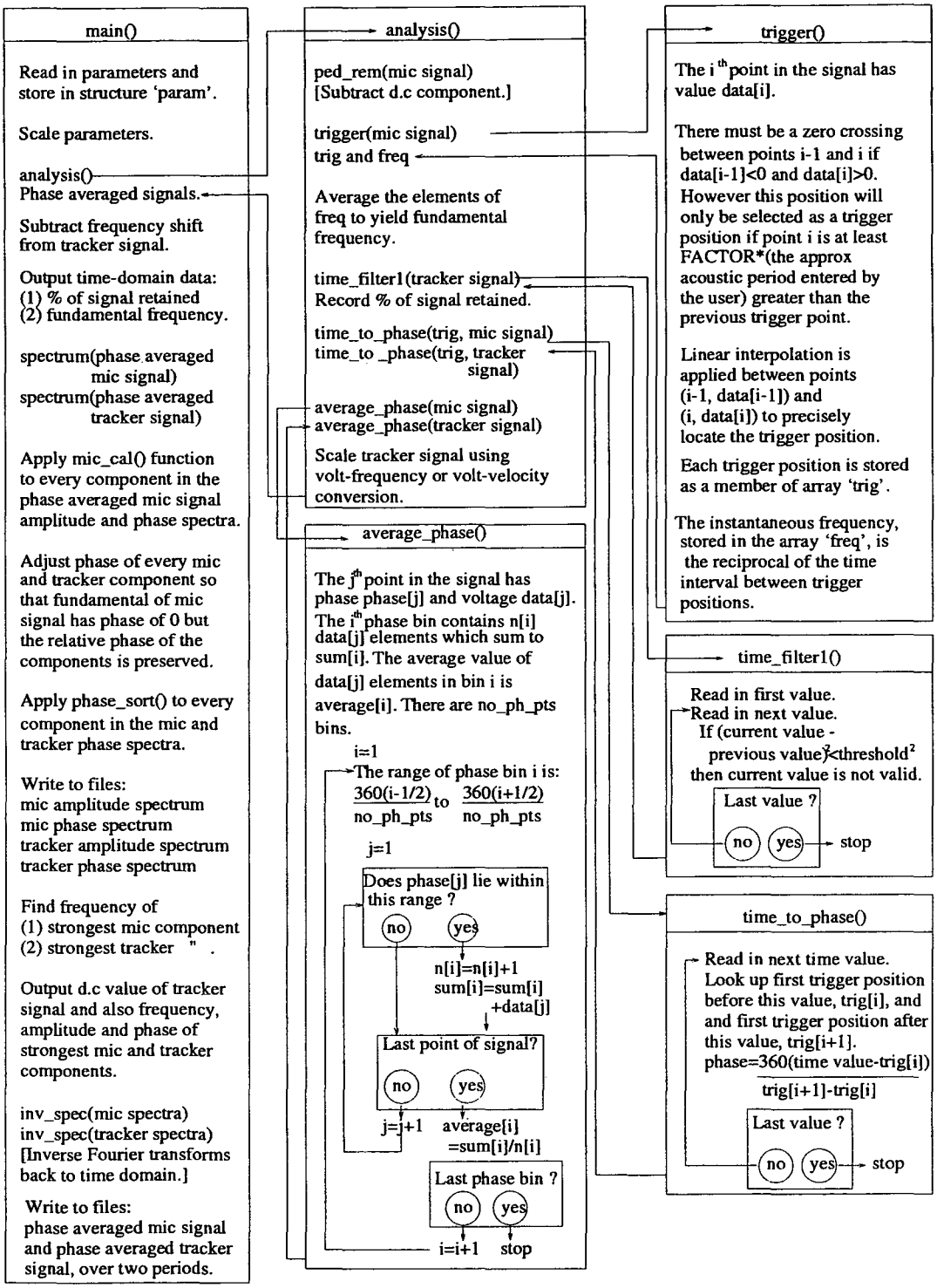

Figure C.2: Structure of the ensemble averaging program.

dropout in that region and both points will be removed from the signal before ensemble averaging.

The program automatically generates output filenames; if the input file containing the microphone and LDA signals is 'filename.txt' then filenames of the form 'filename.ext' will be generated, where '.ext' is one of several possible extensions. The most useful output files generated by the program include 'filename.pre', 'filename.psp' and 'filename.pph', which list respectively the ensemble averaged pressure, the amplitude of harmonic pressure components and the phase of harmonic pressure components. The 'filename.pre', 'filename.psp' and 'filename.pph' files were used to produce the top, middle and bottom graphs, respectively, in the left column of figure 6.20. Similarly 'filename.fre', 'filename.fsp' and 'filename.fph' which list respectively the ensemble averaged velocity, the amplitude of harmonic velocity components and the phase of harmonic velocity components. The 'filename.fre', 'filename.fsp' and 'filename.fph' files were used to produce the top, middle and bottom graphs, respectively, in the right column of figure 6.20.

The program also appends text to an output file which is automatically labelled with the calendar date of the day the program is run. An example of the output text is listed below. The file lists the percentage of the ANALOG OUT signal retained after removal of dropout portions, the shift frequency (scaled in velocity units if 'convention' is set to '1'), the fundamental acoustic frequency, the D.C. component of velocity, the magnitude of the strongest pressure component, the magnitude of the strongest velocity component, the ratio of the magnitude of the strongest pressure component to the magnitude of strongest velocity component, and the phase angle of the strongest pressure component minus the phase angle of the strongest velocity component.

```
filename.txt paramfile

98.999023 percent of signal retained
shift frequency/velocity is 1645.000000
acoustic frequency is 323.112976

mean v (after removing freq. shift)= -43.007355
p cpt 3 is strongest, magnitude = 68.001839 (46.827751 percent of power)
v cpt 2 is strongest, magnitude = 107.537064 (49.735228 percent of power)
comparing strongest components: mag(p/v)= 0.632357 and ang(p/v)= -103.109833
```

In the output text above and in the six output files discussed above pressures are always specified in Pa, phase is always specified in degrees and acoustic frequency is always specified Hz. However velocity/instantaneous frequency is specified in units of velocity or units of frequency, depending on the 'convention' setting, the velocity (frequency) units being mm s^{-1}, (kHz) if 'filter_max is set to 1.0 or below, but m s^{-1} (MHz) if 'filter_max is set to greater than 1.0.

Appendix D

Computer Program Listings

Complete listings of the computer programs 'matrix.c', 'lsf_reson.c', 'auto.c', 'spec.c', 'simul.c', 'rand_part.c', 'lsf_sw.c' and 'phaseav.c' are provided on the attached CD-ROM.

Glossary of Abbreviations

FFT:	fast Fourier transform
FM:	frequency modulation
mf:	mezzo forte
LDA:	laser Doppler anemometry
PMT:	photomultiplier tube
ppp:	piano pianissimo
PSD:	power spectral density
RMS:	root mean square
SNR:	signal–to–noise ratio
SPL:	sound pressure level
SWR:	standing wave ratio
VCO:	voltage controlled oscillator

Bibliography

[1] S. Adachi and M. Sato. Trumpet sound simulation using a two-dimensional lip vibration model. *J.Acoust.Soc.Am.*, 99:1200–1209, 1996.

[2] G. Arfken. *Mathematical Methods for Physicists*, pages 8–9. Academic Press Inc., 3 edition, 1985.

[3] Y. Aurégan and C. Depollier. Snoring : linear stability analysis and in-vitro experiments. *Journal of Sound and Vibration*, 188:39–54, 1995.

[4] D. Ayers. New perspectives on the brass instruments. In *Proc. ISMA 1998*, pages 1959–1960, Leavenworth, WA, USA, June 1998.

[5] J. Backus. Small-vibration theory of the clarinet. *J.Acoust.Soc.Am.*, 35:305–313, 1963.

[6] J. Backus. Input impedance curves for the brass instruments. *J.Acoust.Soc.Am.*, 60:470–480, 1976.

[7] H. Bailliet, X. Pelorson, B. Richardson, and T. Lallouache. Lip vibration and pressure recordings during french horn playing. In *Proc. ISMA 1995*, Dourdan, France, 1995.

[8] R.D. Blevins. *Flow-induced vibration.* Robert E. Krieger Publishing Company, 1986.

[9] V.V. Bolotin. *Nonconservative Problems of the Theory of Elastic Stability.* Pergamon Press, 1963.

[10] H. Bouasse. *Instruments á Vent.* Reprinted (in French) by Delagrave, 1986.

[11] R.N. Bracewell. *The Fourier Transform and its Applications.* McGraw-Hill, 2 edition, 1986.

[12] O. Brandt, H. Freund, and E. Heidemann. Schwebstoffe im schallfeld. *Zeitschrift fur Physik*, 104:511–533, 1937.

[13] H-E. de Bree, P. Leussink, T. Korthorst, and M. Elwenspoek. The two sensor microflown: an improved flow sensing principle. In X. Leuven, editor, *Proc. Eurosensors*, pages 1301–1304, 1996.

[14] Bruel and Kjaer, Denmark. *Condenser microphones and microphone preamplifiers for acoustic measurments*, 1982.

[15] D.M. Campbell. Input impedance measurements on historic brass instruments. *Proc. Institute of Acoustics*, 9:111–118, 1987.

[16] D.M. Campbell and C. Greated. *The musician's guide to acoustics.* Dent, 1987.

[17] R. Caussé, J. Kergomard, and X. Lurton. Input impedance of brass musical instruments– comparison between experiment and numerical models. *J.Acoust.Soc.Am.*, 75:241–254, 1984.

[18] Y.M. Chang. Reed stability. *Journal of Fluids and Structures*, 8:771–783, 1994.

[19] F.C. Chen and G. Weinreich. Nature of the lip reed. *J.Acoust.Soc.Am.*, 99:1227–1223, 1996.

[20] D.C. Copley and W.J. Strong. A stroboscopic study of lip vibrations in a trombone. *J. Acoust. Soc. Am.*, 99:1219–1226, 1996.

[21] I.B. Crandall. *Theory of vibrating systems and sound.* Macmillan & Co., 1927.

[22] J.S. Cullen, J. Gilbert, D.M. Campbell, and C.A. Greated. Acoustical measurements in resonators driven by an artificial mouth, oscillation threshold behaviour. In *Proc. ISMA 1998*, pages 141–146, Leavenworth, WA, USA, June 1998.

[23] J.P. Dalmont and A.M. Bruneau. Acoustic impedance measurement: plane wave mode and first helical-mode contibutions. *J. Acoust. Soc. Am.*, 91:3026–3033, 1991.

[24] J.P. Dalmont, J. Gilbert, and J. Kergomard. Reed instruments, from small to large amplitude periodic oscillations and the helmholtz motion analogy. Accepted for publication in Acustica, 1999.

[25] DANTEC. *Laser Doppler Anemometry*, Aug 1983.

[26] M.R. Davis and K.J. Hews-Taylor. Laser doppler measurement of complex acoustic impedance. *J. Sound Vib.*, 107:451–470, 1986.

[27] P. Dietz and N. Amir. Synthesis of trumpet tones by physical modeling. In *Proc. ISMA 1995*, Dourdan, France, 1995.

[28] DISA. *Instruction Manual for 55N20 Frequency Tracker.*

[29] DISA. *Service Manual for 55N20 Frequency Tracker.*

[30] C.S. Durrani and C.A. Greated. *Laser Systems in Flow Measurement.* Plenum Press, 1977.

[31] F. Durst, A. Melling, and J. Whitelaw. *Principles and practice of laser Doppler anemometry.* Academic Press, 1976.

[32] F.J.M. Eerden, H-E de Bree, and H. Tijdeman. Experiments with a new acoustic particle velocity sensor in an impedance tube. *Sensors and Actuators A*, 69:126–133, 1998.

[33] S.J. Elliot. Non–linear regeneration mechanisms in wind instruments. *Journal de Physique*, 40:341–345, 1982.

[34] S.J. Elliot and J.M. Bowsher. Regeneration in brass wind instruments. *Journal of Sound and Vibration*, 83:181–217, 1982.

[35] S.J. Elliot, J.M. Bowsher, and P. Watkinson. Input and transfer response of brass wind instruments. *J. Acoust. Soc. Am.*, 72:1747–1760, 1982.

[36] R. Di Federico and G. Borin. Synthesis of the trumpet tone based on physical models. *ICMC 97*, pages 410–413, 1997.

[37] N.H. Fletcher. Excitation mechanisms in woodwind and brass instruments. *Acustica*, 43:63–72, 1979.

[38] N.H. Fletcher. Autonomous vibration of simple pressure-controled valves in gas flows. *J. Acoust. Soc. Am. 93*, 93:2172–2180, 1993.

[39] N.H. Fletcher and T.D. Rossing. *The physics of musical instruments*, pages 355–359 & 391–392. Springer-Verlag, 1 edition, 1991.

[40] U. Frisch. *Turbulence: the legacy of A. N. Kolmogorov*, pages 57–67. Press Syndicate of the University of Cambridge, 1995.

[41] F.M Gardner. *Phaselock Techniques.* John Wiley & Sons, 1 edition, 1979.

[42] W. K. George and J. L. Lumley. The laser-doppler velocimeter and its application to the measurement of turbulence. *J. Fluid Mech*, 60:321–362, 1973.

[43] J. Gilbert and J.F. Petiot. Brass instruments, some theoretical and experimental results. In *Proc. ISMA 1997 in Proc. Institute of Acoustics*, volume 19, pages 391–400, Edinburgh, UK, 1997.

[44] J. Gilbert, S. Ponthus, and J.F. Petiot. Artificial buzzing lips and brass instruments: Experimental results. *J. Acoust. Soc. Am.*, 104:1627–1632, 1998.

[45] R.J. Goldstein, editor. *Fluid Mechanics Measurement*, chapter 4. Taylor & Francis, 2 edition, 1996.

[46] N. Grand, J. Gilbert, and F. Laloe. Oscillation threshold of woodwind instruments. *Acustica*, 82:137–151, 1996.

[47] V.A. Grechikhin and B.S. Rinkevichius. Digital holbert transform for processing laser doppler vibrometry signals. In *Proc. 2nd Int. Conf. on Vibration Measurement by Laser Techniques*, Ancona, Italy, 1996.

[48] D.B. Hann. *Simultaneous Measurement of Acoustic Fields and Flow Fields using Optical Methods.* PhD thesis, The University of Edinburgh, 1995.

[49] D.B. Hann and C. Greated. The measurement of sound fields using laser doppler anemometry. *Acustica*, 85:401–411, 1999.

[50] D.B. Hann et al. Laser doppler measurements in complex sound fields. In *Proc. 7th Int. Conf. in Laser Anemometry Advances and Applications*, pages 91–94, Karlsruhe, Germany, 1997.

[51] H.J.F. Helmholtz. *On the sensation of tones (1877).* Translated by A.J.Ellis, reprinted by Dover, 1954.

[52] P. Herzog, J.C. Valiere, and Duffosse S. Laser doppler velocimetry in acoustics: principle and signal processing. In *Proc. 15th Int. Conf. Acous.*, pages 91–94, Trondheim, Norway, 1995.

[53] P. Herzog, J.C. Valiere, V. Valeau, and G. Tournois. Acoustic velocity measurement by means of laser doppler velocimetry. In *Symp. on the application of laser techniques to fluids*, Lisbon, Portugal, 1996.

[54] A. Hirschberg, J. Gilbert, R. Msallam, and A.P.J Wijnands. Shock waves in trombones. *J. Acoust. Soc. Am.*, 99:1754–1758, 1996.

[55] R.J. Hirschberg, J. Kergomard, and G. Weinreich, editors. *Mechanics of musical instruments*, pages 311–317. Springer–Verlag, 1995.

[56] P.J. Holmes. Bifurcations to divergence in flow induced oscillations: a finite dimensional analysis. *Journal of Sound and Vibration*, 53:471–503, 1977.

[57] K. Ishizaka and J. Flanagan. Synthesis of voiced sounds from a two-mass model of the vocal cords. *Bell Syst. Tech. J.*, 51:1233–1268, 1972.

[58] K. Ishizaka, J.C. French, and J. Flanagan. Direct determination of vocal tract impedance. *I.E.E.E. Transactions on Acoustic Speech and Signal Processing*, ASSP-23:370–373, 1975.

[59] D. H. Keefe. Acoustical wave propagation in cylindrical ducts. *J. Acoust. Soc. Am.*, 75:58–62, 1984.

[60] C.H. Keith and J.C. Derrick. Measurement of the particle size distribution

and concentration of cigarette smoke by the 'conifuge'. *Journal of Colliod Science*, 15:340–356, 1960.

[61] L.E. Kinsler, A.R. Frey, A.B. Coppens, and J.V. Sanders. *Fundamentals of Acoustics.* John Wiley & Sons, 3 edition, 1982.

[62] T. Loizeau and Y. Gervais. Measurement of the acoustic velocity by laser doppler anemometry. *Acustica*, 83:945–954, 1997.

[63] C.G. Lomas. *Fundamentals of Hot Wire Anemometry.* Cambridge University Press, 1986.

[64] N.J.C. Lous, G.C.J. Hofmans, R.N.J. Veldhuis, and A. Hirschberg. A symetrical two-mass vocal-fold model coupled to vocal tract and trachea, with application to prosthesis design. *Acustica*, 84:1135–1150, 1999.

[65] D.W. Martin. Lip vibrations in a cornet mouthpiece. *J. Acoust. Soc. Am.*, 13:305–308, 1942.

[66] D. Matovic and C. Tropea. Spectral peak interpolation with application to lda signal processing. *Meas. Sci. Technol.*, 2:1100–1106, 1991.

[67] W.D. McComb. *The Physics of Fluid Turbulence*, pages 61–63. Oxford Science Publications, 1990.

[68] W.D. McComb. *The Physics of Fluid Turbulence*, pages 83–84. Oxford Science Publications, 1990.

[69] R. Msallam, S. Dequidt, S. Tassart, and R. Caussé. Physical model of the trombone including non-linear propagation effects. In *Proc. ISMA 1997 in Proc. Institute of Acoustics*, volume 19, pages 419–424, Edinburgh, UK, 1997.

[70] B. Mulgrew, P. Grant, and J. Thompson. *Digital Signal Processing Concepts & Applications.* Macmillan Press Ltd., 1999.

[71] K. Nadaoka, M. Hino, and Y. Koyano. Structure of the turbulent flow field under breaking waves in the surf zone. *J. Fluid. Mech*, 204:359–387, 1989.

[72] C.J. Nederveen. *Acoustical Aspects of Woodwind Instruments.* Knuf, 1969.

[73] G. Paál, J. Angster, E. Garen, and A. Miklós. Sound and flow in the mouth of flue organ pipes. part 1. fully developed state. In *Proc. ISMA 1997 in Proc. Institute of Acoustics*, volume 19, pages 295–301, Edinburgh, UK, 1997.

[74] X. Pelorson, A. Hirschberg, R.R. Van Hassel, A.P.J. Wijnands, and Y. Auregan. Theoretical and experimental study of quasi-steady flow separation within the glottis during phonation: application to a modified two-mass model. *J. Acoust. Soc. Am.*, 96:3416–3431, 1994.

[75] R.L. Pratt, S.J. Elliott, and J.M. Bowsher. The measurement of the acoustic impedance of brass instruments. *Acustica*, 38:236–246, 1977.

[76] Y. Rocard. *General Dynamics of Vibrations.* Translated and reprinted by Crosby lockwood & son ltd., 1960.

[77] X. Rodet and C. Vergez. Physical models of trumpet-like instruments detailed behaviour and model improvements. In *Proc. ICMC 1996*, Hong-Kong, 1996.

[78] M.J. Rudd. A new theoretical model for the laser doppler meter. *J. Phys. E*, 2:723–726, 1969.

[79] J. Saneyoshi, H. Teramura, and S. Yoshikawa. Woodwind and brasswind instruments. *Acustica*, 62:194–210, 1987.

[80] D.B. Sharp. *Pulse Reflectometry.* PhD thesis, The University of Edinburgh, 1997.

[81] J.P. Sharpe, C.A. Greated, and D.M. Campbell. The measurement of complex acoustic impedance using photon correlation spectroscopy. *Acustica*, 66:266–289, 1988.

[82] F.G. Stremler. *Introduction to Communication Systems.* Addison-Wesley, 1977.

[83] W.J. Strong and J.D. Dudley. Simulation of a player–trumpet system. In *Proc. Stockholm Music Acoustics Conference*, pages 520–524, 1993.

[84] K.J. Taylor. Absolute measurement of acoustic particle velocity. *J. Acoust. Soc. Am.*, 51:691–694, 1976.

[85] K.J. Taylor. Absolute calibration of mirophones by a laser-doppler technique. *J. Acoust. Soc. Am.*, 70:939–945, 1981.

[86] H. Tennekes and J.L. Lumley. *A first course in turbulence*, pages 19–23. MIT Press, 1972.

[87] J.J. Thomsen. *Vibrations and stability, order and chaos.* McGraw-Hill, 1997.

[88] D.L. Tritton. *Physical Fluid Dynamics*, pages 314–319. Oxford Science Publications, 2 edition, 1988.

[89] D.L. Tritton. *Physical Fluid Dynamics*, pages 109–111. Oxford Science Publications, 2 edition, 1988.

[90] D.L. Tritton. *Physical Fluid Dynamics*, pages 7–19. Oxford Science Publications, 2 edition, 1988.

[91] V. Valeau. *Mesure de la vitesse acoustique particulaire par anenometrie laser Doppler: estimation de frequence instantanee a variation sinsoidale, validation de las mesure.* PhD thesis, l'Université du Maine, 1999.

[92] C. Vergez and X. Rodet. Model of the trumpet fundtionning: real time simulation and experiments with an artificial mouth. In *Proc. ISMA 1997 in Proc. Institute of Acoustics*, volume 19, pages 425–432, Edinburgh, UK, 1997.

[93] C. Vergez and X. Rodet. Experiments with an artificial mouth for trumpet. In *Proc. ISMA 1998*, pages 153–158, Leavenworth, WA, USA, June 1998.

[94] J.F. Vignola, Y.H. Berthelot, S. Jones, and J. Jarzynski. Equation of motion of microparticles in suspension in an insonified medium. *J. Acoust. Soc. Am.*, 92:332–334, 1992.

[95] G. Weinreich. Remarks on the reed-air column system as coupled oscillators. In *Proc. 123rd ASA*, page 2374, April 1992.

[96] A.P.J. Wijnands and A. Hirschberg. Effect of a pipe neck downstream of a double reed. In *Proc. ISMA 1995*, pages 148–151, Dourdan, France, 1995.

[97] T.A. Wilson and G.S. Beavers. Operating modes of the clarinet. *J. Acoust. Soc. Am.*, 56:653–658, 1974.

[98] W.E. Worman. *Self-sustained nonlinear oscillations of medium amplitude in clarinet-like systems.* PhD thesis, Case Western Reserve University, 1971.

[99] S. Yoshikawa. Acoustical behavior of brass player's lips. *J. Acoust. Soc. Am.*, 97:1929–1939, 1995.

Publications

Conference Papers

M.O. Van Valstijn, J.S. Cullen and D.M. Campbell. Modeling viscothermal wave propagation in wind instrument air columns. In *Proc. ISMA 1997*, pages 413-418, Edinburgh, U.K., August 1997.

J.S. Cullen, D.B. Hann, D.M. Campbell and C.A. Greated. Methods of processing laser Doppler anemometry signal to extract sound field information. In *Proc. 16th ICA/ 135th ASA*, pages 1959-1960, Seattle, WA, USA, June 1998.

J.S. Cullen, J. Gilbert, D.M. Campbell and C.A. Greated. Acoustical measurements in resonators driven by an artificial mouth, oscillation threshold behaviour. In *Proc. ISMA 1998*, pages 141-146, Leavenworth, WA, USA, June 1998.

J.S. Cullen, J. Gilbert and D.M. Campbell. Mechanical response of artificial buzzing lips (abstract). In *Program of Forum Acusticum 1999*, page S76, Berlin, Germany, March 1999.

Journal Papers

J.S. Cullen, C.A. Greated and D.M. Campbell. LDA measurement of sound: amplitude modulation of laser Doppler signals. *Meas. Sci. Technol.*, 10:812-823, 1999.

J.S. Cullen, J. Gilbert and D.M. Campbell. Brass instruments: linear stability analysis and experiments with an artificial mouth. Accepted for publication in *Acustica*.